Numerical Investigation of Ducted Propellers for Novel Rotorcraft Configurations

by
Tao Zhang

A thesis submitted in partial
fulfillment of the requirements for
the degree of Doctor of Philosophy
University of Glasgow
School of Engineering
May 2022

Declaration

I certify that the thesis presented here for examination for a PhD degree of the University of Glasgow is solely my own work other than where I have clearly indicated that it is the work of others (in which case the extent of any work carried out jointly by me and any other person is clearly identified in it) and that the thesis has not been edited by a third party beyond what is permitted by the University's PGR Code of Practice.

I declare that the thesis does not include work forming part of a thesis presented successfully for another degree.

I declare that this thesis has been produced in accordance with the University of Glasgow's Code of Good Practice in Research.

I acknowledge that if any issues are raised regarding good research practice based on review of the thesis, the examination may be postponed pending the outcome of any investigation of the issues.

September 2021

....

Tao Zhang

Abstract

The ducted propeller is a promising propulsion or lift generator for novel rotorcraft configurations, considering the stringent restrictions on safety, efficiency, and noise/carbon emissions. However, extensive research work is still needed to further understand the aerodynamic and acoustic characteristics of ducted propellers at various conditions. This thesis aims to deliver high-fidelity and systematic investigations of the aerodynamics, acoustics, and optimisation of ducted/open propellers at various conditions.

A detail survey of past works on ducted propellers was first performed to analyse the research status and challenges. Critical assessments of available data sets for validation were also carried out. Numerical validation was then performed to verify the meshing, numerical methods, and simulation strategies for ducted propellers using a test case by NASA. High-fidelity CFD methods and lower-order tools were employed and compared at a range of conditions. Detailed analyses of the aerodynamic performance of ducted/open propellers were later performed at various advance ratios, pitch angles, and crosswind angles. The near- and far-field acoustic features of the ducted/open propellers in axial flight was also computed and inspected closely.

A gradient-based design optimisation framework was also compiled to improve the ducted propeller performance at high advance ratios by varying the duct and blade shapes. The gradients of aerodynamic performance with respect to the design variables were computed using the discrete adjoint CFD methods. The ducted propeller thrust was successfully increased at high advance ratios after the optimisation. The far-field acoustics of the optimised designs was only mildly affected by the optimisation. A parametric study of the equivalent ducted/open propellers was also conducted to further evaluate the influence of different design and operating conditions. An automatic mesh generation tool chain was developed to ease the efforts required for the mesh generation.

The ducted/open propellers were then installed under a main rotor to investigate performance changes due to the aerodynamic interactions. The main rotor downwash induced imbalanced disk loadings and loading variations with complex frequency compositions. The duct was found to provide aerodynamic shielding for the blades enclosed, but it also created considerable blockage to the downwash flow. A simplified modelling approach for the rotor/propeller interactions using actuator disk models was later put forward. By introducing an inflow distortion metric quantifying the aerodynamic interactions, an optimisation framework was compiled to minimise the rotor/propeller interference by changing the propeller position, i.e. the configuration optimisation. The inflow distortion factor was used as the objective, and its gradients with respect to the propeller position were computed using the adjoint method. Gradient-based and gradient-free optimisation approaches were proposed and assessed. With constraints on the pitching and rolling moments, the optimisation managed to effectively reduce the rotor/propeller interference. The optimisation results were further verified using blade-resolved simulations.

Publications

Journal papers:

1. T. Zhang, G. N. Barakos, “High-fidelity Numerical Investigations of Rotor-Propeller Aerodynamic Interactions”, Aerospace Science and Technology (accepted), 2022.

2. D. Han, T. Zhang, G. N. Barakos, “Comparison of Design Features of Quadrotor Aircraft and Helicopters from the Point of View of Flight Performance”, Aerospace Science and Technology (under review), 2022.

3. T. Zhang, G. N. Barakos, “Towards Vehicle-level Optimisation of Compound Rotorcraft Aerodynamics”, AIAA Journal, Vol. 60, No.3, pp. 19371957, 2021.

4. T. Zhang, G. Qiao, D. Smith, G. N. Barakos, and A. Kusyumov, “Parametric Study of Aerodynamic Performance of Equivalent Ducted/Un-ducted Rotors”, Aerospace Science and Technology, Vol. 117, pp. 106984. 2021.

5. T. Zhang, G. N. Barakos, “High-Fidelity Numerical Analysis and Optimisation of Ducted Propeller Aerodynamics and Acoustics”, Aerospace Science and Technology, Vol. 113, pp. 106708, 2021.

6. T. Zhang, G. N. Barakos, “High-fidelity CFD Validation and Assessment of Ducted Propellers for Aircraft Propulsion”, Journal of American Helicopter Society, Vol. 66, No. 1, pp. 1-28, 2021.

7. T. Zhang, G. N. Barakos, “Review on Ducted Fans for Compound Rotorcraft”, The Aeronautical Journal, Vol. 124, No. 1277, pp. 941-974, 2020.

Conference presentations and papers in proceedings:

1. T. Zhang, G. N. Barakos, “Aerodynamic Simulation and Adjoint-based Optimisation of Rotorcraft Configurations,” 47th European Rotorcraft Forum, Glasgow, UK, Sept 2021.

2. T. Zhang, G. N. Barakos, “High-fidelity Numerical Investigation of Ducted Propeller Aerodynamics/Acoustics and Adjoint-based Design Optimisation,” 77th Annual Forum of Vertical Flight Society, May 2021.

3. T. Zhang, George N. Barakos, “High-Fidelity Numerical Analysis of Ducted Propellers Aerodynamics and Acoustics,” WCCM-ECCOMAS Congress 2021 Special Technical Session and in Springer series, Jan 2021.

4. T. Zhang, G. N. Barakos, “Development of Simulation Tools for High Fidelity Analysis of Compound Rotorcraft,” AIAA SciTech 2020, Orlando, USA, Jan 2020.

5. T. Zhang, George N. Barakos. "Towards Optimisation of Compound Rotorcraft." 45th European Rotorcraft Forum, Warsaw, Poland, Sept 2019.

Presentations at workshops (without proceedings):

1. T. Zhang, G. N. Barakos, "Towards Aerodynamic Optimisation of Compound Rotorcraft," 4th UK Vertical Lift Network Workshop, April 2019, Cheshire, UK.

2. T. Zhang, G. N. Barakos, "Numerical Simulation and Adjoint-based Optimisation of Rotor/propeller Aerodynamic Interference," 5th UK Vertical Lift Network Workshop, April 2021, virtual.

Technical Notes:

1. T. Zhang, "Acoustic Computations in the HMB3 Framework," TN-22-01, CFD Laboratory, James Watt School of Engineering, University of Glasgow, 2022.

2. T. Zhang, "New Actuator Disk Modules in HMB3," TN-21-01, CFD Laboratory, James Watt School of Engineering, University of Glasgow, 2021.

3. T. Zhang, "Automatic Geometry Composition and Grid Generation using ICEM CFD," TN-19-01, CFD Laboratory, James Watt School of Engineering, University of Glasgow, 2019.

Acknowledgements

I wish to express my unreserved gratitude to my supervisor Prof. George N. Barakos for all his support and guidance throughout the years. None of these would be possible without his efforts since the very beginning. I also want to extend my thanks to Dr. Mark Woodgate, Dr. Rene Steijl, the GARTEUR group, and the UK Vertical Lift Network, and the University of Glasgow for their kind help and support during my study.

I want to thank every member of the CFD lab at Glasgow for creating a family-like atmosphere in the group, which I sincerely enjoyed and appreciated. Thanks to Ross, Thomas, Blaga, and other senior members for their kind support throughout my study. Special thanks to Federico Rovere for all the hard and good times we have been through. Grazie vecchio!

I also wish to offer my thanks to Ye, Fan, Geng, and all other friends at Glasgow. I appreciate our friendships, all the adventures, and all the dumb things we have been through. I cherish all my memories with you and may our paths cross again soon in the near future.

Special thanks to Ms. Piaopiao Pan for her support, patience, accompany, and love. You are one of the best things that have ever happened to me. I also want to thank my parents, my family, and all my friends back in China for all their love and support, and my apologies for being away for all these years.

The financial support of the University of Glasgow and the China Scholarship Council is also gratefully acknowledged.

Contents

List of Figures

List of Tables

Nomenclature

Latin Symbols

$(\mathbf{F}, \mathbf{G}, \mathbf{H})$ Inviscid Flux Vector

$(\mathbf{F^v}, \mathbf{G^v}, \mathbf{H^v})$ Viscous Flux Vector

$(\mathbf{u}, \mathbf{v}, \mathbf{w})$ Flow Velocity in x, y, z Cartesian Directions, m/s

$\mathbf{I}$ Objective/Cost Function

$\mathbf{R}$ Flow Residual Vector

$\mathbf{W}$ Conservative Flow Variables

A Area, m^2

AoA Angle of Attack, $^\circ$

b Wing Span Length, m

C Chord Length, m

c Sound Speed, m/s

C_d Drag Coefficient, $C_d = Drag/(0.5\rho_{ref}(V_{ref})^2 A_{ref})$

$C_{F_{x,y,z}}$ x, y, z Force Coefficient, $C_{F_{x,y,z}} = F_{x,y,z}/(0.5\rho_{ref}(V_{ref})^2 A_{ref})$

C_l Lift Coefficient, $C_l = Lift/(0.5\rho_{ref}(V_{ref})^2 A_{ref})$

$C_{M_{x,y,z}}$ x, y, z Moment Coefficient, $C_{M_{x,y,z}} = M_{x,y,z}/(0.5\rho_{ref}(V_{ref})^2 A_{ref} L_{ref})$

C_p Pressure Coefficient, $C_p = P - P_{ref}/(0.5\rho_{ref}(V_{ref})^2)$

$C_Q, C_{Q_{UK}}$ Rotor Torque Coefficient, $C_Q = Q/(0.5\rho_{ref}(V_{tip})^2 \pi R^3)$

$C_T, C_{T_{UK}}$ Rotor Thrust Coefficient, $C_T = T/(0.5\rho_{ref}(V_{tip})^2 \pi R^2)$

Cp_{uns} Unsteady Pressure Signal, $Cp_{uns} = 100P - P_\infty/(0.5\rho_\infty(V_{tip})^2)$

$F_{x,y,z}$ Force in x, y, z Directions, N

Ix Axial Inflow Distortion Factor

L/D Lift-to-Drag Ratio, $L/D = C_l/C_d$

L_{ref} Reference Length, m

$M_{x,y,z}$ Moment in x, y, z Directions, Nm

Ma Mach Number, $Ma = V/c$

P Pressure, Pa

p' Sound Pressure, Pa

p_{ref} Acoustic Reference Pressure, $p_{ref} = 2 \times 10^{-5} [Pa]$

Q Torque, Nm

R Blade Radius, m

r Blade Radial Position

Re Reynolds Number, $Re = V_{ref} L_{ref} / \nu_{ref}$

RPM Revolutions Per Minute

RSD Relative Standard Deviation, $RSD(X) = rms(X - X_{avg})/X_{avg}$

SPL Sound Pressure Level, $SPL = 20 log_{10}(rms(p')/p_{ref})$

T Thrust, N

t Time, s

V Flow Velocity, m/s

Greek Symbols

δ_{ij} Kronecker Delta

η Froude Efficiency, $\eta = \frac{TV_\infty}{Q\Omega}$

Γ Circulation, m^2/s

γ Specific Heat Ratio, $\gamma = 1.4$

α Design Variable Vector

■ Duct Expansion Ratio$\Lambda = \frac{D_{exit}}{D_{rotor}}$

λ Adjoint Vector

μ Laminar Viscosity ($kg/(ms)$) or Advance Ratio $\mu = \frac{V_\infty}{V_{tip}}$

μ_t Eddy Viscosity, $kg/(ms)$

ν Kinematic Viscosity, m^2/s

Ω Vorticity Magnitude (s^{-1}) or Rotational Speed (rad/s)

ψ, Ψ Rotor Azimuth Angle, rad

ρ Density, kg/m^3

σ_r, σ_{ax} Radial/Axial Actuator Disk Strength Factor

τ Pseudo Time

τ_{ij} Viscous Stress Tensor, Pa

β Blade Pitch Angle, $^\circ$

Mathematical Symbols

$\dot{(*)}$ Temporal Derivative

$\overline{(*)}$ Reynolds Averaging

$\widetilde{(*)}$ Favre Averaging

$rms(*)$ Root-Mean-Square Value

Subscripts

∞, inf Freestream Value

$_{75}$ Value at 75% Blade Radius

avg Averaged

ax Rotor Axial Direction Value

DP,dp Ducted Propeller

max Maximum

min Minimum

OP,op Open Propeller

ref Reference Value

rt Blade Root Value

t Blade Tangential Direction Value

tip,tp Blade Tip Value

x,y,z Values in x,y,z Cartesian Directions

Superscripts

$''$ Disturbance Values

m,n Time Step

T Transpose

v Viscous

Acronyms

(U)RANS (Unsteady) Reynolds Averaged Navier Stokes

AD Actuator Disk

AD Actuator Line

AIAA American Institute of Aeronautics and Astronautics

BPF Blade Passing Frequency

CFD Computational Fluid Dynamics

CST Class Shape Transformation

DES Detached Eddy Simulation

DFDC Ducted Fan Design Code

EGO Efficient Global Optimisation

EI Expected Improvement

FW-H Ffowcs Williams-Hawkings

GCI Grid Convergence Index

HMB3 Helicopter Multi-Block 3

LES Large Eddy Simulation

NASA National Aeronautics and Space Administration

RRF Rotating Reference Frame

SAS Scale Adaptive Simulation

SLSQP Sequential Least-Square Quadratic Programming

SST Shear Stress Transport

UAV Unmanned Aerial Vehicle

Chapter 1

Introduction[1]

In recent years, a surge in Urban Aerial Mobility (UAM) research and development is noted around the world [1], featuring novel aircraft configurations and Electrical Vertical Take-Off and Landing (eVTOL). The UAM concept has been hailed as the next revolution in aviation, yet significant efforts are needed to form a solid, scientific foundation for design, manufacturing, operations etc. Specifically, future UAMs should be both environment- and community-friendly, while maintaining excellent aerodynamic performance especially at low speeds or hover. There are further demands for low carbon/nitrogen and noise emissions, as well as, safety and less intrusive aircraft wake, since the UAMs will operate mostly in the urban environments. As a core component of aerial vehicles, the choice and optimal design of a propulsor thus becomes the key topic to be settled.

The ducted rotor/propeller can be a very favourable choice of propulsion for future UAMs fulfilling the stringent efficiency and emission requirements. The ducted propeller, or ducted/shrouded fan/rotor, is a propeller enclosed in an annular duct with aerofoil-like sections. This concept was first examined experimentally by Stipa[2] as "intubed propellers" in the 1930s (Figure 1.1(a)), and the experimental prototype *Stipa-Caproni* (Figure 1.1(b)) was built as a demonstration and test-bed. Soon after, this concept was widely studied using theory and further experiments. The presence of

[1] This chapter has been published in Zhang, T. and Barakos, G.N., "Review on ducted fans for compound rotorcraft," The Aeronautical Journal, Vol. 124, No. 1277, 2020, pp.941-974.

the duct alters significantly the inflow conditions of the propeller, thereby altering its performance. Meanwhile, the duct generates additional thrust at no torque cost exploiting the pressure jump by the propeller disk.

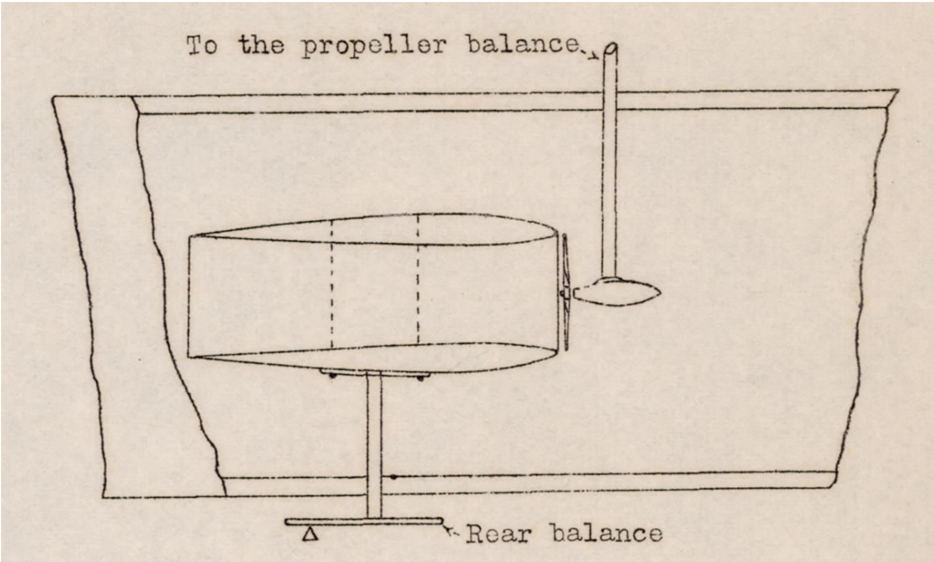

(a) Test rig of the "intubed propeller" by Stipa [2] .

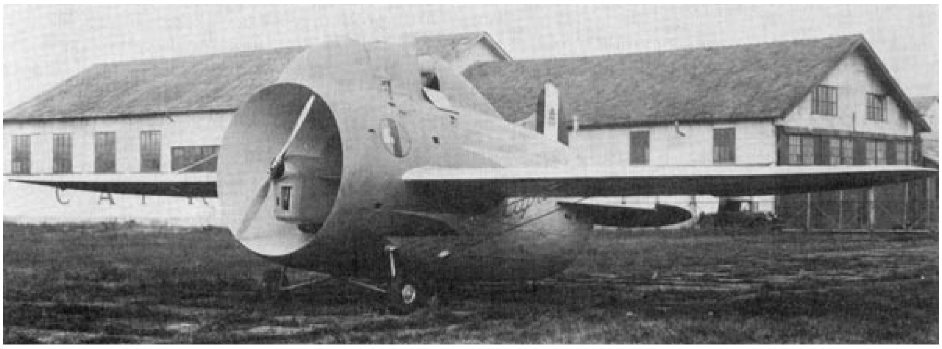

(b) The *Stipa-Caproni* prototype.

Figure 1.1: Early studies of the ducted propeller concept by L. Stipa [2] .

A simple analysis for ideal hover cases can be made using the momentum theory. For the same thrust required, the power reduction P_{dp}/P_{op} can be written as a function of the expansion ratio Λ, i.e. the ratio of the duct exit diameter to the rotor diameter:

$$\frac{P_{dp}}{P_{op}} = \frac{1}{\sqrt{2\Lambda}}, \tag{1.1}$$

where dp stands for ducted propeller and op for open propeller. Given the same power, the thrust improvement T_{dp}/T_{op} can also be defined as a function of the expansion ratio Λ:

$$\frac{T_{dp}}{T_{op}} = \sqrt[3]{2\Lambda}. \tag{1.2}$$

It can thus be seen that performance improvements can be achieved, as long as Λ is kept greater than 0.5. Comparing to conventional open propellers, ducted propellers hence bring very promising improvements in terms of aerodynamic efficiency. Due to the duct shielding, the acoustic emissions are also reduced. Additional safety benefits can also be expected by enclosing the propeller blades. Of course, ducting brings certain penalties. For instance, the duct contributes to drag rather than thrust at high advance ratios and low propeller suction. At crosswind or in edge-wise flight, the duct may suffer from flow separation, if not properly designed. Issues regarding duct weight, structural complexity, and vibration, should also be carefully considered. Nonetheless, the ducted rotor concept has been widely used in different fields. Applications in propulsors for hovercraft, fan-in-wing configurations, or tail-rotor as the fan-in-fin design for helicopters can be noted. Applications to marine propulsion [3], and wind turbines [4][5] have also been reported. Ducted rotors can also be made into UAVs (Unmanned Aerial Vehicle) if adequate control systems are added.

For rotorcraft applications, many novel configurations have adopted ducted propellers for propulsion, e.g. the Piasecki 16H-1A (Figure 1.2(a)) and X-49A (Figure 1.2(b)), and the VFW H3 Sprinter (Figure 1.2(c)). In Johnson's conceptual design for urban compound helicopters[7][6], ducted propellers were chosen for efficiency and safety reasons, and were mounted on wings near the tail under the rotor (Figure 1.2(d)). More applications of ducted propellers are presented in Figures 1.3(a) to 1.3(g), such as on the Bell X-22A aircraft (Figure 1.3(a)) and the Doak VZ-4 (Figure 1.3(c)). More recent applications are shown in Figures 1.4(a) to 1.4(f), such as on the Hybrid Air Vehicle (Figure 1.4(b)) and the Airbus E-fan (Figure 1.4(d)). The recently unveiled Bell Nexus air taxi, as shown in Figure 1.4(f), features 6 tiltable ducted propellers for lift and thrust. Nonetheless, it should be noted that most of these unconventional aircraft were prototypes and never entered production or service. Few analyses regarding the performance of the ducted

(a) Piasecki 16H-1A

(b) Piasecki X-49A SpeedHawk

(c) VFW H3 Sprinter

(d) Coaxial Compound Helicopter (CCH) by Johnson[6]

Figure 1.2: Ducted propellers on compound helicopters.

propellers in these configurations can be found in the public domain.

The following sections in this chapter present a comprehensive survey of published works on ducted propellers for aeronautical applications. Early and recent experiments on full- or model-scale ducted propellers are reviewed. Theoretical studies, lower-order simulations and high-fidelity CFD simulations are also summarised. Test matrices of several experimental and numerical studies suitable for validation are compiled and discussed. Challenges for the ducted propeller research are also summarised.

1.1 Experimental Works on Ducted Propellers

As summarised by Sacks[8], Pereira[9] and Akturk[10], plenty of experimental and theoretical studies on ducted propeller aerodynamics can be found. Recent experimental studies mostly focused on UAV/MAV applications. Therefore, as shown in Figures 1.5 and 1.6, the scale, compressibility, and Reynolds number (based on free-stream speed and duct chord length) of recent studies are only comparable to small, model-sized experiments from years ago. As suggested by Goodson

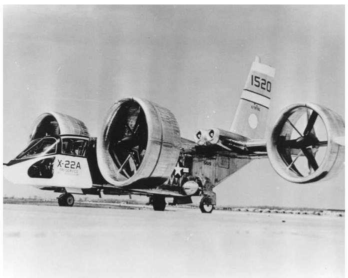

(a) Bell X-22A

(b) Ryan XV-5

(c) Doak VZ-4

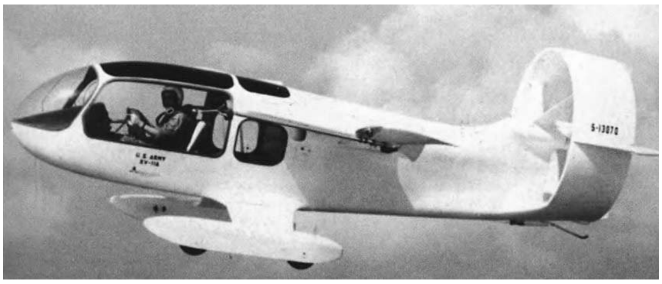

(d) XV 11A Marvel

(e) Nord 500 Cadet

(f) Vanguard Omniplane

(g) Britten-Norman BN-2 Islander

Figure 1.3: Implementations of ducted propellers (20th century).

and Grunwald[11], model-sized tests can be used to approximate full-scale performance, provided that the duct lip separation effects are avoided. However, lip separation is more likely to take place in model-sized tests due to the low Reynolds number. Table 1.1 presents a summary of the experiments, including the model scales and geometries, estimated maximum tip Mach number,

(a) UrbanAero AirMule

(b) Hybrid Air Vehicle

(c) Parker Alienair 1

(d) Airbus E-fan

(e) Airbus CityAirbus

(f) Bell Nexus

Figure 1.4: Implementations of ducted propellers (21st century).

and main objectives of each study. These experiments are discussed in detail in this section, with emphasis put on studies featuring large duct sizes, high Reynolds numbers, and well-documented setups.

1.1.1 Early Experiments on Ducted Propellers

Selected early experiments are listed in Figures 1.7(a) to 1.7(k). Very early experiments before the 1960s (Figures 1.7(a) to 1.7(e)) are summarised briefly in Table 1.1 due to lack of detailed information in the corresponding references. Nevertheless, results and conclusions of these tests are discussed in the summary of research challenges (Section 1.3). This section focuses mostly

Table 1.1: Experiments on ducted propellers

case	c_{duct}/[inch]	D_{in}/[inch]	Max Ma_{tip}	Duct Shape	Centre-Body Shape	Blade Shape	Vane Shape	Recommended for numerical validation	Note
Kruger1944[12]	1.482-10.45	9.5	0.45	A[a] (img)[b]	A	A	NA	N	Various duct shapes and propellers
Platt1948[13]	32.2-40.1	48	0.7	A	NA	A (nbs)[d]	-[c]	N	Dual-rotating rotors
Hubbard1950[14]	9.6-28.8	48	0.62	A	NA	A	-	Y	Acoustic study
Parlett1955[15]	12.25	18	0.42	A (img)	NA	NA	-	N	-
Taylor1958[16]	0.48-16.48	16	NA	A	NA	A	-	N	Fan in wing configuration
Yaggy1961[17]	33	48	0.9	A	A	A (nbs)	A	Y	VZ-4 ducted propeller
Grunwald1962b[18]	10.312	15	0.47	A	A	A	-	Y	*AoA* study
Mort1967[19]	49	84	0.85	A	A	A (nbs)	A	Y	X-22A ducted propeller
Black1968[20]	20(15)	30	0.6	NA	NA	NA	NA	N	Comprehensive study
Abrego2002[21]	10	38	0.5	NA	NA	NA	NA	N	PAV ducted propeller
Fleming2003[22]	6	10	0.47	NA	NA	NA	NA	N	Control methods study
Martin2004[23]	5.77	10	0.37	A (img)	NA	NA	-	N	Panel method validation available
Graf2008[24]	5	10(11.25)	NA	NA	NA	NA	-	N	Lip shape and control methods study
Akturk2008[25]	NA	5	0.25	NA	NA	NA	-	N	PIV measurements
Ohanian2011[26]	NA	NA	NA	NA	NA	NA	-	N	Synthetic jet
Akturk2011[27]	NA	23.6	0.28	A	NA	A	-	N	Tip clearance study
Rhee2013[28]	4.65	9.5	0.21	NA	NA	A (nbs)	-	N	Acoustic study
Yilmaz2013[29]	8.33	8.33	0.23	A	NA	NA	-	Y	Pressure and velocity field measured
Bahram2016[30]	8.66	8.1	0.32	NA	NA	NA	NA	Y	Asymmetric duct

[a] A: Acquirable, NA: Not Acquirable.
[b] img: geometry provided by images
[c] -: not included
[d] nbs: no blade sections available

on the full-scale wind tunnel test campaign performed by NASA (Figures 1.7(f) to 1.7(j)) during the development of two VTOL aircraft, the Doak VZ-4DA and the Bell X-22A, which utilised ducted propellers for propulsion and lift. The experiments focused on examining the aerodynamic performance of the specific designs. Test matrices of these experiments are presented in Tables 1.2, 1.3, and 1.4.

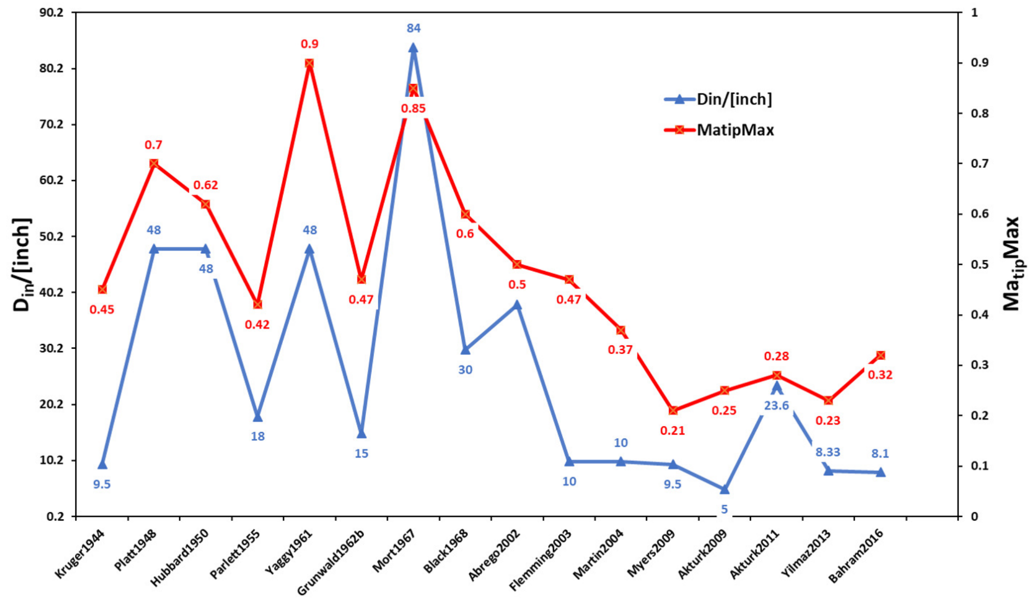

Figure 1.5: Scale (denoted by duct inner diameter D_{in} in *inch*) and compressibility (denoted by maximum blade tip Mach number $Ma_{tip}Max$) comparisons of ducted propeller experiments

The 4-foot-diameter ducted propeller of the Doak VZ-4DA tilt-duct VTOL airplane was tested while mounted at the tip of a semi-span wing representing a real-world design (Figure 1.7(f)). Experiments were systematically conducted and documented [17][32][33][34] to investigate the performance of this specific shape. It is noted that geometric information of the entire wing/ducted-propeller combination was presented in detail, except for the blade sections. The configuration had a complex structure, as the propeller was 8-bladed. A 9-bladed stator was installed to support the centre-body. Either 7 or 14 guide vanes were installed at the duct inlet, and a small tapered wing with a 25% plain flap was placed at the exit as a guide vane.

The experiments accounted for comprehensive variations including free-stream speed, *AoA* of the wing, the ducted propeller's relative angle to the wing, advance ratio, blade pitch angle, power input etc. Power, forces and moments of the ducted propeller and wing combination, stall

Table 1.2: Test matrix for the 7-foot ducted propeller by Mort and Gamse [19].

	Free-stream dynamic pressure/[psf]	*RPM*	μ	*AoA*/[deg]	Vane deflection/[deg]	β/[deg]	Static thrust coefficient [19]	Emphasis
variations	0-106	1200-2590	0∼2.2	0	off/-17∼+20	14∼49	-	-
case1	NA	NA	0∼2.2	0	off/0	14∼49	-	static performance
case2	NA	1810-2590	NA	0∼90	off/-17∼+20	14,19,29	5.0 ∼28.7...	AoA
case3	10.2-67.7	-	-	0∼90	0	-	-	duct alone
case4	0, NA	NA	-	0	-20∼20	19	NA/0.4∼13.5	vane effectiveness
case5	NA	1806	-	30-80		19	5.0	stall boundary

Table 1.3: Test matrix for the 4-foot ducted-propeller/wing combination by Yaggy and Mort [17].

	V_∞/[knots]	*RPM*	AoA_wing/[deg]	AoA_duct/[deg]	Vane deflection/[deg]	Emphasis
variations	0∼140	<6600	0∼20	0∼90	0∼30/0∼20	-
case1	NA	windmill	0∼20/0	0/0∼90	off	static performance
case2	0∼140	3600∼4800	2,6	0∼90	off	force balancing
case3	20∼50	3600∼4800	2,6	balance conditions	off,0,10,20,30/0 10/20	exit vane effectiveness
case4	0∼140	3600∼4800	2,6	40∼80	off,0,10,20,30/0 10/20	force balancing exit vanes

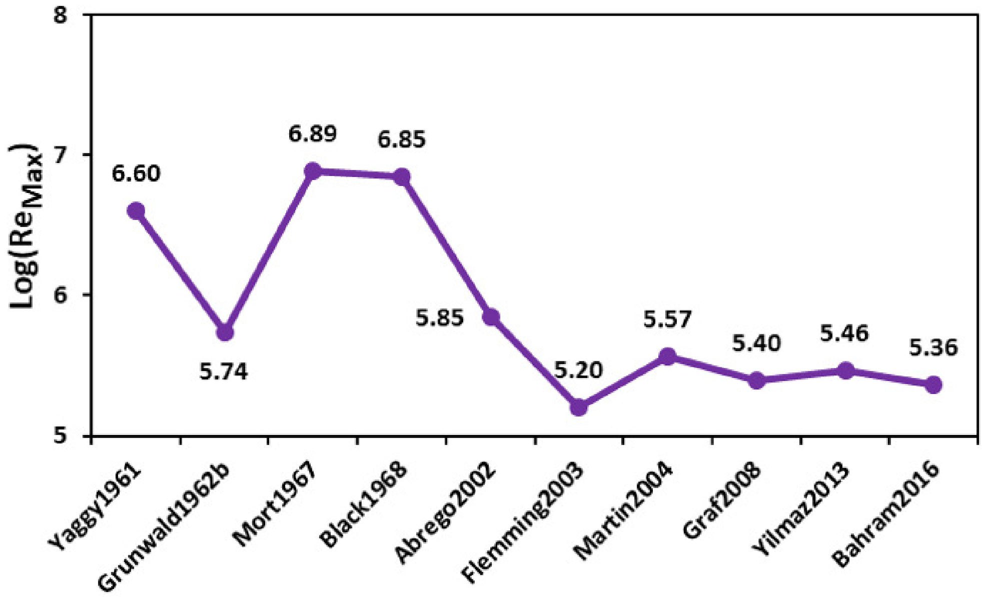

Figure 1.6: Maximum Reynolds number comparisons of ducted propeller experiments (based on V_∞ and c_{duct})

Table 1.4: Test matrix for the 5/16 model-sized ducted propeller by Grunwald and Goodson [18].

	V_∞/[ft/s]	*RPM*	*AoA*/[deg]	β/[deg]	μ	Lip modification	Emphasis
variations	-	8000	-10∼110	24	0-0.595	on/off	-
case1	100	removed/windmilling	0∼100	24	-	on/off	power-off
case2	-	8000	0∼110	24	0∼0.595	on/off	AoA

boundary for the upstream lip (through tuft flow visualisation), and surface pressure were measured. To support future use of the ducted propeller for control purposes, the effectiveness of various means, i.e. inlet vanes to alter the effective pitch angle of the blades, direct change of the blade pitch, and exit vanes to deflect the air, were evaluated. The exit vane was eventually concluded as the most effective method. In these full-scale tests, the maximum Reynolds number based on the free-stream speed and the duct chord length was between 4 to 7 million. The experiments, however, did not provide comprehensive measurements of the isolated ducted propeller (though the isolated wing's performance was measured), as the duct had to be mounted at the wing-tip.

Grunwald and Goodson [11][31] also tested 2 model-sized wing/ducted-propeller combinations (Figures 1.7(g) and 1.7(i)), to investigate the aerodynamic characteristics in hover and transition modes. It was found that the ducted propeller carries a substantial proportion of forces during

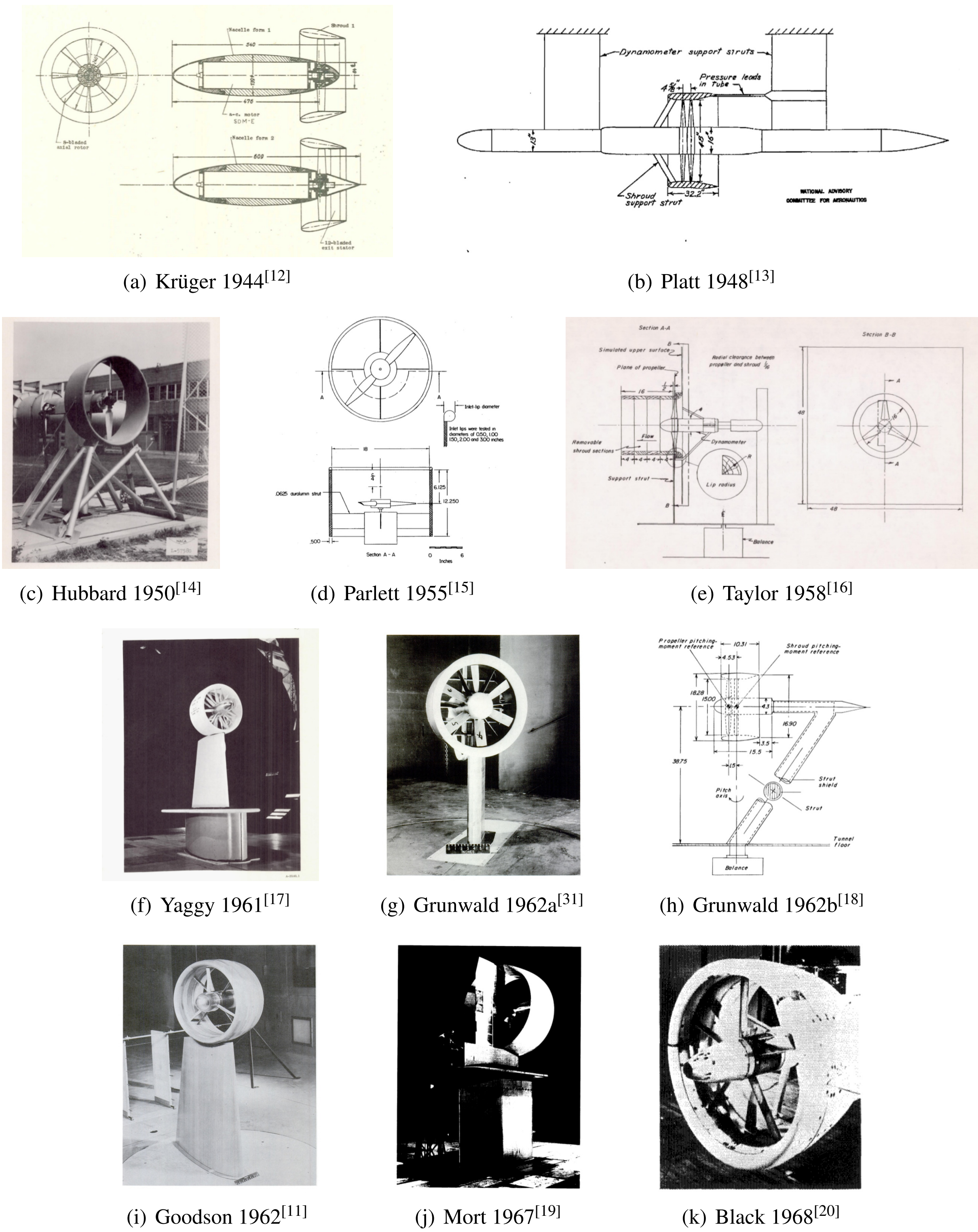

(a) Krüger 1944[12] (b) Platt 1948[13]

(c) Hubbard 1950[14] (d) Parlett 1955[15] (e) Taylor 1958[16]

(f) Yaggy 1961[17] (g) Grunwald 1962a[31] (h) Grunwald 1962b[18]

(i) Goodson 1962[11] (j) Mort 1967[19] (k) Black 1968[20]

Figure 1.7: Early experiments on ducted propellers.

hovering and transitional flight, and causes a large nose-up moment at low speed. With the exit guide vanes, the forces and moments could be trimmed, effectively. However, due to the small scale of the models and the resulting low Reynolds numbers (around 0.5 million), flow separation at the duct lip, which at full-scale may not be present, could not be avoided. Both experiments documented the geometry and the test conditions, but the propeller blade sections were not mentioned. However, it should be noted that, though not stated explicitly in the documents, the same ducted propeller model was apparently used for the wing/ducted-propeller combination study[11] and to study crosswind effects[18] (Figure 1.7(h)), and the blade sections are reported in reference [18].

Later, a Bell X-22A ducted propeller was examined by Mort and Gamse[19] in the NASA Ames 40- by 80-foot wind tunnel during the aircraft development (Figure 1.7(j)). Along with the aforementioned 4-foot experiments, the test was summarised by Kriebel and Mendenhall[35]. Theoretical models were then built and examined. The models could predict well the ducted propeller performance, yet differences could not be avoided due to the unevenly distributed disk loading and flow separation, showing the need for high-fidelity analyses.

Geometric definitions of the duct and the vanes were also presented, but the blade profile was not documented. The structure of the 7-foot-diameter ducted propeller was slightly simpler than the 4-foot one of reference[17]. The duct was 49 inches in length, and had 6 unevenly distributed stator blades to support the centre-body. A 3-bladed propeller was employed. A guide vane, similar to a small wing of rectangular planform, was installed at the flow exit to deflect the outflow. Aerodynamic forces, power, and moments of the isolated ducted propeller were measured, excluding the contributions from the wind tunnel support structure and fairing. Free-stream dynamic pressure, blade pitch angle, rotor RPM, *AoA* of the duct, and the exit vane deflection angle were set as the variables. The maximum Reynolds number based on the length of the duct was around 13 million. However, only dimensionless parameters for the test conditions were documented, making the determination of the specific conditions difficult. Pressure distributions inside and outside the duct surfaces were also provided. The experiments confirmed the high performance of the specific design, and concluded that better high-speed performance could be achieved with design modifications. Pressure distribution measurements were included to identify stall at inlet and outlet. The geometry and stall boundary of the 7-foot duct were similar to those of the 4-foot duct [17][32][33][34]. It was also found that upstream lip stall could easily happen at low power and high duct angle conditions, but stall at the downstream lip was not likely. Initially, the separation was local, and no large changes in performance were observed. As the crosswind angle increased, flow separation occupied the entire duct lip and large changes in aerodynamic loads were noticed. The authors claimed that there is a critical lip radius above which the flow separation would be delayed and vice versa. In general, it can be argued that the duct lip separation depends on the difference between the propeller power and the free-stream speed, the crosswind angle, and the inlet lip geometry.

Experimental, and theoretical studies on more general configurations were also conducted. Black *et al.* [20] systematically investigated the performance of a 3-foot ducted propeller, considering geometric variations of expansion ratio, inlet lip shape, external duct shape, propeller location, inlet/outlet vanes, blade shape, blade number, tip speed, and tip clearance (Figure 1.7(k)). The Mach number varied from 0.2 to 0.6 and comparisons were made against open propeller counterparts, with contributions from the duct and the propeller measured separately. Crosswind effects were not included, but this research represents a comprehensive experimental investigation into the dominant factors of the ducted-propeller static performance. The expansion ratio was identified as the most critical factor, which was consistent with theoretical analyses. A larger expansion ratio would be more beneficial to the static performance, but the cruise performance might be compromised. The authors recommended either specific shape optimisation or deformable shapes, as a way forward.

To study crosswind effects, Grunwald and Goodson [18] conducted experiments on a 15-inch diameter ducted propeller, representing a 5/16 model of the aforementioned 4-foot ducted propeller (1.7(h)), considering duct AoA ranging from $-10°$ to $110°$. Neither inlet nor outlet guide vanes were installed. The maximum Reynolds number, based on the tunnel wind speed and the duct length, was around 0.5 million, corresponding to forward flight transition conditions of a tilt-duct VTOL aircraft. Shroud lip separation was identified as the angle of attack increased. The experiments also uncovered that the propeller contributions to the overall forces and moments were relatively small, highlighting the importance of the duct. Also, at different advance ratios, as long as separation appeared, the ratio of the propeller thrust to the total thrust grew rapidly. This ratio, however, decreased with the duct *AoA* when stall was eliminated, suggesting that stall has a detrimental effect on the duct's performance. It is interesting that a modified lip geometry was proposed to resolve lip stall, and was shown to be effective. This suggests that an asymmetric duct design may be necessary, as also investigated by Bahram[30]. However, it should be pointed out that the stall boundary specified by this model-sized experiment is narrower than full-scale experiments. The duct scale plays an important role in the stall characteristics. As concluded by Mort[33], for ducted propellers that are big enough, e.g. those utilised by the X-22A and the VZ-4, inlet lip stall can only be encountered at very high rates of descent. The reports provided detailed geometric information about the blade and the duct, hence numerical validation can be made. In particular, Xu *et al.* [36] simulated the experiment at the *AoA* of 50° using RANS. The stall on the upstream side was predicted and visualised, then a modified lip shape was added to eliminate the stall. Very limited data comparisons were made; nonetheless good agreement was achieved.

1.1.2 Recent Experimental Studies

A resurgence of ducted propeller research in industry started in the 2000s because of the growth of interest in UAVs, PAVs, and electric propulsion. The models used in more recent experiments are presented in Figures 1.8(a) to 1.8(k). Recent efforts feature a combination of modern experimental technologies and CFD simulations. However, it is noted that the scale of the models examined, and the resulting Reynolds numbers and compressibility were hardly comparable to experiments from the 1960s, as the recent research targeted mostly small-scale UAVs (such as in Figures 1.8(b), 1.8(e), 1.8(g) and 1.8(i). These studies often utilised very high RPM rotors (typically more than 8000 RPM) at low Reynolds number ($10^4 \sim 10^5$). Such combinations do not represent high-speed flight conditions, and can hardly be applied to large aircraft. Nevertheless, the tests are briefly summarised in Table 1.1, and some are further discussed in Section 1.3. Few experiments utilised large-scale models and/or presented inspiring results for aircraft applications, and these are summarised in detail.

(a) Abrego 2002[21]

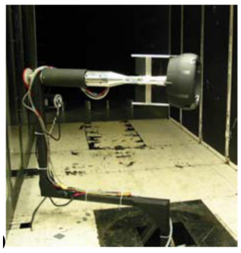

(b) Fleming 2003[22]

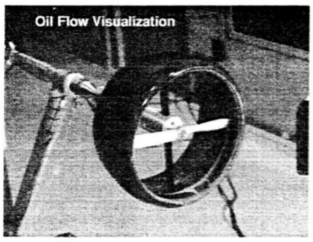

(c) Martin 2004[23]

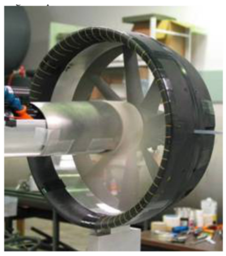

(d) Graf 2008[24]

(e) Pereira 2008[9]

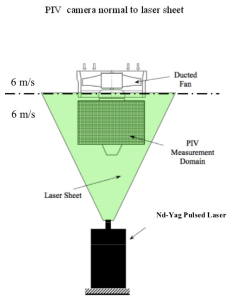

(f) Akturk 2008[25]

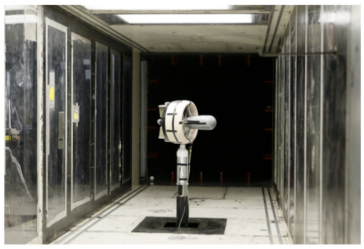

(g) Ohanian 2010[37]

(h) Akturk 2011[27]

(i) Rhee 2013[28]

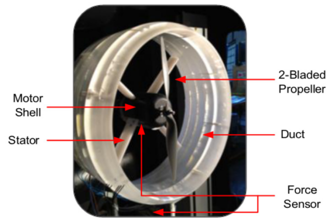

(j) Yilmaz 2013[29]

(k) Bahram 2016[30]

Figure 1.8: Recent experiments on ducted propellers.

Abrego and Bulaga[21] investigated a ducted propeller designed for PAVs. The ducted propeller, as shown in Figure 1.8(a), had a duct inner diameter of 38 inch and a 10-in duct chord. A five-bladed propeller was installed. Two 3-in exit guide vanes were used to vectorise the flow. The experiments accounted for various tunnel speeds, *RPM*, *AoA*, and vane deflection angles. The data and geometry were later adopted for CFD validation by Chang and Rajagopalan [38]. The simulated results matched the corrected experimental data, though the propeller was represented by momentum sources. However, the detailed geometric information is not publicly available. Martin and Tung[23] examined a 2-bladed, 10-inch ducted propeller UAV(Figure 1.8(c)), taking into account variations of the tunnel velocity, *AoA*, *RPM*, tip clearance, and duct leading edge radius. The performance of the ducted propeller, as well as, of the isolated propeller, were measured. Stall boundaries of the isolated duct and the powered configuration were also identified. It was found that increasing the tip gap would severely compromise the overall performance. The experiments also reported that the flow appeared to separate after the rotor blade plane. The ducted propeller model utilised in the tests was simple, and its purpose was to provide validation data for future modelling. However, the geometry of the duct and the blade, including the location of the propeller, are not explicitly defined in the paper. The experiments were later compared against panel method calculations by Lind *et al.* [39], and good correlation within the attached flow region was achieved.

Akturk, and Camci *et al.* [10][25][27][40][41][42] carried out numerical and experimental studies on ducted propeller UAVs. They used PIV to measure the flow field outside a small ducted propeller model[25][41] (Figure 1.8(f)), and the measurements agreed well with CFD simulations, where the rotor was represented by an actuator disk. The inlet flow distortion in crosswind conditions was revealed. However, due to the geometry of the duct, the flow field inside it, and near the blades could not be captured by the experiments. The free-stream speed was only $6m/s$ while the rotor *RPM* reached 9000, which is typical for the ducted propeller UAV studies as mentioned earlier. This is one of the few studies that first employed commercial codes and examined their applicability for ducted flow simulations. Later, Akturk and Camci *et al.* also employed CFD methods in their double ducted fan [10][40] and tip clearance studies 1.8(h)) [27][42].

More recently, Yilmaz and Erdem[29] examined 5 different circular duct shapes using the same 2-bladed propeller and a constant RPM (Figure 1.8(j)). The duct sections were defined by several standard NACA airfoils or their combinations. The duct inner radius and the chord length were kept at $0.2117m$, while the free-stream speed reached up to $25m/s$. The resulting Reynolds

Table 1.5: Test matrix of ducted propeller tests by Yilmaz *et al.* [29]

Duct shape	RPM	V_∞/[m/s]	μ	Tip clearance
NACA0018, 0012, 4312, 7312+4312, M21+4312	7000	0∼25m/s	0.08∼0.4	0.038R

number based on the chord length was around half of Grunwald's experiment. The blade geometry, however, was not described in detail. The performance of the open propeller was measured at different advance ratios for the purpose of further comparisons. The tests mainly explored effects of the advance ratio and the duct shape on the overall performance, and found that as the advance ratio grows, the thrust coefficient decreases and eventually becomes negative. A duct shape that has higher profile camber and higher expansion ratio was shown to provide better performance in the test. Also, the experiments showed that the propeller inside the duct performs poorer than the open propeller, but the overall performance of the ducted propeller is better. Apart from force and power coefficients, the velocity profiles at the inlet and exit were measured and the results were presented. Pressure distributions along the duct inner surface were presented too. This case is suitable for CFD validation despite the low Reynolds number, since the duct geometry is simple, the propeller can be represented by a matched model, and the available measurements are quite elaborate.

As most studies focused on the global shape, or the aft shape of the duct, Graf *et al.* [24] specifically studied the inlet lip (Figure 1.8(d)). The study pointed out that the lip shape defines the lip suction effect and alters the location of the pressure centre, which will further affect the pitching moments. Four different lip shapes were tested at static and crosswind conditions. It is found that an increased lip radius is beneficial for static performance, due to its ability to maintain attached flow longer. However, the profile drag and the pitching behaviour brought by the lip shapes were detrimental. Compromise should therefore be made between the best static and best crosswind performance. It is also interesting that the two symmetric shapes tested, showed poorer static performance, while shapes that generate a larger suction area in the inner surface were more favourable. Nonetheless, the experiments aimed at UAV applications, and the Reynolds number was low. Information on the model geometry and the detailed performance data was also restricted.

1.2 Modelling Ducted Propellers

1.2.1 Theoretical and Low-order methods

Theoretical studies on ducted propeller performance using methods like the annular airfoil theory, lifting line, blade element or panel methods etc. can be found in the literature since many decades ago. Thwaites[43][44] presented detailed analyses for a propeller inside a duct or tunnel based on strip theory, in the early 1950s. Kriebel and Mendenhall[35] compared their theoretical analyses against experimental data, though in many cases, where heavy disk loadings and flow separation were encountered, only qualitative agreement could be achieved. Pereira[9] also presented a detailed theoretical study. More recently, Bontempo and Manna[45]studied the exact solution of incompressible, axisymmetric and inviscid flow through the duct enclosing a non-uniform actuator disk. These methods can rapidly and quite accurately predict the performance in simple cases, and are suitable for fast analysis, of preliminary designs, for parametric studies[46]. However, in many cases, especially where flow separation is encountered, such models can only deliver results in qualitative agreement with test data.

Ahn and Lee[50] proposed an axisymmetric analysis and design method for ducted propellers, based on the extended stream-surface method by Ahn and Drela[51]. Viscous effects were not included. The study investigated the diffuser angle and inlet lip radius, as well as, propeller disk models and tip loss models, but no validation was provided. The duct expansion angle was found to be the dominant factor, as also suggested by many previous studies. The inlet radius was shown to be less important. However, as evidenced by the experiments reported by Taylor [16], smaller lip radii may give rise to inflow separation at the lip. The computational resources required for the aforementioned analyses were very small. Later, an open source code called DFDC (Ducted Fan Design Code) by M. Drela *et al.* [47][52] was also reported (Figure 1.9(a)). The code calculates rotor(s) using a lifting-line representation, blade element models, and vortex sheets, while the duct and center-body are accounted for using axisymmetric panel methods. The code is capable of rapidly predicting the performance of ducted propellers that have multiple rows of rotors and

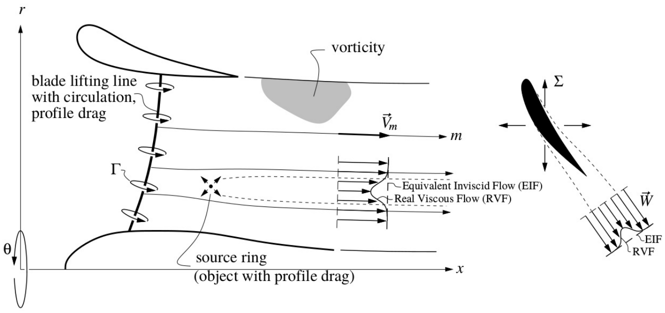

(a) DFDC(Ducted Fan Design Code)[47]
(blade elements, lifting line, panel methods)

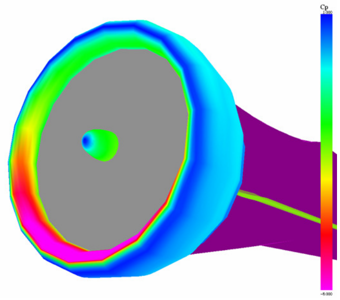

(b) Lind 2006[39]
(blade elements, panel methods)

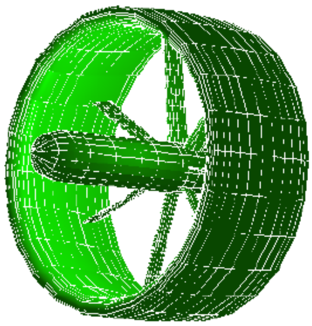

(c) Bi 2009[48]
(blade elements, panel methods)

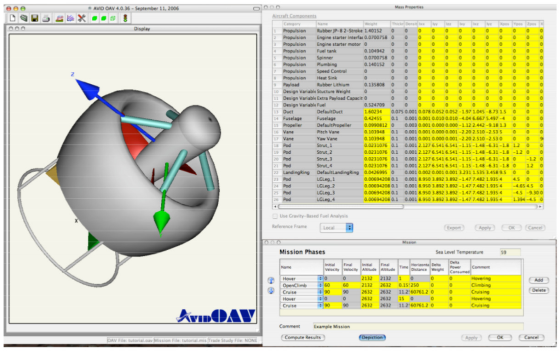

Figure 4: Screenshot of AVID OAV

(d) AVID OAV[49]
(empirical data interpolation, actuator disks)

Figure 1.9: Lower-order simulations of ducted propeller flow.

stators. It is also capable of quick design of ducted propellers given certain performance requirements. DFDC can be found deployed in several analyses and design studies, but its accuracy is not widely validated. In addition, the code can only account for axial flight and steady conditions.

Lind *et al.* [39] adopted panel, as well as, blade element methods based on airfoil tables to model Martin and Tung's experiments[23] for a 10-inch-diameter ducted rotor. The potential flow method (Figure 1.9(b)) predicted the forces well at high rotor *RPM* (9000) and low free-stream speed, for *AoA* up to 90°. However, the discrepancies in the pitching moment results were stronger. It is also noted that no lip separation occurred. At high free-stream speeds, only low *AoA* cases were compared. Nevertheless, the method required very low computer resources, and was seen as suitable for preliminary analyses. Bi *et al.* [48] investigated ducted propellers designed as aerodynamic propulsors for shipboard applications using panel methods for the duct frame, and blade element methods for the propeller (Figure 1.9(c)). The simulations, investigated the effect of variables including advance ratio, compressibility, blade twist, propeller location, and tip clearance. The study showed a decrease of the duct thrust contribution as the advance ratio increased. The inlet blockage was also investigated, and was found that it may induce significant vibration on the fixed and rotating parts of the structure. Validation was made against experiments, however, due to the proprietary nature of the model, quantitative comparisons were not publicly available.

The aforementioned methods can effectively and quickly calculate static performance, but can hardly account for flow separation and arbitrary flight conditions. Hence their usage is limited, and corrections from tests may be necessary. Nonetheless, Ko *et al.* [49] presented a commercial code named AVID OAV (Figure 1.9(d)), which integrates various strategies and multidisciplinary methods. To predict and optimise performance of ducted propeller UAVs, methods like interpolations from empirical data for duct performance, actuator disks or blade vortex element representations of the rotor, empirical equations for control vane performance etc. were considered. The predictions were in good agreement with wind tunnel and flight test data, and the code has been used for several ducted propeller UAV designs such as the iStar[53]. However, as mentioned above, the commercial code aimed at UAV applications, and little information is publicly available.

1.2.2 CFD Simulations

The simulation of ducted propellers, with blades and stators resolved, is within the capability of modern CFD methods and computers. Also, with the rapid development of commercial codes, many CFD simulations on UAV configurations were carried out in combination with practical tests. However, simulations of full-scale ducted propellers for propulsion purposes at high Reynolds numbers are less common, and the same is true for ducted propellers with stators or guide vanes. Simulation works are summarised here, as shown in Figures 1.10(a) to 1.10(k), to show the advancements of CFD techniques, and suggest future development.

In early attempts, actuator disk models for the propeller and incompressible Navier-Stokes simulations were considered. Rajagopalan and Zhang[54] used steady and incompressible Navier-

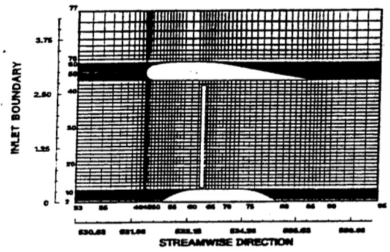

(a) Rajagopalan 1989[54]

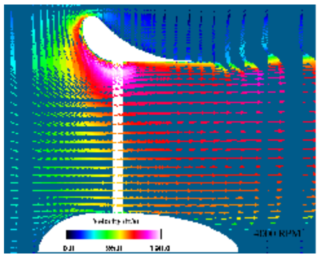

(b) Chang 2003[38]

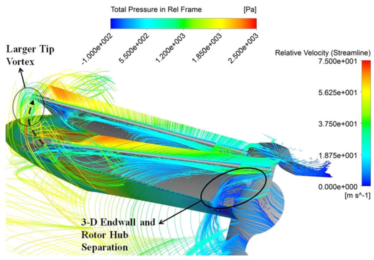

(c) Akturk 2011[27]

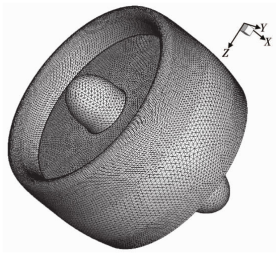

(d) Ye 2013[55]

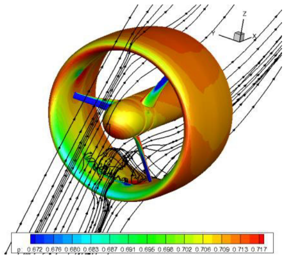

(e) Xu 2015[36]

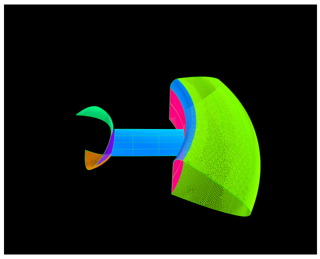

(f) Sheng 2015[56]

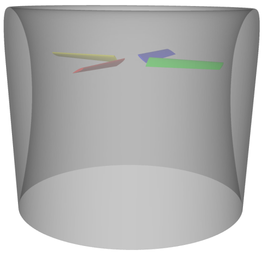

(g) Jimenez 2015[57]

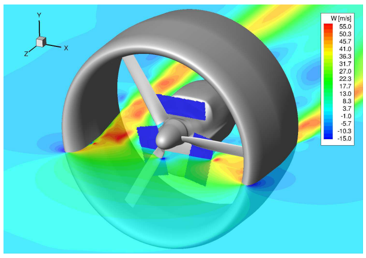

(h) Biava 2016[58]

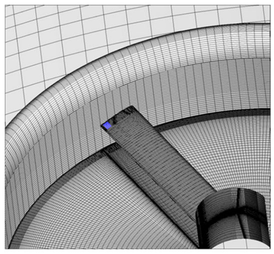

(i) Chen 2018[59]

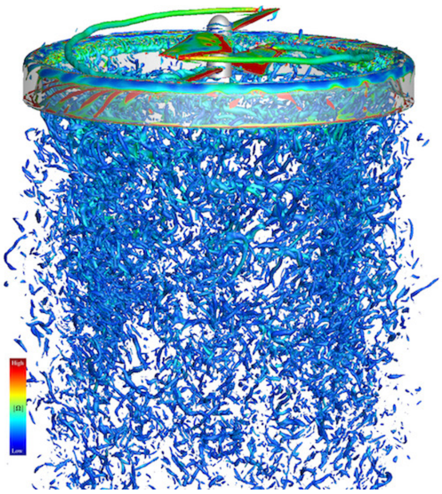

(j) Rubio 2019[60]

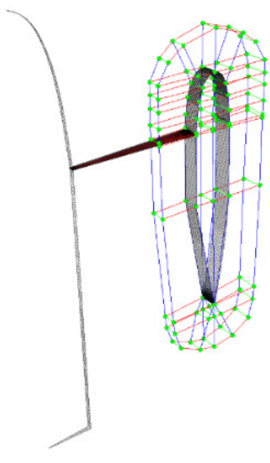

(k) Qing 2019[61]

Figure 1.10: CFD simulations of ducted propeller flow.

Stokes equations, and an axisymmetric reference frame to simulate propellers with and without a duct (Figure 1.10(a)). The propeller was represented by a time-averaged momentum source term, which was defined by the blade geometry and sectional airfoils. However, the presented results failed to capture the pressure jump on the inner duct surface caused by the propeller. Only the propeller performance was presented, but no validation of the overall configuration was provided. Later, using similar methods, Chang and Rajagopalan[38] performed simulations and validated their results against the Abrego and Bulaga[21] experiments. Though the propeller was modelled by a momentum source and only axisymmetric conditions could be accounted for (Figure 1.10(b)), good agreement with the corrected wind tunnel data was reported. Such combinations of actuator disks and incompressible governing equations is common and cost efficient, especially for fast analyses of UAV/MAV designs, but the axisymmetric restriction is usually prohibitive for more realistic situations. In addition, the disk models should be tuned with caution, as the thrust distributions on a propeller disk inside the duct differ considerably from that of an open propeller.

More CFD simulations with resolved propeller blades and compressibility effects accounted for, appeared recently. Akturk and Camci[10][27][42] conducted a series of combined experimental and numerical studies on double ducted propeller designs and tip clearance. Their simulation included realistic blade shapes and various tip shapes (Figure 1.10(c)). Validation, at low Reynolds numbers, proved that modern CFD methods are well-suited for ducted propeller flows. The experiments by Grunwald and Goodson [18] were chosen for CFD validation by several researchers as shown in Figures 1.10(d), 1.10(e) and 1.10(k). As mentioned earlier, Xu *et al.* [36] simulated the case at the *AoA* of 50° using the exact geometry and RANS methods (Figure 1.10(e)). The stall on the upstream side was captured and visualised. Then, the modified lip shape was added and was shown to be effective in eliminating lip stall. Though good agreement with the experimental data was achieved, very limited data was presented.

Sheng *et al.* [56] simulated a 24-inch diameter, 6-bladed ducted propeller in hover (Figure 1.10(f)), representing a simplified fan-in-wing configuration. The study focused on examining effects of the blade twist and inlet lip radius. Comparisons between the ducted and open rotor configurations showed the higher efficiency of the ducted propeller. The presence of the duct was also shown to delay the blade stall at high blade pitch angles. This was expected due to the flow acceleration at the duct lip. The influence of the blade twist was found to be consistent with open

Table 1.6: Test matrix for the generic ducted propeller simulations by Jimenez and Singh [57]

	RPM	β/[deg]	μ	Blade twist/[deg]	Emphasis
variations	1500,2000	5,10,15,19	0,0.06,0.11	-20,0,5	-
case1	1500,2000	5,10,15,19	-	-20,0,5	hover
case2	1500	19	0,0.06,0.11	0	axial

propeller cases. The inlet lip radius was shown to have a significant impact on the hover efficiency, as a larger radius mitigates inlet lip separation. It was noticed that flow separation occurred at the lip, as well as, downstream the blade disk at static conditions. The study detailed the geometry and test conditions, but relevant comparisons with experiments were not included. Numerical simulations by Jimenez and Singh *et al.* [57][62] adopted a simplified and generalised geometry to study the ducted rotor aerodynamics through modern CFD methods (Figure 1.10(g)). The test conditions and geometry were elaborately presented. The test matrix is shown in table 1.6. The duct geometry from Mort's[33] experiments was used, but the propeller was replaced by a four-bladed simple rotor with the sectional profile of NACA23012. Another combination of a Clark-Y duct and NACA0015 blades was also tested. No centre-body was considered. Performance comparisons between the open and ducted counterparts were made in hover, at several rotating speeds, advance ratios and collective angles. Some performance gain at low advance ratios by the duct was observed. In their study, emphasis was put on propeller performance. It was found that due to the duct, the outer portions of the blades carried a higher fraction of thrust, while the inner parts were offloaded. Though no experimental validation was included, the study could be adopted for future experimental or numerical validation. However, some of the flow conditions tested show small shock waves on the blades.

More recently, Chen and Li *et al.* [59][63] modelled a tip-jet driven ducted propeller design using URANS simulations, with the jet channel and the blade geometry resolved (Figure 1.10(i)). Such a jet-driven design was used in lift-propeller configurations like the Ryan XV-5 (Figure 1.3(b)). This design has a simple structure and only a minor fraction of the propeller's torque can be transmitted to the duct. The tip jet noise may, however, be substantial. Successful simulations of such a configuration demonstrated the capability of modern methods and computer hardware. Very recently, Rubio *et al.* [60] carried out high-fidelity DDES (Delayed Detached Eddy Simulation) simulations for small-sized coaxial ducted rotors (Figure 1.10(j)). The 2-bladed rotor was scanned from a commercial quadcopter UAV. A high diameter-to-chord ratio duct was added. Complex flow features were resolved in detail. However, it was noticed that the duct chord was so short that it could barely cover the coaxial rotors. The simulations showed, for both single-rotor and coaxial configurations, the tip vortices were restricted by the duct. The pressure fluctuations were also altered by the duct, suggesting future use of the duct for acoustics control and reduction.

1.2.3 Optimisation Studies

While most simulations focused on validation or performance analysis, design optimisation based on CFD methods has also been attempted. Schaller[64] developed an optimisation framework for small-scale ducts, based on a genetic algorithm coupled with simplified CFD simulations using momentum sources. The optimisation was shown to be effective for single-rotor and coaxial ducted propellers, but the results lacked support from practical tests. Ye *et al.* [55] (Figure 1.10(d)) applied global optimisation methods, based on response surfaces and neural networks, to Grunwald's [18] duct. The static thrust generation was improved by about 20%, but the validation using the static case showed considerable discrepancy with experiments. Steady actuator disks instead of realistic blades were adopted for the flow calculation, and performance at higher advance ratios was not examined.

Very recently, the same optimisation case was revisited by Qing *et al.* [61] (Figure 1.10(k)) using similar but more detailed methods. It is very interesting to notice that the authors replicated the hover tests by Grunwald[18] using the same duct and blade geometry, though they used variable RPM from $2,000$ to $8,000$. At the same test point, where $RPM = 8,000$, the test data agreed better with the simulations by Ye *et al.* [55] and Qing *et al.* [61], rather than with the original experiments by Grunwald[18]. In their simulations, Qing *et al.* [61] employed the incompressible RANS equations, in combination with a momentum source method by Rajagopalan[65] to represent the propeller. Response surface methods and Kriging Surrogate Models were utilised for the optimisation, while the overall *FoM* (Figure of Merit) was chosen as the cost function. The duct inner surface geometry and the propeller chord and twist distributions were set as design variables. The study featured an integrated optimisation of the propeller and the duct, and compared the performance of orthogonal combinations of the base-line/optimised duct/propeller. The integrated optimisation was shown to deliver the best performance in terms of *FoM*. The optimised duct had a larger inlet lip curvature and a higher diffuser angle, resulting in higher suction pressure at the duct lip and higher pressure at the diffuser. The optimised blade had an enlarged tip chord length which was almost comparable to the root chord, while the minimal chord was moved to about 70% span. The twist distribution was changed only slightly. The optimised blade was shown to have the highest induced velocity. The combination of the optimised duct and the base-line propeller caused massive separation on the diffuser surface, right after the rotor disk, and the performance decreased substantially. This was due to an excessive adverse pressure gradient induced by the increased expansion ratio Λ. The optimised propeller, however, brought no flow separation with such large expansion ratio, due to the larger tip chord that injected more momentum into the boundary layer.

However, the optimised propeller was not further validated or analysed using blade resolving CFD. Nonetheless, this study puts forward the significance of the integrated optimisation of the overall configuration. A common drawback of studies that adopted actuator disks, is that disk models can hardly account for aerodynamic interactions. Therefore, the optimisation results, especially for the propeller, may be inaccurate, and need to be further verified.

Optimisation with resolved blade geometries can rarely be found. Biava and Barakos[58] applied high-fidelity URANS methods to the analysis and optimisation of a ducted propulsor for Hybrid Air Vehicles (Figure 1.4(b)). The simulation first accounted for the realistic shape of the propulsor model, including the radiators and coolers (Figure 1.10(h)) , then gradient-based optimisation was applied to the blade and the duct, respectively, using a simplified centre-body geometry. Performance comparisons between the ducted and open propeller configurations were made to outline significant aerodynamic benefits brought by the duct, especially in static and low advance ratio cases. However, the simulation pointed out that at high advance ratios, the duct is detrimental to the overall performance due to an excessive drag force. Optimisation of the blade twist and the duct shape moderately increased the overall efficiency (by 2%). The optimised duct shape had a shorter chord length and a larger exit radius. The calculated results agreed well with experimental data on the same model. However, due to the proprietary nature of the propulsor, neither the geometry nor the specific performance data (numerical and experimental) are publicly available.

1.3 Ducted Propeller Research Challenges

The ducted propeller studies discussed so far, focused on various aspects of duct design and performance. It can be summarised that past studies tried to address 6 research aspects or challenges, as shown in Figure 1.11. These challenges are now discussed in detail.

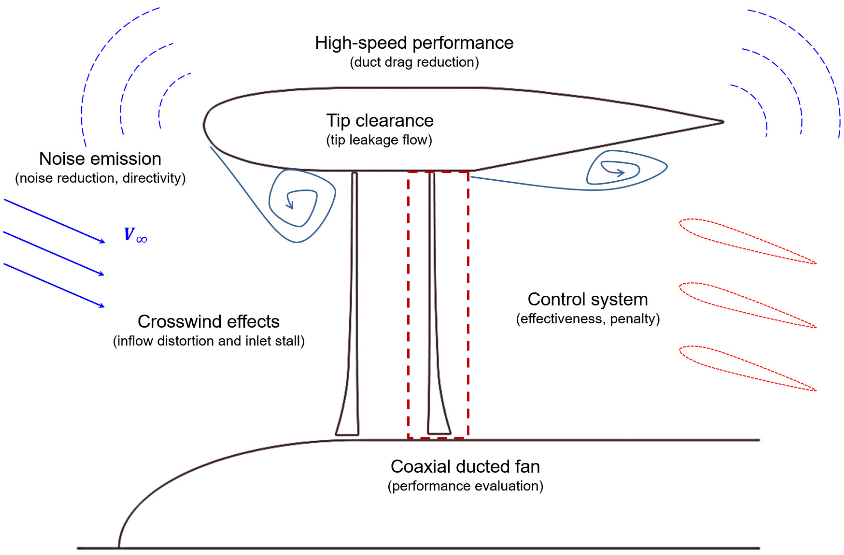

Figure 1.11: Ducted propeller research challenges.

1.3.1 Crosswind Effects

Non-axial inflow results in not only strong aerodynamic forces and moments on the duct, which behaves like an annular wing, but also in imbalanced disk loading that further induces more severe problems such as vibration. Flow separation at the inner or outer duct surfaces may also be encountered. As mentioned earlier, the separation depends on the difference between the propeller power and the free-stream speed, the crosswind angle, and the inlet lip geometry. In fact, several studies[16][56] on fan-in-wing types reported lip separation in hover conditions. It is argued that there could be a critical lip radius of 6% duct diameter, below which separation would take place. However, as tested by Graf *et al.* [24], flow separation was also observed with a radius of 12.5%. Further studies on lip effects were suggested by the researchers.

For tilt-duct aircraft, stall boundaries, as shown in Figure 1.12, need to be specified to guide the flight attitude. The crosswind effects are especially common and severe for ducted propeller UAVs, since they tend to fly forward in an edgewise attitude and the Reynolds numbers are relatively low. Similarly, up-stream side flow distortion and separation result in an increase in drag forces and nose-up pitching moments.

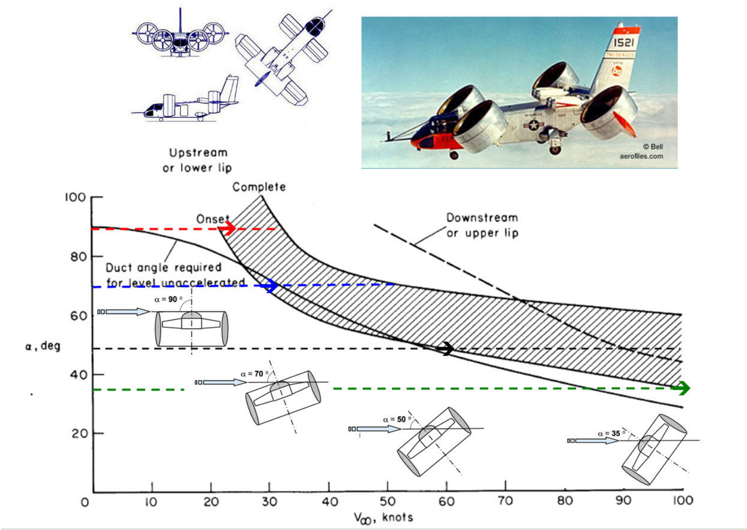

Figure 1.12: X-22A duct lip stall boundaries[19][40]

Several methods have so far been proposed to alleviate the crosswind effects, though mostly validated for UAV applications. A double-duct ducted propeller concept was proposed by Camci *et al.* [10][40]. The idea is to surround the duct with a larger secondary duct. The outer duct is used to adjust the wall static and dynamic pressure allocation, thereby eliminating the inner duct lip separation. Camci *et al.* conducted CFD simulations using actuator disks, and their effectiveness was compared. However, no comparisons with practical tests can be found.

Myers[66] proposed a more straightforward solution by adding vents at the forward flying side of the duct. The vented side almost gives up all benefits brought by the duct, and the asymmetry brings more imbalanced forces. Mechanisms can be introduced to actively open or close the vents according to flight conditions. Grunwald[18] proposed and examined an increased-radius lip solution that could effectively delay the inner surface separation. His solution resulted in an asymmetric duct since only the upper-stream lip was modified. Similarly, Bahram[30] examined asymmetric duct (Figure 1.8(k)) configurations, aiming at tilt-duct UAV applications, both experimentally and numerically. Comparing to a symmetric configuration, the asymmetric duct can provide lift forces and smaller force fluctuations during the transition from hover to axial flight. Nonetheless, such a solution may compromise the static performance and bring complexities in the duct geometry.

Actively morphing the duct geometry would be a much better solution for controlling flow separation. Ohanian[26] and Kondor[67] applied synthetic jets at the inlet and outlet to insert momentum into the boundary layer, thereby triggering or suppressing flow separation. Further, inlet flow separation can be used to decrease the thrust. Such active flow control technique, that can be seen as a “virtually morphed geometry”, can be an effective way to exert control upon the performance at low speed cases. Its effectiveness on high-speed though needs to be verified. Applying collective and cyclic pitch control to the propeller blades, as implemented by Colman *et al.* [68], may also be an effective solution, but requires complex mechanisms and will have to be integrated in the small center body inside the duct. Inlet guide vanes may also be effective in terms of regulating the inflow ahead the rotor disk[69].

Complexity, effectiveness, efficiency, and performance penalties should all be considered to determine the optimal choice. However, whether crosswind stall remains a severe problem for propulsor applications is arguable. As concluded by Mort[33], the scale of the duct plays an important role in the stall characteristics. For ducted propellers that are big enough, e.g. those utilised by the X-22A and the VZ-4, the inlet lip stall can only be encountered at very high rates of descent. Also, in Figure 1.12, it can be observed that only mild up-stream inlet stall was encountered during the transition from hover to high-speed flight.

1.3.2 Tip Clearance

The clearance between the duct inner surface and the blade tip leads to tip leakage flow. The presence of the duct significantly surpasses the extent of the blade tip vortices and regulates the flow to align with the duct surface, given a small tip-duct clearance. Several experiments, for instance Martin and Tung's wind tunnel tests[23] on a 10-inch-diameter ducted propeller, showed that the gap between the blade tip and the duct inner surface, significantly influences the overall thrust and the propeller/duct thrust partition. Increasing the tip gap resulted in the thrust dropping quickly. It is also very difficult for wind tunnel experiments to investigate flow features of the tip leakage, due to the geometry of the duct, the very small tip clearance, as well as the blade rotation. CFD simulation represents a better choice in this respect.

Oweis *et al.* carried out a series of experiments[70][71] to study the tip-leakage flow. Although focused on marine applications, their experiments revealed that the size of the primary tip vortex is of the order of the tip clearance, and is not strongly dependent on the Reynolds number, or the boundary layer thickness. Akturk and Camci[27] combined numerical and experimental investigations for a 599 mm-diameter ducted propeller in hover, and confirmed that a smaller tip gap is beneficial. As shown in Figure 1.13, through CFD flow-field visualisation, it can be seen that the primary leakage vortices impinged on the neighbouring blade, and the total pressure losses were noticed. As the tip clearance increased, the blade-vortex interaction region grew larger towards the mid-span. They also proposed several blade tip treatments[42], including modifying blade tip shapes and adding tip squealers, to mitigate the performance loss by reducing the leakage vortex strength or changing its trajectory. Matin *et al.* [72] proposed a solution by adding a backward step on the duct inner surface near the rotor disk, but its effectiveness was not strong. More treatments, in terms of blade tip shape and duct shape modifications, or active flow control methods, should be studied and applied to aircraft applications.

Recently, Ryu *et al.* [73] studied the effect of tip clearance for a counter-rotating coaxial ducted propeller UAV. Wind tunnel tests were conducted to validate the CFD simulations, while the flow details were studied using CFD. In that study, increasing the front and rear tip clearance

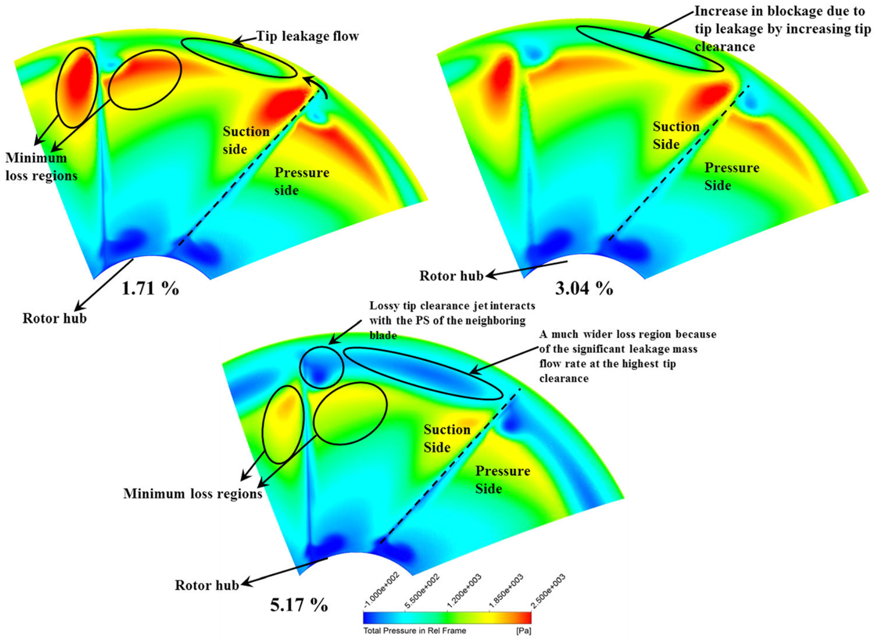

Figure 1.13: Relative total pressure comparison with different tip clearances [27]

caused the *FoM* to drop consistently. However, a smaller front rotor tip clearance, in combination with a larger rear tip clearance, delivered the maximum thrust observed. The thrust gain came from the rear rotor. This indicates that in a coaxial configuration, interactions between the two rotors add more complexity, and more detailed analysis is necessary.

1.3.3 High-speed Performance

As investigated during many of aforementioned experiments, given the same propeller *RPM*, the efficiency of the ducted propeller decreases as the advance ratio increases. However, the ratio of the propeller thrust to the overall propulsion increases in the mean time, indicating that the duct's contribution is diminishing fast.

In high speed axial flight, the drag of the shroud may outweigh its benefits if not carefully designed. Early experiments by Krüger[12] studied a high speed, high thrust loading ducted propeller model, aimed at reaching 400 kg of thrust at 80 km/h, and at an altitude of 8.6 km, when scaled to full size. The results showed that as the forward advance ratio increases, the propeller thrust coefficient can be maintained with larger blade pitch, but the duct thrust drops quickly and consequently the overall thrust decreases with increasing advance ratio. The experiments also suggested that high speed efficiency can be significantly increased by adopting shroud profiles with smaller chord and thickness, yet this is accompanied by a static performance penalty (that could be mitigated by an outward nose ring). Grunwald's experiments[18] also found that the propeller to overall thrust ratios increased from 40% to 70% as the forward advance ratio increased from 0 to 0.595 at zero angle of attack, indicating a reduction of the duct efficiency at high speed. As shown in Figures 1.14(a) to 1.14(c), the experiments of Abrego and Bulaga[21] on a 38-in diameter, fixed-pitch ducted propeller, showed that with increasing advancing ratio, the thrust coefficient and efficiency drops quickly.

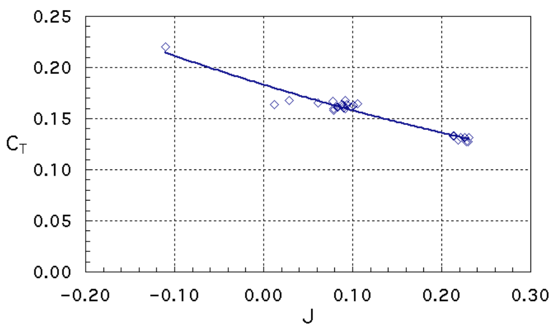

(a) Thrust coefficient changes.

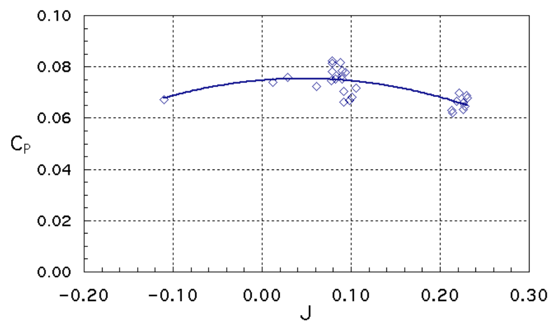

(b) Power coefficient changes.

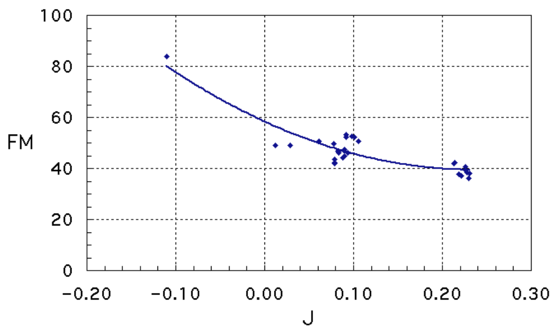

(c) Figure of Merit changes.

Figure 1.14: Ducted propeller thrust, power, and Figure of Merit changes at increasing advance ratios in axial flight tested by Abrego and Bulaga [21].

More recently, Biava and Barakos[58] investigated the effect of the duct using high-fidelity CFD methods and concluded that the duct has a significantly positive effect on the overall thrust and efficiency at low speeds. As an extreme, at zero propeller advance ratio the ducted propeller could generate 24% more thrust with 25% less power. The visualisation of the flow-field pointed out that the rear part of the duct serves as a diffuser to slow down the wake speed and increase the static pressure, thereby increasing the overall thrust comparing to the free propeller. The efficiency, however, gradually decreases as the advance ratio increases and eventually becomes negative. It is reasonable to conclude that the deficiency is mostly attributed to the greater duct drag caused by the higher speed. Geometric optimisation of the duct rear part was also applied, resulting in a shorter chord length, and a higher expansion ratio, bringing a small performance improvement.

1.3.4 Noise Emission

The ducted propeller noise is a separate topic of research. Noise emission of propellers enclosed by a duct of finite/infinite/semi-infinite length has attracted great research interest during the past decades. Applications can be found in turbofan/turbomachinery[74][75][76] and environment control device[77] noise predictions. A more comprehensive review in this respect can be found in references[78][79][80][81].

The ducted propeller noise mostly comes from the rotating propeller and interactions of its wake with the stator/vane. The presence of the duct substantially modifies the acoustic characteristics of a rotating fan/propeller. Stronger radiation directivity and noise reduction, compared to an open propeller, are the two major features as confirmed by several calculations and experiments. Since the first work by Tyler and Sofrin[82] in the 1960s, theoretical/numerical analysis of duct-rotor acoustics has seen significant development. Dunn *et al.* [83] presented a boundary integral equation method for ducted propeller noise prediction, and a prediction tool named TBIEM3D[84] was developed. The methods were examined by simulating the noise emission of a 20-bladed propeller located in the middle of a finite length duct. Twenty spinning point dipole noise sources were placed symmetrically on the propeller disk, and the results clearly showed the directivity of the ducted propeller noise radiation. In their study, the acoustic pressure was shown to be concentrated around 45° off the rotor rotation axis up-stream and down-stream. The axial and normal directions were left to have minimal sound radiation. The results were compared later by Wang *et al.* [85] using FW-H based methods, and good agreement was noticed. That study complements

Hubbard's early experiments[14]. Choi *et al.* [86] simulated the discrete tones of a ducted acoustic source, and also suggested a similar directivity pattern and noise reduction, due to the presence of the duct. Dunn *et al.* [83] also included lined surfaces to evaluate the noise reduction. It was found that inlet and outlet lining is very effective in mitigating the noise radiation.

Most studies mentioned earlier focused on many-bladed, high solidity fans. Though phenomena such as duct reflection and scattering, and rotor/stator interactions, are believed to be similar, fewer analyses can be found for lower solidity ducted propellers. Differences in the blade number, *RPM*, pitch angle etc. may result in a shifted characteristic spectrum. As mentioned earlier, Hubbard[14] compared sound-pressure measurements of five duct-propeller combinations in hover, with an open propeller at approximately the same rotational speed and power. The geometries of the 4 ducts, and the 2 blades tested, along with the test conditions were reported in detail. Total sound pressure, measured 30 feet away, produced by the two-blade shrouded propeller, was constantly lower at all measured angular stations, given no flow separation was present. The maximum measured value was around half that of the open propeller. The measurements also showed clear directivity of the sound radiation. The maximum value was around 70° relative to the rotation axis downstream, while another smaller spike was spotted at about 50° upstream. Lower values were noticed in axial and normal directions to the outer duct surface, with the lowest values along the inflow axis. The results showed that the duct reduced the strength of radiated sound and redistributed the sound energy in different directions. However, when the *RPM* and rotor power were slightly reduced, and flow separation was present at the inner surface near the inlet lip, excessive sound pressure was recorded. The measurements were almost twice as high as the two-bladed open propeller in all directions, and the directivity pattern was maintained. The tests also investigated factors such as the duct chord length, tip clearance, tip speed, and blade number. It was eventually concluded, as also briefly summarised by Bulaga[87] later, that many factors which promote the aerodynamic performance also reduce noise emissions, e.g. smaller tip clearance and avoiding flow separation. Reduced *RPM* and increased blade numbers provided better acoustic performance, while the duct chord length had minor effects on the acoustics. The tests, however, were conducted outdoors, hence environmental uncertainties could not be eliminated.

Regardless, the study revealed that separation, which was likely to appear at low rotational speeds, leads to higher sound pressure levels. Hubbard's works provided the exact geometry of the ducts and blades (including blade sections). However, limited aerodynamic performance data, which was extracted from the duct surface pressure measurements, was presented.

Recent small-sized experiments reported insignificant or negative noise reduction due to the duct. Martin and Boxwell[72] studied the acoustic characteristics of a 10-inch-diameter ducted propeller UAV. They concluded that the shroud does not alter the blade passage frequency noise, but increases the level of the broadband noise component. The influence of the tip clearance was reported as insignificant, but the separation at the inlet lip was found to increase the broadband noise contributions. Rhee and Myers *et al.* [28] also conducted a series of wind tunnel tests to study the acoustic characteristics of the ducted propeller without crosswind effects. The comparisons showed that the noise level of the ducted propeller was slightly higher than for open rotors when producing the same thrust. The directivity feature of the ducted propeller noise was also presented, and was shown to be consistent with Hubbard's tests[14]. They suggested that a perforated liner installed inside the duct would effectively reduce the noise. Reasons for the opposite conclusions are not certain, but they might be related to the low Reynolds numbers and flow separation.

Very recently, Malgoezar *et al.* [88] conducted acoustics experiments on a 30-cm-diameter ducted propeller with a Clark-Y profile. Variations of acoustic source types (an omni-directional source and a propeller) and cases at advance ratios were considered. Comparisons were also made between the ducted and the isolated configurations. The duct was shown to have a significant impact on the frequency distribution and directionality, and noise reduction could be noticed for cases with inflow. For static, hover state, however, noise increase was observed for most harmonics, while the frequency distribution resembled more an omni-directional source. Beamforming was then utilised to discern the acoustic sources, and a new noise source is identified at the duct leading edge. It was argued that the resonance of the duct and the interaction between the blade vortices and the duct boundary layer were the reasons behind the noise increase.

Compared to an open propeller, the acoustic performance of the ducted propeller can be expected to be superior, as the duct provides a basis for further nose treatments e.g. inlet/outlet liners.

Further experiments and high-fidelity simulations on ducted propeller noise should, however, be carried out to explore the acoustic benefits. For future VTOL aircraft, ducted propellers show great potential especially on stringent noise limits to be imposed on future rotorcraft.

1.3.5 Control Systems

Effective and efficient control of ducted propeller performance is another aspect of this survey. Guide vanes are more commonly deployed to vectorise the propulsor thrust. For UAV applications, several methods, as mentioned earlier, such as active flow control at the inlet and outlet[26][67], cyclic pitch control of the blades[68], inlet spoiler [22], exit rotating cylinder using Magnus effects[89][90] etc. show potential for application. Nonetheless, their actual effectiveness and efficiency on aircraft applications remain unclear.

The inlet vanes are capable of altering the effective blade pitch angle, thereby adjusting the overall thrust distribution. In fact, the inlet guide vanes are also useful for regulating the inflow and alleviating the inflow distortion. Outlet vanes, as shown in Figure 1.15(a), are better for deflecting the flow and generating side forces. Nevertheless, all guide vanes bring blockage and weight. Gilmore and Grahame[69] tested inlet and exit guide vanes on a 28.56-in diameter, fan-in-wing ducted propeller model in transitional flight. Ten inlet vanes were allowed to turn individually according to the inflow conditions, while the exit vanes were linked collectively. The experiments showed that the transition performance was improved, by using the inlet vanes for inflow regulation and the exit vanes for aircraft control. As expected, a small performance penalty at static conditions was noticed.

Experiments of the 4-foot ducted propeller[17] [34] also examined both inlet and outlet guide vanes. The experiments concluded that the exit vanes are more effective than the inlet vanes. As shown in Figures 1.15(a) and 1.15(b), tests by Yaggy and Goodson [34] showed that the vane deflection could effectively alleviate the overall pitching moment due to crosswind. Abrego and Bulaga [21] examined a ducted propeller with two 3-inch chord exit vanes, and concluded that exit vanes with flaps are effective in generating side forces. Using a symmetric installation of vanes

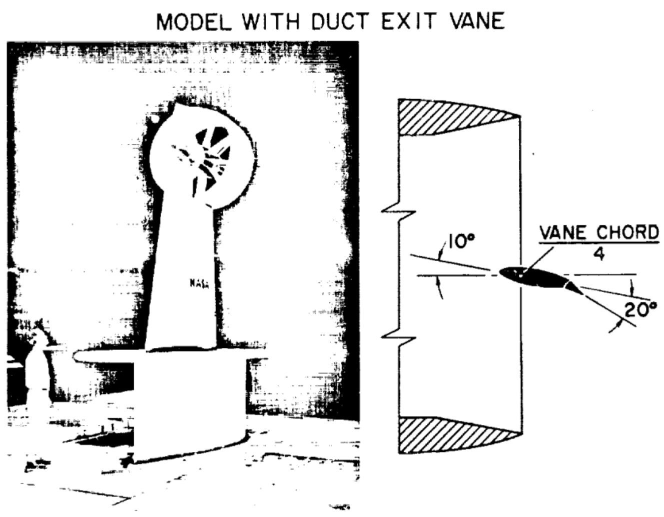

(a) Outlet guide vane configuration.

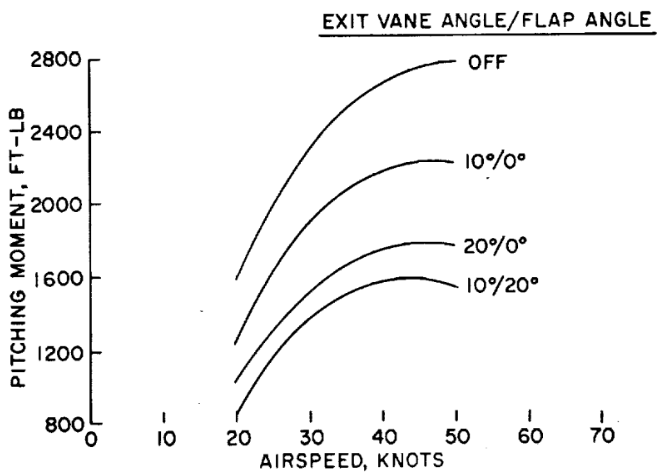

(b) Reduction in the pitching moment due to the vane deflection.

Figure 1.15: Duct outlet guide vane tests by Yaggy and Goodson [34].

and deflection angles (±40°) the force coefficients were not symmetric, and with zero deflection, slightly positive side-forces were generated. This might be the result of manufacturing defects of the model, as suggested by the authors, but it may also be related to the tangential induction of the rotating rotor. Mort and Gamse [19] worked on a full-scale ducted propeller with a large vane, and showed symmetric force changes against symmetric deflection angle changes. They also reported that at positive vane deflection angles, the effectiveness of the vane was significantly lower than expected as the cross wind angle was increased. Such asymmetry may also be related to the arrangement of guide vanes. For most tests mentioned herein, the vanes were aligned either in columns or rows, which in itself represents an asymmetry. Other arrangements, such as even distributions along the radius or angular directions, should be considered and evaluated.

Active flow control and cyclic blade pitch control might be possible solutions, as well, but performance penalties should be carefully evaluated. It is to be noted that only few experimental studies considered the effect of the guide vanes, and relevant numerical studies can hardly be found.

1.3.6 Coaxial Ducted Propeller Systems

Adding a second row of rotor blades to the ducted propulsor is important either for emergencies or torque balancing. As mentioned earlier, the contra-rotating coaxial design is also essential to make the ducted propeller a compact, removable propulsion unit, which has great potential for future eVTOL aircraft. However, as stated earlier, more complexity in performance analysis should be expected due to the interaction of the two rotors.

Concerning the contra-rotating coaxial ducted propeller system, few studies can be found in the open domain and most focused on UAVs, such as the Sikorsky Cypher UAV developed in the late 1990s. Lee[91] tested both contra-rotating and single-rotor ducted propeller UAV models. It was found that, in contrast to the ducted single rotor, shrouding a contra-rotating rotor does not always deliver better performance. Sensitivities to different design parameters, e.g. inlet radius, tip radius, and propeller location, are important. Based on Lee's work, Geldenhuys[92] studied a similar coaxial system numerically, using the same duct geometry but used a different rotor design. The DFDC code and incompressible CFD simulations were used for the analysis. The results and experiments matched well, in general, but differences were presented for several cases. It is notable that the DFDC configuration file and elaborate geometric information were provided, making it possible for further validation and investigation. Jiang *et al.* [93] conducted combined numerical and experimental studies on a general coaxial ducted propeller configuration. The study mainly investigated three factors: the blade pitch angle, free-stream speed and the rotor spacing. Combinations of these factors gave distinct performance results, yet the CFD results agreed with the experiments very well. Nemnem*et al.* [94] discussed the parameters of coaxial ducted propeller design, but the study lacks the support from either experiments or simulations. Overall, performance and determining factors of the coaxial ducted propeller need to be further investigated.

1.4 Summary of the Literature Survey

In summary, previous research works suggest that the ducted propeller concept has promising aerodynamic and acoustic benefits, and it could be the promising choice of auxiliary thrust or lift for novel rotorcraft configurations. Yet more quantitative investigations are needed to understand the aerodynamics and acoustics.

Early experiments examined the ducted propeller concept mainly using balance measurements, although mostly focused on the performance examination of specific designs. Nonetheless, improved aerodynamic performance was reported at low speeds, while the high-speed performance was found penalised. Modern experiments employed more advanced measurements such as PIV and wake survey, but the research works mostly focused on small-scale UAV applications. The Reynolds numbers and compressibility effects are hardly comparable to early experiments. Nevertheless, many modern studies attempted to look into specific aspects such as duct shapes, tip clearance, flow control, etc. These results can be indicative for future ducted propeller designs. Still, experiments typically struggle to measure detailed flow features due to the duct blockage and blade motions, which hinders the understanding of the flow physics. This highlights the need for numerical methods for the flow investigation.

Theoretical and lower-order methods are available for the performance prediction of ducted propellers, but their accuracies are limited by stringent assumptions and simplifications. They are suitable for fast preliminary designs but are incapable of complex conditions such as crosswind. High-fidelity CFD approaches are necessary for the accurate performance prediction of ducted propellers. The simulation is within the capability of modern CFD methods, and a few high-fidelity numerical studies using resolved blades emerged in very recent years. Still, the simulation remains challenging due to the complex geometries, motions, and flow features. In addition, effective design optimisation is enabled through high-fidelity simulations, but few studies in this respect can be found, especially with blades resolved.

From previous studies, it is learnt that the ducted propeller has improved aerodynamic performance at low advance ratios and poorer performance at high advance ratios, and this is likely caused by the increasing duct drag. However, further investigations are needed to understand how the additional duct thrust is resulted, and how it is affected by the axial speeds, duct shape, or propeller suction. It is also not clear how the duct thrust is converted into drag forces subject to increasing axial speeds. It is also unclear whether the performance penalty can be avoided by changing the blade pitch or the duct shape. Coaxial designs or swirl recovery systems could also be considered to further improve the performance.

The ducted propeller noise emission is another important topic of interest for the current study. Few studies looked into the acoustic performance of ducted propellers but mostly concluded noise reductions due to the duct blockage. Such a noise reduction is very promising for future rotorcraft operating in urban environments. Yet few data are available for quantitative comparisons or further investigations into the physics. With high-fidelity CFD simulations, it is feasible to extract and study the near-field acoustic features directly from the flow solutions. Far-field acoustics can also be computed upon near-field flow solutions.

At crosswind, the ducted propeller often generates large sideways forces and moments. Flow separation at the duct surface is also expected at very high crosswind angles. It is of interest to understand how the performance changes responding to the crosswind angles and how the sideways loads are resulted, and what is the working condition of the ducted blades at crosswind. Thrust vectorising devices, such as exit guide vanes, could also be employed to mitigate the sideways loads. These results are important for rotorcraft applications considering the main rotor downwash.

Overall, exsiting research work on the aerodynamic performance focused mostly how the aerodynamic forces and moments change at different operating conditions, and rarely further explored the flow physics behind these changes, due to limitations such as experimental methods or numerical fidelity levels. Design optimisation studies can be found but mostly used reduced-order modelling of blades for simplicity. In term of acoustic investigation, experimental studies were rare and most numerical investigations suffer from the modelling fidelity.

In light of these, the current thesis aims to comprehensively and systematically investigate the aerodynamic and acoustic performance of the ducted propeller concept using high-fidelity methods, and to assess its application on future novel rotorcraft configurations. For the aerodynamic investigation, this thesis focuses on the performance at high axial speeds and crosswind conditions. Apart from conventional aerodynamic loading evaluations that are common in previous studies, this work aims to further explore the flow physics using high-fidelity methods to understand how the ducting benefits are resulted and changed at different conditions. Moreover, this works also aims to evaluate the ducted propeller performance under non-uniform downwashing flows to assess its performance on future novel rotorcraft configurations, which is rarely explored in the literature. High-fidelity design optimisation study with blades resolved is also among the objectives to explore how changes in the geometry and in the installation position can improve the perofrmance. For the acoustic study, this thesis aims to investigate the near- and far-field noise features of the ducted propeller concept in axial flight. The fly-by noise evaluation is also among the objectives to explore how the noise dynamically changes while the propulsor unit is in motion. In addition, comparisons with the open propeller concept are presented through out to bring out the advantages and disadvantages of the ducted propeller concept.

This thesis on ducted propellers for applications on novel rotorcraft configurations is organised as follows. Chapter 2 details the numerical methods proposed and employed for the current numerical study. Chapter 3 presents the validation of the employed geometry, meshing, simulation strategy, and numerical methods. Chapter 4 analyses and compares the aerodynamic and acoustic performance of ducted and open propellers at various conditions. Chapter 5 presents an optimisation study of ducted propellers for improved performance at high advance ratios. Far-field acoustics of the optimised designs is also presented. Chapter 6 investigates the performance and aerodynamic interactions of the ducted/open propellers installed under a main rotor. Chapter 7 proposes a simplified modelling approach for rotor/propeller aerodynamics. An optimisation framework for minimised aerodynamic interference by altering the propeller position is also presented and examined. Conclusions and future works are summarised in Chapter 8. Last but not least, a parametric study of the equivalent ducted/open propellers is presented in Appendix A. The far-field acoustic code built for the current study is also presented in Appendix B.

Chapter 2

Numerical Methods

This chapter details the numerical methods employed and developed for the aerodynamic, optimisation, and acoustic investigations in this study. A novel implementation method of actuator disk models in the Helicopter Multi-Block 3 (HMB3) solver is put forward. A new automatic grid generation framework is also detailed. Various optimisation methods and frameworks constructed for the ducted propeller and rotorcraft configuration optimisation are also elaborated. Acoustic methods and a new acoustic solver is also presented. Advantages and disadvantages of the methods, as well as, the reasons they are used in this study, are discussed in detail in this section.

2.1 Helicopter Multi-Block 3 (HMB3) Solver

All flow simulations performed in this thesis are performed using the Helicopter Multi-Block 3 (HMB3) Solver[95, 96, 58]. The HMB3 solver is an in-house CFD solver based on the finite volume discretisation of RANS equations with a variety of turbulence modelling options. It also supports various mesh methods, e.g. mesh motions and deformations, sliding planes and overset grids. The HMB3 solver has been widely used in previous rotorcraft [97, 98] studies, and rotor and wind turbine simulations[99, 100, 101].

2.1.1 Governing Equations

The governing Navier-Stokes equations describing the conservation of mass, momentum, and energy can be written in the following dimensional tensor form

$$\begin{cases} \frac{\partial \rho}{\partial t}+\frac{\partial}{\partial x_i}(\rho u_i)=0 \\ \frac{\partial}{\partial t}(\rho u_i)+\frac{\partial}{\partial x_j}\left(\rho u_i u_j+P\delta_{ij}-\tau_{ij}\right)=S_i \\ \frac{\partial}{\partial t}(\rho E)+\frac{\partial}{\partial x_j}\left(\rho u_j E+P u_j+q_j-u_i\tau_{ij}\right)=S_e \end{cases}, \tag{2.1}$$

where ρ is the density, u_i is the velocity component, and P is the pressure. δ_{ij} is the Kronecker delta. E is the total energy per unit mass, which is a combination of the internal energy e and the kinetic energy following $E=e+u_iu_i/2$. S_i and S_e represent any momentum or energy sources, respectively. In the present research, the source terms are involved when using the rotating reference frame and actuator disk models, which will be elaborated in later sections.

Here, τ_{ij} is the viscous stress tensor that can be detailed as

$$\tau_{ij}=\mu\left[\left(\frac{\partial u_i}{\partial x_j}+\frac{\partial u_j}{\partial x_i}\right)-\frac{2}{3}\delta_{ij}\frac{\partial u_k}{\partial x_k}\right]. \tag{2.2}$$

The molecular viscosity μ is evaluated through the Sutherland's law

$$\mu=\mu_0\left(\frac{T}{T_0}\right)^{3/2}\frac{T_0+T_S}{T+T_S}, \tag{2.3}$$

where μ_0 is a reference viscosity at the temperature T_0. These values are taken as $\mu_0=1.7894\times 10^{-5}\ kg/(m.s)$ and $T_0=288.16K$ throughout the present work. T_S is the Sutherland temperature taken as $T_S=110.4K$.

The heat flux q_i in Equations 2.1 can be written as

$$q_i=-C_p\frac{\mu}{Pr}\frac{\partial T}{\partial x_i}, \tag{2.4}$$

C_p is the flow heat capacity at constant pressure. $Pr=0.72$ is the laminar flow Prandtl number. T is the fluid temperature.

In this work, the governing equations are further cast into a dimensionless and more generalised form through a set of reference values as follows

$$x_i = \frac{x_i^*}{L_{ref}},\ u_i = \frac{u_i^*}{V_{ref}},\ t = \frac{t^*}{t_{ref}}, \tag{2.5}$$

$$\rho = \frac{\rho^*}{\rho_{ref}},\ \mu = \frac{\mu^*}{\mu_{ref}},\ P = \frac{P^*}{\rho_{ref} V_{ref}^2}, \tag{2.6}$$

$$T = \frac{T^*}{T_{ref}},\ e = \frac{e^*}{V_{ref}^2}, \tag{2.7}$$

where the subscript $*$ denotes values with real dimensions, and the subscript refers to the reference values.

The dimensionless form of the three-dimensional Navier-Stokes equations can be written in the following differential, vector form in a Cartesian coordinate system as

$$\frac{\partial \mathbf{W}}{\partial t} + \frac{\partial (\mathbf{F} - \mathbf{F^v})}{\partial x} + \frac{\partial (\mathbf{G} - \mathbf{G^v})}{\partial y} + \frac{\partial (\mathbf{H} - \mathbf{H^v})}{\partial z} = \mathbf{S}, \tag{2.8}$$

where $\mathbf{W}$ is the conservative variable vector. $(\mathbf{F}, \mathbf{G}, \mathbf{H})$ and $(\mathbf{F^v}, \mathbf{G^v}, \mathbf{H^v})$ are the convective and viscous flux terms, respectively. The term $\mathbf{S}$ on the RHS is non-zero when there are surface or volume sources.

The conservative variables $\mathbf{W}$ and the convective flux terms $(\mathbf{F}, \mathbf{G}, \mathbf{H})$ are written in full as

$$\mathbf{W} = \begin{bmatrix} \rho \\ \rho u \\ \rho v \\ \rho w \\ \rho E \end{bmatrix}, \mathbf{F} = \begin{bmatrix} \rho u \\ \rho u^2 + P \\ \rho uv \\ \rho uw \\ \rho uH \end{bmatrix}, \mathbf{G} = \begin{bmatrix} \rho v \\ \rho vu \\ \rho v^2 + P \\ \rho vw \\ \rho vH \end{bmatrix}, \mathbf{H} = \begin{bmatrix} \rho w \\ \rho wu \\ \rho wv \\ \rho w^2 + P \\ \rho wH \end{bmatrix}, \tag{2.9}$$

where H is the total enthalpy.

The viscous flux terms $(\mathbf{F^v}, \mathbf{G^v}, \mathbf{H^v})$ are written in full as

$$
\begin{aligned}
\mathbf{F}^{\mathbf{v}} &= \frac{1}{Re}\left[0, \tau_{xx}, \tau_{xy}, \tau_{xz}, u\tau_{xx} + v\tau_{xy} + w\tau_{xz} - q_x\right]^T, \\
\mathbf{G}^{\mathbf{v}} &= \frac{1}{Re}\left[0, \tau_{xy}, \tau_{yy}, \tau_{yz}, u\tau_{xy} + v\tau_{yy} + w\tau_{yz} - q_y\right]^T, \\
\mathbf{H}^{\mathbf{v}} &= \frac{1}{Re}\left[0, \tau_{xz}, \tau_{yz}, \tau_{zz}, u\tau_{xz} + v\tau_{yz} + w\tau_{zz} - q_z\right]^T.
\end{aligned}
\tag{2.10}
$$

Here, $Re = \rho_{ref} L_{ref} V_{ref} / \mu_{ref}$ is the Reynolds number. To close the system, the governing equations also require the following ideal gas relations describing the correlations between the total enthalpy H, total energy E, internal energy e, pressure P, density ρ, and static temperature T

$$H = E + \frac{P}{\rho}, \;\; E = e + \frac{1}{2}\left(u^2 + v^2 + w^2\right), \tag{2.11}$$

$$P = (\gamma - 1)\rho e, \;\; T = \gamma Ma_{ref}^2 \frac{P}{\rho}, \tag{2.12}$$

where $\gamma = 1.4$ is the specific heat ratio. $Ma_{ref} = V_{ref}/c_{ref}$ is a reference Mach number resulted from the nondimensionalisation, with $c_{ref} = \sqrt{\gamma P_{ref}/\rho_{ref}}$ being the reference sound speed.

2.1.2 Spatial Discretisation

Following the method of lines, the governing differential Equation 2.8 is first discretised in space in the HMB3 solver. The differential equations are put into integral forms as

$$\frac{d}{dt}\iiint_{V(t)} \mathbf{W} dV + \iint_{\partial V(t)} \left(\mathbf{F} - \mathbf{F}^{\mathbf{v}}, \mathbf{G} - \mathbf{G}^{\mathbf{v}}, \mathbf{H} - \mathbf{H}^{\mathbf{v}}\right) \cdot \mathbf{n} dS = \iiint_{V(t)} \mathbf{S} dV, \tag{2.13}$$

where $V(t)$ is the control volume with $\partial V(t)$ being the boundaries. Note here that the volume is a function of time to account for time-dependent motions. The Arbitrary Lagrangian Eulerian (ALE) formulation is hence used here, and the time-dependent mesh velocities are included in the velocity components of the flux terms. $(\mathbf{F} - \mathbf{F}^{\mathbf{v}}, \mathbf{G} - \mathbf{G}^{\mathbf{v}}, \mathbf{H} - \mathbf{H}^{\mathbf{v}})$ are the combined convective and viscous flux vectors as in Equation 2.8. $\mathbf{n}$ is the volume surface normal vectors pointing outwards. $\mathbf{S}$ is again the source term vector which will be detailed later.

The integrations in Equation 2.13 are evaluated following the cell-centred Finite Volume method (FVM) on fully-structured, multi-block grids in HMB3. Osher's upwind scheme[102] is used to discretise the convective flux terms for the stability and accuracy. The 3^{rd}-order MUSCL[103] (Monotone Upstream-centred Schemes for Conservation Laws) variable extrapolation is adopted here to improve accuracy. To prevent spurious oscillations around discontinuities, the Van Albada limiter [104] is implemented. The viscous terms are discretised using 2^{nd} central differences. Boundary conditions are implemented through ghost cells in the exterior of the computational domain.

The partial differential equations in Equation 2.8 are eventually assembled as a system of ordinary differential equations in time as follows

$$\frac{d}{dt}\left(\mathbf{W}_{i,j,k}V_{i,j,k}\right) + \mathbf{R}_{i,j,k}(\mathbf{W}) = 0. \tag{2.14}$$

where i, j, k denotes the cell index, and $V_{i,j,k}$ is the cell volume. $\mathbf{R}$ is the residual vector containing the integrations of the convective and viscous flux terms, as well as, the source terms.

2.1.3 Temporal Discretisation

The ordinary differential system of Equation 2.14 can be typically solved using forward or backward finite difference schemes in time, leading to explicit or implicit schemes, respectively. In general, the explicit scheme depends solely on already known values and is hence easy and simple to implement, but it suffers from restricted time step sizes due to the numerical stability. In comparison, the implicit scheme suffers less from the stability and can use much larger time steps. However, the implicit scheme has non-linear formulations due to the inclusion of unknown variables in future time steps. To solve the non-linear formulations, the popular approach is to linearise the non-linear systems into linear systems with a little sacrifice of accuracy, and solve the linear system using iterative methods.

In practice, both explicit and implicit methods are widely used. For simulations focusing on flow features with very small time scales, e.g. DNS (Direct Numerical Simulation) simulation of turbulence structures, the use of explicit schemes such as multi-stage stepping is suitable and easy. The implicit scheme brings more complexity and poses more requirements on the computational resources, but the benefits of larger time steps still outweigh the drawbacks in many occasions for engineering applications. For simulations of flows dominated by large time scales, such as rotor flow-fields that are mostly dominated by the Blade Passing Frequency (BPF), implicit schemes with large time steps are more favourable. In particular, for steady state solutions evolved from initial conditions, the implicit scheme is especially suitable. In the current study, implicit schemes are used for both steady and unsteady problems as detailed in the following subsections.

2.1.3.1 Steady State Probelms

The current work follows the popular time-evolving approach for steady state problems and uses the backward Euler formulation to discretise the the ordinary differential system of Equation 2.14. The implicit scheme for discretisation in a specific cell at index (i, j, k) is as follows

$$\frac{\mathbf{W}^{n+1}-\mathbf{W}^{n}}{\Delta t}=-\frac{\mathbf{R}(\mathbf{W}^{\mathbf{n+1}})}{V} \tag{2.15}$$

the superscript n denotes the n^{th} time step at $n\Delta t$, and $n+1$ refers to the next step. V is the local cell volume. Equation 2.15 is essentially a set of non-linear algebraic equations. It can be typically solved by linearising the residual term R using

$$\begin{aligned}\mathbf{R}(\mathbf{W}^{\mathbf{n+1}}) &= \mathbf{R}(\mathbf{W}^{\mathbf{n}})+\frac{\partial \mathbf{R}}{\partial t}(\mathbf{W}^{n})\Delta t+O(\Delta t^{2})\\ &\approx \mathbf{R}(\mathbf{W}^{\mathbf{n}})+\frac{\partial \mathbf{R}}{\partial \mathbf{W}}(\mathbf{W}^{n})\frac{\partial \mathbf{W}}{\partial t}\Delta t\\ &\approx \mathbf{R}(\mathbf{W}^{\mathbf{n}})+\frac{\partial \mathbf{R}}{\partial \mathbf{W}}(\mathbf{W}^{n})\Delta \mathbf{W},\end{aligned} \tag{2.16}$$

where $\Delta \mathbf{W}=\mathbf{W}^{n+1}-\mathbf{W}^{n}$. Equation 2.15 now becomes a linear system

$$\left[\frac{V}{\Delta t}\mathbf{I}+\frac{\partial \mathbf{R}}{\partial \mathbf{W}}(\mathbf{W}^{n})\right]\Delta \mathbf{W}=-\mathbf{R}(\mathbf{W}^{\mathbf{n}}). \tag{2.17}$$

Solving such a linear system using a direct approach is prohibitive due to its large size and strong stiffness. Alternatively, the linear system is solved using a Generalised Conjugate Gradient (GCG) method considering its accuracy, efficiency, and reasonable memory requirements. A Block

Incomplete Lower-Upper (BILU) factorisation [105] is used for the preconditioning of the system. In the early stage of this implicit scheme, a few explicit iterations are performed using the forward Euler scheme to provide a fine initial solution. An approximate Jacobian matrix [106], which is more diagonally dominant and with fewer non-zero entries, is used to reduce the CPU time and memory requirements.

2.1.3.2 Unsteady State Problems

For unsteady calculations, the implicit dual-time stepping approach proposed by Jameson [107] is adopted. The idea is to use an implicit scheme with a larger stability region, and to solve the implicit equations at each real time step using inner iterations as steady state problems in the pseudo time. In practice, such an approach allows the same steady solver to be re-used and retains its advantages in unsteady computations, and is hence widely used for unsteady CFD problems.

The ordinary system of Equation 2.14 is first discretised in real time using the following implicit scheme

$$\frac{1}{V}\mathbf{R}^{*} = \frac{3\mathbf{W^{n+1}} - 4\mathbf{W^{n}} + \mathbf{W^{n-1}}}{2\Delta t} + \frac{1}{V}\mathbf{R}(\mathbf{W^{n+1}}) = 0. \tag{2.18}$$

By introducing a pseudo time term τ, Equation 2.18 can be converted into a format very similar to the steady formulation in Equation 2.15

$$\frac{\mathbf{W}^{n+1,m+1} - \mathbf{W}^{n+1,m}}{\Delta\tau} + \frac{1}{V}\mathbf{R}^{*}(\mathbf{W}^{n+1,m+1}) = 0, \tag{2.19}$$

where m refers to the m^{th} time step in terms of the pseudo time τ. The non-linear system of Equation 2.19 can hence follow the same solution approach as the steady state problem, and the CFD code can re-use the exactly same subroutines built for the steady discretisation.

2.1.4 Turbulence Modelling

Fully resolving turbulence directly using only the Navier-Stokes equations (Direct Numerical Simulation) is still a challenge today. The difficulty is to resolve flow features that have drastically different temporal and spatial scales at the same time. Excessive temporal and spatial resolutions are hence needed for even very simple geometries and conditions, which leads to prohibitive computational costs. In comparison, the Large Eddy Simulation (LES) approach introduces a few simplifications by modelling small-scale vortices using subgrid-scale models (SGS) while fully resolving the large-scale ones. However, the computational cost is still high for large practical applications. The Reynolds-Averaged Navier-Stokes (RANS) approach introduces further simplifications by decomposing the flow variables into mean and fluctuating parts. Although extra assumptions and models are needed to close the RANS equations, this approach has been popularly used for engineering applications due to its relatively low computational cost and robustness. Generally, the RANS approach is capable of capturing the dominant flow features, but has difficulties resolving the delicate turbulent details. Hybrid approaches are hence proposed to bridge the LES and RANS approaches, e.g. the Detached Eddy Simulation (DES), that combine the low cost of RANS and some of the turbulence resolving ability of LES. These hybrid approaches mostly use RANS simulations in boundary layers and switches to LES in free-stream regions. Nonetheless, the DES approach often has strong dependency on the grid scale to switch models, and non-physical, grid-induced solutions may result because of this.

A variety of turbulence modelling options have been implemented in the HMB3 solver, including RANS, hybrid RANS/LES, and LES, but for the current study, the RANS k-ω SST (Shear Stress Transport) approach is used for most cases, considering the large number of simulations of rotary wings and rotorcraft required for performance analysis and design optimisation. For most cases in this study, turbulent effects are regarded as a secondary concern. However, for a few cases, where massive separation is present, the Scale Adaptive Simulation (SAS), which operates in the RANS mode but has a scale-resolving ability, is invoked.

The simulation requirements for these two approaches are similar as they share plenty of similarities in their formulations. In terms of spatial resolution, the grid y+ values were kept near 1 for most of the simulation cases in this thesis. The near-body grids adopted uniform distributions wherever possible, and the cell sizes were kept around 0.1 to 0.25 times of rotor blade chord length, which is typical for rotary-wing simulations [108]. Further, grid refinement studies were performed for the validation cases to further verify the spatial resolution In the temporal resolution aspect, most simulation cases in this work adopted time step sizes that are less than or equal to $1^{\circ}/step$, which corresponded to at least 360 steps within the major flow frequency. For simulations of rotary-wing systems, the rotor blade passing frequency (BPF) and its harmonics are typically the dominant frequencies of the flow field, and they are often much higher than other secondary vortex shedding or flow separation frequencies. The $1^{\circ}/step$ step size was also reduced whenever necessary to provide finer flow resolution and to verify the temporal resolution required. Details of the turbulence modelling methods are presented in the following subsections.

2.1.4.1 Favre Averaging

Resolving turbulent flows based on the Reynolds-Averaged Navier-Stokes (RANS) equations is hence a more practical and efficient approach for simulations of rotors and rotorcraft in the current study. The RANS equations are derived by considering the Reynolds averaging of a time-dependent, primitive flow variable ϕ as follows

$$\phi = \bar{\phi} + \phi', \tag{2.20}$$

where $\bar{\phi}$ is the time-averaged mean value of ϕ, while ϕ' is a small fluctuating term representing the turbulent influence.

However, when the flow density shows large variations, the Reynolds averaging results in lots of non-zero terms when applied to e.g. the momentum or energy equations. It is hence necessary to further introduce the density-weighted Favre averaging for compressible flows

$$\tilde{\phi} = \overline{(\rho\phi)}/\bar{\rho}, \tag{2.21}$$

$$\phi = \tilde{\phi} + \phi'', \tag{2.22}$$

where $\overline{(\cdot)}$ is the time averaging operation. $\tilde{\phi}$ is the Favre-averaged value, and ϕ'' is the corresponding disturbance. Applying Equation 2.22 to the primitive variables in Equation 2.1, we have

$$\begin{cases} \frac{\partial \bar{\rho}}{\partial t} + \frac{\partial}{\partial x_i}(\bar{\rho}\tilde{u}_i) = 0 \\ \frac{\partial}{\partial t}(\bar{\rho}\tilde{u}_i) + \frac{\partial}{\partial x_j}\left(\bar{\rho}\tilde{u}_i\tilde{u}_j + \bar{P}\delta_{ij} + \overline{\rho u_i'' u_j''} - \widetilde{\tau_{ji}} - \overline{\tau_{ji}''}\right) = 0 \\ \frac{\partial}{\partial t}(\bar{\rho}\tilde{E}) + \frac{\partial}{\partial x_j}\Big(\bar{\rho}\tilde{u}_j\tilde{E} + \bar{P}\tilde{u}_j + c_p\overline{\rho u_j'' T} + u_i\overline{\rho u_i'' u_j''} + \frac{1}{2}\overline{\rho u_j'' u_i'' u_i''} \\ \qquad\qquad + \bar{q}_j - \tilde{u}_i\tilde{\tau_{ij}} - \overline{u_i''\tau_{ij}} - \tilde{u}_i\tau_i\bar{j}''\Big) = 0 \end{cases} . \tag{2.23}$$

Equation 2.23 is referred to as the Favre-Averaged Navier-Stokes equations (in dimensional form), or more commonly still the Reynolds-Averaged Navier-Stokes equations. The equations can be made dimensionless following the same process in previous sections. Note that the energy term $\tilde{E}$ now has a slightly different definition due to the averaging

$$\tilde{E} = \tilde{e} + \frac{\tilde{u}_k\tilde{u}_k}{2} + k, \tag{2.24}$$

where $k = \widetilde{u_k'' u_k''}/2$ is the turbulent kinetic energy and is now an extra unknown variable. A number of other unknown variables, i.e. the Reynolds stress tensor $\overline{\rho u_i'' u_j''}$, molecular diffusion $\overline{u_i''\tau_{ij}}$, turbulent transport $\frac{1}{2}\overline{\rho u_j'' u_i'' u_i''}$, and turbulent heat flux $c_p\overline{\rho u_j'' T}$, also arise from the averaging in Equation 2.23. These must be modelled with extra correlations, and this is known as the closure problem of the RANS equations. Various turbulence models have been proposed to close the RANS equation. In particular, the following Boussinesq approximation of the Reynolds stress τ_{ij}^{turb} and the gradient assumption for the turbulent heat flux q_j^{turb} are popularly used

$$\tau_{ij}^{turb} = -\overline{\rho u_i'' u_j''} \approx \mu_t\left(\frac{\partial \tilde{u}_i}{\partial x_j} + \frac{\partial \tilde{u}_j}{\partial x_i} - \frac{2}{3}\frac{\partial \tilde{u}_k}{\partial x_k}\delta_{ij}\right) - \frac{2}{3}\bar{\rho}k\delta_{ij}, \tag{2.25}$$

$$q_j^{turb} = c_p \overline{\rho u_j'' T} \approx -c_p \frac{\mu_t}{Pr_t} \frac{\partial \tilde{T}}{\partial x_j}, \tag{2.26}$$

where μ_t is the turbulence viscosity, and $Pr_t \approx 0.9$ is the turbulent Prandtl number. The present research has chosen the two-equation k-ω SST model [109] for most of the simulations, due to its known solid performance for both adverse pressure gradients and free shear layers. However, for cases where excessive flow separation is present, the Scale Adaptive Simulation (SAS) approach is employed. These are detailed in the following subsections.

2.1.4.2 k-ω SST (Shear Stress Transport) Turbulence Model

The original k-ω model was developed by Wilcox [110] with two transport equations for the turbulent kinetic energy k and the specific dissipate rate ω to close the RANS equations. The k-ω model follows the eddy viscosity assumption of the Reynolds stresses and expresses the eddy viscosity μ_t as

$$\mu_t = \rho \frac{k}{\omega}. \tag{2.27}$$

The k-ω model can handle adverse pressure gradients near the wall, but its performance becomes poorer when dealing with free shear layers. Therefore, Menter [109] proposed a blending between the k-ω model and the k-ε models, which has a better ability in free streams. The blended two transport equations are

$$\begin{cases} \frac{D}{Dt}(\rho k) = \tau_{ij} \frac{\partial u_i}{\partial x_j} - \beta^* \rho \omega k + \frac{\partial}{\partial x_j}\left[(\mu + \sigma_k \mu_t) \frac{\partial k}{\partial x_j}\right] \\ \frac{D}{Dt}(\rho \omega) = \frac{\gamma}{\nu_t} \tau_{ij} \frac{\partial u_i}{\partial x_j} - \beta \rho \omega^2 + \frac{\partial}{\partial x_j}\left[(\mu + \sigma_\omega \mu_t) \frac{\partial \omega}{\partial x_j}\right] + 2\rho(1 - F_1)\sigma_{\omega 2} \frac{1}{\omega} \frac{\partial k}{\partial x_j} \frac{\partial \omega}{\partial x_j} \end{cases}. \tag{2.28}$$

Here, $\frac{D}{Dt}(\cdot)$ is the substantial differentiation operation. $\nu_t = \mu_t/\rho$ is the turbulent kinematic viscosity. β^*, σ_k, σ_ω, and $\sigma_{\omega 2}$ are constants [109]. F_1 is a blending factor combining the k-ω and k-ε models. Let ϕ_1 denote any constant from the original k-ω model and ϕ_2 from the k-ε model, the blending works as follows

$$\phi = F_1\phi_1 + (1 - F_1)\phi_2. \tag{2.29}$$

Further, the k-ω SST model also uses Bradshaw's assumption, i.e. the shear stress is proportional to the turbulent kinetic energy in the boundary layer, with the eddy viscosity assumption to account for the shear stress transport effect to improve the handling of adverse pressure gradients. The blending is formulated as follows

$$\mu_t = \rho \frac{a_1 k}{max(a_1\omega; \Omega F_2)}, \tag{2.30}$$

where F_2 is a function that has the value one for flows inside the boundary layers and zero for free shear layers, thereby switching between the Bradshaw's assumption and the eddy viscosity assumption. However, the k-ω SST model tends to produce high turbulent viscosities in unsteady regions, which in turn leads to large flow length scales. This can be resolved, to some extent, by introducing the Scale Adaptive Simulation (SAS) detailed in the next subsection. More detailed descriptions of the formulations, boundary conditions, values of the closure coefficients, as well as, definitions of the blending factors can be found in Ref [109].

2.1.4.3 Scale Adaptive Simulation (SAS)

The Scale Adaptive Simulation (SAS) model is capable of resolving the turbulent spectrum in unsteady flow regions, while also operating in standard RANS mode. In some cases, it automatically balances the contributions of modelled and resolved turbulent stress much like the hybrid LES/RANS approach. However, the SAS model has a weaker dependence on the grid cell size and has moderate computational cost by simply adding extra source terms.

The SAS concept was proposed by Menter and Egorov [111, 112], based on Rotta's model [113] considering the integral length scale. Menter and Egorov proposed their first scale-resolving model named the KSKL [114] model by adopting the second derivative of the velocity field in the scale-defining equation, which leads to the von Karman length scale. It was shown that this approach can be combined with classic two-equation models. For the k-ω SST model, the SAS capability can be added by an extra source term to the dissipation rate

$$Q_{SAS} = max\left[\rho\xi_2\kappa S^2\left(\frac{L}{L_{vk}}\right)^2 - C_{SAS}\frac{2\rho k}{\sigma_\psi} * max\left(\frac{1}{k^2}\frac{\partial k}{\partial x_j}\frac{\partial k}{\partial x_J}, \frac{1}{\omega^2}\frac{\partial \omega}{\partial x_j}\frac{\partial \omega}{\partial x_j}\right), 0\right], \tag{2.31}$$

where F_{SAS}, ξ_2, C_{SAS} are coefficients. l is the length scale of the modelled turbulence. L_{vk} is the von Karman length scale, which needs to be limited by the local grid size to allow for energy dumping at high wave numbers. More details of the formulations and constants can be found in Ref[111].

2.1.5 Rotating Reference Frame

For simulations of cases with only rotational motions and axisymmetry, such as propellers in hover or axial flight, it is convenient to use the non-inertial, rotating reference frame to eliminate the unsteadiness and save computational costs. A popular approach is to formulate and discretise the governing equations in Equation 2.1 in a rotating reference frame in which the rotor blades are stationary. This results in an addition of a momentum source term representing the non-inertial forces as

$$S = [0, -\rho\omega \times \vec{u}_h, 0]^T, \tag{2.32}$$

where ω is the rotational speed, and $\vec{u}_h$ is the local flow velocity in the rotating reference frame. Meanwhile, extra translational motions, along the rotational axis e.g. axial flight velocities, are accounted for by introducing mesh velocities. With the help of periodic planes, the computational cost can be further reduced by using only a fraction of the entire computational domain. The rotational reference frame is widely used for simulations of propellers and ducted propellers in hover or axial flight. For ducted propellers, special boundary conditions are implemented by imposing opposite surface speeds to account for stationary walls in the rotating reference frame.

2.2 Automatic Grid Generation

As a key part of CFD analyses and optimization, mesh generation demands a significant amount of effort and human interaction, especially for complex components. Unstructured grids can ease the mesh generation efforts to some extent, but the flow solution often suffers from the irregular cell shapes. The data structure of unstructured grids also may not be friendly when it comes to element or point searching, and the resulting memory and computation costs can be high. In contrast, structured grids often have much better mesh quality and highly efficient data structure, and this is why the current work adopted fully-structured grids. The difficulties, however, are mostly associated with the mesh generation. Multi-block structured grids, i.e. dividing the computational domain first into many blocks then filling the blocks with structured elements, add more flexibility to the mesh generation and help ease the difficulties slightly. Nonetheless, enormous human efforts are still required, especially for complex geometries.

To ease the effort of structured mesh generation and for future parametric/optimization studies, an automation framework for geometry composition and grid generation is therefore proposed and examined in the present work using the ICEM Hexa^{TM} mesher.

The ICEM Hexa^{TM} mesher is a commercial package for the generation of structured, hexahedral, and body-fitted grids. It incorporates a shell interface in Tcl/tk language with an extended library of commands, so that automation can be realized through high-level programming. The proposed automation framework is designed to deliver not only ready-to-run, multi-block, structured grids for CFD solvers, but also geometry models for CAD tools, all from a given set of parameters. Comparing to many in-house automatic grid generation codes, the framework features a high degree of versatility and simplicity for distinct shapes. For instance, in contrast to delivering only solver-compatible grid files, grids generated using the current framework can be easily further manipulated using ICEM Hexa^{TM}. Compatibility with many modern CAE tools in terms of both input and output is also ensured.

A schematic of the current framework is presented in Figure 2.1. The framework is implemented using in-house codes, ICEM Hexa^{TM} scripts, and Unix shell scripts. Through in-house pre-processing codes, the input geometry is analysed and parameterized. Features, like sectional profiles, are extracted and exported in ICEM-compatible formats. Parameters governing the geometry generation, as well as, the meshing process, e.g. outer boundary size, nodes bunching, are taken as input. Modules of the ICEM scripts are also presented in Figure 2.1. NURBS (Non-

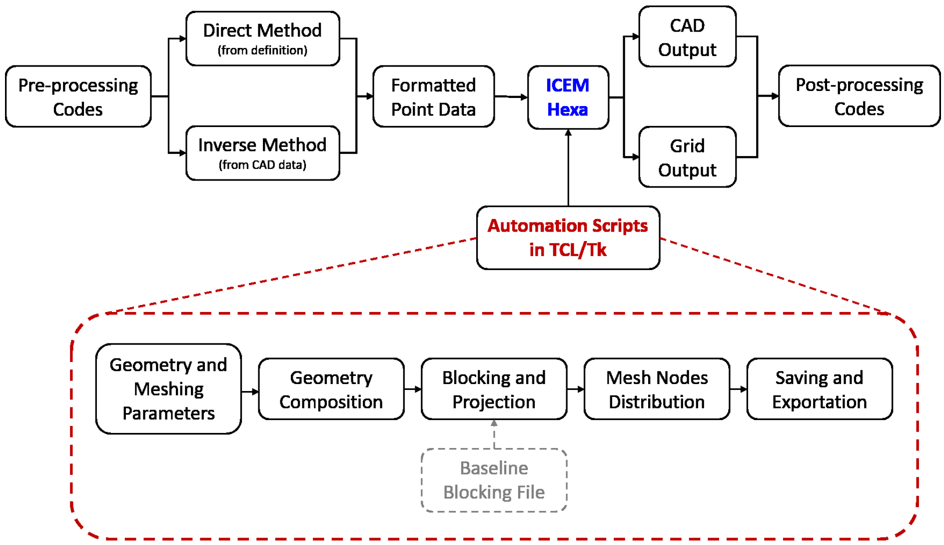

Figure 2.1: Flow-chart of the automation framework for geometry composition and mesh generation.

Uniform Rational B-Spline) based geometries are composed using the geometry module of ICEM Hexa^{TM}. The generation of multi-block mesh topologies, which is a major part of the mesh generation that needs significant human interaction, is realized by importing pre-defined and robust mesh topologies. The design of these topologies for particular applications still needs human effort in advance, but block vertices, edges, and faces are handled by the scripts, according to the specific geometry and the parameters input. The post-processing codes convert the output to CFD solvers and external CAD tools.

The proposed framework can be easily tuned and applied to various specific shape patterns, e.g. blade/wing, fuselage, and duct/centre-body for the present study. Grids are assembled using chimera overlapping strategy for the HMB3 and Fluent^{TM} simulation. The time needed for grid preparation can be reduced from hours to just a couple of minutes. This is very promising for further optimisation or parametric studies such as in Appendix A.

2.3 Actuator Disk Models and New Implementation in HMB3

This section presents a novel implementation of actuator disk models in HMB3. The implementation features a smooth distribution function. The new actuator disk modules in HMB3 has also been differentiated with the help of automatic differentiation to provide gradient information for optimisation purposes.

The actuator disk is an efficient alternative for modelling rotary wing systems, by simplifying rotor disks or blades as equivalent sources of momentum and energy, in CFD simulations. This modelling approach drastically reduces the computational costs thanks to the largely reduced amount of grid cells, since there is no need to resolve the geometry, the associated boundary layers, and sometimes the blade motions. The modelling fidelity is of course penalised by the simplifications, still, the actuator disk modelling is capable of resolving the dominant flow features, e.g. the slip stream, pressure jumps, tip vortices, and super vortices, with adequate accuracy for preliminary analyses of engineering designs. Comparing to blade-resolved simulations, the actuator disk modelling is incapable of resolving small flow details caused by boundary/shear layers and the subsequent interactions near the blades. Therefore, the actuator disk modelling is especially suitable for situations where the rotor-induced flows or interactions are of the main interest, while the flow details near the rotor disk are of minor concern. The actuator disk models have been widely used for studies of rotor/fuselage interactions [65, 115], wind turbines, and propeller/rotor or propeller/wing interactions [116].

The actuator disk models are usually implemented in CFD solvers as special porous boundary conditions or volumetric source terms. While using fully-structured grids, such as in this study, the volumetric source term implementation is especially easy, as locating cell centres close to the rotor disk is easy with the help of the structured grid indices, plus there is no need to account for the special boundary condition while meshing. The general process of adding the volumetric sources is listed below:

1. Find the cell centres closest to the designated rotor disk shape;
2. Compute the momentum and energy source terms according to the rotor geometry and aerodynamics;
3. Add source terms to the residual functions, and the Jacobian matrix in implicit iterations;

4. Update the flow solution.

Essentially, the rotor disk is represented by a cloud of points that are conforming with designated rotor disk shapes in the current study. The momentum and energy source terms for each cell are written as

$$S_{AD} = \begin{bmatrix} 0 \\ f_x \\ f_y \\ f_z \\ f_x u + f_y v + f_z w \end{bmatrix}, \tag{2.33}$$

where $\vec{\mathbf{f}} = (f_x, f_y, f_z)$ is the force vector imposed by the rotor disk at a specific cell centre, which is determined by the loading distribution on the rotor disk. The term $f_x u + f_y v + f_z w$ denotes the work done due to the imposed forces and the local flow velocities.

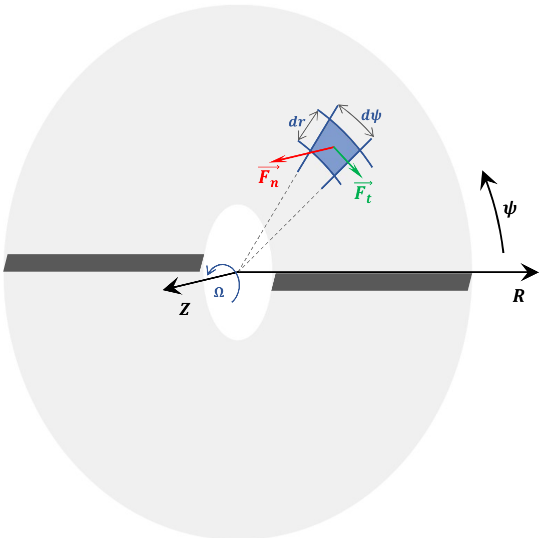

Figure 2.2: Rotor disk in a cylindrical coordinate system.

Dividing a rotor disk into infinitesimal segments in a polar system centring at the rotor centre of rotation, as shown in Figure 2.2, the local force vector for a specific cell is correlated with the pressure jumps as

$$
\begin{aligned}
\vec{\mathbf{f}} &= \vec{\mathbf{F}}_n + \vec{\mathbf{F}}_t \\
&= (\Delta P \vec{\mathbf{n}}_{AD} + \Delta P_t \vec{\mathbf{n}}_{tAD}) r dr d\psi,
\end{aligned}
\tag{2.34}
$$

where (r, ψ) are the local polar coordinates on the disk. $\vec{\mathbf{n}}_{AD}$ and $\vec{\mathbf{n}}_{tAD}$ are normal vectors in the disk normal and tangential directions, respectively. $\Delta P(r, \psi)$ and $\Delta P_t(r, \psi)$ are axial and tangential pressure jump distribution functions, respectively, depending on the rotor aerodynamic characteristics. In numerical implementations, the area term $rdrd\psi$ can be replaced by the local cell face area projected in the disk normal direction.

The total rotor thrust T and torque Q can be expressed in integral forms as follows

$$
\begin{aligned}
T &= a_x \int_0^{2\pi} \int_{R_{rt}}^{R_{tp}} \Delta P(r, \psi) g(r, \psi, t) \sigma(x, y, z) r dr d\psi, \\
Q &= a_t \int_0^{2\pi} \int_{R_{rt}}^{R_{tp}} \Delta P_t(r, \psi) g(r, \psi, t) \sigma(x, y, z) r^2 dr d\psi,
\end{aligned}
\tag{2.35}
$$

where the subscripts $_{rt}$ and $_{tp}$ denoting the root and tip values, respectively. a_x and a_t are scaling factors ensuring that the total thrust and torque imposed to the flow-field are equal to the amount designated.

Here, $\sigma(x, y, z)$ is a disk strength distribution function introduced to help the numerical implementation of actuator disk models in HMB3 and to allow for adjoint computations. In the current solver, each computational cell is assigned a disk strength σ according to the distance between its cell centre and the designated rotor disk shape. This is to eliminate the discontinuities across the disk boundary to allow for the computation of flow sensitivities, as well as, to improve the numerical stability. The $\sigma(x, y, z)$ function has the value 1 when the cell centre is exactly on the rotor disk, and quickly reduces to 0 if the cell centre is far away from the disk.

The $\sigma(x, y, z)$ function can be further detailed as

$$
\sigma = \sigma_r \cdot \sigma_{ax}, \tag{2.36}
$$

where σ_r is the radial distribution and σ_{ax} is the axial distribution.

In the radial direction, the jumps at the tip and the root are replaced by smooth sine functions in Equation 2.37, as shown in Figure 2.3.

$$\sigma_r = \begin{cases} 0.5sin(\frac{r-r_0}{2\delta}\pi)+0.5, & r_0-\delta < r < r_0+\delta; \\ 1, & r_0+\delta \le r \le r_1-\delta; \\ 0.5sin(\frac{r_1-r}{2\delta}\pi)+0.5, & r_1-\delta < r < r_1+\delta; \\ 0, & otherwise. \end{cases} \tag{2.37}$$

where r is the radial distance of a cell centre from the disk centre, r_0 and r_1 are respectively the root and the tip radial coordinates. δ is a tolerance factor that adjusts the size of the smooth area. δ usually takes the value of the dimensionless cell size at the disk edge.

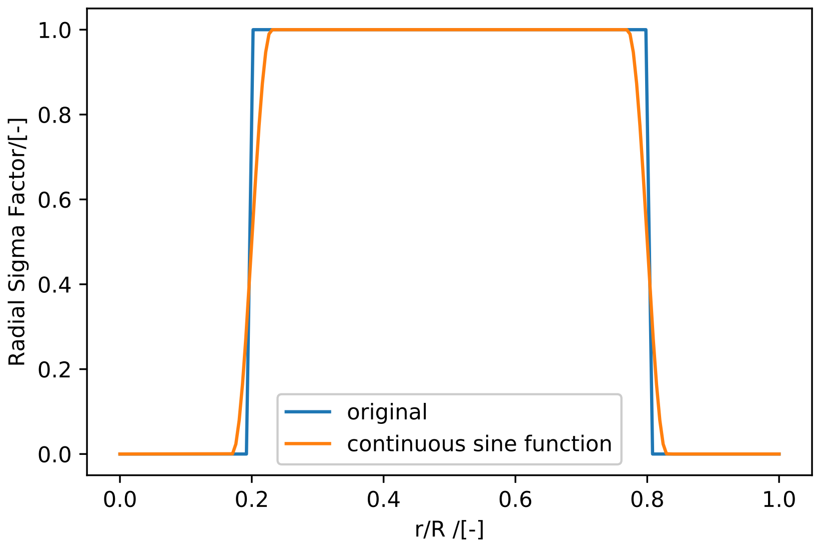

Figure 2.3: Radial distribution $\sigma_r(\alpha)$.

In the axial direction, the jump can be replaced by a Gaussian function or a cosine square function (Equation 2.38) as shown in Figure 2.4.

$$\sigma_r = \begin{cases} cos^2(\frac{\delta Z\pi}{2\varepsilon}), & -\varepsilon < \delta Z < \varepsilon; \\ 0, & otherwise. \end{cases} \tag{2.38}$$

where δZ is the normal distance of a cell centre to the disk plane. ε is a tolerance value adjusting the the size of the smooth area, which can be set as 1 or 2 times the dimensionless cell size in the norm direction. The power can also be adjusted to control the ratio of change. Also presented in

Figure 2.4 are comparisons with the Gaussian distribution. The Gaussian function tends to have a smoother transition to zero. Nonetheless, the cosine square function has been chosen for its simple form for the convenience of the later gradient computations.

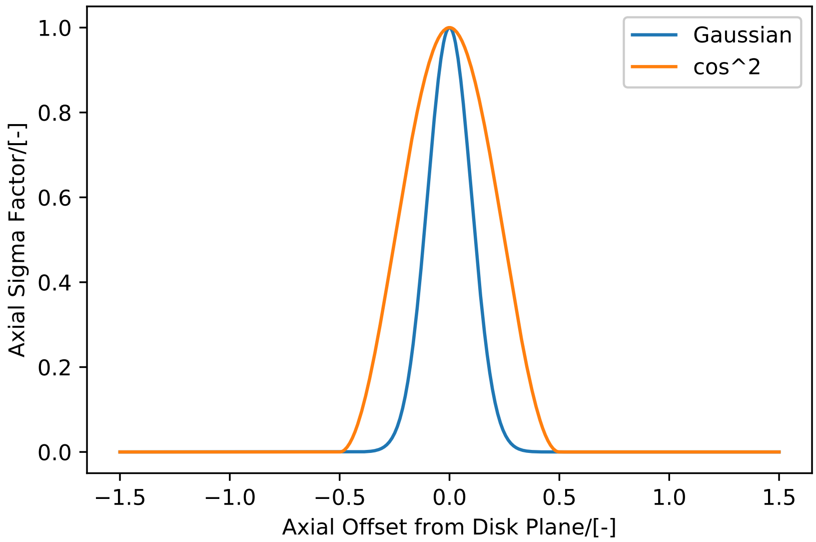

Figure 2.4: Axial distribution $\sigma_{ax}(\alpha)$.

The function $g(r,\psi,t)$ is a time-dependent Gaussian. In unsteady simulations, this function redistributes the initial pressure jump to conform with the time-resolved blade shape [117]. This is to resemble the time-resolved blade motions of rotors, thereby allowing a more realistic resolution of tip/root vortices systems and of the induced flow features. Since it concentrates the momentum sources on the discrete rotor blades, this model is often referred to as the Actuator Line (AL) approach. In steady simulations, $g(r,\psi,t)$ is set to a constant value of 1. The Gaussian function is detailed as follows

$$g = \frac{\sqrt{\pi}(r - r_{rt})}{0.75 N_b c} \Sigma_{k=1}^{Nb} e^{(-L_k^2/\varepsilon_k^2)}, \tag{2.39}$$

where Nb is the number of blades, and c is the nominal blade chord length. r is the local radial position and r_{rt} is the radial position of the nominal root cut out. This term before the exponential is to ensure the overall integration is 1. The azimuth distance L_k between the local cell centre and the kth blade is defined as

$$L_k = \pi cos^{-1}(cos(\Delta\psi)), \tag{2.40}$$

where $\Delta\psi$ is the azimuthal difference between the local point and the kth blade. The spatial distribution ε_k is written as

$$\varepsilon_k = \begin{cases} c\frac{2r}{R}, & 0 < r \leq 0.5R, \\ c, & 0.5R < r \leq R, \end{cases} \tag{2.41}$$

where R is the nominal blade radius. This function concentrates the Gaussian on the discrete blades. It also moves more blade loadings towards the tip to approximate a more realistic distribution. A sample Gaussian distribution for a three-bladed rotor is presented in Figure 2.5 illustrating how the discrete blades are resembled.

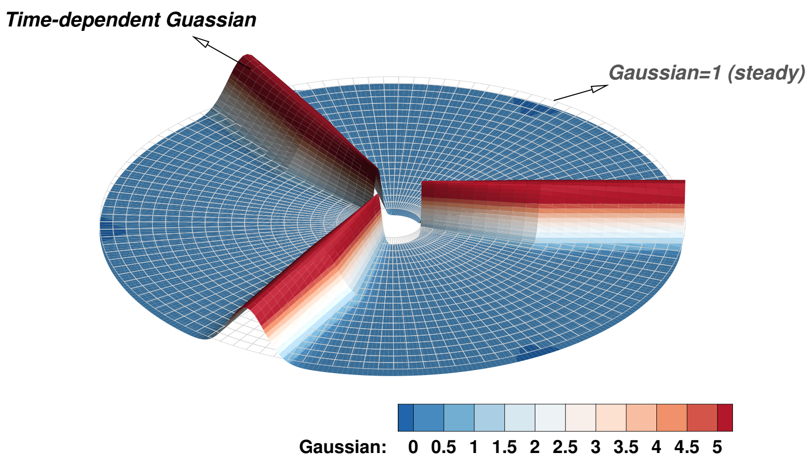

Figure 2.5: Sample time-dependent Gaussian for a three-bladed rotor.

Equation 2.35 is nominally evaluated at each computational cell. The thrust value is then converted to equivalent volumetric momentum and energy sources and added to the discretised governing flow equations. Comparing to blade-resolved simulations of rotors, the actuator disk models resolve fewer flow details due to the lack of accurate geometries/motions, boundary/shear layers etc., but the computational cost is greatly reduced due to the easy convergence and the reduction in grid sizes. The actuator disk models are hence a good option for quick or preliminary studies of complex flow-fields involving rotors, with reasonable accuracy and at much reduced computational costs.

Finally, the pressure distribution functions $\Delta P(r,\psi)$ and $\Delta P_t(r,\psi)$, which play dominant roles in the actuator disk modelling, can be defined in various ways, e.g. from experimental/empirical data, simplified assumptions, or using lower-order tools. These are detailed in following sections.

2.3.1 Uniform Disk Model

The uniform disk model assumes a constant pressure jump ΔP across the disk. By solving the integration in Equation 2.35, the pressure jump ΔP in the disk normal direction can hence be written as

$$\Delta P = \frac{T}{\pi(R^2 - R_{rt}^2)} = \frac{C_{T_{UK}} 0.5 \rho_\infty V_{tip}^2 \pi R^2}{\pi(R^2 - R_{rt}^2)} = \frac{C_{T_{UK}} 0.5 \rho_\infty V_{tip}^2}{(1 - (\frac{R_{rt}}{R})^2)}, \tag{2.42}$$

where R_{rt} is the radial position where the root cut-out begins, and R is the radius of the rotor.

In HMB3 calculations, ΔP should be made dimensionless using the reference pressure $\rho_{ref} V_{ref}^2$

$$\Delta \bar{P} = \frac{\Delta P}{\rho_{ref} V_{ref}^2} = \frac{C_{T_{UK}} 0.5 \bar{\rho}_\infty \bar{V}_{tip}^2}{(1 - (\frac{\bar{R}_{rt}}{\bar{R}})^2)}, \tag{2.43}$$

where barred values are made dimensionless using corresponding reference values. Note that the radius and blade cut out are also implicitly normalised using the reference length. In most cases, we have $\rho_{ref} = \rho_\infty$, hence $\bar{\rho}_\infty = 1$. For the reference speed V_{ref}, usually we use the free-stream velocity, but it is also quite common to use a blade tip speed when the free-stream speed is unfavourably small, such as in hover. Therefore, the dimensionless tip speed $\bar{V}_{tip} = \frac{V_{tip}}{V_{ref}}$ must be specified explicitly in the input file.

The tangential momentum can be accounted for in the same manner. Assuming the function ΔP_t is also a constant in Equation 2.35, ΔP_t can be solved from the integration as

$$\Delta P_t = \frac{3Q}{2\pi(R^3 - R_{rt}^3)} = \frac{3C_{Q_{UK}} 0.5\rho_\infty V_{tip}^2 \pi R^3}{2\pi(R^3 - R_{rt}^3)} = \frac{3C_{Q_{UK}}\rho_\infty V_{tip}^2}{4(1 - R_{rt}^3/R^3)}, \tag{2.44}$$

Similarly, ΔP_t is also made dimensionless using $\rho_{ref} V_{ref}^2$:

$$\Delta \bar{P}_t = \frac{3C_{Q_{UK}}\bar{\rho}_\infty \bar{V}_{tip}^2}{4(1 - \bar{R}_{rt}^3/\bar{R}^3)}. \tag{2.45}$$

2.3.2 Non-uniform Disk Models

The non-uniform models, termed 41 and 42 in HMB3 are based on empirical data and the vortex theory [117]. The local pressure jump is expressed based on Joukowski's lift theorem

$$\Delta P = \frac{1}{2\pi r}\rho_\infty U(r,\psi)\Gamma(r,\psi), \tag{2.46}$$

U is the local tangential velocity and Γ is the circulation distribution. The velocity distribution U has the form

$$U(r,\psi) = \Omega r + \Omega R \mu sin(\psi), \tag{2.47}$$

where Ω is the rotating rate, R is the rotor radius.

The circulation distribution is defined as:

$$\Gamma(r,\psi) = \Gamma_4 \bar{\gamma}_4(r,\psi), \tag{2.48}$$

$$\Gamma_4 = \frac{\pi V_\infty^2}{\Omega}\frac{C_{T_{UK}}}{\mu^2}, \tag{2.49}$$

$$\bar{\gamma}_4(r,\psi) = \bar{\gamma}_r(\bar{r}) + \bar{\gamma}_s(\bar{r},\mu)sin(\psi) + \bar{\gamma}_c(\bar{r},\mu)cos(2\psi), \tag{2.50}$$

where $\bar{r} = r/R$. The terms $\bar{\gamma}$, $\bar{\gamma}_s$, and $\bar{\gamma}_c$ are formulated as

$$\bar{\gamma}_r(\bar{r}) = \frac{12}{5}\bar{r}^2(2 - \bar{r}^2 - \bar{r}^4), \tag{2.51}$$

$$\bar{\gamma}_s(\bar{r},\mu) = K\bar{\gamma}_r(\frac{1}{\bar{r}} - \frac{14}{5}\bar{r}), \tag{2.52}$$

$$\bar{\gamma}_c(\bar{r},\mu) = K\bar{\gamma}_r(1 - W\bar{r}^2). \tag{2.53}$$

The coefficients $K(\mu)$ and $W(\mu)$ are regarded as functions of μ. They can be determined by prescribing their functional forms and introducing extra constraints on the rolling and pitching moments. The current study assumes that the forward-flight rotor is trimmed to have zero rolling and pitching moments. For the model 41, simple linear functions are assumed for K and W. For the model 42, however, a more complex functional format is used for K, which offers loading distributions in better agreement with empirical data. More details can be found in Ref [117]. The solutions are obtained using symbolic algebra and are detailed as follows

$$\begin{cases} K = \frac{125}{57}\mu, W = 25/13, & \text{model 41,} \\ \\ K = \frac{250\mu}{3(15\mu+38)}, W = 16/13, & \text{model 42.} \end{cases} \tag{2.54}$$

Overall, Equation 2.46 can be finally written as

$$\begin{aligned} \Delta P &= \frac{1}{2\pi r}\rho_\infty U(r,\psi)\Gamma(r,\psi) = \frac{1}{2\pi r}\rho_\infty(\Omega r + \Omega R\mu sin(\psi))(\frac{\pi V_\infty^2}{\Omega}\frac{C_{T_{UK}}}{\mu^2})\bar{\gamma}_4(r,\psi) \\ &= \frac{1}{2}(1+\frac{R}{r}\mu sin\psi)\frac{\rho_\infty V_\infty^2 C_{T_{UK}}}{\mu^2}\bar{\gamma}_4(\bar{r},\psi). \end{aligned} \tag{2.55}$$

Here, $\bar{\gamma}_4(\bar{r},\psi)$ is not extended as it is a dimensionless term. The normalisation of the ΔP is the same as the uniform disk case above, taking the reference pressure $\rho_{ref}V_{ref}^2$

$$\Delta\bar{P} = \frac{\Delta P}{\rho_{ref}V_{ref}^2} = \frac{1}{2}(1+\frac{\bar{R}}{\bar{r}}\mu sin\psi)\frac{\bar{\rho}_\infty \bar{V}_\infty^2 C_{T_{UK}}}{\mu^2}\bar{\gamma}_4(\bar{r},\psi), \tag{2.56}$$

2.4 Optimisation Frameworks

The general formulation of a non-linear optimisation problem can be written as

$$
\begin{aligned}
Find &: \\
& min(I(\alpha)), \\
\text{by varying:} & \\
& \alpha_{i,min} \leq \alpha_i \leq \alpha_{i,max}, i \in 1, ..., n, \\
\text{subject to:} & \\
& g_j(\alpha) \leq 0, j \in 1, ..., m, \\
& h_k(\alpha) = 0, k \in 1, ..., p.
\end{aligned}
\tag{2.57}
$$

where $I(\alpha)$ is the objective or cost function to be minimised (or maximised), subject to m inequality constraints $g_j(\alpha)$ and p equality constraints $h_k(\alpha)$. $\alpha = (\alpha_1, ..., \alpha_n)$ is the design variable vector of n dimensions.

To handle the optimisation problem 2.57, various algorithms [118] have been developed in the literature[118]. For aerodynamic optimisation, gradient-based and gradient-free approaches have been popular due to their efficiency, flexibility, and fine compatibility with existing numerical tools. In this study, gradient-based and gradient-free optimisation frameworks are compiled and compared. The gradient-based approach is based on the adjoint computation of gradients and the Sequential Least-Square Quadratic Programming algorithm (SLSQP), while the gradient-free approach uses the Kriging surrogate model in combination with the Efficient Global Optimisation (EGO) algorithm. Details of the methods and the framework are present below.

2.4.1 Discrete Adjoint Method

For many aerodynamic optimisation problems, the cost function I, or the objective function, can be written in a general format as:

$$I = I(W(\alpha), \alpha), \tag{2.58}$$

where α is the independent design variable vector. $W(\alpha)$ is the flow variable vector (in conservative or primitive format), which is subject to α implicitly.

To formulate an optimisation problem to find the local extrema of I, the key point is solving the gradients of I w.r.t design variables α to navigate in the design space. The full derivative of I w.r.t α is written as

$$\frac{dI}{d\alpha} = \frac{\partial I}{\partial W}\frac{\partial W}{\partial \alpha} + \frac{\partial I}{\partial \alpha}. \tag{2.59}$$

The difficulty falls on resolving the first term on the r.h.s $\frac{\partial I}{\partial W}\frac{\partial W}{\partial \alpha}$, especially on $\frac{\partial W}{\partial \alpha}$. The correlation between W and α is highly implicit and vague. In the context of CFD, the two are implicitly coupled in the governing flow equation for steady state problems

$$\mathbf{R}(\mathbf{W}(\alpha), \alpha) = 0, \tag{2.60}$$

where $\mathbf{R}(\mathbf{W}(\alpha), \alpha)$ is the residual function of the governing equations. Since R is constantly zero for steady problems, its derivative w.r.t any input is also zero. Thus we should have $\frac{dR}{d\alpha}$ as

$$\frac{dR}{d\alpha} = \frac{\partial R}{\partial W}\frac{\partial W}{\partial \alpha} + \frac{\partial R}{\partial \alpha} = 0. \tag{2.61}$$

This forms a linear system through which we can solve for the term $\frac{\partial W}{\partial \alpha}$. More explicitly, the linear system is formulated as:

$$\frac{\partial R}{\partial W}\frac{\partial W}{\partial \alpha} = -\frac{\partial R}{\partial \alpha}. \tag{2.62}$$

The evaluation of the Jacobian matrix $\frac{\partial R}{\partial W}$ is often straightforward as it is typically required by implicit temporal methods while using Newton iterations. The term $\frac{\partial R}{\partial \alpha}$ is also easy to determine as the correlation can be expressed explicitly. Hence, by solving the linear system in Equation 2.62 for $\frac{\partial W}{\partial \alpha}$, we can eventually get the gradients in Equation 2.59. This forms the direct approach to solve the sensitivity. The benefit of the direct approach is that the linear system of 2.62 scales with the number of design variables, and its size is independent of the number of objective functions. This is suitable for situations where there are many objective and constraint functions, but just a few design variables, e.g. aircraft trimming via pitch control. However, it is obviously not suitable for problems with many design variables and fewer objectives, such as aerodynamic shape optimisation.

Another idea to tackle the term $\frac{\partial W}{\partial \alpha}$ is through the Lagrangian multiplier approach by introducing an intermediate vector λ to correlate $\frac{\partial I}{\partial W}$ and $\frac{\partial R}{\partial W}$, so that the product of these two can be related to $\frac{\partial R}{\partial \alpha}$ as in Equation 2.62. The intermediate vector λ, which is also often called the adjoint vector, works as follows:

$$\lambda^T \frac{\partial R}{\partial W} = -\frac{\partial I}{\partial W} \Rightarrow (\frac{\partial R}{\partial W})^T \lambda = -(\frac{\partial I}{\partial W})^T. \tag{2.63}$$

Note the transpose signs here are necessary here to form the linear system by switching sequences of vector/matrix productions. After solving the adjoint vector λ, the $\frac{\partial I}{\partial W}$ term in the sensitivity equation 2.59 can be substituted as:

$$\frac{dI}{d\alpha} = -\lambda^T \frac{\partial R}{\partial W}\frac{\partial W}{\partial \alpha} + \frac{\partial I}{\partial \alpha} = \lambda^T \frac{\partial R}{\partial \alpha} + \frac{\partial I}{\partial \alpha}. \tag{2.64}$$

This forms the adjoint approach to solve the sensitivity. The benefit of the adjoint approach, in contrast to the direct approach, is that the linear system of Equation 2.63 scales only with the number of objective/constraint functions, so the size is irrelevant to the number of design variables. This is especially suitable for situations where there are many objectives but just a few objectives need to be considered, such as aerodynamic shape optimisation.

2.4.2 Automatic Differentiation

As noted in previous section, either the direct or the adjoint approach requires intensive computations of gradients of the residual and objective functions w.r.t design variables and flow variables. These evaluations of course can be accomplished through manual derivation and programming, but the efforts required can be prohibitive given the complexity of the formulations, especially when turbulence modelling is involved. To solve this issue, the automatic differentiation (AD) [119, 118] technique is used.

Automatic differentiation is a programming technique to evaluate the derivatives of functions implemented as computer programs. Comparing to finite differences, the AD approach computes the derivatives analytically and suffers little from cancellation errors. Comparing to symbolic differentiation, it bypasses the complexity and delivers directly the code. There are mainly two types of automatic differentiation methods, i.e. Operator Overloading (OO) and Source Code Transformation (SCT). The OO approach amends data types with derivative variables and yields fewer modifications to the source code, but it requires the language to support high-level features such as user-defined data type and operator overloading. Also, the overloaded codes tends to have lower efficiency. The SCT approach, on the other hand, directly generates new codes, which may be less readable but benefit from higher efficiency and compiling optimisation. In this work, the Tapenade [119] package is used for the automatic differentiation, which supports C and FORTRAN languages and follows the Source Code Transformation approach.

There are mainly two modes of automatic differentiation, i.e. the forward (or tangent) mode and the backward (or reverse) mode. The forward mode is straightforward and follows the chain rule for each operation involved to compute the derivatives. On the other hand, the reverse mode first executes the original code, then computes the derivatives in a reverse sequence. Consider a simple function $z = xsin(y)$ with x and y being the independent values, and the example differentiated pseudo codes are presented in Table 2.1. The forward mode takes two extra inputs x_d and y_d and gives one extra output $\frac{\partial z}{\partial x}x_d + \frac{\partial z}{\partial y}y_d$. This is equivalent to computing $\mathbf{J} \cdot [x_d, y_d]^T$, where $\mathbf{J} = [\frac{\partial z}{\partial x}, \frac{\partial z}{\partial y}]$ is the Jacobian matrix. In comparison, the reverse mode takes one extra input z_b and gives two extra outputs $\frac{\partial z}{\partial x}z_b$ and $\frac{\partial z}{\partial y}z_b$. This is equivalent to computing $\mathbf{J}^T \cdot [z_b]$.

More generally speaking, the forward mode computes the “sensitivity” of a function, i.e. the product of the Jacobian matrix and an input vector $\mathbf{J} \cdot \mathbf{b}$. If the function has only one input and many outputs, by setting the input vector $\mathbf{b} = [1]$, the forward mode produces derivatives of all outputs w.r.t. the input at one time. The backward mode delivers the “gradient” of a function, i.e. the product of the transpose of the Jacobian matrix and an input vector $J^T \cdot b$ (or the vector and matrix product $b^T \cdot J$). If the function has just one output and many inputs, by setting the input vector $\mathbf{b} = [1]$, we obtain the Jacobian matrix of the function. Either mode can be used to compute the

Table 2.1: Examples of the forward and backward modes of automatic differentiation.

Forward mode

```
func_d( x,  xd,  y,  yd) {
    a1 = x;
    a1d = xd;
    a2 = sin(y);
    a2d = cos(y)*yd;
    a3 = a1*a2;
    a3d = a2*a1d + a1*a2d;
    z = a3;
    zd = a3d;

    return z, zd;
}
```

Original code

```
func( x,  y)
{
    a1 = x;
    a2 = sin(y);
    a3 = a1*a2;
    z = a3;
    return z;
}
```

Reverse mode

```
func_b( x, y, zb)
{
    a1 = x;
    a2 = sin(y);
    a3 = a1*a2;
    z = a3;

    a3b = zb;
    a1b = a2*a3b;
    a2b = a1*a3b;
    yb = cos(y)*a2b;
    xb = a1b;

    return z, xb, yb;
}
```

differentiation of a function, and the choice mainly depends on the number of function inputs and outputs. In practice, both modes are needed to efficiently differentiate large and complex codes.

2.4.3 Gradient-based Optimisation

The gradient-based optimisation drives design changes according to the gradients of the cost functions/constraints w.r.t design variables. The optimisation algorithm solves for the searching direction and the step size in the design space using the input information about the objectives, constraints, and gradients. The optimisation framework is shown in Figure 2.6. Based on the initial objective, constraint, and gradient information, the optimiser solves for the searching directions in the design space and step sizes. The design variables are then modified accordingly, and new CFD computations are launched to acquire the new cost function value and gradients. The optimisation iterates until the gradients or step size are approaching zero, or the maximum iteration has been reached.

The Sequential Least-Square Quadratic Programming (SLSQP) algorithm[120] as provided in the *NLopt* library [121] is used as the optimiser in this study. The SLSQP algorithm solves for the searching direction and step size through a sequence of least-square/quadratic approximations of the objectives functions and linear approximations of the constraints. This algorithm is commonly used due to its effectiveness and efficiency. Besides, it only occasionally requests the gradient

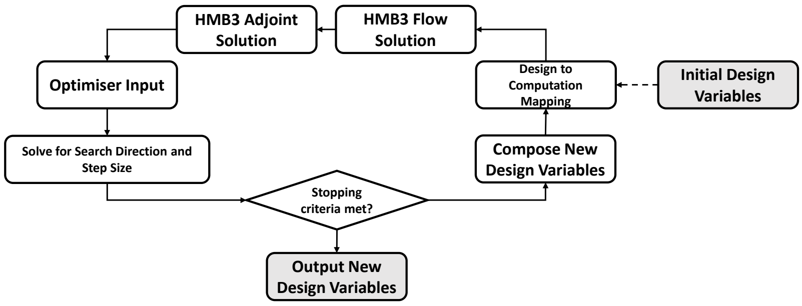

Figure 2.6: Optimisation framework of the gradient-based approach based on adjoint computations.

input, therefore saves the computational costs.

The main advantage of the gradient-based optimisation is that it requires fewer objective evaluations, especially when dealing with large amount of design variables. This makes the gradient-based optimisation especially suitable for aerodynamic shape optimisation. The main drawback, besides the stringent continuity requirement, is that it may be trapped in local minima during the optimisation, depending on the modality of the cost functions. This is demonstrated in Figure 2.7 using a simple objective function $y = xsin(1.5x/\pi)$. The SLSQP algorithm is used here to find the minimum within $0 \leq x \leq 25$. It can be noted here that the optimisation is sometimes trapped in local minima, depending on the starting point of the optimisation. However, both optimisation processes managed to deliver the converged solution within just 4 iterations, highlighting the efficiency of the gradient-based approach.

2.4.4 Kriging Surrogate Model

As the dimension of optimisation problem grows, the required cost function evaluations for gradient-free optimisation can increase drastically [118]. This can be excessively expensive when combined with high-fidelity CFD methods. A popular approach to alleviate this is to bridge the optimisation algorithm and the cost function evaluation with approximation models, or surrogate models, that

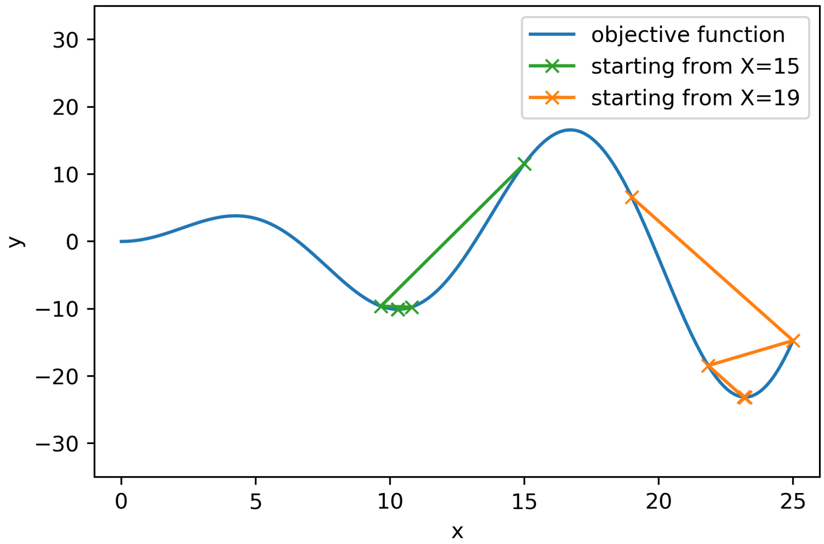

Figure 2.7: Demonstration of the gradient-based optimisation using the SLSQP algorithm.

have adequate accuracy and much reduced computational cost. The Kriging model is hence used in the current work.

The Kriging surrogate model [122] is a spatial interpolation method based on Gaussian regression. It predicts the value of an unobserved evaluation point using a predictor function plus a small, stochastic variance as follows

$$Z(\mathbf{x}) = Z_0 + \varepsilon(\mathbf{x}), \tag{2.65}$$

where $Z(\mathbf{x})$ is the prediction at the unknown location $\mathbf{x}$. Here, Z_0 is the mean value of the data set. $\varepsilon(\mathbf{x})$ is a random variable depending on the distance between the unknown point and the sampling points and has the mean value of zero. In most cases, it is common that values at the interpolation point are very similar to its immediate known neighbours, and have less correlations with sampling points that are far away. The Kriging model hence uses prescribed variograms to describe the correlation between the sampling points and prediction points, thereby solving for the term $\varepsilon(\mathbf{x})$ for the interpolation. Kriging models can be categorised into different types, depending the function types of Z_0 and $\varepsilon(\mathbf{x})$ used. The current work adopts the Ordinary Kriging with Z_0 denoted by a constant and $\varepsilon(\mathbf{x})$ assumed normal distribution.

Comparing to deterministic interpolation methods e.g. radial-base function or polynomial approximation, the benefit of Kriging approximation is that it provides not only predictions of function values at unobserved points, but also the uncertainty of the predictions. Kriging has hence been widely used in geostatics and aerodynamic shape optimisation studies. The drawbacks are the slightly larger computational cost for solving linear systems (which scales with the number of sampling points) and a few assumptions on the data set in terms of stationarity and compliance with normal distributions. Nonetheless, these disadvantages are almost trivial, as the demanded computational cost is much smaller than CFD simulations, and the assumptions can be examined by verifying and assessing the interpolation results.

In the current work, the Kriging model was first used in Chapter 7 to analyse the rotor/propeller aerodynamic interactions, with variations in the propeller position, rotor/propeller thrust ratio, and free-stream velocity. The constructed Kriging models was later incorporated in the gradient-free optimisation framework to optimise the propeller position for minimised aerodynamic interferences. The Kriging model was also used for data interpolation for the parametric study of the equivalent ducted/open rotors in Chapter A. In the present work, the Surrogate Modelling Toolbox of Python [123] is used.

2.4.5 Gradient-free Optimisation

Comparing to gradient-based optimisation discussed earlier, gradient-free approaches do not need the gradient information and hence have no continuity limitations. They are also much less likely to be trapped in local optima. The disadvantage is usually the large amount of objective evaluations required during the optimisation process. This can be prohibitively expensive when combined with CFD methods. Even with the help of surrogate models, the computational cost can still be excessively large when handling a large amount of design variables.

For the gradient-free optimisation in this study, the Efficient Global Optimisation (EGO) [124] algorithm is used. The framework is shown in Figure 2.8. A demonstration of the EGO algorithm for the same objective function $y = xsin(1.5x/\pi)$ is presented in Figures 2.9(a) to 2.9(d). This

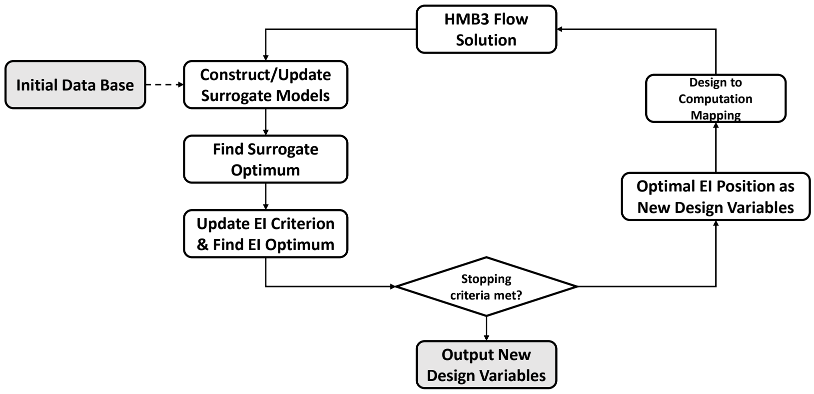

Figure 2.8: Optimisation framework of the gradient-free approach based on the EGO algorithm.

algorithm first finds the global optima within the initial Kriging approximation of the cost function and computes the corresponding Expected Improvement (EI) criterion[124], which is defined as

$$EI(x) = (f_{min} - f^*)\Phi(\frac{f_{min} - f^*}{s}) + s\phi(\frac{f_{min} - f^*}{s}), \tag{2.66}$$

where the f^* denotes the predicted function value at point x, and s is the standard error of this prediction. f_{min} is the current minimum value found. Here, $\phi(\cdot)$ is the normal density function and $\Phi(\cdot)$ is the normal distribution function. In this work, the EI criterion is evaluated from the uncertainty assessment of the Kriging approximation. This gives a rough indication of the possible improvement to the current Kriging optima due to uncertainty. The algorithm then finds the maximum EI, which suggests the best possible improvement, and uses its position in the design space as the next sampling point to evaluate the objective function. The new objective function value is later added to update the Kriging model and the optimisation loop iterates. The stopping criteria usually limit the number of iterations or the value of the EI indicator. Such an algorithm strikes a balance between improving the surrogate accuracy and saving the computational cost, as it only refines the surrogate model locally near the global optima position. To solve for the global optima of the Kriging model and its EI indicator subject to constraints, the classic genetic algorithm as provided in the *pymoo* package [125] is used.

As shown in the demonstration of Figures 2.9(a) to 2.9(d), the EGO algorithm mostly refines

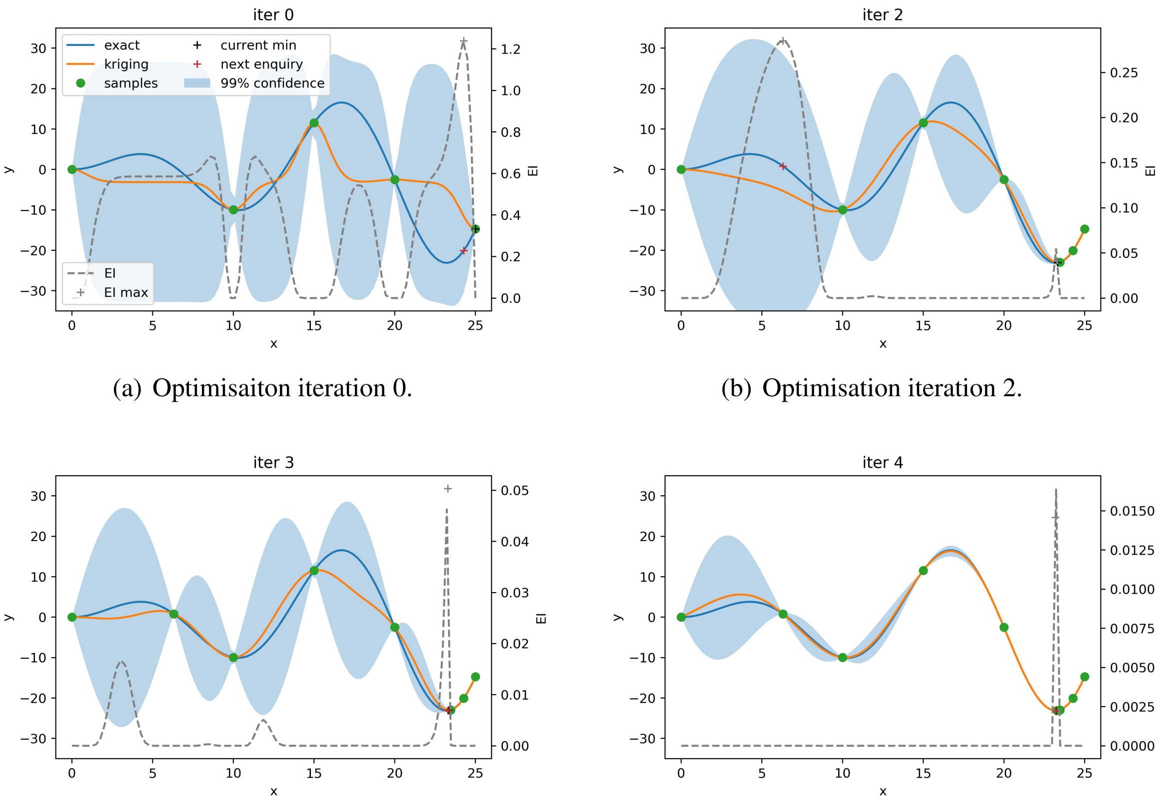

(a) Optimisaiton iteration 0.

(b) Optimisation iteration 2.

(c) Optimisation iteration 3.

(d) Optimisation iteration 4.

Figure 2.9: Demonstration of the EGO optimisation algorithm.

the Kirging model near the global optimum and managed to find the solution within 5 iterations. However, 4 initial data points are used to construct the initial Kriging model. As the dimension of the optimisation problem grows, the number of sampling points required to construct a fine initial model grows in a factorial manner, and so increases the computational cost.

Choices between the gradient-based or gradient-free optimisation should be made with careful considerations of the problem characteristics, complexity, and computational cost. A hybrid approach combining both methods is of course possible and will be assessed in later sections. The hybrid approach takes the output of the first few gradient-free iterations as the starting point for the gradient-based approach. This is to avoid the gradient-based approach being trapped in local optima very close to the original design point. However, the optimisation result may still end up a different local optimum.

2.5 Acoustic Methods

2.5.1 Near-field Acoustics

In this study, the near-field acoustics is directly derived from pressure fields resolved with high-fidelity HMB3 simulations. The sound pressure signal is extracted by subtracting the time-averaged pressure field. The similar approach can be seen used in propeller acoustic analyses using HMB3 [126]. This approach requires high-order schemes and fine spatial/temporal resolution. For the acoustic study of the ducted and un-ducted propellers in the current work, the 3rd-order MUSCL scheme is used, and the background grid is carefully made to guarantee at least 10 mesh points for the wave length targeting at 4 times the Blade Passing Frequency (BPF) in the near-field region. Fine temporal resolution is ensured either through small time steps or through strong steady convergence in the rotating reference frame.

2.5.2 Far-field Acoustics

To resolve the far-field acoustics, it is impractical to use the same approach applied to the near-field acoustics, considering the excessive computational cost to resolve the large computational domain with fine resolution. To evaluate the far-field acoustics with adequate accuracy and at relatively computational cost, the Ffowcs Williams-Hawkings (FW-H) equation [127] is used in this work, following the non-porous Farassat Formulation 1A [128]. The non-porous form is adopted as it can directly take as input the high-fidelity CFD solutions of the surface pressure fields. The formulation has been widely used for far-field noise predictions of aircraft, wind turbines[129], and propellers[130]. The Farassat Formulation 1A [128] solves surface terms of the FW-H equation, i.e. the thickness noise and the loading noise, in the time domain, by introducing the retarded time concept. The formulation results in two linear equations, respectively for, the thickness noise in Equation 2.67, and the loading noise in Equation 2.68

$$4\pi p_T'(\mathbf{x},t) = \int_{\bar{f}=0} \left(\frac{\rho_0 \dot{v}_n}{r(1-M_r)^2} + \frac{\rho_0 v_n \hat{r}_i \dot{M}_i}{r(1-M_r)^3} + \frac{\rho_0 v_n c(M_r - M_i^2)}{r^2(1-M_r)^3} \right)_{ret} dS, \tag{2.67}$$

$$4\pi p_L^{'}(\mathbf{x},t) = \int_{\bar{f}=0} \left(\frac{\dot{l}_i \hat{r}_i}{cr(1-Mr)^2} + \frac{(l_i \hat{r}_i)\hat{r}_i \dot{M}_i}{cr(1-M_r)^3} + \frac{l_i \hat{r}_i - M_i l_i}{r^2(1-M_r)^2} + \frac{l_i \hat{r}_i (M_r - M_i^2)}{r^2(1-M_r)^3} \right)_{ret} dS. \quad (2.68)$$

Here, the subscription $\bar{f} = 0$ denotes the wall surface. $()_{ret}$ denotes that the formulation within is evaluated at emission time τ, which correlates with the receiver time t with $t = \tau + |\mathbf{x} - \mathbf{y}(\tau)|/c$ with $\mathbf{x}$ being the receiver position and $\mathbf{y}$ being the emission point on the wall surface at emission time τ. Further definitions of the variables of Equations 2.67 and 2.68 are listed in Table 2.2.

Table 2.2: Variable notations in Equations 2.67 and 2.68.

Symbol	Variable
c	Sound speed(assumed constant at low flow speeds)
$p_T^{'}$	Thickness noise received at $(\mathbf{x},t)$
$p_L^{'}$	Loading noise received at $(\mathbf{x},t)$
ρ_0	Free-stream density
$v_n = v_i n_i$	Surface normal velocity in tensor form
$r_i = x_i - y_i$	Space vector between receiver and source positions
$\hat{r}_i = \frac{r_i}{r}$	Normalised directivity vector
$M_i = \frac{v_i}{c}$	Mach number vector
$M_r = M_i \hat{r}_i$	Projected Mach number vector in the radiation direction
$li = (p - p_0)n_i$	Loading vector, p is the local surface pressure and p_0 is the free-stream pressure
$\dot{v}_n$	Temporal derivative of the surface normal velocity
$\dot{M}_i$	Temporal derivative of the Mach number vector
$\dot{l}_i$	Temporal derivative of the loading vector

The current far-field acoustic approach ignored the quadrupole sources which require expensive integrations over volumes and has also assumed infinite impedance of solid surfaces. These assumptions surely lead to lower solution accuracy, nonetheless, the current approach is efficient and sufficiently accurate for the purposes of the engineering analysis conducted here based on CFD results, considering the subsonic nature of the current study. Similar approaches were adopted for noise predictions by Luo et.al. [131] for ducted axial fans and by Dighe et.al. [129] for ducted wind turbines. Additionally, the current implementation is an extension of the existing acoustic code HFWH (Helicopter Ffows Williams-Hawkings)[130] in the high-level Julia programming language. The code is attach in Appendix B. Extensive code-to-code comparisons have been performed to verify the current implementation.

2.6 XRotor, DFDC and Ansys Fluent^{TM} Tools

The XRotor and DFDC (Ducted Fan Design Codes) are open-source tools developed by Drela et.al. [132, 47, 52]) for performance predicting and design of ducted/un-ducted propellers. The codes are based on extended classic blade-element/vortex theories, in combination with lifting line and panel methods. They are capable of quickly predicting, or matching the performance for specific geometries, as well as solving the inverse design problem. However, only axisymmetric conditions, e.g. hover or axial flight can be accounted for. The XRotor and DFDC codes are used in this work for comparisons with HMB3 results, as well as, to add more confidence to HMB3 results when experimental data is absent.

The general-purpose Ansys Fluent ^{TM} solver is also used for simulations of the duct geometries (without the propeller) for comparison purposes with HMB3. Simulations using the two solvers are performed on the same grids to minimise the uncertainties, either with or without chimera/overset interfaces. Closest possible numerical settings to HMB3 were configured in Fluent ^{TM}, i.e., compressible ideal gas model, pressure far-field boundary conditions, implicit linear solver, and k-ω SST model for turbulence modelling.

Chapter 3

Numerical Verification[1]

This chapter focuses on the numerical validation of the employed tools, geometries and meshing, and simulation strategies in this thesis. The key results and novelties of this chapter are the systematic high-fidelity simulations of various configurations over a range of conditions, as well as, detailed comparisons between methods and modelling strategies.

This validation work mostly focuses on a ducted propeller design by NASA[18] in the 1960s. Nevertheless, evaluations of the actuator disk models are also presented. Brief discussions on the aerodynamic performance are also presented in this chapter and will be further detailed in the next chapter. An evaluation of the proposed automatic grid generation framework is first presented. Numerical simulations were then performed using the HMB3 solver, as well as, lower-order methods and commercial solvers, to validate the geometry, meshing, and simulation strategies. The blade-resolved simulations were then exploited to validate the actuator disk modelling of rotors in axial flight. The actuator disk models were further verified for rotors in edge-wise flight using a rotor/wing interaction case tested by Leishman and Bi [133].

The ducted propeller test case by Grunwald [18] was chosen for its detailed geometry and test information. In addition, the ducted propeller model tested was a 5/16-scaled model of the real-world design that was used on the Doak VZ4D tilt-duct aircraft, but with a different propeller

[1] This chapter has been published in Zhang, T. and Barakos, G. N., High-fidelity CFD validation and assessment of ducted propellers for aircraft propulsion, Journal of the American Helicopter Society, Vol. 66, No. 1, 2021, pp. 128.

design with 3 blades. Regardless, considering the age of these experiments, some uncertainty in the geometry, and test data is expected. The duct geometry is presented in Figure 3.1. Note the centre-body was approximated for the simulations since no detailed information was given in the tests[18]. The blade geometry is detailed in Figure 3.2.

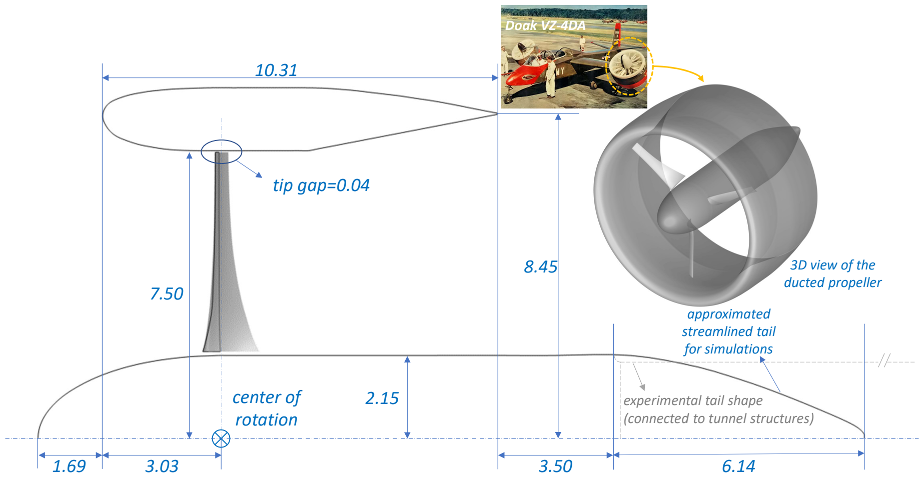

Figure 3.1: Key parameters of the Grunwald ducted propeller. Details of the duct shape can be found in Ref. [18]. Note the centre-body tail is sealed with a streamlined shape, whereas in the experiments it is connected to tunnel structures. The ducted propeller has the same shape of the real-world design used on the Doak VZ-4D aircraft, but with a different propeller design.

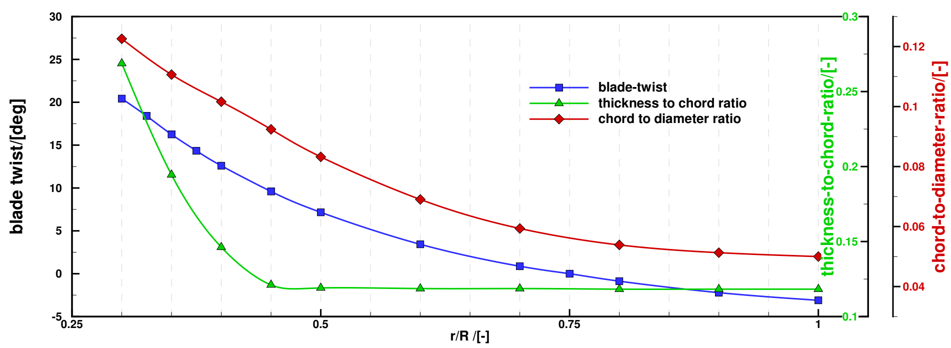

Figure 3.2: Key parameters of the blade shape of the Grunwald ducted propeller [18]. The blade sections is a NACA6412 aerofoil. The default blade pitch in the simulations is set as $\beta_{0.75} = 29.58°$, which is given by DFDC predictions, in contrast to the nominal experimental setting of $\beta_{0.75} = 24°$.

A detailed test matrix is given in Table 3.1. Apart from the experimental conditions for validation, off-design operating conditions, i.e. at high advance ratios and high angles of attack, are also explored and presented in the following chapters to investigate performance limitations of ducted propellers.

Table 3.1: Test matrix for ducted propeller validation and analysis.

Case Series	Geometry Configuration	Freestream Velocity (m/s)	Advance Ratio μ	Angle 1 (°)	Angle 2 (°)
1	Empty Duct	30.48	-	0 to 90	-
2	Ducted Propeller	30.48	0.19	0.0	20.0
3	Open Propeller	0.00-102.88	0.00-0.64	0.0	20.0
4	Ducted Propeller	0.00-102.88	0.00-0.64	0.0	-

Case Series	Angle 3 (°)	No. Blades	Tip Clearance (mm)	Rotational Speed (RPM)	Nominal Tip Mach	Purpose
1	-	-	-	-	-	Duct behaviour study
2	50.00	3	1.016	8000	0.4694	Validation and crosswind study
3	-	3	-	8000	0.4694	Comparisons with open propeller
4	-	3	1.016	8000	0.4694	Advance ratio study

Simulations were first performed on the empty duct without the propeller at increasing angles of attack to verify the duct geometry, and to study the duct behaviour as an annular wing. Comparisons were also made against Ansys Fluent^{TM} simulations using the same grids at low angles of attack. Axial fight conditions at increasing advance ratios were then investigated using the HMB3 solver. The Reynolds number based on the duct chord and the blade tip speed is around 2.86×10^6, whereas based on the tip speed and the blade tip chord it is about 2.08×10^5. In the current work, the higher Reynolds number of 2.86×10^6 was used and the flow is considered as fully turbulent. Initial simulations are also performed referring to the tip chord and speed (resulting in the lower Reynolds number), and slightly larger differences from experiments are noted. The same operating conditions were also applied to the open propeller with the duct removed. Due to the lack of detailed experimental data, the DFDC and XRotor[132, 47, 52] codes were also utilised for comparisons in axial conditions and to add more confidence in HMB3 results in the absence of experimental data.

3.1 Evaluation of the Meshing Tool-chain

The proposed automation framework for mesh generation is first evaluated, to highlight its advantages. As mentioned earlier, the framework has good flexibility and versatility for different shapes and large geometric variations, e.g. blades with various sections, swept, anhedral/dihedral, and ducts with different radii, variable sections, etc. Different grid topologies are also supported. An alternative grid topology, combining the centre-body/duct in the same grid, is presented in Figure 3.3(a). A manually generated grid with the similar topology is presented Figure 3.3(b). This grid was intended for the non-chimera simulations, and the results and comparisons are presented in the later section. Note that automatically-generated grids were put together by individual components and were assembled using chimera methods. This guarantees the flexibility and convenience of altering positions and combinations of components for further parametric studies. Examinations of this simulation strategy are presented in the following sections.

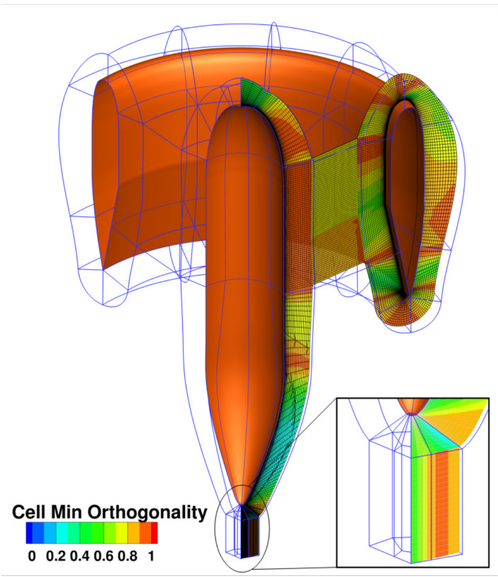

(a) Automation grid with an alternative topology combining the duct and the centre-body. This grid is to be embedded in a background grid using chimera approach.

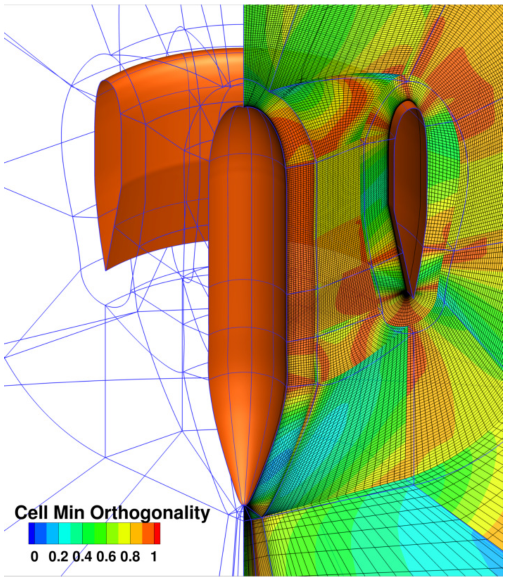

(b) Manually generated non-chimera grid for the duct and centre-body.

Figure 3.3: Topologies and comparisons of the automation grid and the manually generated grid. The geometry corresponds to the experiments of Grunwald and Goodson [18].

Details and quality comparisons of these two grids are tabulated in Table 3.2. The automation framework took only about 1 minute to compose the geometry and generate the fully-structured with higher quality. It should be stated that the manually generated grid (Figure 3.3(b)) can be further improved, given more time and effort. The results shown here took about 8 hours, yet it needs more to reach the same quality as the automation grid. For the manually generated grid, the generation of the near-field grids required most of the time and effort, while the extension of blocks to the far-field took only a small fraction. Counting in the preparation for the background grid and for assembling the entire computational domain, the time need for the chimera simulation in this case was less than 30 minutes using the automation framework. This highlights the significant efficiency boost brought by the automation tool-chain.

Table 3.2: Grid quality comparisons between the automation grid and the manually generated grid. The quality criteria are evaluated using ICEM Hexa^{TM} and are all normalized ranging from 0 to 1, with 0 denoting the worst and 1 being the ideal, perfect hexahedral element.

	Grid size /[million cells]	Block Number	Min Determinant of Jacobian/[-]	Worst Distortion /[-]	Worst Skewness /[-]	Time Elapsed
Automation grid	1.9	62	0.717	0.841	0.317	∼1min
Manual grid	2.7	144	0.525	0.702	0.219	∼8h

Most of the grids used in this study, including background and local refinement grids, were therefore generated using the automation framework. The time needed for the pre-processing was generally reduced to minutes from hours, thus more effort can be devoted to the simulations and analyses of the results. Grids of different sizes were also quickly generated for the purpose of mesh independence study. In particular, the automation framework helped greatly with geometric modifications in the parametric study in Appendix A.

3.2 Validation of the Empty Grunwald Duct

Simulations were first performed on the empty Grunwald [18] duct at increasing pitch angles without the propeller. The tests measured aerodynamic characteristics of the bare duct with the propeller removed at increasing angles of attack. Note that the centre-body shape was only approximated in this study, as no accurate information is provided in the NASA report [18]. The rear part of the centre-body was sealed with a smooth shape, as opposed to the support structures in the experiments. The impact of the accurate centre-body shape was regarded as minor comparing to the duct and the propeller, but more uncertainties with respect to experiments should be expected. Especially in empty duct simulations, due to the absence of strong propeller influences, uncertainties brought by the approximated centre-body shape may be more salient.

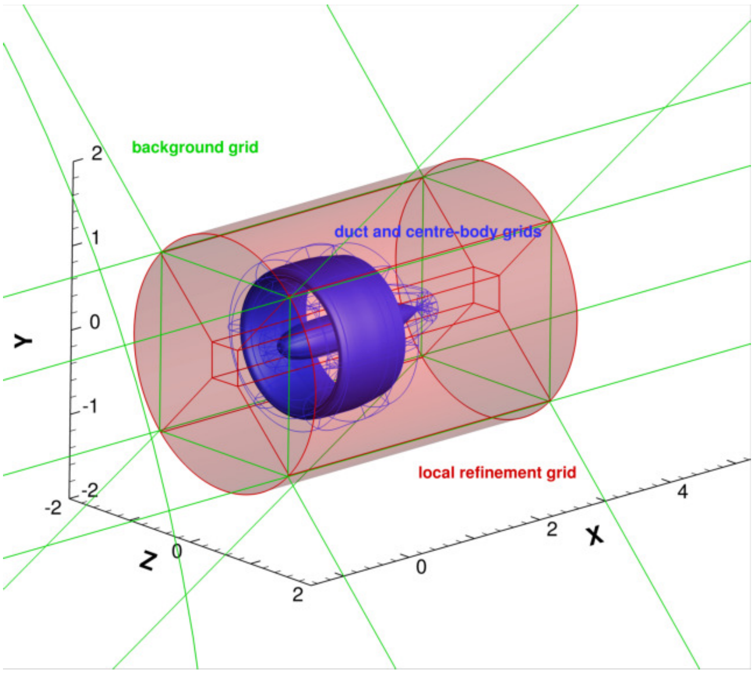

Figure 3.4: Geometry and chimera grid topology of the empty duct case (generated using the automation framework).

Topologies of the chimera grids are presented in Figure 3.4. The grids and geometries for the centre-body, the duct, the refinement, and the background, were all generated using the automation framework. Whereas for the non-chimera grids in Figure 3.3(b), geometries and grids are composed manually. Note that HMB3 and Fluent^{TM} can run on the output of the automation framework without further modifications.

A mesh convergence study for chimera simulations was carried out. Detailed descriptions of grid sizes are presented in Table 3.3. The near-field grids were varied while the background grids were always kept the finest. This to ensure enough cells in the background for the Chimera interpolation. For grids with different sizes, the first layer height of the grids was maintained the same while varying the density. Figures 3.5(a) to 3.5(c) present the surface y+ distributions for the fine, medium, and coarse grids, along with the surface mesh points. It can be noted the y+ values were maintained around 1 and the distributions were almost identical for all grids.

The mesh convergence study was carried out at $AoA = 10°$ using grids of 3 different cell sizes and steady RANS simulations. Note that the mesh convergence study for the non-chimera grids was not included in the present paper, since most current simulations were performed using

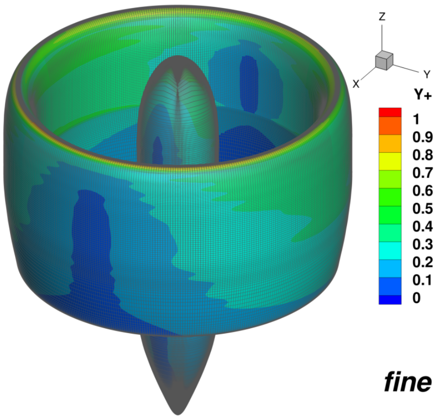

(a) Fine grid.

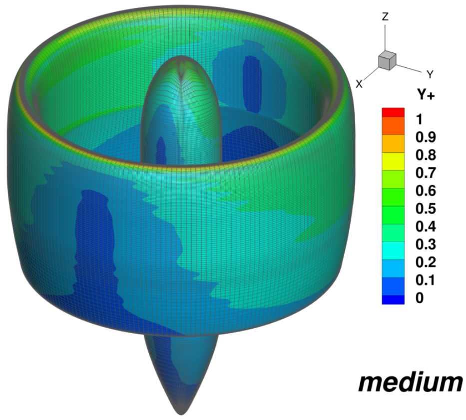

(b) Medium grid.

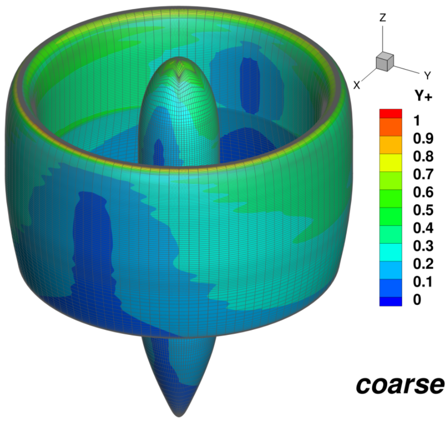

(c) Coarse grid.

Figure 3.5: Surface y+ contours extracted from the HMB3 solutions for the empty duct cases.

the automation framework and the chimera method. Non-chimera simulations were performed at few conditions for comparisons, to verify the chimera strategy for current cases. As shown in the following sections, the agreement to chimera results is excellent, despite the differences in the grids and numerical methods used.

Table 3.3: Component grid details (million cells) for the mesh convergence study of the chimera method.

Grid Size/ [Million Cells]	Background	Local Refinement	Centre-body	Duct	Near-field Total	Total
Coarse			0.77	1.08	1.85	6.97
Medium	0.74	4.38	1.54	2.16	3.70	8.81
Fine			3.08	4.31	7.39	12.51

It is difficult to perform grid convergence studies for complex cases such as the current one, especially when chimera grids are involved. The capability of adjusting component grids independently using chimera grids adds to the flexibility of the simulation framework, but the grid convergence study is made more complicated. Moreover, due to the hole cutting process, the actual number of cells involved in computations may vary with different grid combinations. To tackle the difficulties of the chimera grid convergence study, in the current work, cell numbers of the near-field grids, i.e. the duct and the centre-body, were progressively halved from the finest grids. Meanwhile, the background and local refinement grids, as shown in Figure 3.4, were kept constant with sufficient cells. This was mainly due to the fact that the chimera interpolation requires a sufficient amount of cells in the background grids for interpolation. Nevertheless, this strategy also ensured similar amounts of computational cells after the hole cutting in the background, for foreground grids of various cell numbers.

The calculated aerodynamic loads using the chimera grids, as well as, the finest non-chimera grid of Table 3.3, are presented in Table 3.4. The agreement between the chimera and non-chimera results was favourable, despite differences in grids and numerical methods. There were very small differences between the geometry used in the chimera/non-chimera grids, as the chimera geometry was composed automatically using the automation framework while the non-chimera geometry was composed manually. For the chimera results, changes in lift values are almost negligible with respect to the grid refinement. The drag and lift-to-drag ratio predictions are changing slightly and monotonically. Lift-to-drag ratio variations over volume sizes (h^3) are plotted in Figure 3.6 for the 3 grid sets. In the present study, the cell size h is represented by $1/N_{cell}^{1/3}$, with N_{cell} denoting the number of cells of the grid of concern. Such a definition is a compromise yet an effective alternative, due to the complex grid topologies and geometries which make the overall cell size hard to determine. The Richardson extrapolation [134] of the current results to zero cell size yields only minor differences with the coarse grid results (within 0.6%).

The Grid Convergence Index (GCI) proposed by Roache [134, 135] was calculated using the lift-to-drag values in order to quantify the grid convergence. Detailed discussions and definitions

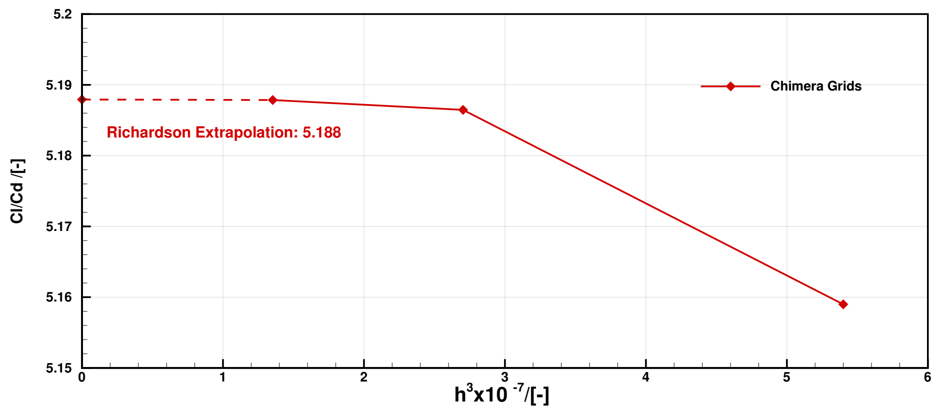

Figure 3.6: Lift-to-drag variations with varying volume sizes h^3. The cell size $h = 1/N_{cell}^{1/3}$, where N_{cell} takes the sum of the near-field grid cell numbers as presented in Table 3.3.

Table 3.4: Aerodynamics loads comparisons of the empty duct at $AoA = 10^\circ$ computed using the chimera grids of three different sizes and the finest non-chimera grid.

Grid Type	Grid Size	Total Cell Numbers	Lift C_l	Drag C_d	Lift-to-Drag Ratio C_l/C_d
	Coarse	6.97	0.670	0.130	5.159
Chimera	Medium	8.81	0.670	0.129	5.186
	Fine	12.51	0.670	0.129	5.188
Non-Chimera	Fine	15.26	0.641	0.126	5.084

of the GCI calculations can be found in References [134, 135]. A GCI ratio close to 1.0 indicates the grid convergence is entering the asymptotic range and further reducing the cell size will only marginally improve the result. In the current work, the refinement ratio r was defined as $\frac{h_f}{h_m}$ or $\frac{h_m}{h_c}$, where h_f, h_m, h_c are grid sizes of the fine, medium, and coarse grids as defined earlier. A constant grid refinement ratio throughout the study is ideal for the GCI calculation, while integer refinement such as grid doubling is not essentially necessary [134]. In the present study, for the near-field grids, the refinement ratio was constantly 1.26. While for the total grids, the refinement ratios were around 1.1 with slight variations.

The GCI values calculated for the 2 levels of refinement in the present study are given in Table 3.5. With cell sizes denoted using either near-field or total grids, the GCI values were small and were decreasing with the refinement, suggesting that the relative errors were reducing with finer grids. For both cell size representations, the GCI ratio value approached 1, indicating that the grid convergence was entering the asymptotic range. Overall, the grid convergence study suggested that, using the current simulation strategy, grids of around 8 to 12 million total cells can reach the sufficient convergence for the empty duct simulation.

Table 3.5: Grid Convergence Index (GCI) [135] calculations using the lift-to-drag ratio values with the 3 levels of grid sets in Table 3.3, using both near-field and overall cell size representations.

	Near-Field Grids		
	Refinement Ratio	GCI	GCI Ratio
Coarse-Medium	1.26	3.53×10^{-4}	99.97%
Medium-Fine	1.26	1.78×10^{-5}	
	Overall Grids		
	Refinement Ratio	GCI	GCI Ratio
Coarse-Medium	1.08	3.39×10^{-4}	99.97%
Medium-Fine	1.12	3.76×10^{-6}	

A further comparison was made in Figure 3.7 by comparing the duct and centre-body surface pressure distributions, extracted from simulations using the coarse chimera/non-chimera grids and the two CFD solvers. In general, very good correlations between solvers were observed. The agreement between different grid methods was also favourable, except that the overset simulations see more small pressure oscillations, which is noted in both HMB3 and Fluent^{TM} results. This may be due to the differences of geometry composition. Larger differences were mostly noted at sharp geometry transitions (diffuser exit and centre-body transitions), where the chimera grids and the Fluent^{TM} solver tended to give smoother predictions. Requirements of computational resources for the Fluent^{TM} and HMB3 steady simulations using the same baseline grid (6.6 million cells) are tabulated in Table 3.6. It can be seen that the HMB3 solver required significantly lower resources over the general-purpose commercial solver in the present work.

Table 3.6: Computational resources comparisons between HMB3 and Ansys Fluent^{TM} using the same baseline grid.

	Grid size (cells [Million])	Memory Consumption ([GB])	CPU Time ([cores*hours])
Fluent^{TM}	6.6	∼40	∼384
HMB3	6.6	∼21	∼100

Further steady RANS simulations ($AoA < 15°$) of the empty duct configuration were thus

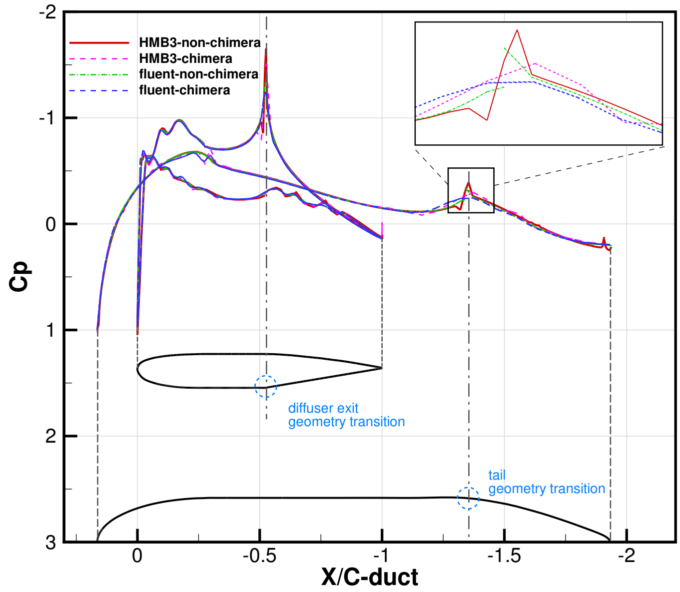

Figure 3.7: Comparisons of duct and centre-body surface pressure distributions extracted from HMB3 and Fluent^{TM} results, using non-chimera and overset grids.

performed using coarse chimera grids of 6.6 million cells with both HMB3 and Ansys Fluent^{TM}. The use of this coarse grid here is mainly due to the large computational resource requirements of Fluent^{TM}. Steady HMB3 simulations using fine chimera grids of 10.2 million cells were also performed, but only minor differences were obtained, as can be expected from the previous grid refinement study. However, the fine chimera grid is used for unsteady HMB3 SAS simulations at high cross-wind angles. Lift and drag variations with increasing angles of attack are shown in Figures 3.8(a) and 3.8(b). Fluent^{TM} RANS results using the same coarse chimera grid with overset interfaces are also plotted.

Lift coefficients (Figure 3.8(a)) derived from the steady RANS simulations, by HMB3 and Fluent^{TM} solvers, were in favourable agreement with experimental data, until approximately $AoA >$ $15°$. The drag predictions (Figure 3.8(b)) saw larger discrepancies. Yet HMB3 results managed to predict well the trend of drag variations with respect to increasing AoA, while the Fluent^{TM} results showed a different trend.

Beyond $AoA = 15°$, large differences were observed between tests and steady simulations in lift predictions. Both solvers showed difficulties predicting the loads using steady methods, as

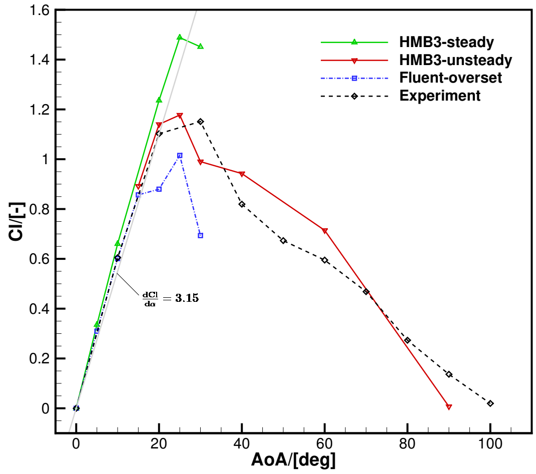

(a) Lift coefficient variations with AoA for the empty Grunwald duct.

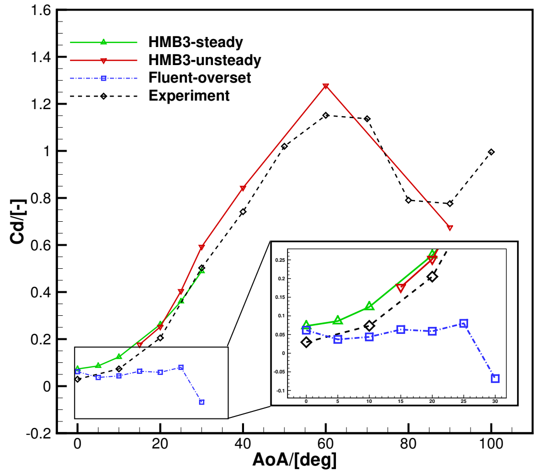

(b) Drag coefficient variations with AoA for the empty Grunwald duct.

Figure 3.8: Aerodynamic force variations with increasing AoA for the empty Grunwald duct.

large separation is expected on the up-stream inner and the down-stream outer surfaces at higher incidences. Thus unsteady SAS simulations on the fine chimera grid using HMB3 were preferred for higher cross-wind angles. SAS simulations were not performed using Fluent^{TM}, as the SAS methods were not yet supported with the overset grid features in the employed release (2019R3). Shown in Figures 3.9(a) to 3.9(e) are iso-surfaces of dimensionless vorticity magnitude equal to 1, indicating the shedding vortices. Dimensionless y-vorticity contours on the middle plane (Y=0) are presented in Figures 3.9(b) to 3.9(f) for $AoA = 20°, 30°, 40°$, respectively. Flow separation arose from increasing AoA, first at the upstream diffuser exit, especially after the abrupt geometry expansion where a sudden adverse pressure gradient should be seen. As the AoA further increased, as shown in Figures 3.9(d) at $AoA = 30°$ and 3.9(f) at $AoA = 40°$, complex separation dominated the entire inner upstream surface starting from the leading edge. Large separation was also seen on the downstream outer surface. The wake of the upstream separation was also hitting the centre-body surface, creating more complex secondary flows. The 3D iso-surfaces, as shown in Figures 3.9(a) to 3.9(e), suggested low-frequency, large, hair-pin-like vortices shedding from the downstream outer surface, arising from the lip. While high-frequency, smaller vortices were seen shedding from the upstream diffuser surface. For more quantitative comparisons, as plotted in Figures 3.8(a) and 3.8(b), the aerodynamic loads were well predicted in reasonable agreement with the test data at high angles of attack, despite the large separation shown in Figures 3.9(a) to 3.9(e).

3.3 Validation of Ducted Propeller in Axial Flight

Simulations for the ducted propeller in axial flight in this section were performed using the Rotating Reference Frame (RRF) approach mentioned earlier. The axisymmetric, stationary walls, e.g. the duct surface, were resolved by imposing opposite rotational velocities. Note that simulations are were performed of the un-ducted propeller with the duct removed, under the same pitch and RPM settings. Computations using the lower-order codes DFDC and XRotor were also performed, respectively, for the ducted propeller and the open propeller.

It should be mentioned that the blade pitch $\beta_{0.75}$ documented in the experimental report [18] is 24°. This setting was applied and examined using both DFDC and HMB3 codes, and yielded significantly lower thrust and torque. The pitch angle was then corrected by varying the pitch to match the total thrust using the DFDC code. This resulted in a $\beta_{0.75}$ of 29.58° under the same *RPM*, free-stream speed and geometries. The same pitch setting was then applied in the CFD simulations and delivered favourable agreement with the test data.

A grid convergence was also performed for CFD simulations of the ducted propeller in axial flight at $\mu = 0.191$. The grid convergence was again carried out by progressively and systematically varying the near-field grids, i.e. the duct, the centre-body, and the blade. The far-field grid, however, was always the finest and kept constant. Detailed cell numbers of the grids of 3 sizes and 2 refinement levels are listed in Table 3.7. The resultant grid refinement ratio in the near field was about 1.25, which means cell numbers were doubled through each refinement level. For the total grid the ratio was lower at about 1.08, due to large cell numbers in the background grid. The GCI and the GCI ratios were calculated using the Froude efficiency values in order to quantify the convergence. For all near-field grids, while varying the grid cell numbers, the first layer height was kept the same. Figures 3.10(a) to 3.10(c) present the y+ contours on the ducted propeller surface for the fine, medium, and coarse grids, along with the surface mesh points. The y+ values and

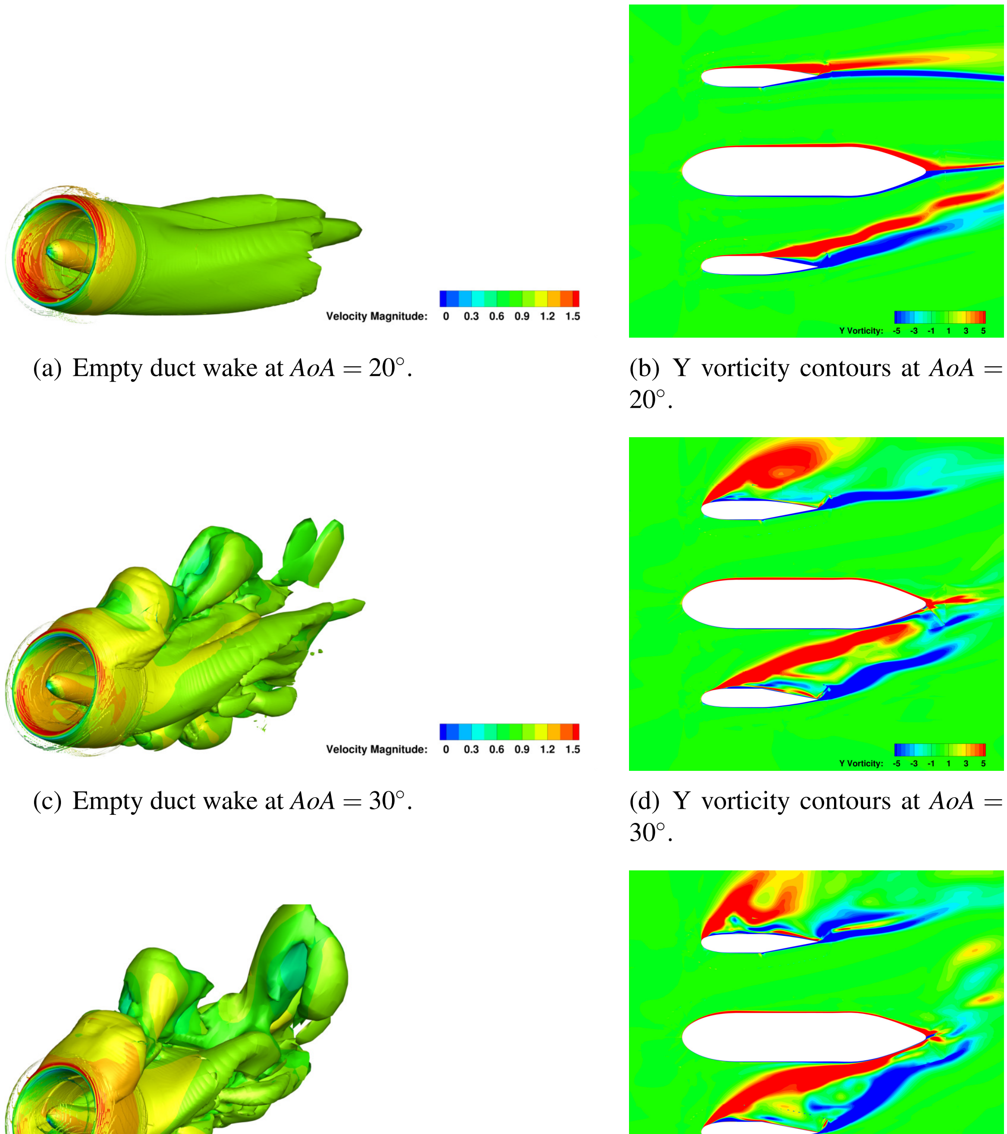

(a) Empty duct wake at $AoA = 20°$.

(b) Y vorticity contours at $AoA = 20°$.

(c) Empty duct wake at $AoA = 30°$.

(d) Y vorticity contours at $AoA = 30°$.

(e) Empty duct wake at $AoA = 40°$.

(f) Y vorticity contours at $AoA = 40°$.

Figure 3.9: Instantaneous iso-surfaces of non-dimensional vorticity magnitude equal to 1 for the empty duct at $AoA = 20°, 30°, 40°$ using SAS simulations, coloured with non-dimensional velocity magnitude.

distributions were almost identical for all grids. The y+ values were mostly maintained around 1 on the duct and centre-body surfaces. On the blade upper surface, the computed y+ values at mesh points near the maximum camber were around 2, which could be associated with the strong local flow conditions. Overall, the y+ values were maintained of the magnitude of 1 for grid convergence study.

Table 3.7: Details of the Chimera grids used for ducted propeller simulations in axial flight (in million cells).

	Blade	Centre-body	Duct	Near-field Total	Background	Total
Coarse	1.33	0.243	0.385	1.958	8.72	10.678
Medium	2.13	0.513	0.77	3.413	8.72	12.133
Fine	4	1.27	1.54	6.81	8.72	15.53

Table 3.8: Grid convergence study for simulations of the ducted propeller in axial flight at $\mu = 0.191$.

	Refinement Ratio	Near-field Grid Convergence Index (GCI)	GCI Ratio
Coarse-Medium	1.20	2.80×10^{-3}	99.82%
Medium-Fine	1.26	5.00×10^{-4}	
	Refinement Ratio	**Total Grid Convergence Index (GCI)**	**GCI Ratio**
Coarse-Medium	1.04	2.40×10^{-3}	99.82%
Medium-Fine	1.08	1.00×10^{-4}	

As can be noted in Table 3.8, the GCI values, calculated using both near-field and total grids, are small and are decreasing with refined grids. The GCI ratio values are very close to 1.0, indicating that the convergence is in the asymptotic region. The Richardson extrapolation [134] based on Froude efficiency results from the 3 at infinitely small cell size is very close to the fine grid result, with a relative error within 0.5%.

Flow-fields of the ducted/un-ducted propellers at $\mu = 0.191$ in axial flight with the finest grids are shown in Figures 3.11(a) and 3.11(b). The tip vortices are visualised using iso-surfaces of dimensionless q-criterion of 0.5. The axial velocity V_z is normalised by the free-stream velocity.

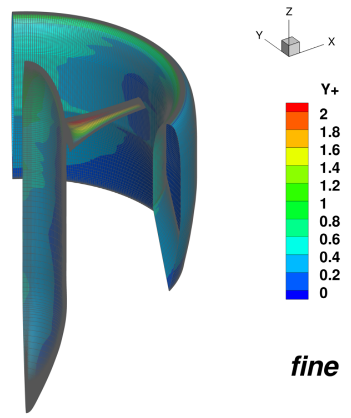

(a) Fine grid.

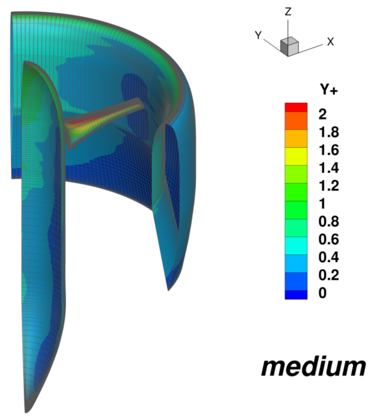

(b) Medium grid.

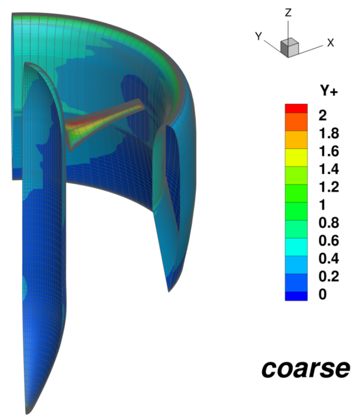

(c) Coarse grid.

Figure 3.10: Surface y+ contours extracted from HMB3 solutions for the ducted propeller cases.

The ducted propeller is shown to produce weaker tip vortices and the wake is slower and smoother, comparing to the un-ducted counterpart at this axial speed. This is due to the duct diffuser that expands and slows down the exit flow, recovering the kinetic energy to pressure energy. These result in higher duct thrust, as well as, less intrusive wake to the environment, which is particularly favourable for operations near communities.

Figures 3.12(a) and 3.12(b) show good correlation between the methods for averaged pressure distributions along the centre-body and duct. The pressure coefficients from HMB3 simulations were averaged over azimuth to compare with the axisymmetric results from DFDC.

Comparisons between experiments and HMB3 simulations, as well as, the breakdown of propulsion forces, are listed in Table 3.9 and shown in Figure 3.13(a) and 3.13(b), and good agree-

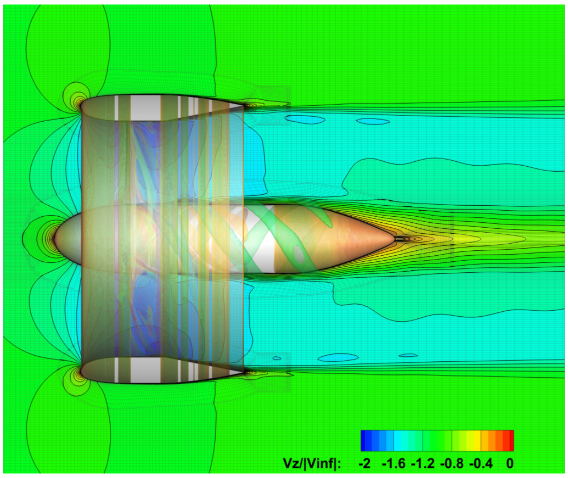

(a) Ducted propeller wake and axial velocity contours.

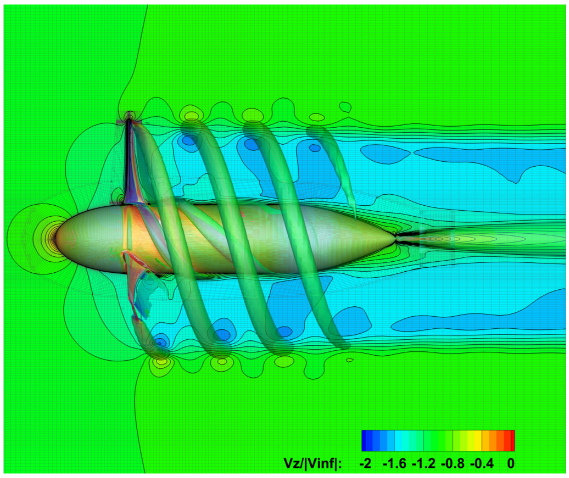

(b) Open propeller wake and axial velocity contours.

Figure 3.11: Instantaneous flow-fields of the ducted/un-ducted propellers at $\mu = 0.191$ in axial flight with the finest grids (k-ω SST). The tip vortices are denoted by iso-surfaces of dimensionless q-criterion of 0.5. The axial velocity V_z is normalised by the free-stream velocity.

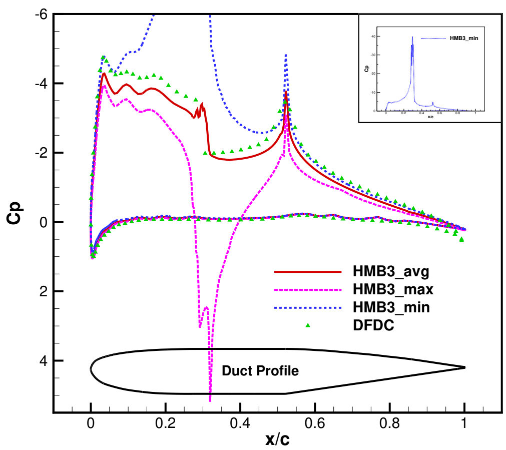

(a) Cp distribution on the duct

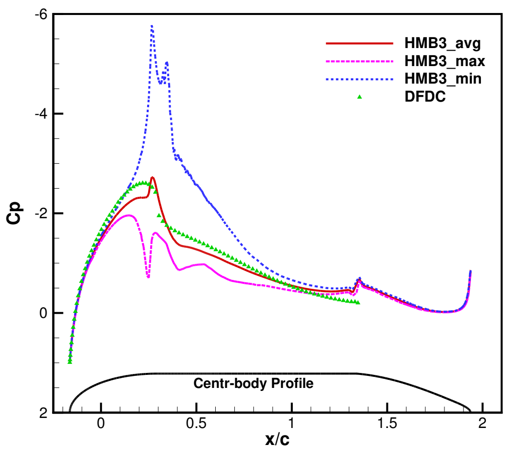

(b) Cp distribution on the centre-body

Figure 3.12: Time-averaged pressure coefficient distributions along the duct and centre-body surface. The peak and averaged values predicted by HMB3 are compared with the method of M. Drela [47, 52].

ment can be noticed between CFD, simpler predictive methods, and the test data. Note that all force and moment data were normalized using the far-field dynamic pressure, the duct chord length C_{dp}, and the projected duct area $S_{dp} = C_{dp} \times D_{exit}$, where D_{exit} is the duct exit diameter. Also presented are results for the open propeller configuration at the same pitch and RPM from HMB3 and XRotor [132]. The XRotor results were regarded as less accurate due to the lower-order nature. The purpose was to add more confidence to HMB3 results in the absence of experimental data, and the agreement between methods seen here was favourable. At this advance ratio($\mu = 0.191$) and pitch setting, the ducted and un-ducted configurations produce similar amount of total thrust, but the ducted propeller generates about 10% less torque and is hence slightly more efficient. Relative differences with respect to the experimental results are presented in Table 3.10. The error was defined as

$$[ERROR] = \frac{[prediction] - [exp]}{[exp]} \times 100\%, \tag{3.1}$$

where $[prediction]$ denotes predicted values and $[exp]$ denotes the corresponding experimental data. It can be noted that differences between the HMB3 results and the experiments were minor in this case. The DFDC code offered fast and reasonable thrust predictions, but the torque was highly over-predicted.

Table 3.9: Aerodynamic loads breakdown and comparisons between experiments, HMB3 simulations and simpler predictive methods (OP stands for Open Propeller here).

C_{Fx}	EXP	Contribution	DFDC	Contribution	HMB3	Contribution	HMB3_OP	Contribution	XRotor_OP
Total	1.40	100%	1.416	100%	1.396	100%	1.355	100%	1.39
Rotor	1.00	71.4%	0.912	64.4%	0.985	70.6%	1.418	104.7%	1.39
Duct(with CB)	0.40	28.5%	0.504	35.6%	0.410	29.4%	-	-	-
Centre-body	-	-	-	-	0.068	4.9%	-0.063	-4.7%	-
Propeller C_{Mx}	0.27	-	0.391	-	0.279	-	0.313	-	0.391
Efficiency η	0.713	-	0.498	-	0.687	-	0.594	-	0.489

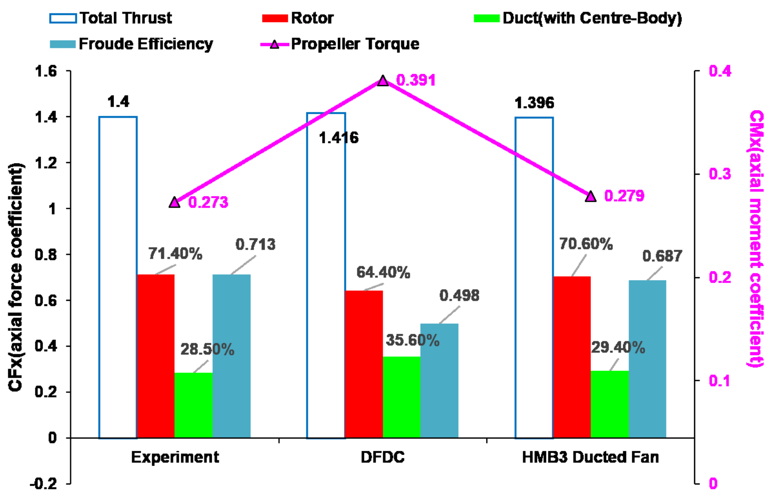

(a) Ducted propeller loads breakdown at $\mu = 0.191$ and comparisons between HMB3, experiments, and DFDC.

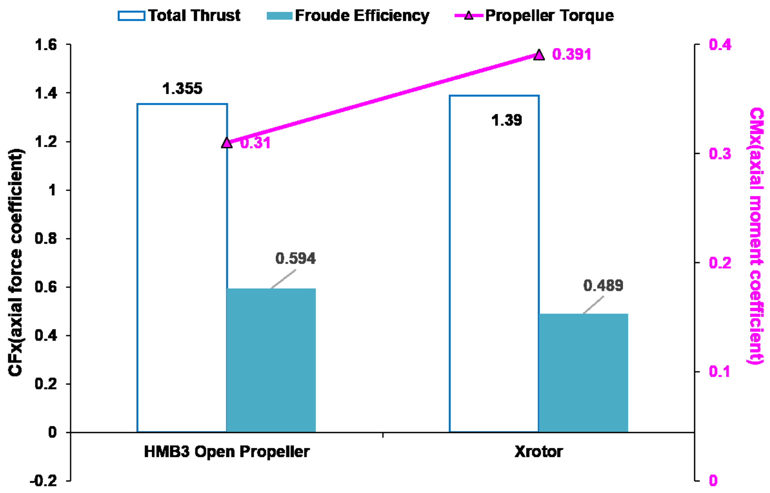

(b) Un-ducted propeller loads breakdown at $\mu = 0.191$ and comparisons between HMB3 and XRotor.

Figure 3.13: Aerodynamic load breakdown of the Grunwald[18] ducted/un-ducted propellers at $\mu = 0.191$ and comparisons between HMB3, experiments, and DFDC/XRotor results.

Table 3.10: Relative errors with respect to the experimental data of DFDC and HMB3 predictions for the Grunwald [18] ducted propeller at $\mu = 0.191$.

	Total Thrust	Rotor Thrust	Duct&Centre-body Thrust	Propeller Torque	Froude Efficiency
DFDC	1.14%	-8.80%	26%	44.81%	-30.15%
HMB3	-0.32%	-1.47%	2.56%	3.35%	-3.65%

3.4 Validation of Ducted Propeller at Cross-wind

Validation of the ducted propeller at cross-wind was also attempted. For these simulations, the complete computational domain and blade motions had to be used. The grid size for the ducted propeller simulation is of around 16.5 million cells considering the computational cost. Simulations of the open propeller were also performed at the cross-wind angle of 20° for comparisons. The ducted propeller simulations are performed at $AoA = 20°$ and $AoA = 50°$ at the advance ratio of 0.191. Unsteady SAS simulations [112] were utilized, because of the large unsteadiness and the possibly large-scale separation on the duct surface at cross-wind. The simulations adopted a time step of $1°/step$. The dominant vortex shedding frequency of the duct is around 28 Hz estimated from the cylindrical shape, while the propeller blade passing frequency is around 400 Hz. The $1°/step$ step size is fine enough for both propeller and separation flows. Finer time steps are of course desirable, but they are restricted by computational costs. The DFDC code cannot be used in these cases as the axisymmetry assumption no longer applies.

Wake features of the ducted propeller operating at $AoA = 20°$ and $AoA = 50°$ are presented in Figures 3.14(a) to 3.14(c), respectively. At $AoA = 20°$, the open propeller wake was preserved well by the high-fidelity HMB3 simulation. The wake was generally shifted by the free-stream, and vortices were noticed forming up behind the cylindrical centre-body. The ducted propeller wake was seen less strong, but consisted mostly of the blade tip vortices with slight distortion by the free-stream. It was also observed in the aerodynamic loads measurements in Figures 3.15(a) and 3.15(b) that this test point remained in the linear regime. At $AoA = 50°$, complex flow features were noted as in Figure 3.14(c). The tip vortices were interacting with the separation flow from the duct inner surface. Separation was also observed at the downstream outer surface.

Aerodynamic load variations with increasing angles of attack are plotted in Figures 3.15(a) and 3.15(b). Note that the $AoA = 0°$ data was taken from the previous steady RRF simulations. The unsteady loads are averaged over azimuth. The $AoA = 0°$ data was extracted from axial flight simulations. Very good agreement with test data is seen at $AoA = 20°$. At $AoA = 50°$, good agreement was seen in the lift prediction, but larger discrepancies were seen in the drag and consequently the

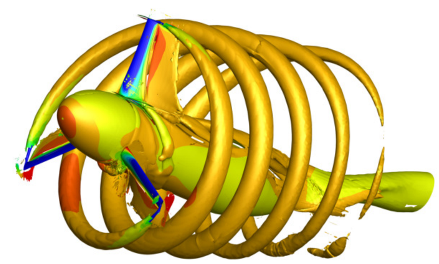

(a) Open propeller wake at $AoA = 20°$.

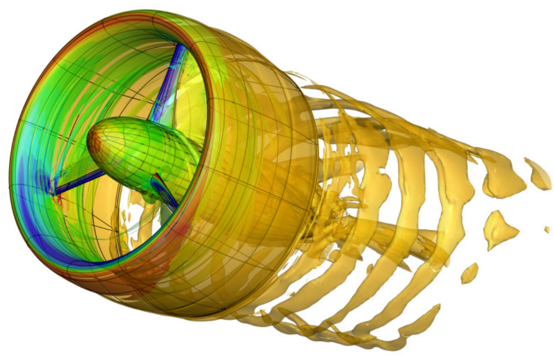

(b) Ducted propeller wake at $AoA = 20°$.

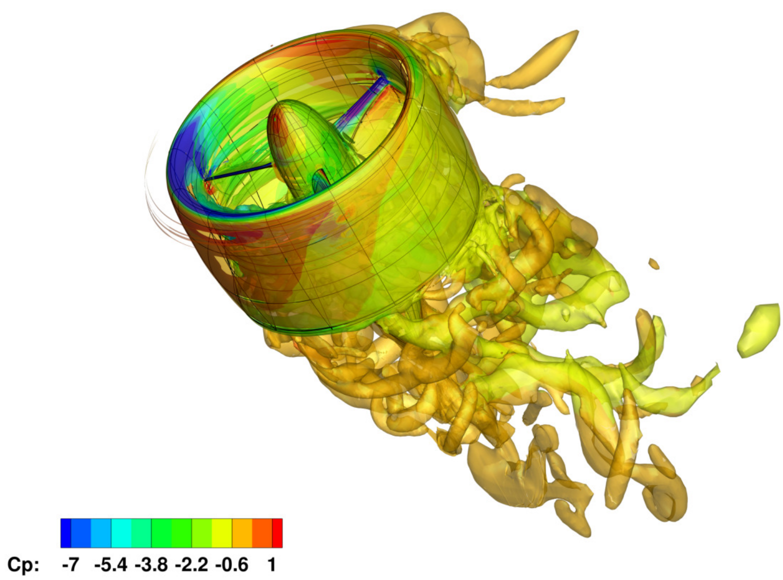

(c) Ducted propeller wake at $AoA = 50°$.

Figure 3.14: Instantaneous iso-surfaces of dimensionless q-criterion=5.0 (normalized by free-stream speed) for the ducted propeller at $AoA = 20°$ and $50°$, coloured with pressure coefficients.

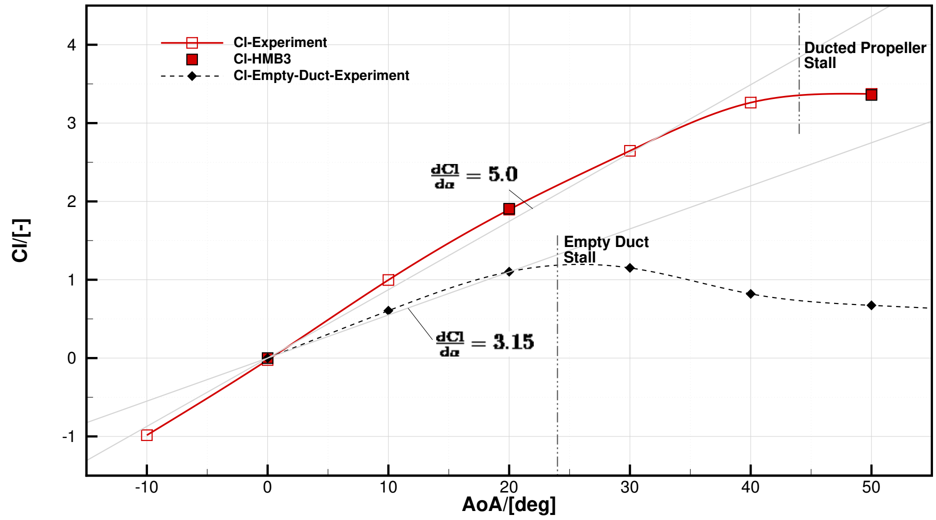

(a) Lift coeffcients of the ducted propeller at increasing *AoA*.

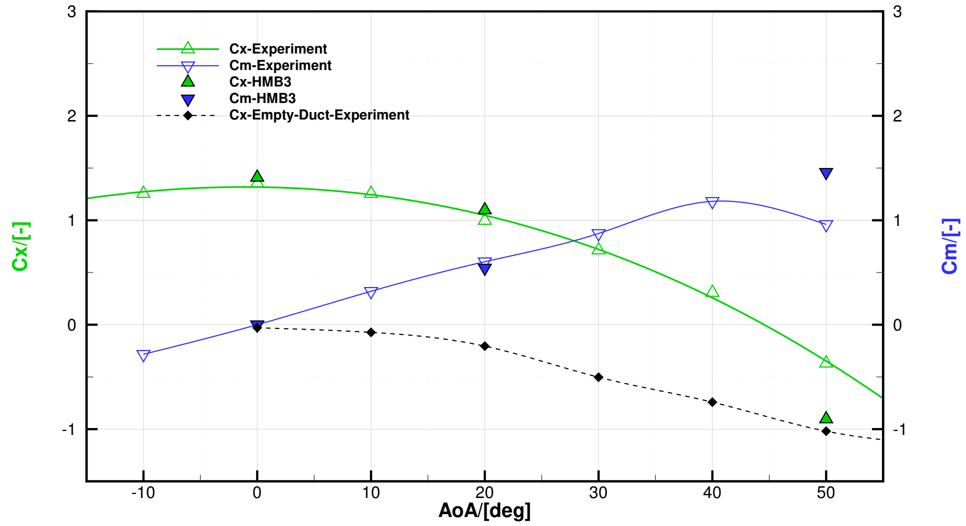

(b) Longitudinal force(drag or propulsion) and pitching moment coefficients of the ducted propeller at increasing *AoA*.

Figure 3.15: Aerodynamic loads on the Grunwald ducted propeller working at high *AoA* conditions.

moment prediction. The current simulation at $AoA = 50°$ showed reasonable agreement despite the large separation and unsteadiness, but it could perhaps be improved with finer grids and time steps, to resolve better the complex flow features shown in Figure 3.14(c). In reality, however, such an extreme condition of high advance ratio and high cross-wind angle is hardly encountered for practical vehicles [19]. Hence the focus was more placed on the performance at $AoA = 20°$.

3.5 Evaluation of Actuator Disk Models

3.5.1 Ducted propeller in axial flight

To evaluate the performance of actuator disks representing rotors in axial flight, the ducted propeller test case by NASA [18] was reused here. The same advance ratio of 0.191 with the same RPM of 8000 and $\beta_{0.75} = 29.58°$ was chosen. At this condition, the propeller disk was carrying about 70% of the total thrust and all the torque with approximately $C_T = 0.036$ and $C_Q = 0.014$ as discussed in previous sections.

The current simulations used actuator disk models with simply uniform thrust distributions on grids of about 9 million cells without the blades, which are more than sufficient according to previous grid sensitivity study. The tangential disk loadings, i.e. the torque contributions, were also examined here by introducing a uniform torque distribution. First, comparisons of the duct and centre-body thrust are presented in Table 3.11. Comparing to the blade resolved simulation, the simple uniform actuator disks gave very close predictions of the duct and centre-body thrust. When the tangential loading was included, the duct thrust predictions were very slightly higher while the centre-body thrust was slightly lower.

Table 3.11: Duct and centre-body thrust comparisons between resolved blades and actuator disk models at $\mu = 0.191$.

Rotor modelling	Duct thrust/[N]	Centre-body thrust/[N]
Resolved blades	42.29	8.83
Uniform(with tangential loading)	44.73	10.28
Uniform(without tangential loading)	43.52	11.02

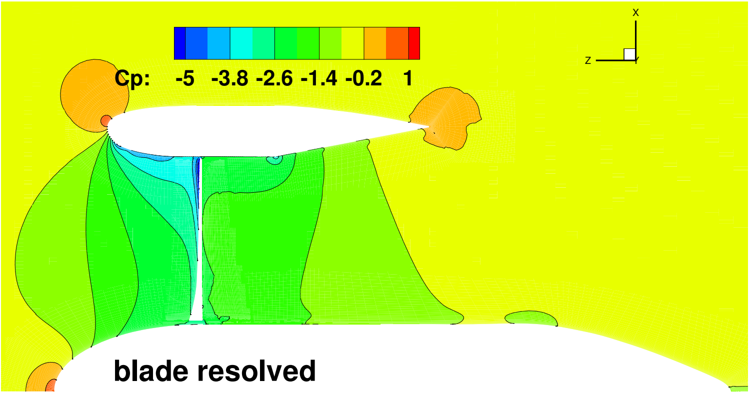

(a) Resolved blades.

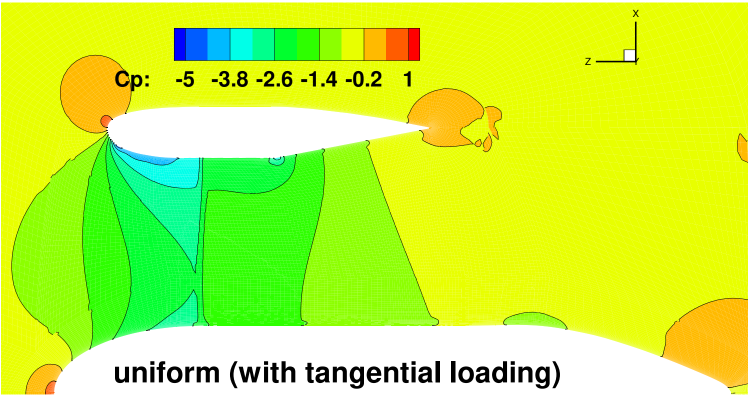

(b) Uniform actuator disk with tangential loadings.

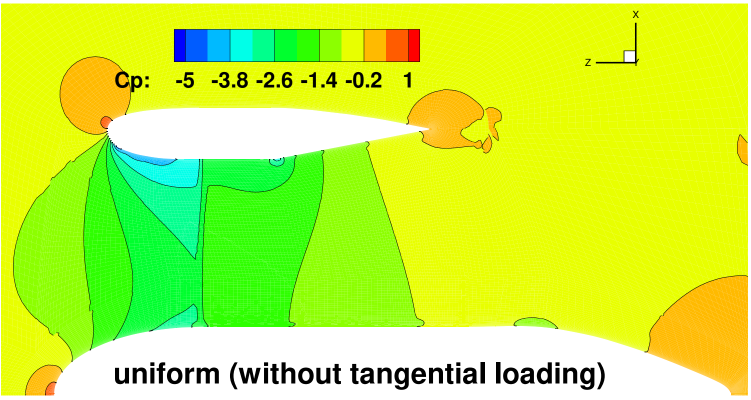

(c) Uniform actuator disk without tangential loadings.

Figure 3.16: Time-averaged pressure coefficient contour comparisons between the resolved blades and uniform actuator disk with and without tangential loadings (k-ω SST).

Comparisons of flow-fields are presented in Figures 3.16(a) to 3.16(c) in terms of time-averaged pressure coefficient contours, while the time-averaged surface pressure coefficients are presented in Figures 3.17(a) and 3.17(b). The uniform actuator disk models induced very similar pressure fields compared to the blade-resolved simulation. The simplified model predicted well the duct surface pressure, and only minor differences were seen by the tangential loading. The differences are mostly limited in regions near the blade root and the centre-body trailing edge. The uniform actuator disks induced larger suctions at the blade root. When the tangential loading was included, the pressure at the centre-body's trailing edge was reduced because of the swirl velocity and was hence closer to the blade-resolved simulation. Overall, the uniform actuator disk model was shown capable of modelling rotors in axial flight with sufficient accuracy, and the tangential loading caused only minor differences.

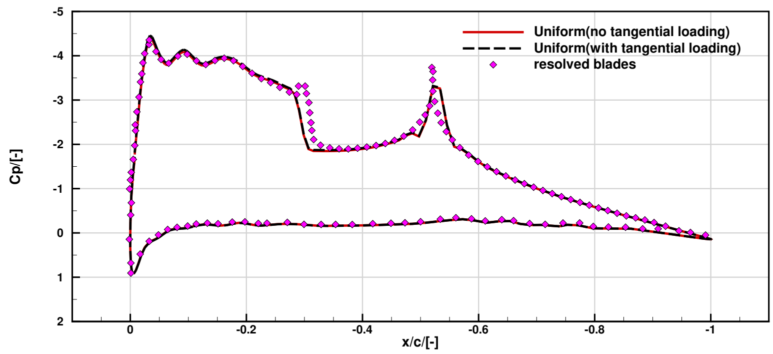

(a) Duct surface.

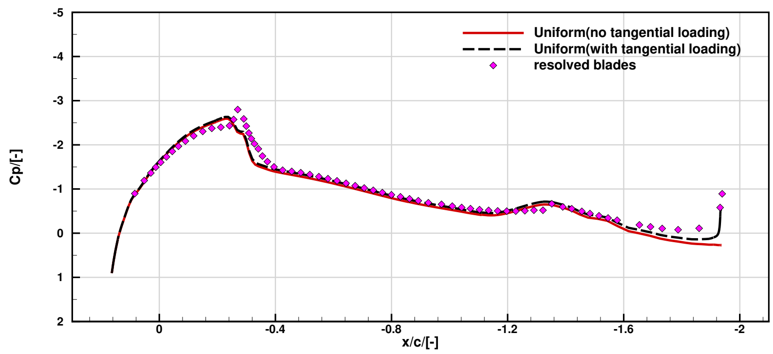

(b) Centre-body surface.

Figure 3.17: Time-averaged surface pressure coefficient distributions on the duct and centre-body surfaces using resolved blades and uniform actuator disk with and without tangential loadings.

3.5.2 Rotor/wing Interactions

To verify the actuator disk/line representation for rotors in edgewise flight, a rotor/wing interaction test case by Leishman and Bi [133] was adopted. This test was chosen for the simple geometry, conditions, and the well documented steady and unsteady data. The test configuration consists of a rotor, a lifting surface, and a simplified fuselage, as shown in Figure 3.18. Details of the geometries can be found in Refs[133, 136]. The experiments varied the advance ratio and the position of the lifting surface, but only limited data was available in the public domain. For the current work, two advance ratios were selected with the lifting surface on the rotor advancing side, as listed in the test matrix in Table 3.12. The rotor trimming data was acquired from CFD simulations by Sugawara and Tanabe [136]. Simulations were performed with the rotor modelled using resolved blades, the steady non-uniform actuator disk, and the unsteady actuator line for comparisons. The actuator disk/line models here adopted the same non-uniform disk loading based on empirical data [117] representing a trimmed edge-wise flight rotor.

The grid topologies are shown in Figure 3.18. Grids were generated separately for each component to ensure high quality. The grids were later assembled for computation using the Chimera method. Uniform grids were used as the off-body grids. Near the main rotor, the cell size was kept at 15% of the rotor blade chord, as recommended by previous grid convergence study by Sugawara and Tanabe [136]. The overall grid for the blade-resolved simulations had about 26 million points. Replacing the blades with actuator disk models reduced the grid size by about 10 million points. The simulations were performed using the 3^{rd}-order MUSCL scheme and the $k-\omega$ SST model. The simulations were performed using 360 time steps for one main rotor revolution. Different time steps were examined, but only minor influence on the results was noted. In terms of computational costs for the current simulations, the blade-resolved simulations required about 18 CPU hours for one unsteady time step, while the actuator line approach required only about 3 CPU hours to reach the same convergence level for each unsteady step.

Table 3.12: Current test matrix for the rotor/wing configuration by Leishman and Bi [133].

Case Series	Rotor model	Advance ratio	Wing position
1	resolved blades		
2	steady actuator disk	0.075, 0.25	advancing side
3	unsteady actuator line		

Flow details resolved by the steady actuator disk, unsteady actuator line, and the resolved

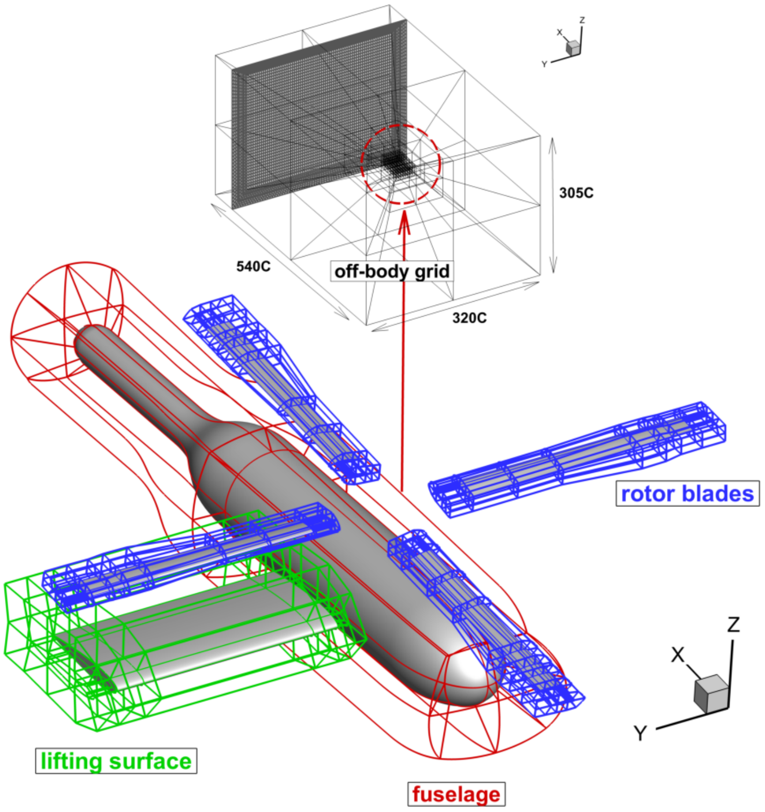

Figure 3.18: Geometry and grid topology of simulations of the wing/rotor interaction tests [133].

blades approaches are shown in Figures 3.19(a) to 3.19(c) at the lower advance ratio of 0.075, and in Figures 3.19(d) to 3.19(f) at the higher advance ratio of 0.25, respectively. The actuator disk models filtered out most flow details and provided a somewhat averaged flow solution, mostly induced by the rotor downwash velocities. Compared to the blade-resolved simulations, the aerodynamic phenomena resolved by the actuator line approach are very similar. The main aerodynamic features, i.e. rotor tip and root vortex systems, their mutual interactions and interactions with the fuselage and the wing, and the super vortex forming up in the wake, are all resolved with reasonable accuracy by the actuator lines at much reduced computational costs, especially at the higher advance ratio of 0.25. Nonetheless, the actuator line approach could not resolve more flow details comparing to the blade resolved simulations, e.g. the blade vortex interactions and the shear layers trailing the rotor blades. Also, it should be noted that the actuator line approach gives lower vorticity magnitudes, compared to the resolved blades, although the obtained wake shapes are very similar. This is apparently due to the lack of boundary layers and shear layers in the actuator line model.

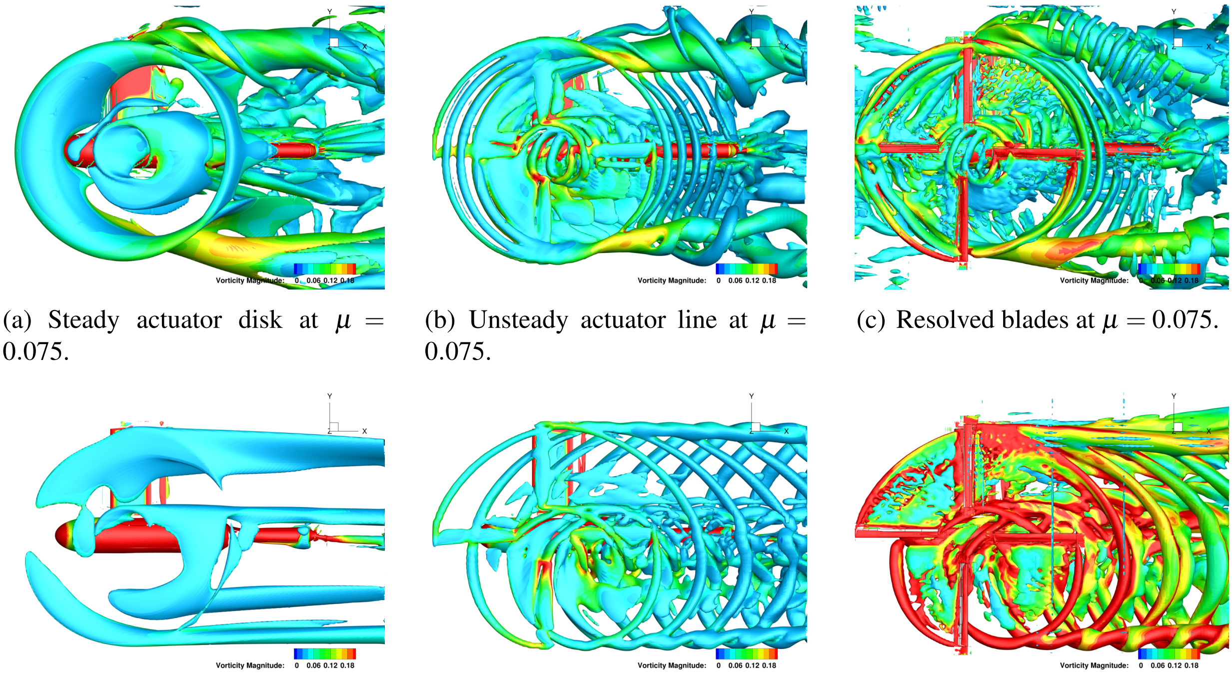

(a) Steady actuator disk at $\mu = 0.075$.

(b) Unsteady actuator line at $\mu = 0.075$.

(c) Resolved blades at $\mu = 0.075$.

(d) Steady actuator disk at $\mu = 0.25$.

(e) Unsteady actuator line at $\mu = 0.25$.

(f) Resolved blades at $\mu = 0.25$.

Figure 3.19: Instantaneous iso-surfaces of dimensionless q-criterion = 0.0001 (normalised by tip speed) with actuator disk, actuator line, and resolved blades representations at $\mu = 0.075$ and $\mu = 0.25$, coloured with vorticity magnitudes (k-ω SST).

More quantitative comparisons, in terms of unsteady pressure signals at a pressure sensor located at 65% span and 11.5% chord on the wing upper surface, are presented in Figures 3.20(a) and 3.20(b), respectively for the lower and higher advance ratios. Also presented are the experimental measurements. The experiments [133] recorded pressure fluctuations at several stations on the wing surface at different advance ratios, but only limited data can be found in the public domain. Note that the data shown here have been subtracted from their respective mean magnitude, as small uncertainties in the free-stream pressure cause large shifts in the absolute values of the signal due to the way the data is normalised. Regardless, the numerical results have shown very good agreement with the test data, in terms of the wave forms, frequencies, and magnitudes of signals. In general, the blade-resolved signals contain more details and agree better with the test data. The actuator lines resolved the dominant frequencies but filtered out higher harmonic components due to the lack of details in the resolved flow-fields. The actuator lines smoothed out the peaks because the

Gaussian used tends to spread the loads out, and the interaction with the wing is hence less intense.

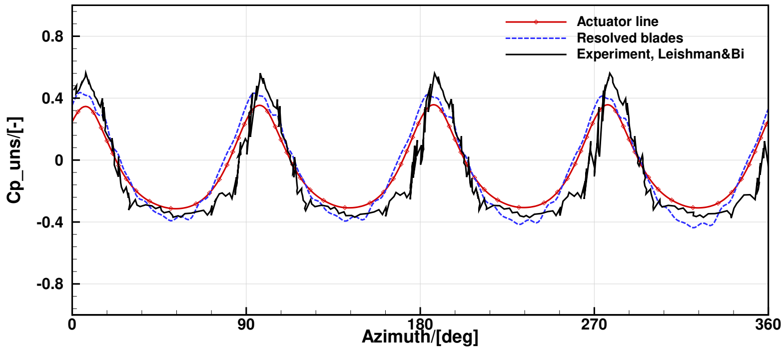

(a) Surface pressure signal at $\mu = 0.075$.

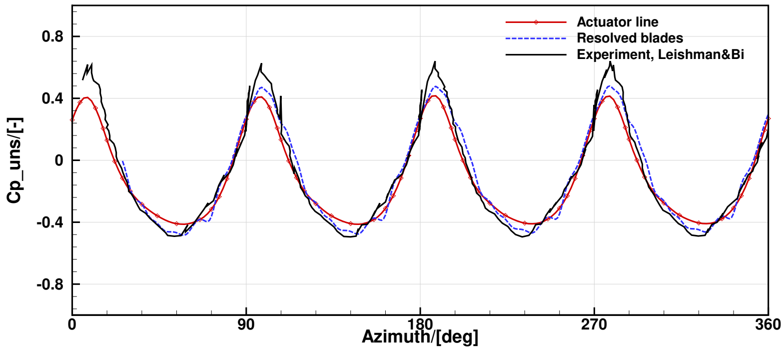

(b) Surface pressure signal at $\mu = 0.25$.

Figure 3.20: Comparisons of unsteady wing surface pressure signal variations between simulations and tests by Leishman and Bi [133].

Frequency domain analyses of the pressure signals are presented in Figures 3.21(a) and 3.21(b). The frequency values were normalised using the blade passing frequency (BPF). It can be observed that the frequency composition of the pressure signal mostly corresponded to the BPF and its harmonics. The experimental data contain more contents at the high frequency region due to effects such as flow separation and turbulence. The blade-resolved simulations captured the low frequency compositions well and resolved some of the medium to high frequency contents, but higher frequencies were filtered out. The actuator line method managed to resolve the first 3 to 4 major harmonics, but missed the rest of the frequency components.

Time-averaged wing surface pressure distributions solved using resolved blades, actuator disk, and actuator line models at 3 wing stations are presented in Figures 3.22 to 3.24, along with

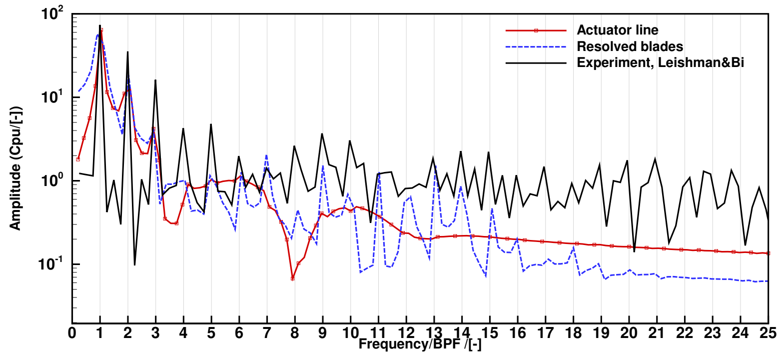

(a) Surface pressure signal at $\mu = 0.075$.

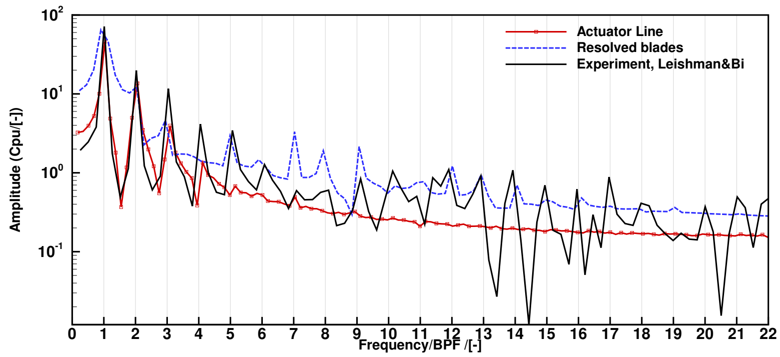

(b) Surface pressure signal at $\mu = 0.25$.

Figure 3.21: Frequency domain comparisons of unsteady wing surface pressure signal variations between simulations and tests by Leishman and Bi [133]. The frequencies were normalised using the blade passing frequency (BPF).

time-averaged flow details resolved by the actuator disk models and the resolved blades to highlight their comparisons. Influence of the tangential loading component of the actuator disk model was also examined here by adding a uniform torque distribution.

As can be noted from the presented flow-fields, at this low advance ratio of 0.075, a large proportion of the wing lower surface was suffering from excessive flow separation up from the wing leading edge. The resolved blades and the actuator line model hence offered better pressure predictions at $y/b = 0.3$. The differences on the wing lower surface were larger due to the inherent limitations of URANS approaches when handling massive separation. Still, the blade-resolved and actuator line predictions were rather close to the experimental data.

At $y/b = 0.6$ section, the blade-resolved simulations provided accurate predictions on the wing upper surface, but the differences on the lower surface were larger. Discrepancies of the actuator disk and actuator line predictions were notably larger at this section, especially for the actuator line model on the wing upper surface. These should be due to size differences of the separation region predicted by different models. As can be noted in the flow field comparisons in Figure 3.23, no flow separation was present at the wing lower surface according to the actuator disk/line model predictions, while the blade-resolved simulations predicted complete separation on the wing lower surface.

At $y/b = 0.8$, the pressure coefficient differences were small and close to zero. The blade-resolved prediction had reasonable agreement but deviated slightly from the test data. This was also reported by Sugawara and Tanabe [136] in their simulations. The actuator line model provided accurate predictions near the leading edge, and the discrepancies were larger near the trailing edge. This station is close to the wing tip and is also impinged by the rotor tip vortices, hence finer spatial and temporal resolutions may be necessary to resolve the delicate flow details.

The AD models induced similar flow features as shown in Figures 3.22 to 3.24 compared to the blade-resolved simulations. In general, the tangential loads brought only marginal improvement to the results due to the inclusion of swirl velocities. The flow convergence, however, was seriously hindered as also have been suggested by Chaffin et. al.[137] Regardless of the tangential loading, flow separation below the wing was induced properly by the actuator disk models, but the separation region was smaller and extended less in the span-wise direction than that of the resolved blades, as shown in Figure 3.23. Still, as a first modelling approach, the actuator disk offered results in reasonable agreement with the test data for this complex flow. The actuator line model managed to resolved the dominant flow features with more details thanks to the blade motions. However, the downwash induced by the actuator line model was slight weaker than the actuator disk model. This is reflected in the smaller size of the separation region predicted under the wing. This suggests that the time-dependent Gaussian kernel should be improved to preserve the disk strength.

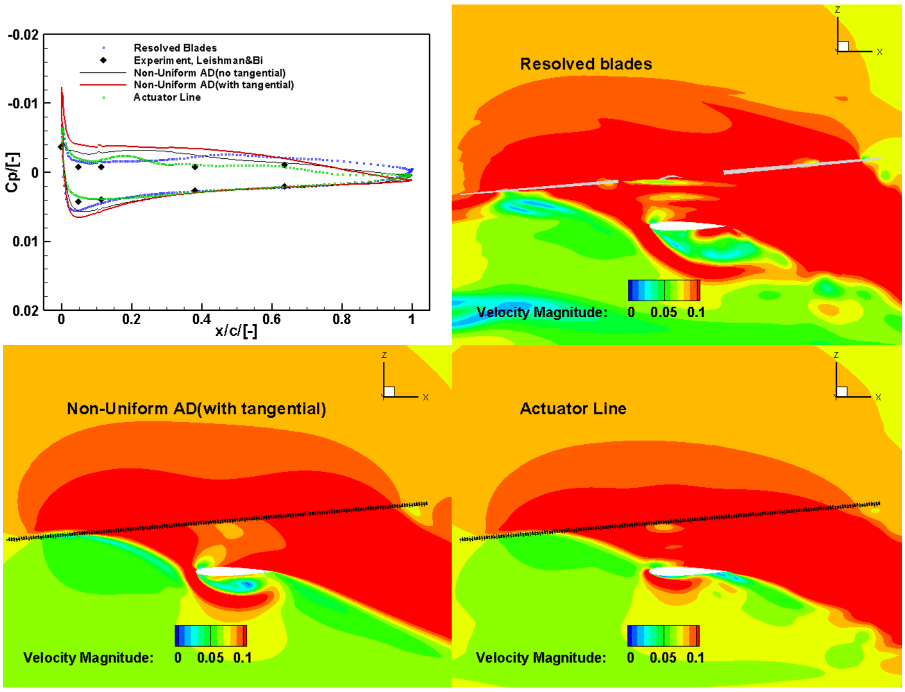

Figure 3.22: Time-averaged wing surface pressure coefficient and instantaneous flow field comparisons at wing section $y/b = 0.3$ at $\mu = 0.075$.

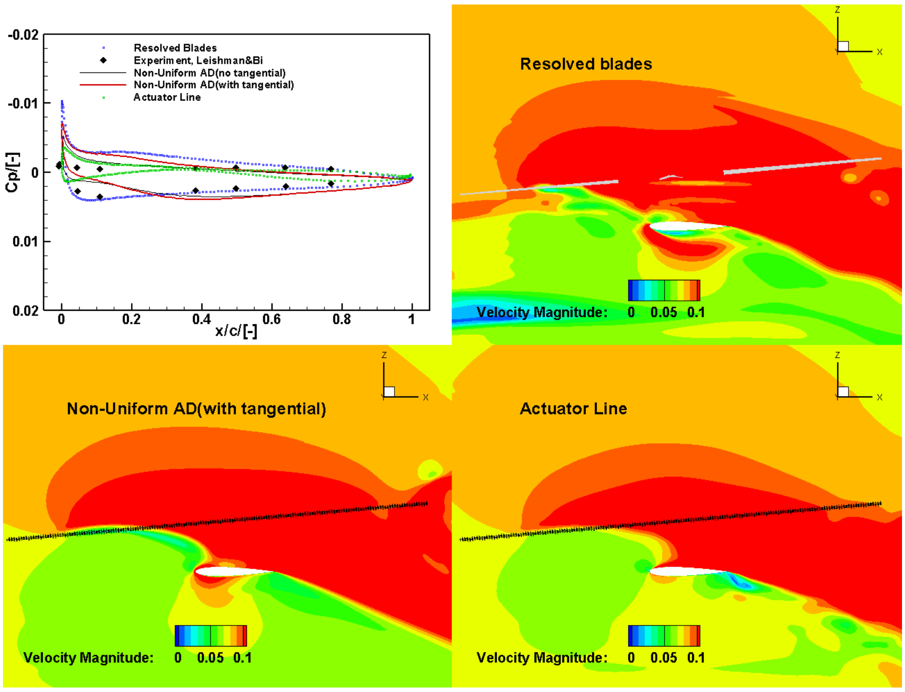

Figure 3.23: Time-averaged wing surface pressure coefficient and instantaneous flow field comparisons at wing section $y/b = 0.6$ at $\mu = 0.075$.

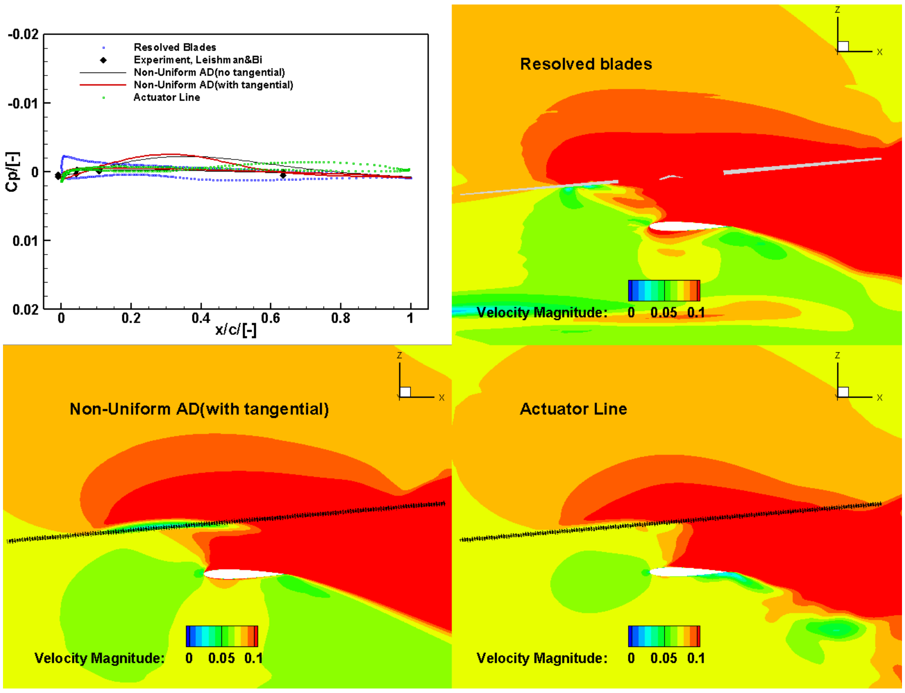

Figure 3.24: Time-averaged wing surface pressure coefficient and instantaneous flow field comparisons at wing section $y/b = 0.8$ at $\mu = 0.075$.

3.6 Chapter Summary

This chapter presented the validation of numerical methods, geometry, meshing tools, and simulation strategies for open and ducted propellers. HMB3 validation results on the empty duct and ducted propeller configurations at various operating conditions, as well as, evaluations of the actuator disk/line models have shown very good agreement with test data, lower-order predictive methods, and commercial CFD solvers. The following conclusions can be derived from the validation study in this chapter:

1. The automatic meshing tool was first examined. The meshing toolchain is capable of generating high-quality and ready-to-run grids for various geometries and different CFD solvers. With this meshing toolchain, the efforts required for mesh generation is greatly reduced from hours to minutes. This toolchain was used throughout the thesis to assist the mesh generation and was later used for a parametric study of ducted/open propellers.

2. Numerical methods of variable fidelity levels for ducted/open propeller simulations are

evaluated and validated. Aerodynamic simulations of the ducted propeller test case[18] were performed using various numerical tools (HMB3, Fluent^{TM}, DFDC/XRotor), different grids (chimera/non-chimera), modelling strategies (steady RRF/ unsteady mesh motions) and turbulence modelling options (RANS/SAS), and at various operating conditions. The high-fidelity HMB3 results showed very good agreement with experimental data, commercial solvers, and lower-order predictive methods. The lower-order codes, DFDC and XRotor, offered rapid and reasonable performance predictions in axial flight, but the torque was often highly overpredicted (45% off the experiments). Crosswind conditions could not be accounted for by simple methods. The HMB3 solver required significantly lower computational resources (about 75% less) compared to the commercial code Fluent ^{TM}.

3. Strategies for high-fidelity aerodynamic simulations of ducted/open propellers are verified. The Rotating Reference Frame implementation in HMB3 was proven well-suited for ducted/open propeller simulations in axial flight or hover. Grid motions with chimera methods in HMB3 were successfully applied to cross-wind simulations. The HMB3 RANS and SAS modelling managed to predict the empty duct and ducted propeller loads at increasing cross-wind angles. Overall, the HMB3 solver has shown great accuracy, efficiency, and flexibility for simulations of ducted/open propellers at various operating conditions.

4. The actuator disk (AD) or actuator line (AL) modelling of rotors in axial or edgewise flight can deliver flow predictions with reasonable accuracy at much reduced computational cost. The AD and AL modelling approaches were carefully examined and compared with blade-resolved simulations. For the ducted propeller in axial flight, the uniform actuator disk modelling brought quite accurate predictions of duct thrust and flow details. For the wing/rotor interaction case, the AD and AL modelling brought reasonably accurate predictions of steady and unsteady pressure fields, as well as, the flow details including excessive flow separation below the wing. The tangential disk loading was found to have limited improvements on the results, but the convergence was hindered due to the swirl velocities.

The next chapter presents more details and discussions derived from these simulations.

Chapter 4

Aerodynamics and Aeroacoustics of the Ducted/Open Propellers [1]

To examine the suitability of the ducted propeller as auxiliary propulsion or lift for novel rotorcraft configurations, performance at various operating conditions was investigated and discussed in this chapter. The key results and novelties from this chapter are the systematic performance analysis at various operating conditions, and the detailed flow analysis to provide more insights into the flow physics resolved by high-fidelity simulations, as well as, near- and far-field acoustic features of the ducted/open configurations.

The advance ratio range in axial flight was extended to explore performance changes at low and high speeds. More flow details were extracted from simulations at cross-wind and analysed. Comparisons were also made against the open propeller configuration, working at the same *RPM*, blade pitch, and free-stream velocities. Moreover, the near- and far-field acoustic performance of the ducted/open counterparts in axial flight was also computed and studied.

[1] This chapter has been published in Zhang, T. and Barakos, G. N., High-fidelity CFD validation and assessment of ducted propellers for aircraft propulsion, Journal of the American Helicopter Society, Vol. 66, No. 1, 2021, pp. 128.

4.1 Aerodynamic Performance in Axial Flight at $\mu = 0.191$

From the numerical validation results in the previous chapter, it can be noticed that at $\mu = 0.191$ the total thrust of the ducted propeller was slightly higher than the open propeller, while the torque was lower, as presented in Table 3.9 and Figures 3.13(a) and 3.13(b). This section aims to identify the origin of the performance benefits of the ducted propeller at this baseline operating condition.

To compare the thrust contributions, the axial momentum and pressure contours for the ducted/un-ducted propellers are shown in Figures 4.1(a) to 4.1(d). The presence of the duct accelerated the flow ahead of the propeller but slows down the wake downstream. Further, as shown in Figures 4.1(a) and 4.1(b), the inflow was accelerated by the duct curvature at the inlet. This led to a lower local static pressure and caused the blades to work at higher inflow velocities. The blades were hence offloaded and produced only 70% of the total thrust.

The axial mass and momentum flow rates measured at the diffuser exit for both configurations are presented in Table 4.1. The presence of the duct increased the mass and the momentum flow rates in the axial direction at this advance ratio, which corresponds to the higher overall thrust. The same qualitative result can also be derived from simple momentum theory analyses of ducted rotors, considering the forced expansion of the wake at the diffuser exit.

Table 4.1: Axial mass and momentum flow rates from HMB3 simulations for the ducted and un-ducted propellers at $\mu = 0.191$, integrated over the diffuser exit section (see Figures 4.1(a)).

Configuration	Axial mass flow rate $\dot{m}$	Axial momentum flow rate $\dot{m}u$
Open propeller	1.363	1.946
Ducted propeller	1.439	2.139

To further verify the contribution of the duct, which carried about 30% of the total thrust as presented in Table 3.9, the pressure coefficient distribution and surface pressure vectors at $\mu = 0.191$ were extracted and presented in Figure 4.2(b). It is clearly shown that the leading edge suction and the recovered pressure at the diffuser, both contributed to the thrust gain of the ducted propeller. The propeller suction further decreased the pressure on the inner side of the duct, especially at the inner side leading edge before the rotor disk, where the suction forces resided. A pressure jump is caused by the rotor disk. A low pressure peak limited to a very small area can

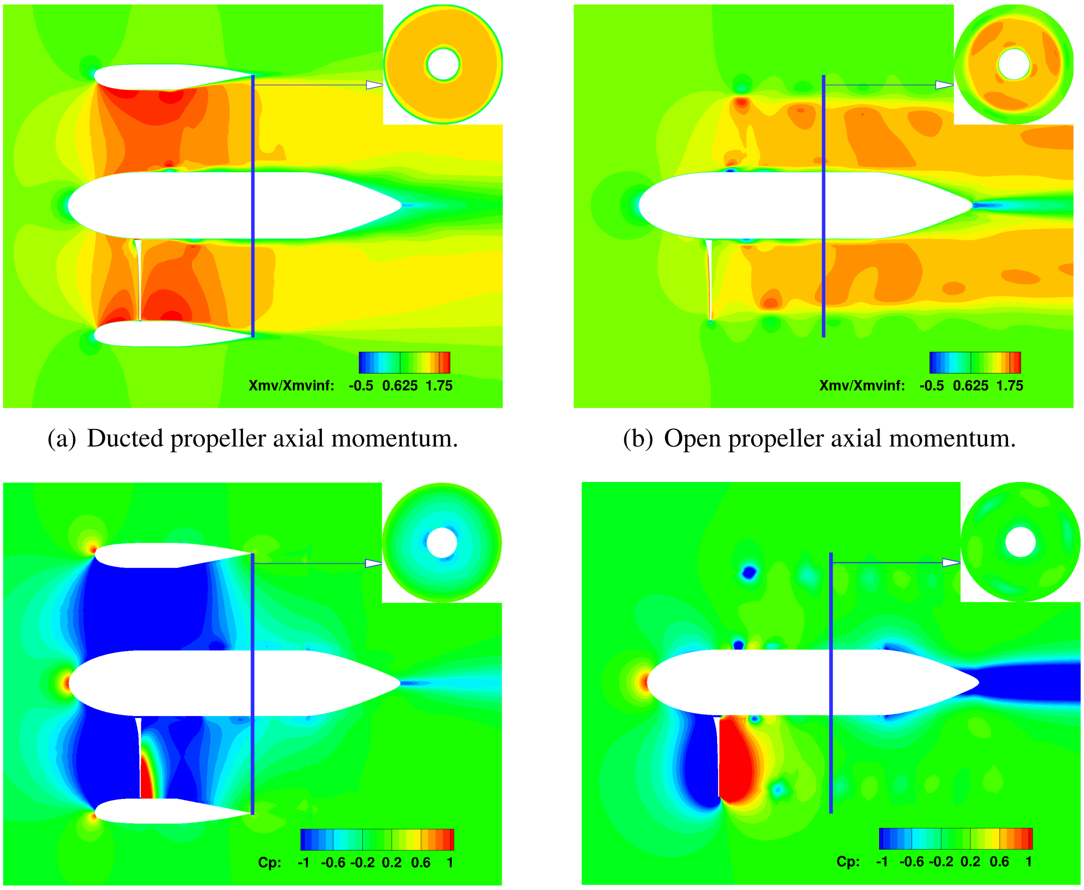

(a) Ducted propeller axial momentum.

(b) Open propeller axial momentum.

(c) Ducted propeller pressure coefficient contours.

(d) Open propeller pressure coefficient contours.

Figure 4.1: Instantaneous axial momentum (normalized by the far-field axial momentum) and pressure coefficient comparisons between the ducted propeller and the open propeller at $\mu = 0.191$, $\psi = 0°$. Thick blue lines denote the diffuser exit sections.

be observed due to the sudden transition of the geometry at the diffuser. The static pressure then gradually recovers inside the diffuser. Overall, the pressure formed a slightly inwards force that has a large axial propulsive component.

Table 4.2: Axial moments breakdown for the Grunwald [18] ducted propeller and the open propeller at $\mu = 0.191$. Contributions from the centre-body were negligible and were not presented here.

C_{Mx}	HMB3$_{dp}$	Contribution	HMB3$_{op}$	Contribution
Total	0.282	100%	0.314	100%
Rotor	0.279	99.07%	0.313	99.8%
Duct	0.0027	0.96%	-	-

In terms of torque contributions, as shown in Table 4.2, the ducted propeller produced lower

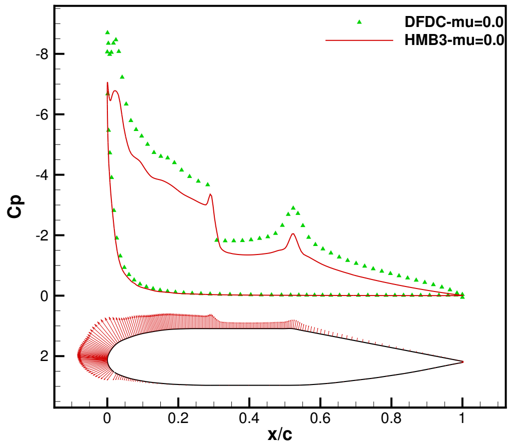

(a) Azimuth-averaged duct surface pressure distribution at $\mu = 0.0$.

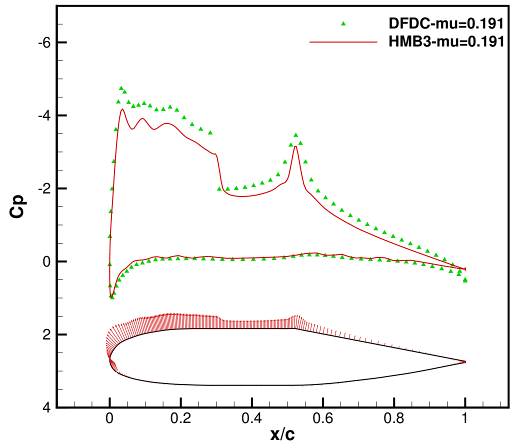

(b) Azimuth-averaged duct surface pressure distribution at $\mu = 0.191$.

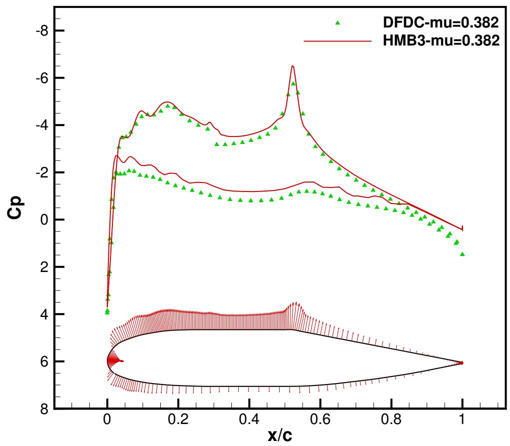

(c) Azimuth-averaged duct surface pressure distribution at $\mu = 0.382$.

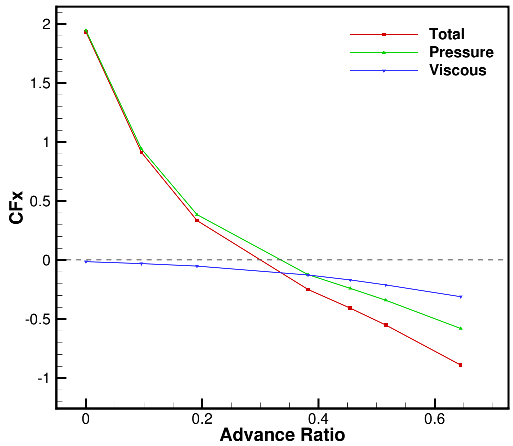

(d) Duct pressure and viscous forces breakdown at increasing advance ratios.

Figure 4.2: Comparisons of duct surface pressure distributions (azimuth averaged) at low, medium, and high advance ratios, using HMB3 and DFDC calculations. Surface pressure force vectors are extracted from HMB3 simulations.

torque than the open propeller, which is due to the higher inflow and hence offloaded propeller loading. Further, the torque almost all came from the rotor with negligible contributions from the duct and the centre-body. For the current case at $\mu = 0.191$, the combination of the slightly higher overall thrust and the reduced overall torque led to a higher propulsive efficiency (Froude efficiency) of the ducted propeller by about 0.1 compared to the open propeller. This performance improvement was only moderate due to the advance ratio in this case, which was the highest advance ratio throughout the experiments [18].

Overall, it can be concluded that the duct increases the overall performance by offloading the propeller and offering extra thrust at no torque cost. However, it is of interest to know whether the ducting benefits can be maintained and how would they change at different operating conditions. This is investigated in the following sections.

4.2 Performance Changes with Advance Ratios Variations

As investigated by several previous experiments and calculations [58, 12, 21], the efficiency of the ducted propeller drops as the advance ratio increases. The ratio of the propeller thrust to total propulsion increases in the meantime, indicating some losses of efficiency of the ducting at high advance ratios. In this light, the advance ratio range of the Grunwald ducted/open propellers [18] in axial flight was extended from 0.0 (hover) to 0.6447. The advance ratio was changed by changing the free-stream speed while maintaining the same propeller RPM and blade pitch. The lower-order codes DFDC and XRotor were used in this section due to the lack of experimental data to provide additional comparisons.

The thrust breakdown of HMB3 and DFDC results at increasing advance ratios is plotted in Figures 4.3(a) and 4.3(b). Experimental data was available for validation only for $\mu = 0.0$ and $\mu = 0.191$. Nevertheless, good correlations between the test data and HMB3 results, in terms of total and component thrust, can be seen in both cases. The DFDC calculations were also in favourable agreement with HMB3 simulations, especially at lower advance ratios.

Figure 4.3(b) shows that as the advance ratio grew, the thrust produced by each component dropped gradually and soon became negative. Note that at low advance ratios ($\mu < 0.1$), for the cases investigated, the duct contributed more propulsion than the propeller. However, the ratio of the duct thrust to total thrust dropped quickly as the advance ratios increased, and was soon overtaken by the propeller thrust.

The same advance ratios were also applied to the open propeller using both HMB3 and XRotor calculations. The agreement was good at low advance ratios, while slight discrepancies

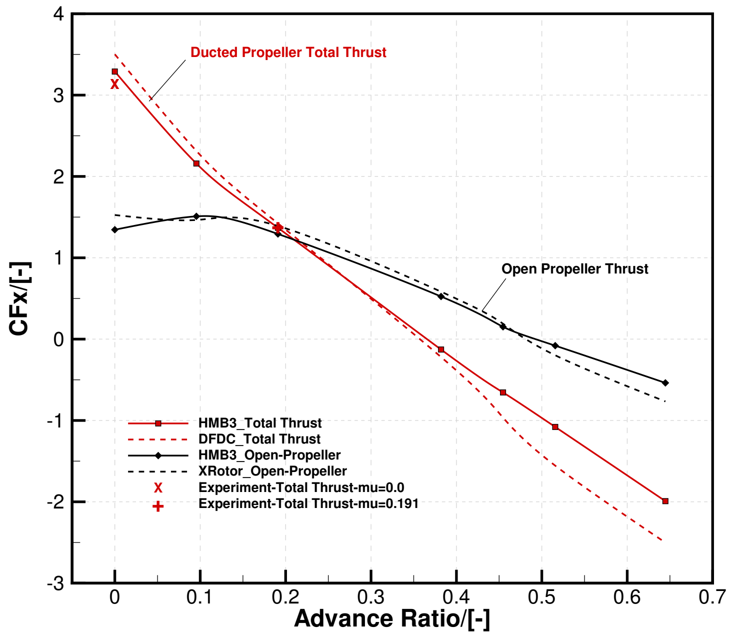

(a) Total thrust of the ducted/un-ducted propellers at increasing advance ratios.

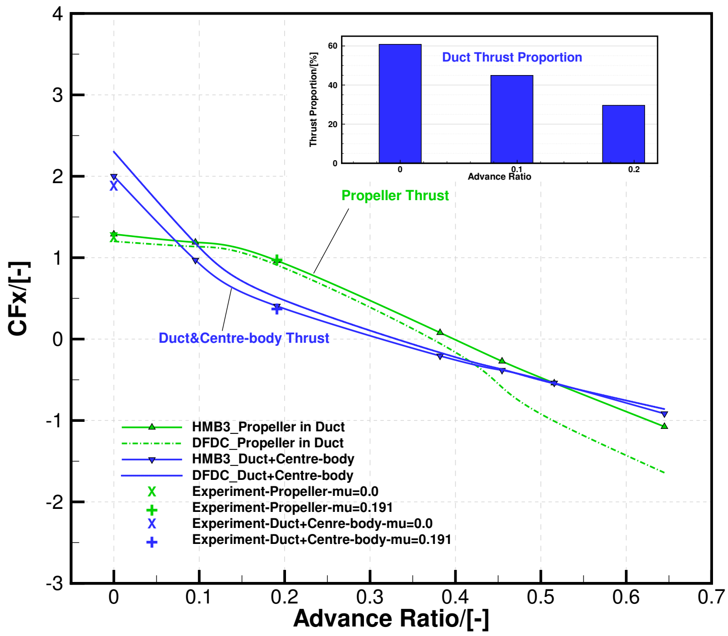

(b) Propeller and duct/centre-body thrust variations at increasing advance ratios.

Figure 4.3: Ducted and un-ducted propellers thrust breakdown at increasing advance ratios. All values normalized by the free-stream speed at $\mu = 0.191$ for comparison.

can be seen at high advance ratios. This can be attributed to the fact that at the high advance ratios studied, the local angles of attack for the blade elements become negative and the blade mostly works near stall conditions. Due to the duct induced inflow, the ducted propeller experienced more severe stall conditions in this situation, and the difference between the DFDC and HMB3 results was hence larger. Nevertheless, the same trend can be observed for the ducted propeller calculations, and predictions for the duct force remained in good agreement at high advance ratios. The un-ducted propeller was able to produce only half the thrust of the ducted counter-part in hover. As the advance ratio increased, the ducted and open rotor thrust decreased following a similar trend. Meanwhile, the total thrust of the ducted propeller dropped faster due to the increasing duct drag and was overtaken by the un-ducted propeller at around $\mu = 0.2$.

Comparisons of the propeller torque for ducted and un-ducted propellers are presented in Figure 4.4(a). The DFDC and XRotor codes generally over-predicted the propeller torque, yet the predictions had the same trends as the HMB3 results. The open propeller torque increased slightly as the advance ratio increased from 0 to 0.2, then dropped quickly as μ was further increased. For the ducted propeller, however, both predictions indicate that torque decreases monotonically with the advance ratio. The Froude efficiency ($\eta = \frac{TV_\infty}{Q\Omega}$) comparisons are shown in Figure 4.4(b). Results from different methods exhibited the same tendency and were in favourable agreement. The efficiency of the ducted propeller was higher than the open propeller by about 0.1 below $\mu =$ 0.2, indicating the superior efficiency. However, the ducted propeller quickly became inefficient than the open propeller at high advance ratios. The negative efficiency was due to the negative thrust at $\mu = 0.382$.

Strength and features of the propulsor wake at low advance ratios are also of great interest. As future civil compound rotorcraft, serving as air taxi or air ambulance, tend to operate in close proximity to the ground in urban environments. Less intrusive wakes are therefore favourable. The axial velocity magnitude measurements, extracted from the ducted and un-ducted simulations at $\mu = 0.0955$ and $\mu = 0.191$, are presented in Figures 4.5(a) and 4.5(b). The velocities were extracted from the section one duct chord length downstream the diffuser exit, and averaged over the azimuth. The dashed lines denote the local minima and maxima at each radial station, representing

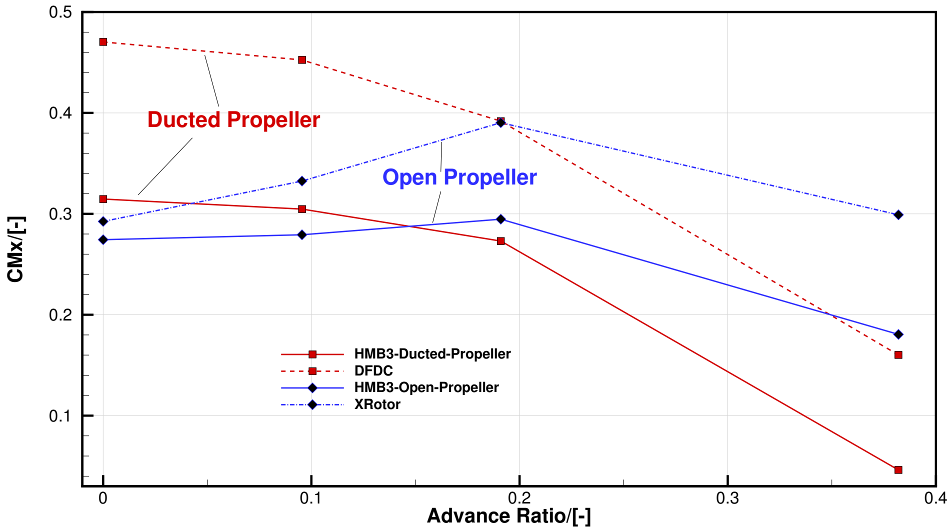

(a) Propeller axial moment (torque) variations with increasing advance ratios.

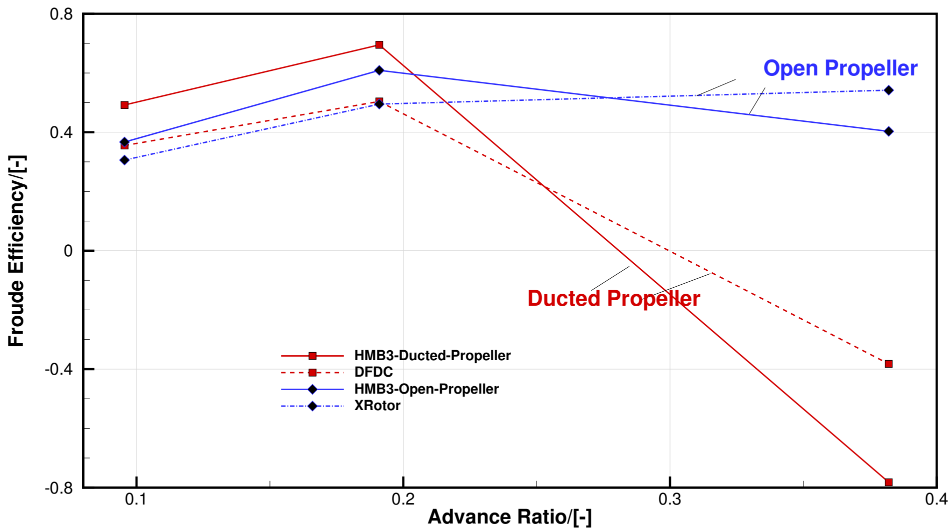

(b) Froude efficiency variations at different advance ratios.

Figure 4.4: Propeller torque and Froude efficiency comparisons for the ducted and un-ducted propellers at different advance ratios. All values normalized by the free-stream speed at $\mu = 0.191$ for comparison.

the speed variations with respect to the average. The velocity profiles qualitatively agree with the wake survey by Yilmaz et. al. [29], albeit at different scales and conditions. As presented in Figure 4.5(a), the propeller wake shows a typical contraction with higher velocities concentrating in a small region. Also, larger speed variations can be noted. In comparison, velocities in the ducted propeller wake were expanded and averaged over the disk, and smaller speed fluctuations were observed.

When the advance ratio is increased to $\mu = 0.191$, as shown in Figure 4.5(b), similar features are observed, but the gap between the maximum velocities became smaller. In Figures 4.5(a) and 4.5(b), the vertical lines denote the averaged axial mass flux (calculated as $\frac{\iint \rho V_x ds}{\iint ds}/(\rho_\infty V_{x\infty})$) over the extraction section and normalised by the free-stream axial mass flux. Both ducted and open propellers produced higher mass flux than at the lower advance ratio of 0.0995, while the ducted propeller produced about 30% higher than the un-ducted at this low advance ratio. At $\mu = 0.191$, the ducted and un-ducted configurations produced similar mass flux magnitudes over the section, with the ducted having about 4% higher. Overall, the ducted propeller is shown to have less intrusive and smoother wake features over its un-ducted counter part at low advance ratios for the case studied.

To further highlight the duct thrust change at different advance ratios, the azimuthally-averaged duct surface pressure distributions from HMB3 simulations are presented in Figures 4.2(a) to 4.2(c), along with the DFDC results. Favourable agreement between the methods was again noted at different advance ratios. The pressure force vectors on the duct surface were also extracted from HMB3 results. It is clearly shown that the duct leading edge provided a significant suction force in hover ($\mu = 0.0$). As the advance ratio increased, the pressure force on the outboard side of the leading edge gradually became negative. This region of negative forces grew and moved gradually inboard as the advance ratio was further increased, resulting in a net drag on the duct. As the free-stream speed increased, the pressure jump imposed by the rotor disk was no longer the dominant flow feature. The diffuser exit worked regardless, but the region producing drag force was also increasing. At $\mu = 0.382$ as shown in Figure 4.2(c), pressure forces on the duct outer surface were not to be ignored. Contributions of pressure and viscosity are given in Figure 4.2(d). The major component had always been due to pressure, but the viscous part, which always contributed to the drag, also grew slightly with the advance ratio.

Overall, the ducted configuration showed higher efficiency over its open propeller counterpart, in hover or at lower advance ratios. However, at fixed pitch and RPM, the benefits diminished at higher advance ratios due to the duct thrust loss. In practice, however, the thrust and torque

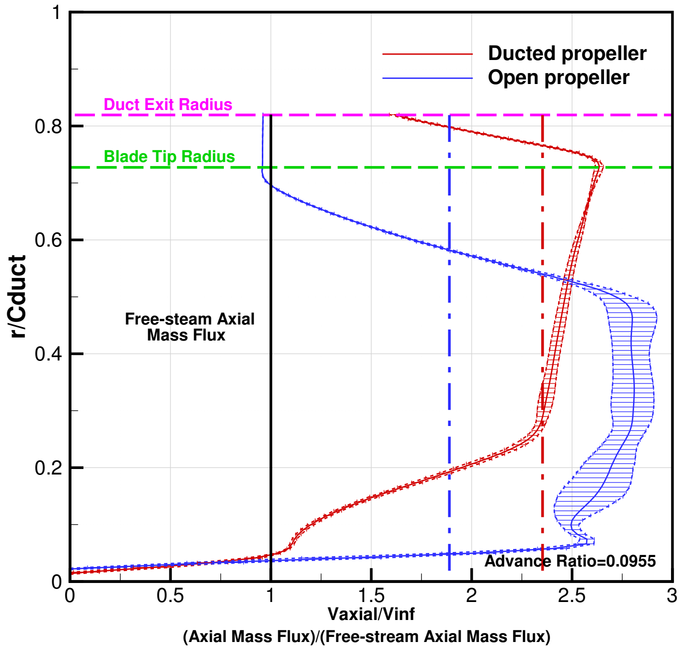

(a) $\mu = 0.0955$.

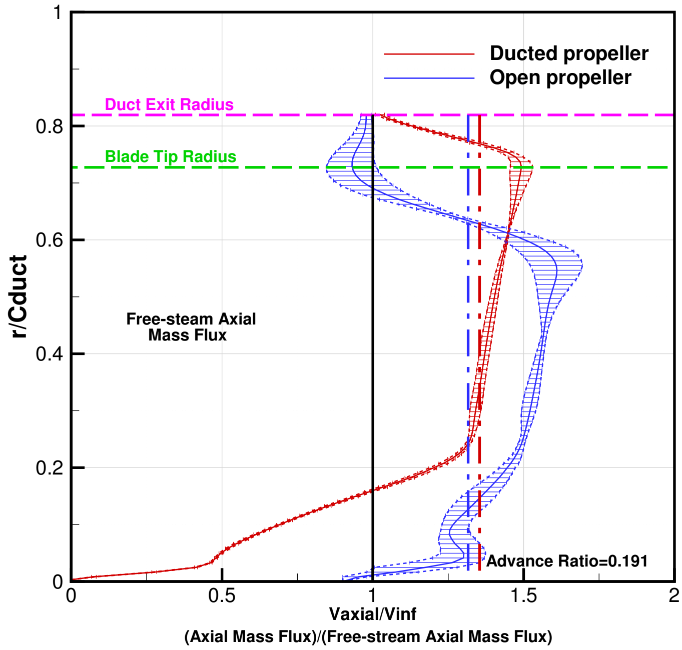

(b) $\mu = 0.191$.

Figure 4.5: Axial velocity profile profile comparisons of the ducted and un-ducted propellers. The error bars denote the variation envelope of the velocity profile. The thick vertical lines represent the averaged axial mass flux.

output at high speeds is often adjusted by varying the rotor RPM or the blade pitch. The RPM variation alters the advance ratio of the propulsor, besides changing the absolute velocity of the blade surface. The performance variations can be reasonably expected from the investigations of advance ratios, as long as prominent compressibility effects are not present. It is then of interest to see if the ducted benefits can be retained at increased pitch angles at high speeds.

4.3 Performance Changes with Blade Pitch Variations

High-fidelity HMB3 simulations and lower-order calculations using XRotor and DFDC at positive and negative pitch changes relative to the original pitch setting of $\beta_{0.75} = 29.58^\circ$ at $\mu = 0.191$ and 0.382 are performed and analysed. Larger pitch ranges are investigated using the lower-order codes due to the low computation cost. In HMB3 simulations, the pitch change was mostly achieved using RBF (Radial Basis Function)-based mesh deformations. In few cases where the deformation was causing issues for chimera interpolation, the grids were adjusted manually with the assistance of the automation framework.

Total thrust, propeller torque, and Froude efficiency variations over pitch changes at $\mu = 0.191$ and 0.382 are presented in Figures 4.6(a) to 4.8(b). The lower-order predictions of thrust by DFDC and XRotor showed very favourable agreement with HMB3 results at both advance ratios. However, the torque was still highly over-predicted by the lower-order methods in both cases, compared to HMB3 and experiments. This has also been noticed in previous investigations. This consequently led to lower efficiency predictions. Nevertheless, the lower-order predictions and high-fidelity HMB3 calculations of torque and efficiency agreed qualitatively well and were showing the same trends responding to pitch variations at both advance ratios.

At $\mu = 0.191$, the ducted propeller showed a larger thrust to pitch change ratio compared to the open configuration (Figure 4.6(a)). The same feature was noted in the torque results as shown in Figure 4.7(a). This suggested that the thrust and torque outputs of the ducted propeller were more sensitive to pitch changes. This can be attributed to the fact that the propeller inside the duct is subject to higher axial flow speeds due to the duct induction. The ducted propeller thrust was showing an almost linear response to pitch variations below $+8^\circ$. The Froude efficiency (Figure 4.8(a)) calculated from thrust and torque results indicates the existence of an optimal pitch angle

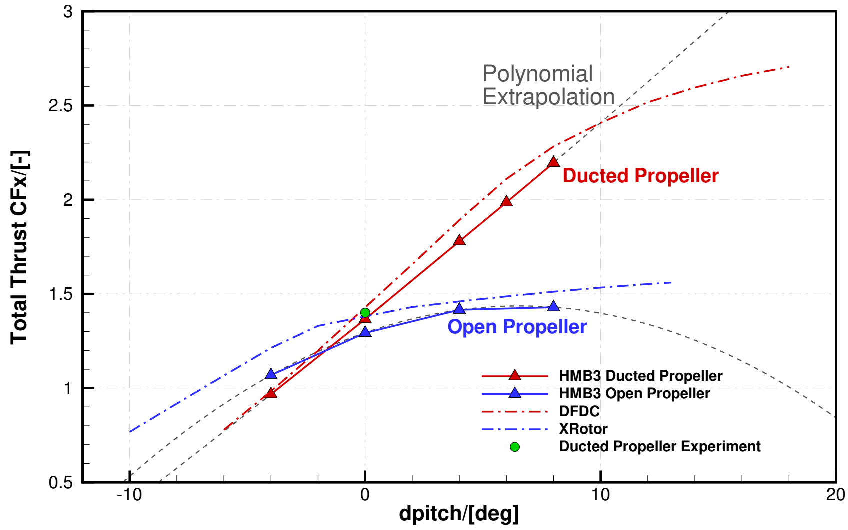

(a) Ducted/un-ducted propeller thrust variations at $\mu = 0.191$.

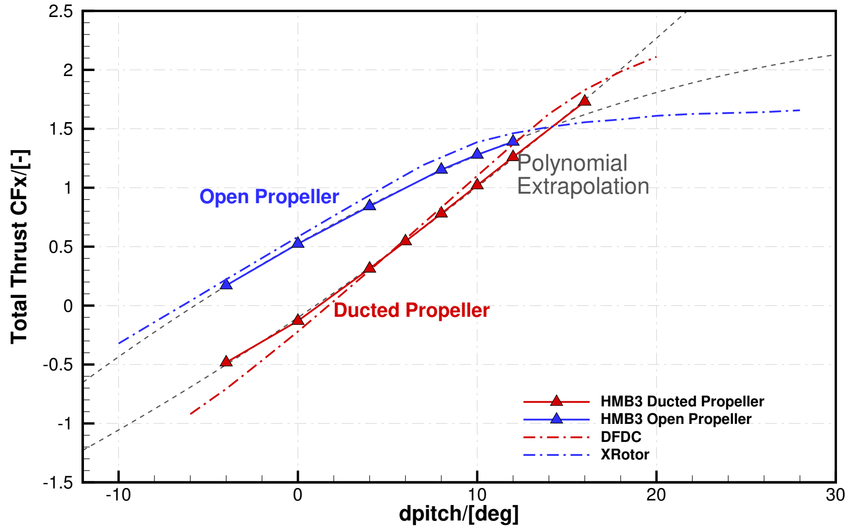

(b) Ducted/un-ducted propeller thrust variations at $\mu = 0.382$.

Figure 4.6: Thrust variations with respect to pitch changes relative to the initial $\beta_{0.75} = 29.58°$ for ducted/un-ducted propellers at $\mu = 0.191$ and $\mu = 0.382$.

for the maximum efficiency at this speed. The optimal pitch angle for the ducted configuration was near the original setting of 29.58° as in the experiments, while for the open propeller the optimal angle was about 3° lower. However, at higher pitch angles, the ducted propeller showed constantly higher efficiency over the open propeller by about 0.1, indicating the superior efficiency was maintained.

The thrust-torque map at varying pitch angles is plotted in Figure 4.9(a). It can be seen that the ducted propeller was able to offer much higher thrust at higher pitch angles. Moreover, for the same thrust required, the ducted configuration required much less power input at higher pitch angles and thrust, compared to the open propeller.

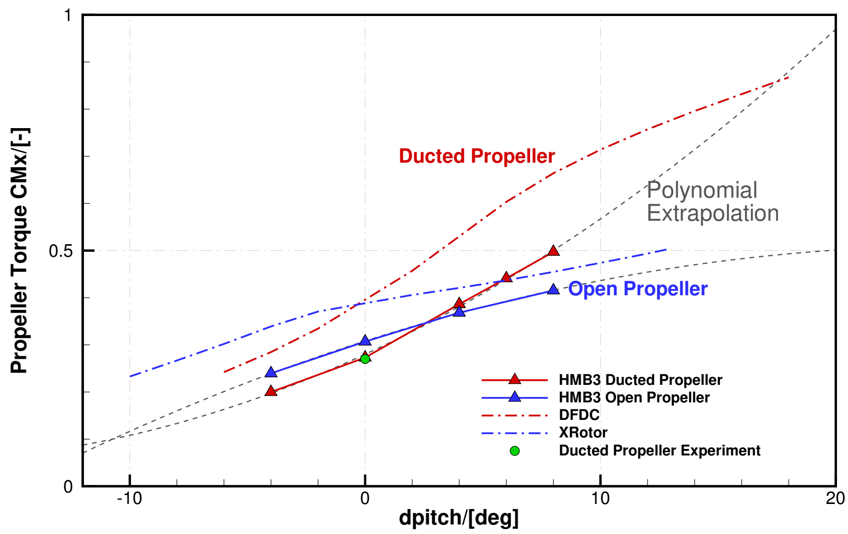

(a) Ducted/un-ducted propeller torque variations at $\mu = 0.191$.

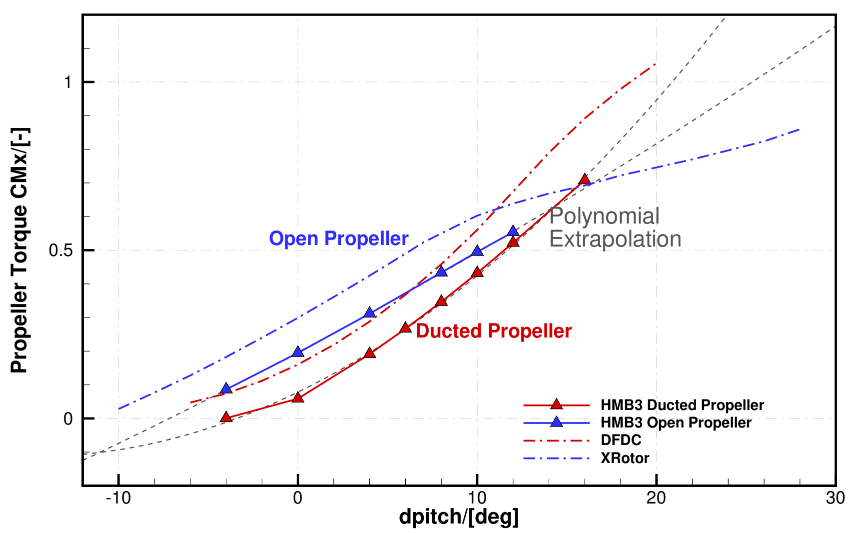

(b) Ducted/un-ducted propeller thrust variations at $\mu = 0.382$.

Figure 4.7: Torque variations with respect to pitch changes relative to the initial $\beta_{0.75} = 29.58°$ for ducted/un-ducted propellers at $\mu = 0.191$ and $\mu = 0.382$.

At the much higher advance ratio of 0.382, favourable correlations between methods and

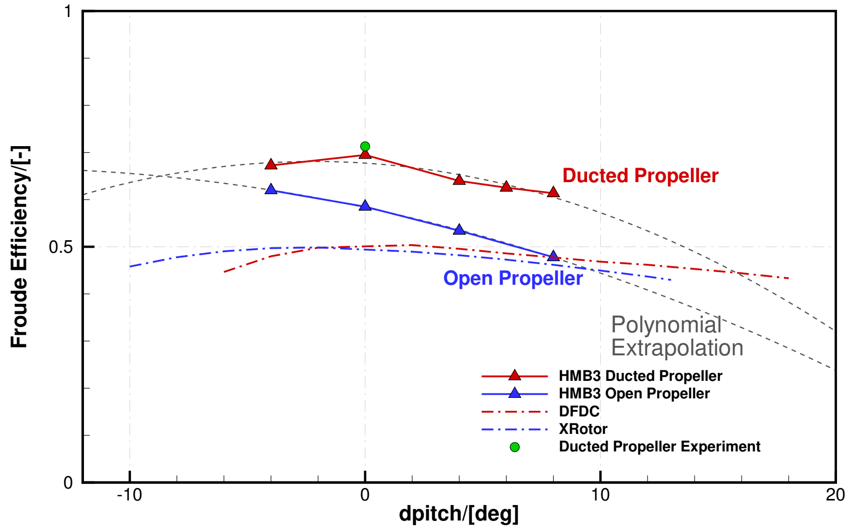

(a) Ducted/un-ducted propeller efficiency variations at $\mu = 0.191$.

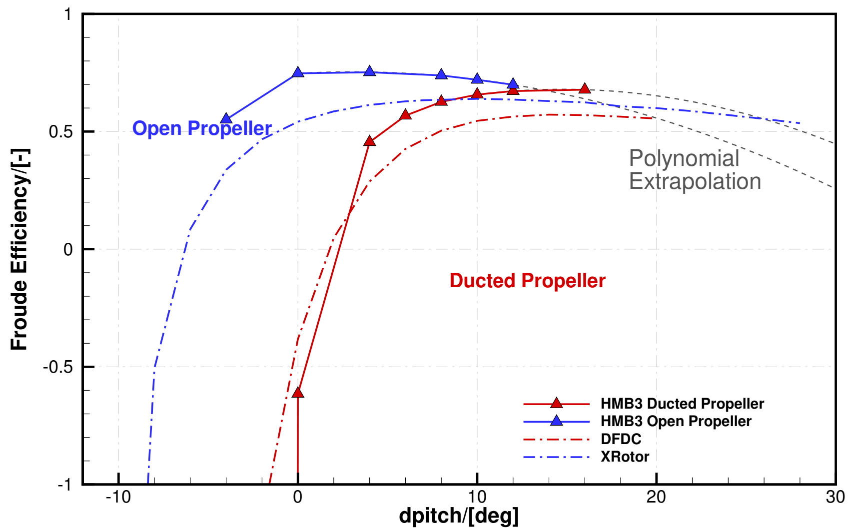

(b) Ducted/un-ducted propeller efficiency variations at $\mu = 0.382$.

Figure 4.8: Froude efficiency variations with respect to pitch changes relative to $\beta_{0.75} = 29.58°$ for ducted/un-ducted propellers at $\mu = 0.191$ and $\mu = 0.382$.

similar responses to pitch changes were also noticed. The ducted propeller was still more sensitive to pitch variations. However, the ducted propeller generated constantly lower thrust than the open propeller (Figure 4.6(b)), until very high pitch increases ($> +12°$) as indicated by lower-order predictions. The same was also noted in the torque results (Figure 4.7(b)). The existence of optimal pitch settings for maximum efficiency was also observed in Figure 4.8(b). Nevertheless, the open

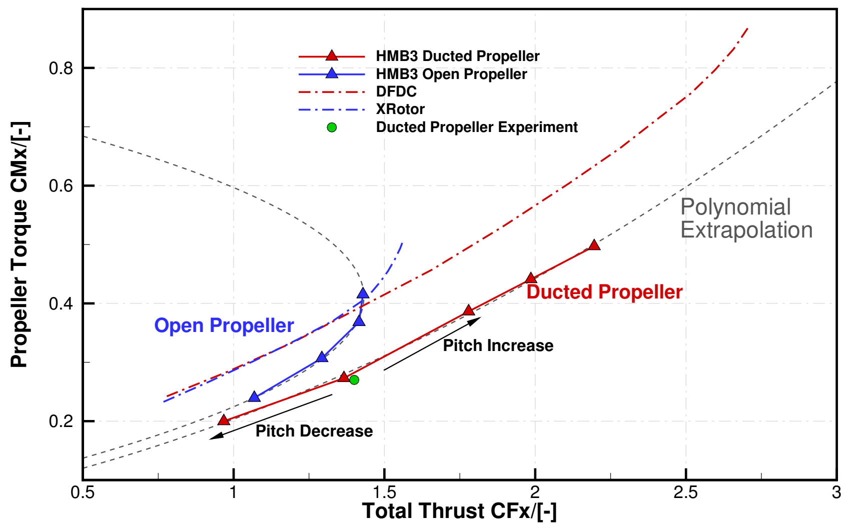

(a) Thrust-torque map over pitch changes at $\mu = 0.191$.

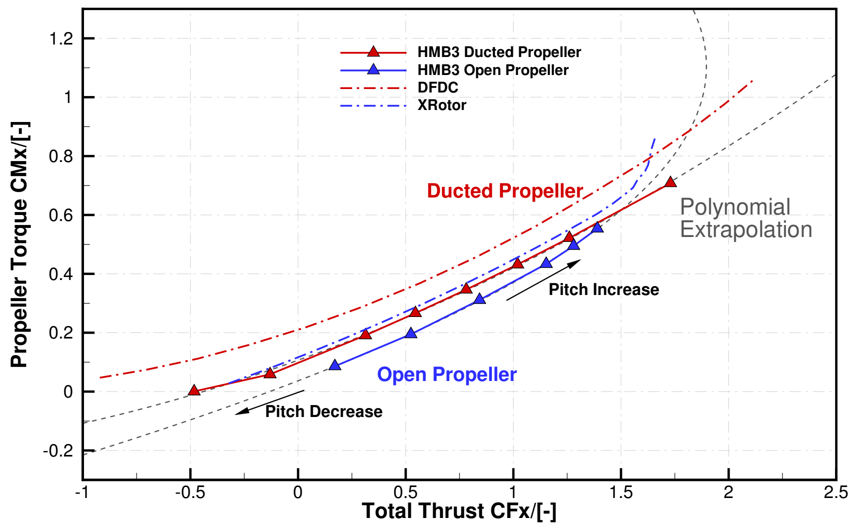

(b) Thrust-torque map over pitch changes at $\mu = 0.382$.

Figure 4.9: Thrust-torque map of the ducted/un-ducted propellers with respect to pitch changes relative to $\beta_{0.75} = 29.58°$ at $\mu = 0.191$ and $\mu = 0.382$.

propeller efficiency was constantly higher than the ducted configuration at this high advance ratio. Regardless, it was noted that the efficiency gap between the two configurations was reducing with increasing pitch, although their respective efficiency values were dropping in the meantime. Extrapolations of the lower-order efficiency predictions indicate a possible intersection point beyond $+30°$. The thrust-torque map at varying pitch angles at this high advance ratio is presented in

Figure 4.9(b). For the same amount of thrust required, the ducted propeller was only more efficient at very high pitch increases ($> +14^\circ$).

Positive correlations between the propeller thrust and the duct thrust were also noted, as shown in Figures 4.10(a) and 4.10(b). At the same axial flow speed and advance ratio of 0.191, the duct thrust was increased by 100% while the propeller thrust was increased by 40%, when the pitch was increased by $+8^\circ$ from the original setting as shown in Figure 4.10(a). In Figure 4.10(b) at $\mu = 0.382$, the duct axial force was recovered to positive values beyond $+8^\circ$ changes. It can be thus argued that the duct thrust in axial flight is determined by the relative strength of the propeller suction and the far-field velocity, rather than solely on the advance ratio or the absolute axial velocity. Stronger propeller suction alters the velocity and pressure fields around the duct in favour of improving the duct thrust for the case studied.

Overall, it can be concluded that the ducted propeller performance is more sensitive to pitch changes. At high advance ratios and low pitch settings, the open propeller showed better efficiency over the ducted counterpart. Nevertheless, it is shown that the superior performance of the ducted propeller can be retained at high advance ratios by increasing the blade pitch. Beyond certain, high pitch angles, the ducted propeller was able to outperform the open propeller at high advance ratios. Higher pitch angles were required at higher advance ratios to increase the propeller suction and to recover the duct thrust to maintain the aerodynamic benefits.

4.4 Aerodynamic Performance at Crosswind

This section presents the performance analysis of the ducted/open propellers at crosswind with non-axial inflows. For fixed-wing aircraft, non-axial inflow conditions are often encountered during landing, taking off, or manoeuvre. However, for novel rotorcraft configurations, the ducted/open propellers may be constantly subject to the main rotor downwash, such as in the X^3 case. It is hence of special interest to investigate the non-axial inflow conditions for the ducted/open propellers.

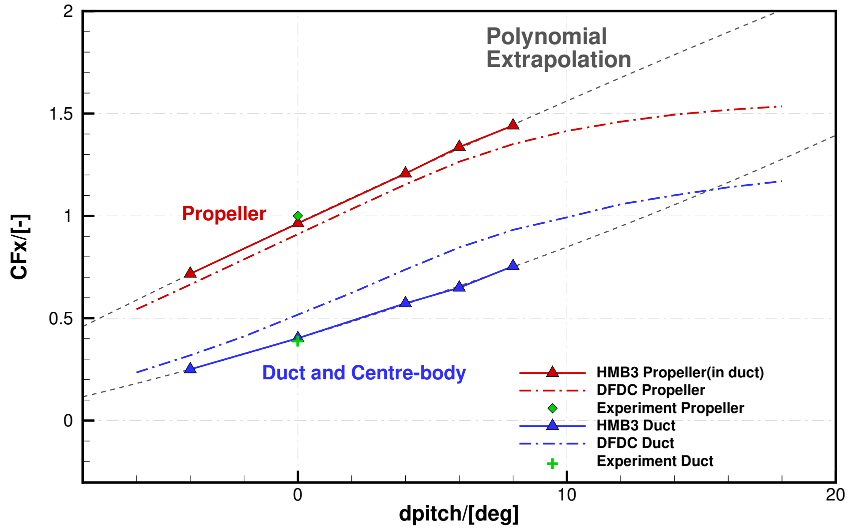

(a) Propeller and duct thrust variations at $\mu = 0.191$.

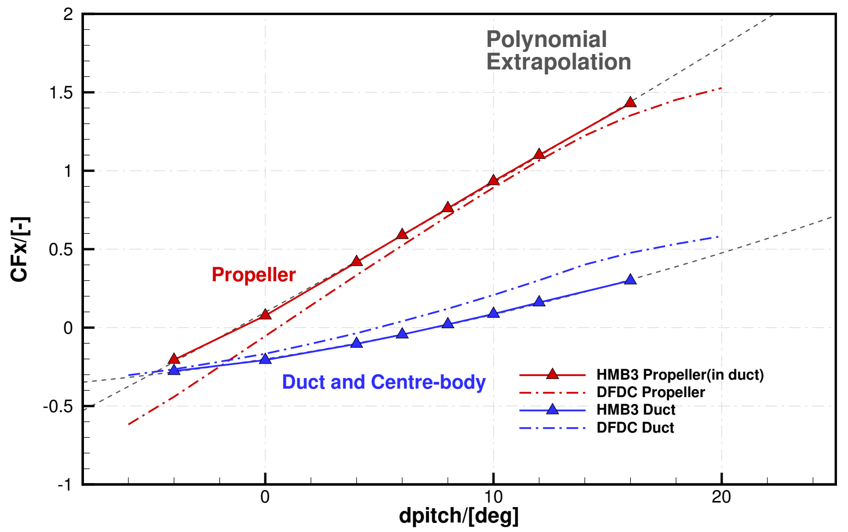

(b) Propeller and duct thrust variations at $\mu = 0.382$.

Figure 4.10: Propeller and duct thrust variations of the ducted propeller with respect to pitch changes relative to $\beta_{0.75} = 29.58°$ at $\mu = 0.191$ and $\mu = 0.382$.

4.4.1 Aerodynamic Loads Breakdown

To inspect the ducted propeller performance at cross-wind, a first study was focused on the behaviour of bare duct at angles of attack as presented in Chapter 3. It can be derived from Figure 3.8(a) that the empty duct itself, without the propeller, produced considerable aerodynamic loads and followed an almost linear response to AoA variations before stall. It is possible to use the ducted propeller for lift generation as an annular wing [138], while still delivering propulsion. The lift slope in the linear region for the duct tested, as shown in Figure 3.8(a), was around 3.15, and the stall boundary was about 23°. When the propeller is installed, as shown in Figure 3.15(a), the lift slope approached 5, and the stall was delayed to about $AoA = 45°$ thanks to the propeller suction [23]. The propulsion, i.e. the axial force, in Figure 3.15(b), dropped slowly at small cross-wind angles. As suggested by Mort et al. [19], for a tilt-duct aircraft, the ducted propeller is most likely to work in axial flight or at AoA within the stall boundary.

For the ducted propeller configuration, the breakdown of aerodynamic loads at $AoA = 20°$ were presented in Table 4.3. At incidence of 20°, the ducted propeller generated a total force significantly higher than in the axial condition, of which the lift component was twice as much as the propulsion. A nose-up pitching moment was also noticed. In Table 4.3, the duct claimed the most contributions to the lift and the nose-up pitching moment, while the propeller contributed the most to the forward propulsion. The centre-body only had small effects for the case analysed.

Table 4.3: Aerodynamic load breakdown for the Grunwald ducted propeller [18] at $AoA = 20°$.

	C_l	Contribution	C_{F_x}	Contribution	C_m(pitching)	Contribution
Total	1.922	-	1.096	-	0.504	-
Duct	1.483	77.17%	0.120	10.96%	0.440	87.32%
Propeller	0.405	21.09%	0.923	84.25%	0.064	12.68%

Further comparisons with the un-ducted propeller at $AoA = 20°$ are presented in Table 4.4. The open propeller offered more forward thrust (C_{F_x}, hence the Froude efficiency was slightly higher. About 40% of the total thrust contributed to the lift. The ducted propeller produced about three times the lift, while producing 20% less thrust than the open propeller. The ducted propeller can be seen as the combination of a lifting surface and a propulsor at cross-wind, and the lifting force was mostly derived from the duct. Nevertheless, this also suggests that the duct may create large blockage under main rotor downwash when applied to novel rotorcraft configurations.

To further investigate the duct contribution, the duct surface pressure was extracted, time-averaged over revolutions, and presented in Figures 4.11(a) to 4.11(d). The surface pressure coefficient contours are presented in Figure 4.11(a). With the cross-wind coming from the 180° azimuth,

Table 4.4: Comparisons of aerodynamic loads of the ducted and un-ducted propellers at $AoA = 20°$.

	C_l	C_{F_x}	Propeller C_T	Propeller C_Q	Froude Efficiency η
Ducted Propeller	1.922	1.096	0.037	0.014	0.534
Open Propeller	0.603	1.259	0.050	0.015	0.570

a large region of low pressure can be noticed near the upstream (from 90° to 270° azimuth) inlet lip. The downstream lip saw generally higher pressure, as the stagnation area were moved more inboard.

Sectional pressure coefficients and force vectors for the 90° and 270° azimuth were calculated and presented in Figure 4.11(b). The pressure distributions at these two sections were almost identical, with only small differences seen at the inner leading-edge regions. The duct had slightly lower pressure at the rotor advancing side (90° azimuth). Large differences can be noted, however, for the 0° and 180° sections, as shown in Figures 4.11(c) and 4.11(d), respectively. The upstream section (180°) produced a large leading-edge suction on the inner surface. Whereas for the downstream section (0°), the leading-edge stagnation was moved inboard due to the sideways flow and milder suction can be noticed on the outer surface. In this light, asymmetric geometric modifications may be made to the upstream and downstream lips to accommodate local flow conditions under non-axial inflows.

In summary, at 20° crosswind for the case studied, the ducted propeller produced about twice as much lift as the thrust. The duct contributed the most to the lift, while the propulsion mostly came from the propeller blades. At the advance ratio studied, the ducted and open configurations produced similar torque, but the open propeller had a higher propulsive efficiency due to the higher propulsive force. On the other hand, the duct offered slightly lower thrust but much higher lifting forces than the open propeller. This features may be exploited for lift generation for future rotorcraft configurations, but it may also create large blockages under the main rotor as has been stressed. This will be further discussed in later chapters.

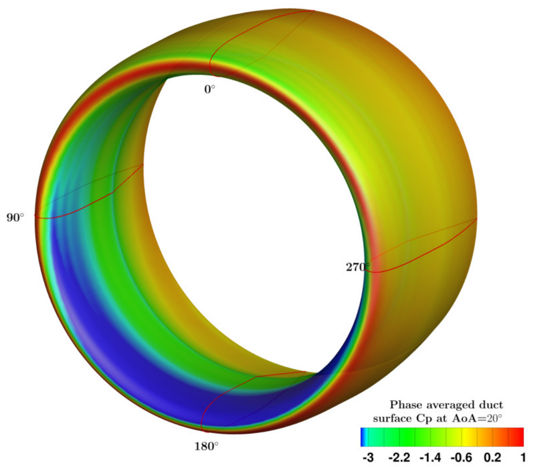

(a) Phase averaged duct surface pressure coefficient contours for the Grunwald ducted propeller at $AoA = 20°$.

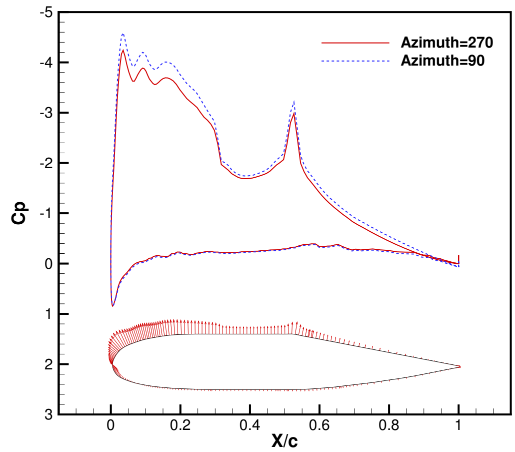

(b) Sectional pressure coefficient and vector distributions at 90° and 270° azimuth at $AoA = 20°$.

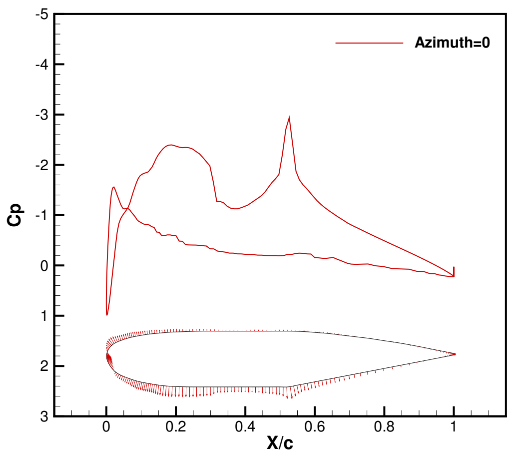

(c) Sectional pressure coefficient and vector distributions at 0° azimuth at $AoA = 20°$.

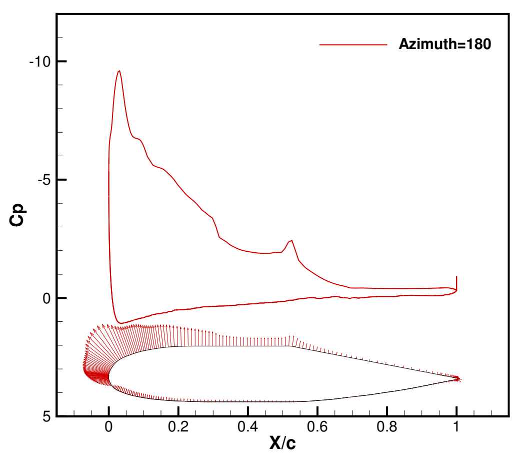

(d) Sectional pressure coefficient and vector distributions at 180° azimuth at $AoA = 20°$.

Figure 4.11: Phase averaged duct surface Cp contours and vectors for the Grunwald [18] ducted propeller at $AoA = 20°$.

4.4.2 Induction and Propeller Disk Loadings

Investigations on the induction and the disk loading of the ducted and un-ducted propellers at cross-wind were also carried out and presented in this subsection to identify the aerodynamic interactions. Comparing to the open propeller, the duct was expected to regulate the inflow and reduce inflow distortion. When installed on novel rotorcraft configurations, this is can be an important advantage as the propulsor may work under constant main rotor downwash. In addition, it is also interesting to verify the induction brought by the propeller, the duct, and their mutual interactions. The inflow profiles, the induction characteristics, and the resultant disk loading were analysed and presented in this subsection.

Thrust distributions on the propeller disk at $AoA = 0°$ and $20°$, for the ducted and un-ducted propellers, are presented in Figures 4.12(a) to 4.12(d). In axial flight, (Figures 4.12(a) and 4.12(b)), the open propeller experienced higher disk loadings due to lower inflow ratios. High thrust areas are seen near the blade tip and slightly inboard. The ducted propeller saw lower disk loadings due to the duct induction. Also, the smaller high loading area is moved towards the blade tip and near the duct surface. At $AoA = 20°$, the open propeller saw higher disk loadings than the ducted propeller again. A large high thrust area was presented at the advancing side near the blade tip. As for the ducted propeller, the high thrust loading was spread between azimuth $0°$ and $180°$ near the blade tip and the duct surface. Due to the duct induction, the ducted propeller was off-loaded in both axial and cross-wind conditions. At cross-wind, it is also noticed that the unbalanced disk loading was more averaged around the azimuth, but more concentrated to the blade tip. The axial force variations on the ducted and un-ducted propeller blades are shown in Figure 4.12(e). The open blades saw higher averaged blade loadings (the dashed lines) and larger force variations.

Further investigations were made on the induction characteristics at cross-wind to identify the aerodynamic interactions. The velocity $\mathbf{V}_p$ seen by the propeller blade elements can be decomposed as:

$$\mathbf{V}_p = \mathbf{V}_\infty + \mathbf{V}_{ip} + \mathbf{V}_{id} + \mathbf{V}_{ie}. \quad (4.1)$$

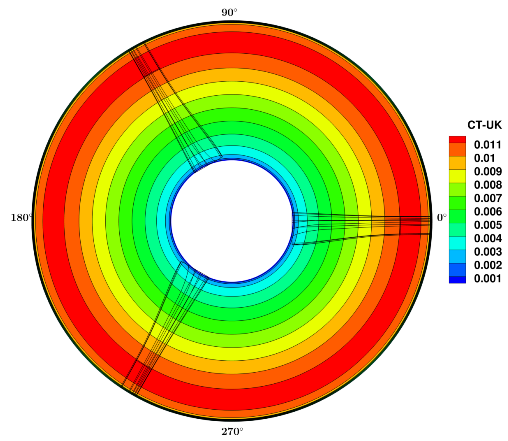

(a) Un-ducted propeller disk normal force distribution at $AoA = 0°$.

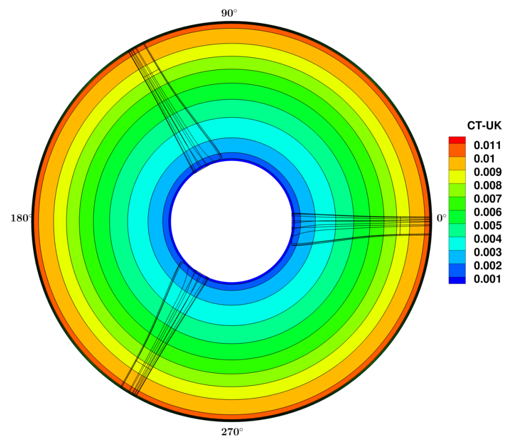

(b) Ducted propeller disk normal force distribution at $AoA = 0°$.

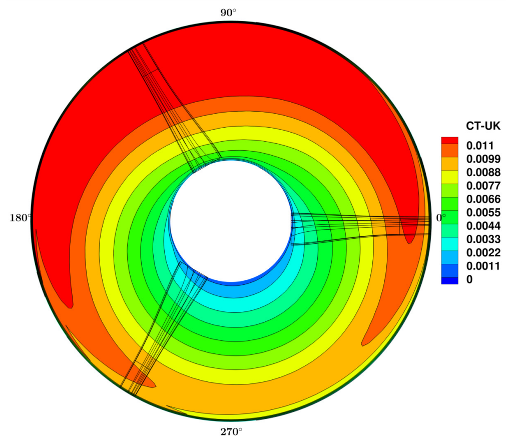

(c) Un-ducted propeller disk normal force distribution at $AoA = 20°$.

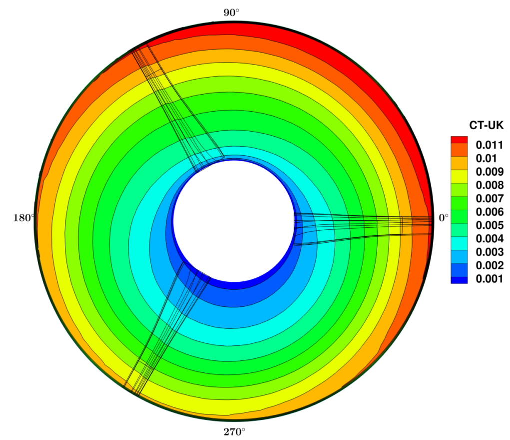

(d) Ducted propeller disk normal force distribution at $AoA = 20°$.

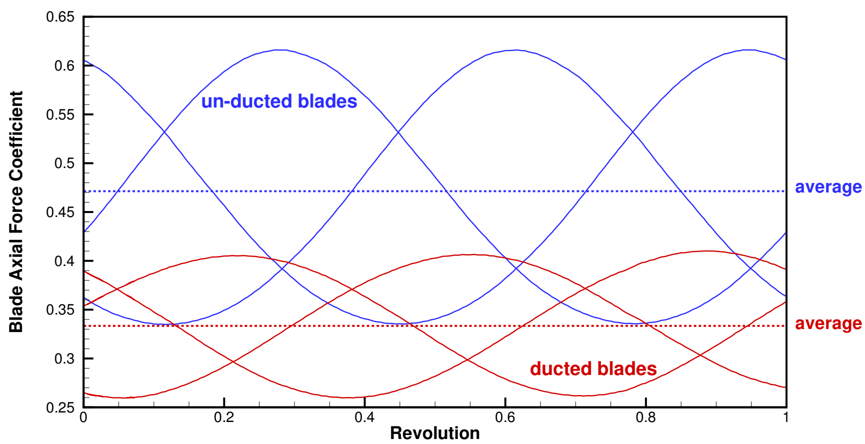

(e) Axial forces variations (including friction contributions) on the ducted and un-ducted propeller blades.

Figure 4.12: Ducted and un-ducted propeller disk normal force distributions (computed using the pressure field) at $AoA = 0°$ and $AoA = 20°$.

where $\mathbf{V}_\infty$ is the free-stream velocity that represents the baseline inflow condition; $\mathbf{V}_{ip}$ is the induced velocity by the propeller, which can be subtracted from open propeller simulations; $\mathbf{V}_{id}$ is the duct induction, which can be subtracted from empty duct simulations; and $\mathbf{V}_{ie}$ is the extra induction by the duct/propeller combination.

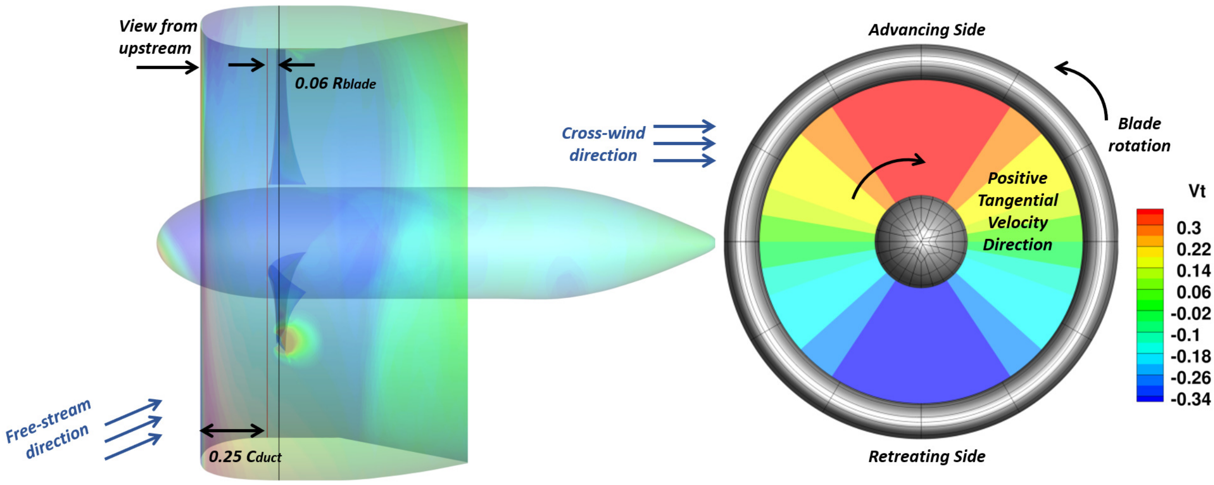

Figure 4.13: Velocity extraction position and baseline tangential velocity profile due to free-stream $\mathbf{V}_\infty$ at $AoA = 20°$.

This decomposition approach assumes a very simple model, which considers component contributions individually and is often used in lower-order analyses such as blade element methods. Surely interference effects must be accounted for by corrections while using lower-order methods. The purpose of adopting this approach in the present study is to investigate the aerodynamic interference between components at crosswind. Similar approaches have also been seen used in interference analyses for propellers in yaw [139] and for compound rotorcraft [140]. Particularly, the term $\mathbf{V}_{ie}$ indicates the strength of the mutual interaction, and highlights the importance of accurate interaction models for lower-order methods for non-axial flight conditions.

The axial and tangential velocity profiles at cross-wind ($AoA = 20°, \mu = 0.191$) were extracted and analysed. Velocity data were extracted from the section $0.06R_{blade}$ upstream the rotor disk, as illustrated in Figure 4.13, and were decomposed into axial and tangential components.

Note that the values shown were normalised using the free-stream velocity, and the flow-field was time-averaged over one propeller revolution.

The baseline tangential velocity profile by the free-stream speed, when there was a cross-wind angle of 20°, is shown in Figure 4.13. Tangential velocities opposite to the blade rotation were taken as positive, as illustrated in Figure 4.13. Subject to such a free-stream tangential speed profile, the propeller tends to generate higher thrust on the advancing side, the same as a helicopter rotor in forward flight. The axial velocity profile was the same over the propeller disk, simply as a fraction of the free-stream speed.

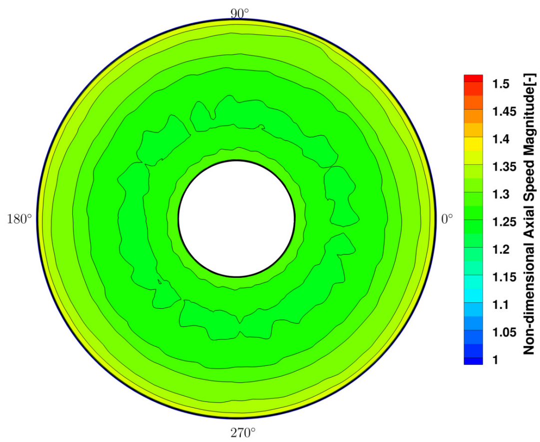

(a) Axial induction factor (normalized by free-stream speed) contours before the rotor disk of the empty duct simulation at $AoA = 0°$.

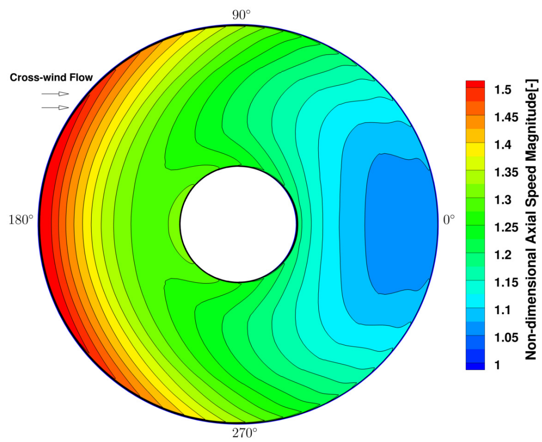

(b) Axial induction factor (normalized by free-stream speed) contours before the rotor disk of the empty duct simulation at $AoA = 20°$.

Figure 4.14: Inflow velocity profiles for the rotor disk induced by the empty duct.

Induced velocity features by the empty duct were first extracted, as they represent the baseline inflow conditions the propeller inside was about to experience. The axial velocity profiles (normalized by free-stream speed) right above the rotor disk are presented in Figures 4.14(a) and 4.14(b) for incidences of 0° and 20°, respectively. Due to the induction of the duct, at $AoA = 0°$, the propeller saw a 30% higher baseline inflow velocity for the case simulated. The radial speed distribution is almost even, with slightly higher values positioned near the duct inner surface. For the cross-wind condition (Figure 4.14(b)), the propeller experienced an unbalanced inflow profile.

The axial ($\mathbf{V_{ix}}$) and tangential ($\mathbf{V_{it}}$) components of the induced velocities by the duct, the

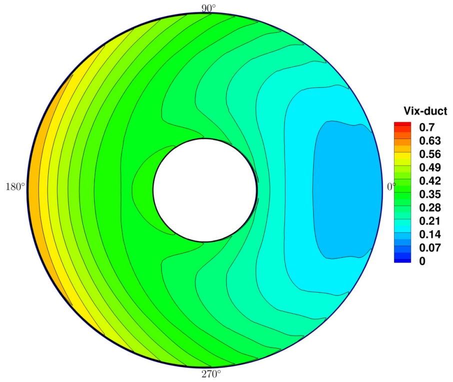

(a) Axial induced velocities by the duct, extracted from simulations of the empty duct at $AoA = 20°$.

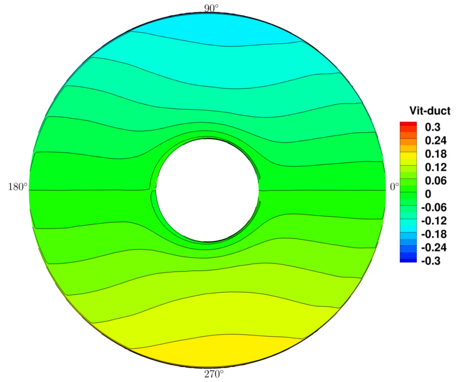

(b) Tangential induced velocities by the duct, extracted from simulations of the empty duct at $AoA = 20°$.

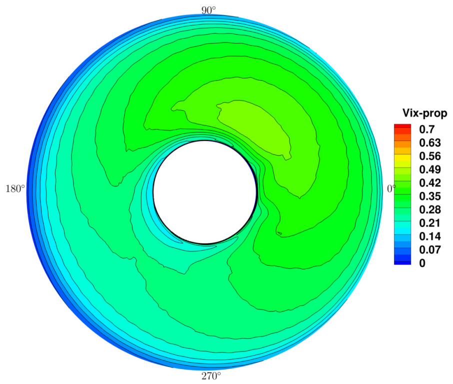

(c) Axial induced velocities by the propeller, extracted from simulations of the open propeller at $AoA = 20°$.

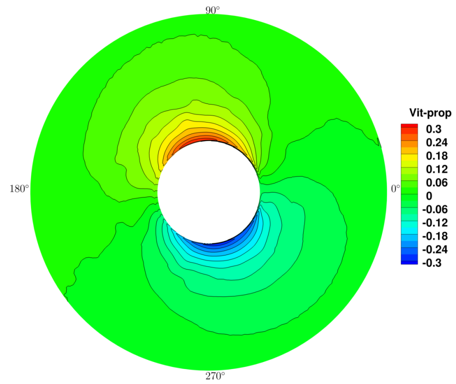

(d) Tangential induced velocities by the propeller, extracted from simulations of the open propeller at $AoA = 20°$.

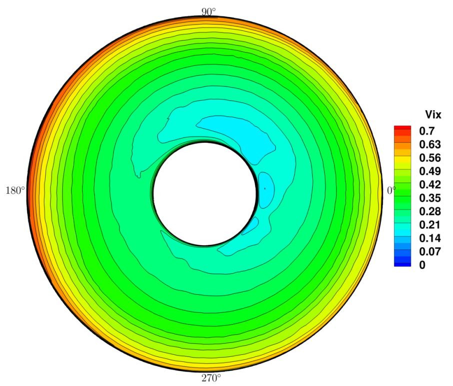

(e) Axial induced velocities by the duct/propeller combination, extracted from simulations of the ducted propeller at $AoA = 20°$.

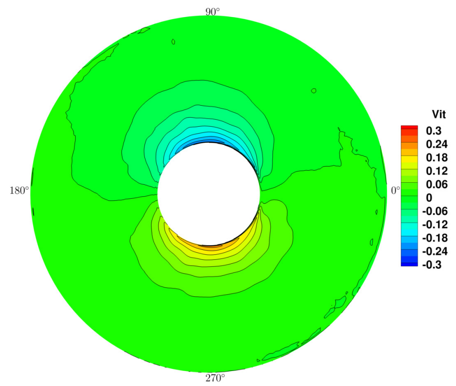

(f) Tangential induced velocities by the duct/propeller combination, extracted from simulations of the ducted propeller at $AoA = 20°$.

Figure 4.15: Induced velocities by the duct, the propeller, and the duct/propeller combination, as decomposed in Equation 4.1.

propeller, and the combination, as defined in Equation 4.1, are presented in Figures 4.15(a) to 4.15(f). The duct induction was estimated by subtracting the free-stream contributions from the empty duct simulation. At the cross-wind angle analysed ($AoA = 20°$), the duct induced higher axial speeds as shown in Figure 4.15(a). Nevertheless, the speed distribution was asymmetric stream-wise, and higher values were observed on the upstream side. The tangential induction by the duct is presented in Figure 4.15(b). The duct reduced the velocity on the advancing side and increased the speed on the retreating side, especially near the duct inner surface (by about 60%). This is very favourable as it eases the unbalanced flow condition experienced by the propeller at cross-wind.

The propeller induction was obtained by subtracting the free-stream contributions from the open propeller simulation at $AoA = 20°$. The results agreed qualitatively well with the study of an open propeller at yaw by Higgins et al.[139] Higher axial inductions were observed mid-span near the advancing side. The maximum and minimum tangential inductions were seen near the blade root, with positive values on the advancing side. The combined induction features were in good correlation with the disk loading results shown in Figure 4.12(c).

The induction by the duct/propeller interference, as shown in Figures 4.15(e) and 4.15(f), was estimated by subtracting the free-stream, the duct induction, and propeller induction. The resulting velocities were due to the interaction of the duct and propeller. As shown in Figure 4.15(e), further higher axial inductions were observed, especially near the duct surface. This resulted in even higher mass flows through the propeller disk. A reduction in tangential speed on the advancing side was noted, while an increase can be seen on the retreating side. This was again favourable since it eased the unbalanced flow condition as did the duct induction.

The resultant induction features of the propeller inside the duct were subject to the combination of the induction from the open propeller and the extra induction contributions. The combined propeller inductions are shown in Figures 4.16(a) and 4.16(b), and the results agreed well with the disk loading features presented in Figure 4.12(d).

Overall, the duct induction and the flow interactions increased the axial induction through

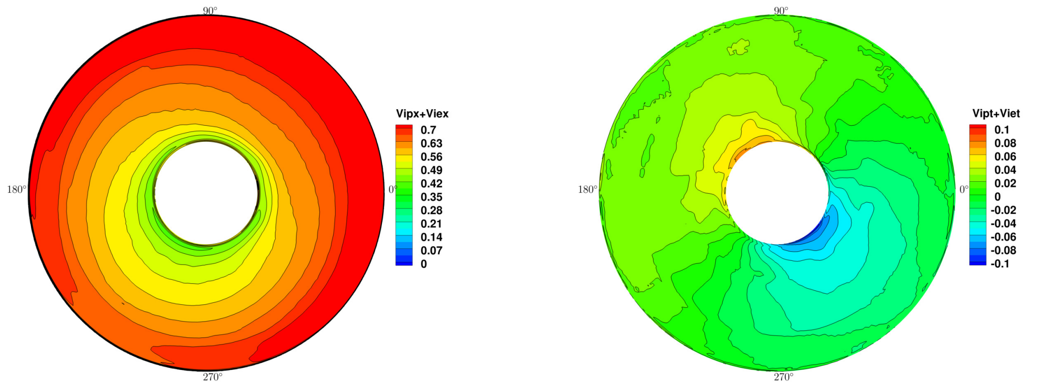

(a) Superposition of propeller axial induction and extra axial induction.

(b) Superposition of propeller tangential induction and extra tangential induction.

Figure 4.16: Axial and tangential propeller induction for the Grunwald ducted propeller at $AoA = 20°$.

the propeller disk. The induction distributions were also altered compared to the open propeller at cross-wind. The unbalanced tangential velocities owing to the cross-wind were eased by the duct and the propeller/duct integration. It can be concluded that the propeller inside the duct showed less unbalanced loading at cross-wind due to the shielding of the duct.

4.5 Aeroacoustics in Axial Flight

For future rotorcraft, the noise restriction can be especially stringent, as they tend to serve in urban areas as air ambulances or taxis. It is hence of interest to investigate the acoustic performance of the ducted and open propellers as propulsors. This section outlines the near- and far-field acoustics of the ducted/un-ducted propellers at the advance ratio of $\mu = 0.191$ based on the high-fidelity CFD results, while the two configurations produce similar amounts of aerodynamic loads. The near-field acoustics was calculated by directly extracting the acoustic pressure field from the CFD results, hence both surface and volume acoustic sources, including any resolved broadband components were considered. The far-field acoustics was calculated using the Farassat Formulation 1A as detailed in Chapter 2, which takes the CFD results of surface pressure fields as input. This approach considers only surface terms by the thickness and loading components, but it is suitable for the current study in the far-field in the sub-sonic region and has been widely adopted in previous studies of open and ducted rotor acoustics [130, 131, 129].

4.5.1 Near-field Acoustic Patterns

The near-field acoustics is of interest as it strongly affects cabin noise. It is also the source of far-field noise. In the present work, the near-field acoustics in close proximity to the ducted and un-ducted propellers was directly extracted from high-fidelity CFD simulations. Pressure signals at microphone points were recorded, and the mean values were subtracted to obtain the acoustic pressures. Sound Pressure Levels (SPL) were then derived and analysed.

To ensure the necessary resolution for acoustic waves, the grids used for the simulations were carefully generated to ensure at least 10 points for the wave length at the 4^{th} blade passing frequency. The 3^{rd}-order MUSCL scheme was adopted to provide high-order spatial accuracy. The temporal resolution was guaranteed by strong convergence in the Rotating Reference Frame (RRF).

A first analysis was made on the $Azimuth = 0°$ slice at $\mu = 0.191$. The sound pressure fields of the ducted/un-ducted were extracted directly and the instantaneous sound pressure contours on the $azimuth = 0°$ planes are shown in Figures 4.17(a) and 4.17(b). The acoustics generation and propagation are illustrated clearly, including components by the tip vortices and aerodynamic interactions. It can be seen that the ducted propeller tip vortices contributed a minor part to the overall acoustics and lasts for only about 3 blade radii, while the open propeller tip vortices caused strong pressure fluctuations and extended to about 6 blade radii downstream. The open propeller saw generally higher pressure fluctuations. Patterns of the acoustic propagation are also different due to the duct presence. It can be seen in Figure 4.17(a) that the duct blocks the propeller acoustics, and most noise emits from the inlet lip.

To further quantify the acoustic strength, the Sound Pressure Level (SPL) contours were calculated and are shown in Figures 4.18(a) and 4.18(b), respectively for the ducted and un-ducted propellers. It is clearly shown that the duct blocks the acoustics generated by the propeller, pre-

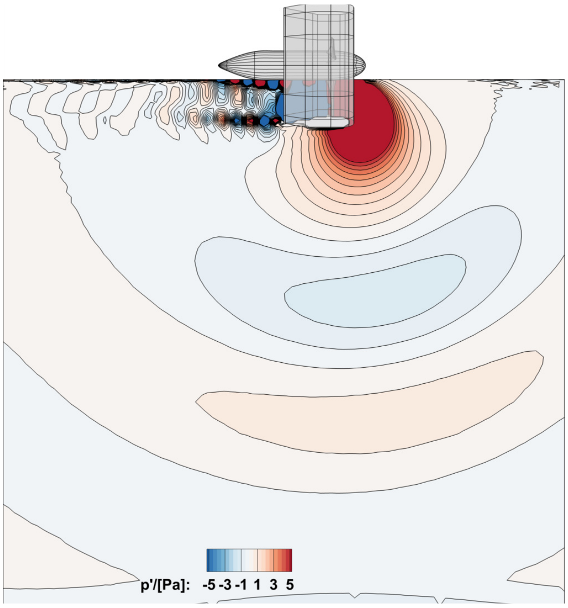

(a) Instantaneous sound pressure contours of the ducted propeller on the $Azimuth = 0°$ plane at $\mu = 0.191$.

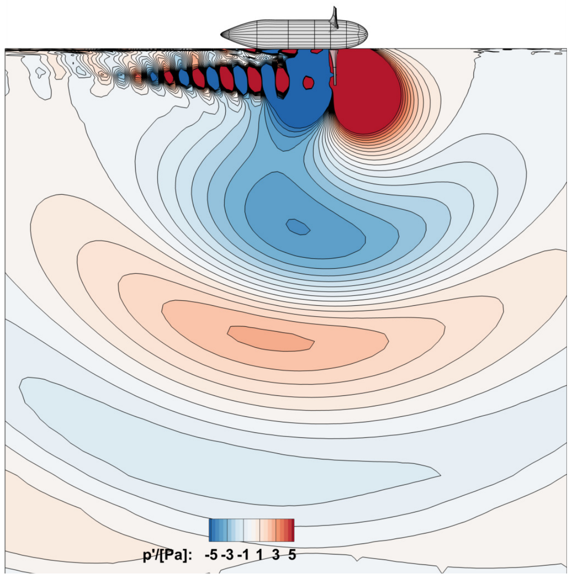

(b) Instantaneous sound pressure contours of the unducted propeller on the $Azimuth = 0°$ plane at $\mu = 0.191$.

Figure 4.17: Instantaneous sound pressure contours at the $azimuth = 0°$ slice for the ducted/unducted propellers at $\mu = 0.191$.

venting high sound pressure levels from propagating to the far-field. This is, however, under the assumption that the duct is rigid. Due to the duct shielding, the ducted propeller sound emission mostly comes from the duct inlet lip and diffuser exit. The wake downstream the duct also makes a small contribution. For the open propeller, the acoustic waves travel freely from the propeller disk to the far-field. The propeller wake is also making a large contribution in the near-field.

To further inspect the near-field acoustic directivity features, a spherical receiver array enclosing the propulsor was utilised, as shown in Figure 4.19(a). The receiver points were two duct chords away from the propeller centre of rotation.

The SPL contours on the spherical receiver surface are shown in Figures 4.20(a) and 4.20(b). The spherical surfaces are projected to planes for clarity. For both configurations, large areas of high SPL values are noticed near the propeller disk, while the peak values are noticed in small regions in the wake. For the ducted propeller, the major acoustics emissions are originating from above the propeller disk at about 100 dB. The peak SPL value is about 113 dB in the small wake region. For the open propeller, the most acoustics is emitted from the propeller disk plane at about

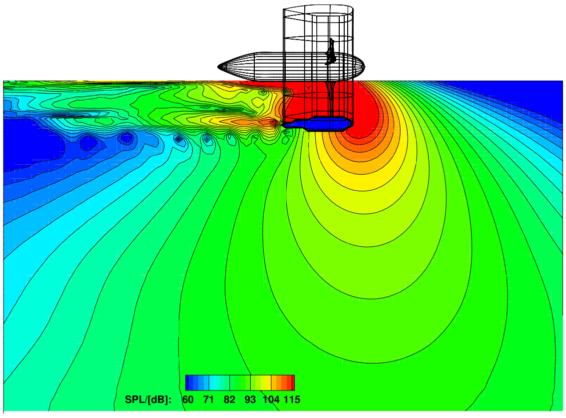

(a) Ducted propeller SPL contours on $Azimuth = 0°$ plane at $\mu = 0.191$.

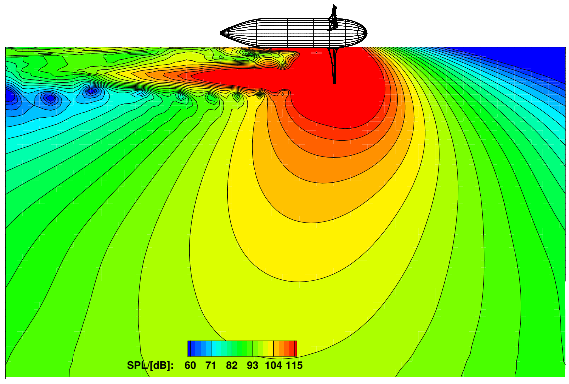

(b) Un-ducted propeller SPL contours on $Azimuth = 0°$ plane at $\mu = 0.191$.

Figure 4.18: Near-field Sound Pressure Level contours on $Azimuth = 0°$ at $\mu = 0.191$ for the ducted and un-ducted propellers.

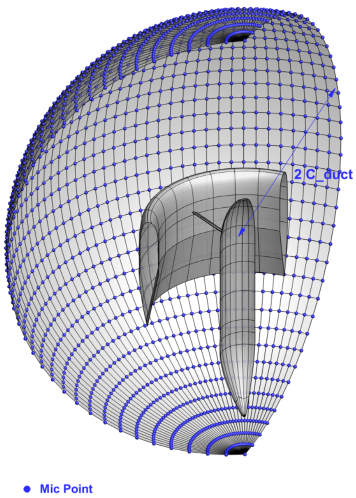

(a) Spherical microphone array enclosing the propulsor for near-field acoustic directivity investigations.

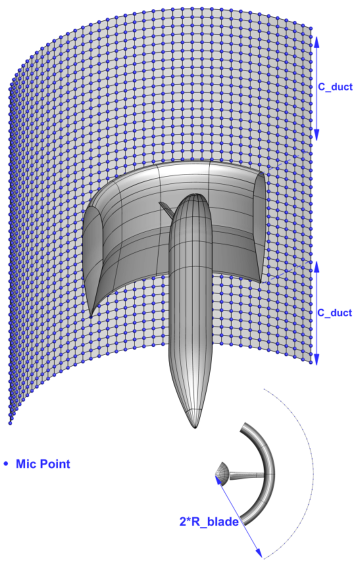

(b) Cylindrical microphone array around the propulsor for near-field acoustic investigation along the azimuthal direction.

Figure 4.19: Microphone arrays for near-field acoustic investigations of the ducted/un-ducted propellers.

110 dB. The peak SPL value of about 120 dB is located in the large wake region. These agree with the analysis in Figures 4.18(a) and 4.18(b) as the noise propagation is blocked by the duct and the acoustics mostly escapes from the inlet lip and diffuser exit. The ducted propeller wake is also shown, and has lower acoustic emissions compared to the open propeller, possibly due to the less

intrusive wake and weaker tip vortices as shown in previous sections.

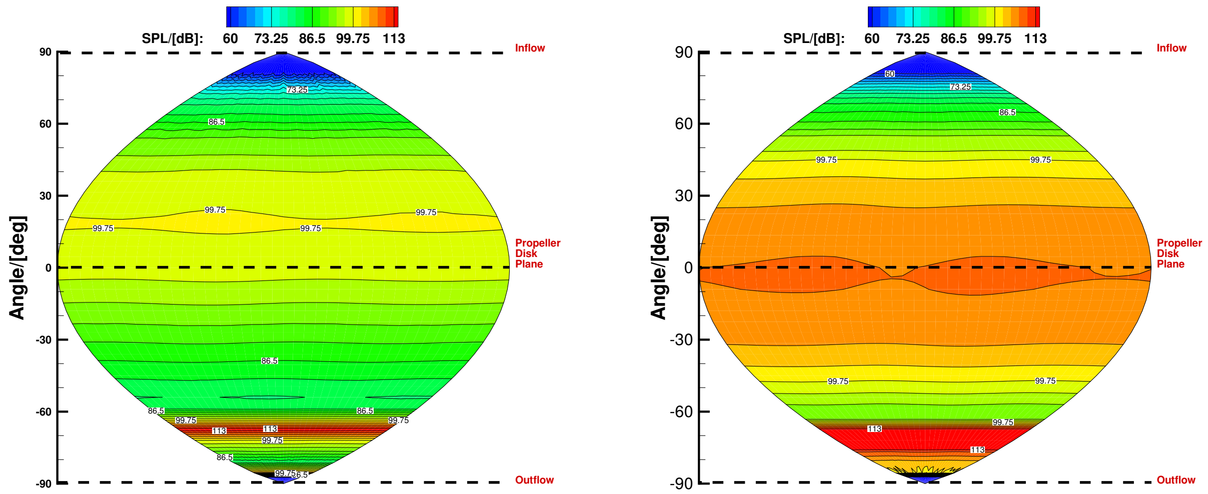

(a) Ducted propeller SPL contours (mapped to plane).

(b) Un-ducted propeller SPL contours (mapped to plane).

Figure 4.20: Near-field SPL contours on the receiver surface in Figure 4.19(a) at $\mu = 0.191$ for the ducted and un-ducted propellers. The spherical surfaces are projected to planes for better clarity.

Acoustic data in the azimuthal direction was also extracted on the surface shown in Figure 4.19(b) in order to briefly investigate the cabinet noise. The receiver surface is twice the blade radius away from the centre of rotation surrounding the propulsor, a scenario where typically the cabin noise is perceived. The corresponding SPL results are shown in Figures 4.21(a) and Figure 4.21(b). For the ducted propeller, the peak SPL stands at about 105 dB in a small region near the duct inlet. For the open propeller, the peak value stands at about 115 dB in a larger region near the propeller disk. This shows again the duct shielding effects in the near-field.

Overall, the ducted propeller produces lower SPL levels than the un-ducted configuration by about 10 dB in the near-field for the case studied. The near-field acoustic directivity features are also altered. Due to the blockage effect of the duct, the acoustic peaks are redirected to directions of the duct inlet and exit. Again, rigid duct and blades were assumed.

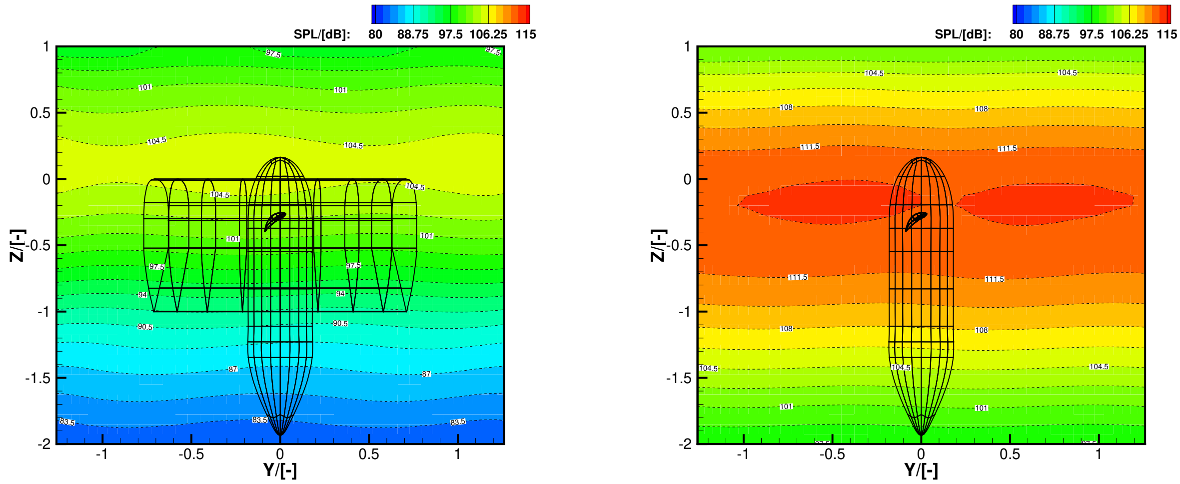

(a) Near-field SPL contours of the ducted propeller on the surface in Figure 4.19(b) at $\mu = 0.191$.

(b) Near-field SPL contours of the un-ducted propeller on the surface in Figure 4.19(b) at $\mu = 0.191$.

Figure 4.21: Near-field Sound Pressure Level contours on the receiver surface in Figure 4.19(b) at $\mu = 0.191$ for the ducted and un-ducted propellers.

4.5.2 Far-field Acoustic Patterns

The far-field acoustics of the ducted/un-ducted propellers was analysed using an in-house acoustic code based on the classic FW-H equation solved with Farassat Formulation 1A. The CFD solutions of the surface pressure fields were used as input for the acoustic tool. The centre-body was not included in the far-field acoustic calculation, as its contribution is regarded as minor due to the low loading.

As stated earlier, the current implementation of the far-field acoustic prediction is an extension of the existing acoustic code HFWH[130] in the high-level programming language Julia. Extensive code-to-code comparisons have been performed to verify the current implementation. Nonetheless, to further validate the current acoustic tool, a ducted propeller acoustic test case by Hubbard [14] was adapted. The experiments measured the acoustics of different propeller/duct combinations in hover. Although the model size was large (4-foot-diameter blades), the acoustic tests were performed outdoors, and this may have affected the results. The acoustic directivity was measured 30 ft away from the centre of rotation, all around the propulsor, and on the ground. The tests provided no loading measurements other than the duct thrust through sectional pressure integrations, hence the case is not ideal for aerodynamic or acoustic validation as large uncertainties must be expected. Regardless, this case is the most suitable among the very few experimental studies concerning acoustics of large ducted propellers.

Comparisons between numerical and experimental results of the ducted propeller acoustic directivity for the Hubbard case [14] are presented in Figure 4.22. Note that the experiments measured the acoustics at ground level, while ground effects were not considered in the CFD simulation or the acoustic calculation. Despite these uncertainties and shortcomings, the agreement between the numerical prediction and the test data is still favourable, with SPL values of about 90 to 95 dB at this distance. This strengthens the confidence of the present acoustic tool and strategy for the noise prediction of ducted propellers.

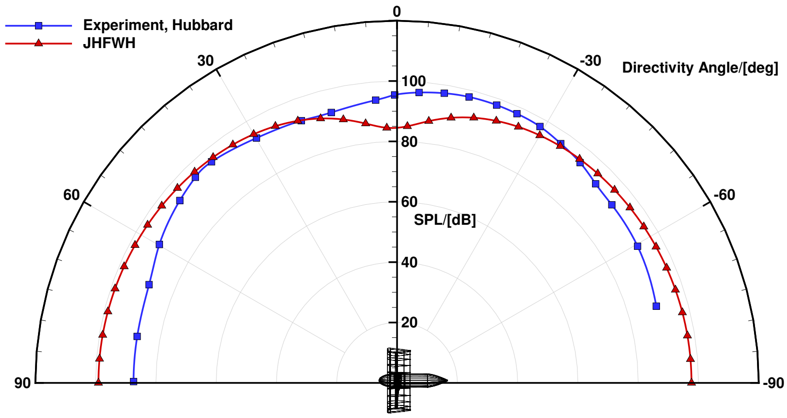

Figure 4.22: Comparisons between numerical and experimental results of the ducted propeller acoustic directivity 30 ft away for the ducted propeller of Hubbard [14].

Acoustic calculations of the ducted/un-ducted propellers of Grunwald [18] were later conducted using 400 evenly-distributed microphones on a full sphere enclosing the propulsor, 20 duct chords away from the centre of rotation, to investigate the far-field acoustic directivity. The results are shown in Figure 4.23. For both configurations, the acoustics varies little along the propeller azimuth, hence detailed comparisons of the directivity features are made on the azimuth station of 0°. Also, for both configurations the loading components contribute the most to the total noise.

As shown in Figure 4.23, the un-ducted propeller produces almost evenly distributed acoustics in all directions around 80 dB, with a small increase to about 85 dB between $-40°$ to $30°$ directivity angles. This is consistent with its near-field acoustic features that the peak noise is around and slightly aft the propeller disk (0° directivity angle). As for the ducted propeller, its noise around -90° and 90° is almost the same at about 80 dB. However, in the range between -70° and 60°, the acoustic level was clearly lower than the un-ducted counterpart by up to 15 dB. The lowest acoustic level is perceived at -30° at about 65 dB, while a local maximum is noted at around 15° at about 75 dB. These features are also consistent with the near-field acoustic patterns of the ducted propeller that the acoustics is blocked by the duct.

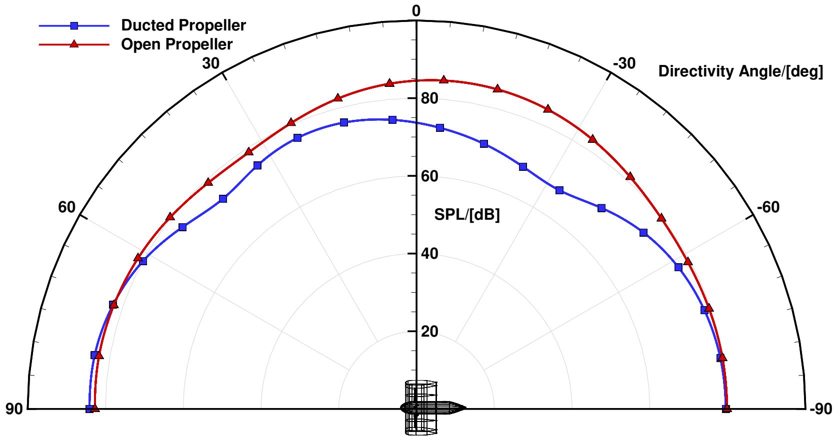

Figure 4.23: Total noise SPL directivity of the ducted/un-ducted propellers noise signals at 20 duct chord away (90° is the inflow direction).

Investigations were also made on the acoustic projection on a plane below the propulsor, while the propulsors are in level flight. This approximates the acoustics projected on the ground while the aircraft flies over. The microphone array used is illustrated in Figure 4.24. The propulsors were placed $20C$ above the centre of the array, where C is the duct chord length. Note the microphones were assumed translating with the propulsors in level flight with a constant speed of $30.48 m/s$. Acoustic signals perceived at fixed ground microphones are to be discussed later.

The calculated SPL contours for the ducted/un-ducted propellers on the microphone array in Figures 4.24 are presented in Figures 4.25(a) and 4.25(b). For the ducted propeller in Figure 4.25(a), the peak values are around 73 dB and are seen slightly ahead the propeller disk below the ducted propeller. High SPL values tend to spread in 4 directions ahead and after the ducted propeller. For the un-ducted configuration, The peak values are about 10 dB higher at about 83 dB, and are seen slightly below the propeller disk. High SPL values tend to spread simply to

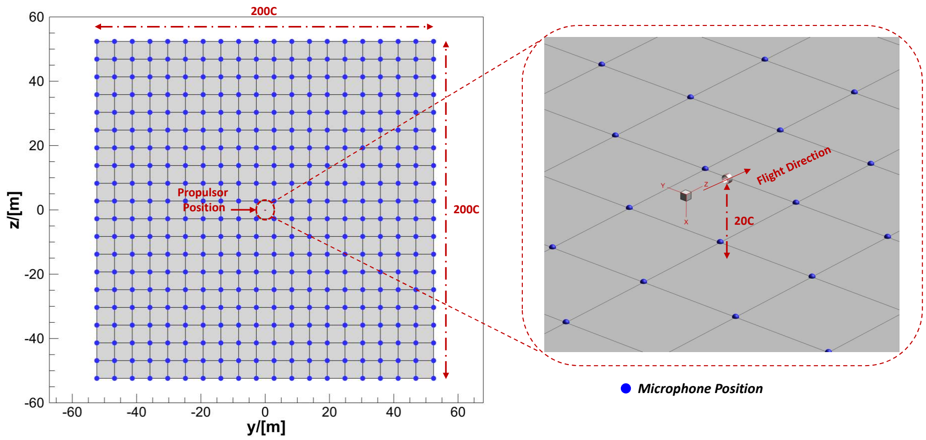

Figure 4.24: Microphone positions for the ground acoustic projection study. In total 400 microphone points were used (the blue dots) on a 200C by 200C region, where C is the duct chord. The propulsors were placed 20C above the plane. The microphones were assumed translating with the propulsors.

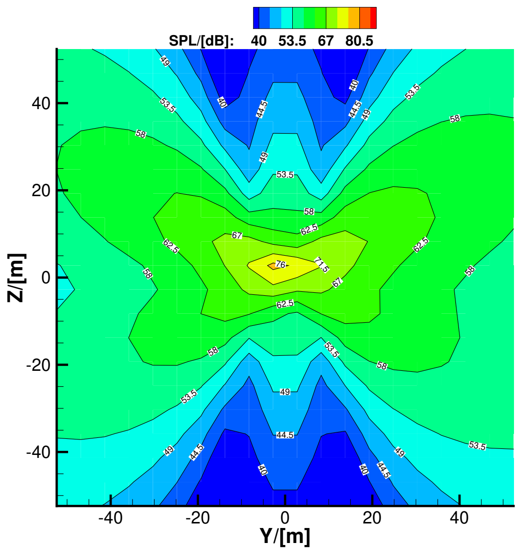

(a) Ducted propeller SPL map on $X = 5.24m$ plane at $\mu = 0.191$.

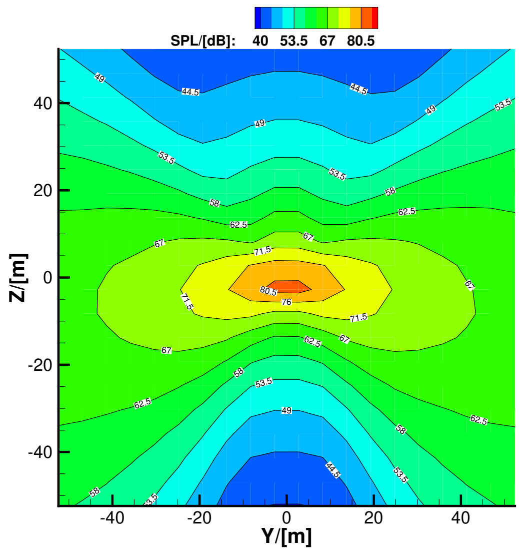

(b) Un-ducted propeller SPL map on $X = 5.24m$ plane at $\mu = 0.191$.

Figure 4.25: Ground SPL contours for the ducted and un-ducted propellers.

the port and star sides slightly after the open propeller. This agrees well with the previous acoustic directivity study, as the duct blocks the acoustic propagation and most acoustic signals are emitting from the duct inlet and exit. For both configurations, low acoustics regions are noted far ahead and behind the propulsor especially under the flight path. This suggests that the strong noise directed in the axial direction projects less on the ground. In general, the ducted configuration shows a lower acoustic level on this plane by about 5 to 10 dB comparing to the un-ducted counterpart, showing the benefits of the duct acoustic shielding.

4.5.3 Fly-by Acoustic Signals

The fly-by noise, i.e. the noise signals recorded by ground-fixed microphones while the propulsor or aircraft is flying over, was also calculated. This scenario is illustrated in Figure 4.26. This is often encountered in certification tests. The noise calculations employed the same FW-H equation and Farassat 1A formulation, with changes of relative positions between acoustic panels and receiver points accounted for. The acoustic signals for the Grunwald ducted/un-ducted propellers were calculated while flying over fixed microphones 10 and 20 duct chords below. The propulsors started from [0, 0, 0] (in m) and was translating in Z direction with a constant speed of $30.48m/s$. The microphones were fixed at [2.619, 0, 10] (in m) and [5.238, 0, 10] (in m), corresponding to 10 and 20 duct chords below the propulsors. The propeller disk was right above the receiver points about $0.328s$ after starting.

The acoustic signals for both configurations are presented in Figures 4.27(a) and 4.28(a). The vertical lines in the figures denote the moment when the propeller disk was right above the microphones, i.e. the propeller disk passage time. As can be noted in Figure 4.27(a) at 10 duct chords, the two configurations produce acoustic signals of similar shapes. However, the ducted signal has only a quarter or half the magnitude of the un-ducted. At 20 duct chords away as shown in Figure 4.28(a), these features still hold except that the signal magnitudes are further reduced.

To further verify the acoustic strength, the moving root-mean-square (RMS) values of the acoustic signals were calculated and are presented in Figures 4.27(b) and 4.28(b). The moving RMS values were calculated using signals within a time window of one propeller revolution, i.e. 0.0075s. It can be seen in Figure 4.27(b), for the un-ducted configuration, the averaged peak is slightly after the propeller passage. This agrees with the previous near- and far-field acoustic directivity analysis for the un-ducted propeller that noise peaks are seen at and slightly after the propeller disk. For the ducted propeller, however, 2 acoustic peaks can be noticed. The first peak is

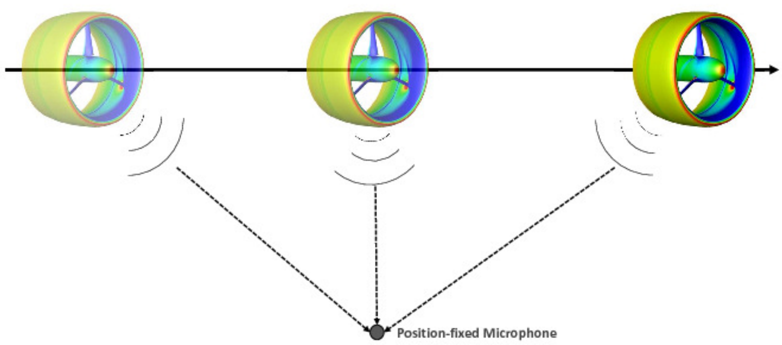

Figure 4.26: Illustration of the microphone position and the propulsor motions for the fly-by noise calculation. The microphone was fixed while the propulsors were translating in the arrow direction.

only slightly higher than the second. The first peak is perceived before the propeller disk passage and before the first open propeller peak. A low noise area is noted near the blade passage. Later, the weaker second peak is perceived. At 20 duct chords away as shown in Figure 4.28(b), the features are very similar but have lower strength and fluctuations. The ducted features remain very similar at this position with the low noise region noted during the blade passage. This agrees well with the previous near- and far-field acoustic directivity investigations for the ducted propeller. The duct blocks the acoustic propagation directly from the propeller disk and redirects the acoustics towards the inlet and outlet. In general, the peak acoustic strength of the ducted configuration is only a quarter or half the magnitude of the un-ducted. In addition, a low noise area is generated during the propeller passage by the ducted propeller. This feature can be further used in flight path optimisation to minimise the acoustic perception at specific locations where noise restrictions apply.

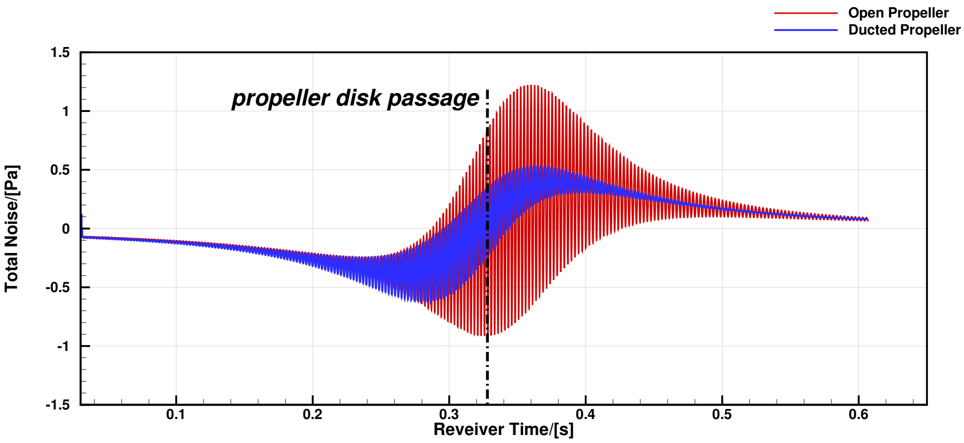

(a) Acoustic signals recorded at the receiver point 10 duct chords below (Figure 4.26) for the ducted/un-ducted propellers.

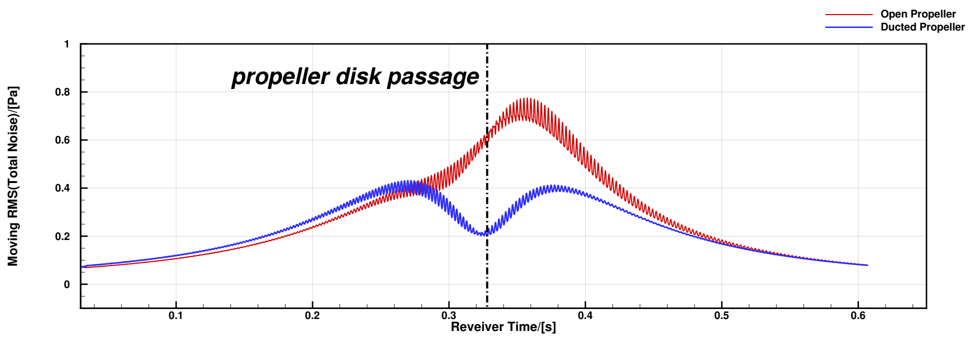

(b) Moving root-mean-square (RMS) values (calculated using a time window of one blade rotation 0.0075s at each time point) of the acoustic signals recorded at the receiver point 10 duct chords below (Figure 4.26) for the ducted/un-ducted propellers.

Figure 4.27: Fly-by noise calculations at fixed receiver points 10 duct chords below as in Figure 4.26. The dash-dot line denotes the time point when the propeller disk was right above the receiver point.

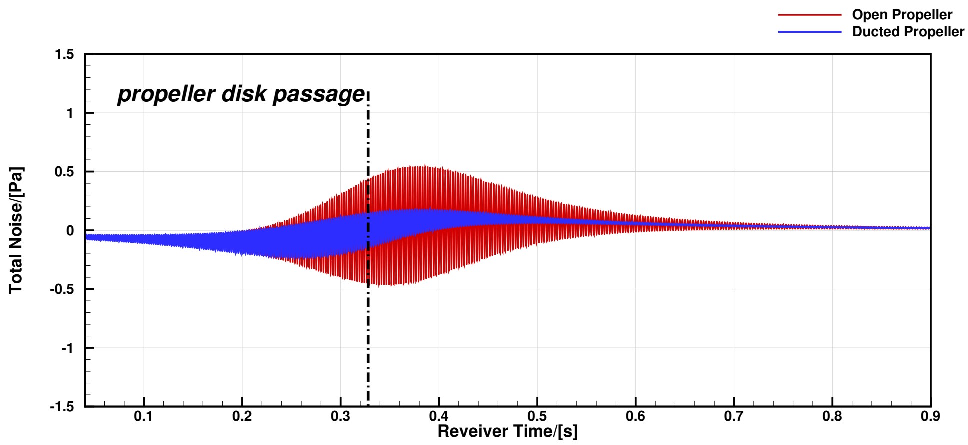

(a) Acoustic signals recorded at the receiver point 20 duct chords below (Figure 4.26) for the ducted/un-ducted propellers.

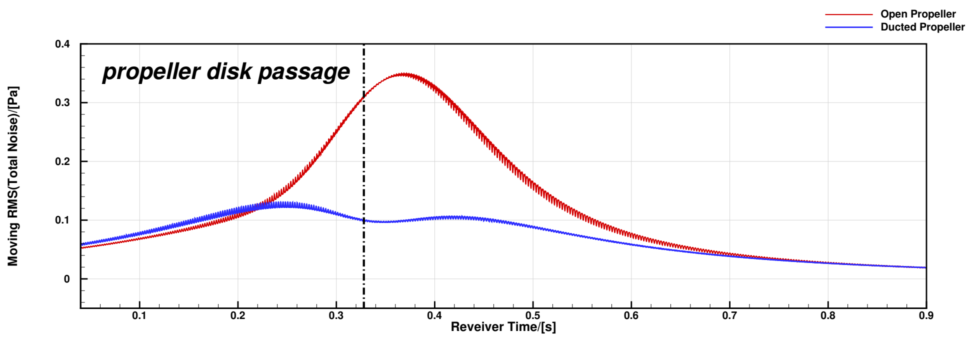

(b) Moving root-mean-square (RMS) values (calculated using a time window of one blade rotation 0.0075s at each time point) of the acoustic signals recorded at the receiver point 20 duct chords below (Figure 4.26) for the ducted/un-ducted propellers.

Figure 4.28: Fly-by noise calculations at fixed receiver points 20 duct chords below as in Figure 4.26. The dash-dot line denotes the time point when the propeller disk was right above the receiver point.

4.6 Chapter Summary

This chapter presented the analyses and comparisons of aerodynamic and acoustic performance of the ducted/open propeller configurations at various conditions. The investigations of the aerodynamic performance can be summarised as follows:

1. The ducted propeller showed superior aerodynamic performance over the open propeller counterpart in hover or at low advance ratios. For the case studied, the ducted configuration produced more thrust than its un-ducted counterpart up until about $\mu = 0.2$, at the same blade pitch and RPM. At low advance ratios, the duct contributed to the extra thrust at no torque cost. Particularly, in hover, the ducted propeller generated twice as much thrust with the duct carrying about 50% of the total thrust. The Froude efficiency of the ducted configuration was higher by about 0.1 below $\mu = 0.2$. However, at high advance ratios, the ducted propeller quickly became less efficient than the open propeller. As the advance ratio increased, the duct thrust dropped quickly and eventually turned to drag.

2. Velocity and pressure fields of the ducted/un-ducted propellers in axial flight were investigated using high-fidelity CFD results. In axial flight, at least 25% higher mass and momentum flow rates due to the duct induction were noticed at lower advance ratios less than 0.2. The wake survey suggested that the ducted propeller produced less intrusive wakes while producing more thrust at low advance ratios, due to the diffuser expansion. Through the azimuthally-averaged surface pressure study, the performance gain was specified as from the duct leading-edge suction and the recovered pressures at the diffuser. The propeller inside the duct saw a higher baseline axial velocity due to the induction of the duct and was therefore off-loaded. However, the benefits diminished with increasing advancing ratios. A high-pressure region at the duct leading edge was found growing with increasing flight speeds, thereby reducing the duct propulsion. Nevertheless, the duct thrust and the ducted benefits were found recovering while increasing the blade pitch, which resulted in higher propeller suction.

3. The pitch variation study at $\mu = 0.191$ suggests that the thrust capacity of the ducted propeller studied is much higher (more than twice) than the open propeller at the same RPM. And for the same amount of thrust required, the ducted propeller requires less power input at higher pitch angles (at least 10%). This holds for the higher advance ratio of $\mu = 0.382$ beyond a higher pitch increase (by about $+14°$). It can be concluded that for the ducted propeller the duct thrust is affected by the propeller suction, while the propeller performance is determined by the duct induction which determines the inflow condition. These are further subject to conditions such as advance ratios, blade pitch, RPM, duct shapes etc. It is also noticed that the ducted propeller performance is more sensitive to pitch changes.

4. High-fidelity CFD simulations of the empty duct and the ducted propeller case at crosswind were also performed and analysed. The empty duct lift responded linearly to the increasing AoA before stall at around $AoA = 23°$. The stalled flows were predicted by the HMB3 SAS formulations with favourable agreements. The duct stall was delayed when the propeller was installed. Also, at $AoA = 20°$, the duct lift was found significantly augmented (twice as much), while still producing considerable thrust. This suggests that the ducted propeller can also be utilised for lift generation in aircraft applications. However, if installed under a main rotor, and working under downwash, the duct lift could be translated into a large blockage. The duct also produced a large nose-up pitching moment due to the non-axial velocities. At crosswind, the ducted blades were also offloaded and suffered lower levels of thrust variations compared to the open propeller.

5. Disk loadings, flow interactions, and induction features of ducted propellers were also investigated, and the duct shielding at cross-wind was analysed in detail. The ducting offloaded the propeller disk and altered the disk loading distributions. For the ducted configuration, higher loadings moved towards the blade tip near the duct surface. The disk loading was also less unbalanced at crosswind comparing to the open propeller. Induced velocities were decomposed to identify contributions from each component and to study their interactions. The duct-induced inflow increased the overall axial inflow velocities but

reduced the unbalanced flow conditions at the advancing and retreating sides. A large extra induction due to the mutual interaction of the duct/propeller was also identified. This induction represented a large part of the entire induction and further eased the unbalanced inflow in axial and tangential directions. Overall, the duct accelerated and regulated the propeller inflow at crosswind. The ducted blades hence suffered less from thrust variations due to non-axial inflows.

Investigations of the aeroacoustics of ducted and open configurations in axial flight were also presented in Chapter 4 and can be summarised as follows:

1. The near-field acoustics of the ducted/open propellers was directly extracted from the high-fidelity CFD simulations. The near-field acoustic propagation was visualised and the duct blockage was clearly illustrated. Comparing to the open propeller, the averaged acoustic strength of the ducted configuration was reduced by about 10 dB in the near-field, while the two configurations were producing a similar amount of aerodynamic loads. For the open propeller, the acoustics mostly originated from the propeller disk and the propeller wake. For the ducted propeller, the noise emission mostly radiated from the duct's inlet lip.

2. The far-field acoustics of the ducted/open propellers was also computed following the FW-H equations using the CFD solutions as input. The far-field acoustic features agreed well with the near-field results. In the far-field, the open propeller noise was around 80 dB in all directions. The ducted propeller showed similar acoustic levels in the axial directions up- and downstream. However, in the large directivity angle range between -70° and 60°, the ducted configuration showed a noise reduction by about 5 to 10 dB due to the duct shielding.

3. Acoustic signals recorded at ground-fixed microphones while the two configurations were flying over was also computed. As the open propeller was approaching the microphone, its noise level increased and reached the peak slightly after the propeller passage. The acoustic level decreased gradually as it was flying away. For the ducted configuration,

it produced slightly higher acoustics while approaching the microphone. As the ducted propeller further approached the microphone, its acoustic strength first reached a local peak and then decreased to a local minimal near the propeller blade passage. With the ducted propeller moving away, its acoustic level first recovered to reach a second peak and then slowly decayed to the similar level to the open propeller. This feature due to the duct shielding may be exploited in flight path optimisation to minimises community annoyance.

A further parametric study of the equivalent ducted/open propellers was also conducted in Appendix A. The next chapter will focus on aerodynamic shape optimisation to improve the ducted propeller performance at high advance ratios.

Chapter 5

Adjoint-based Design Optimisation for Ducted/Open Propellers [1]

As presented in the previous section, at $\mu = 0.191$ (with $RPM = 8000$ and $\beta_{0.75} = 29.58°$), the ducted/un-ducted configurations of Grunwald [18] show similar aerodynamic performance at this operating condition, with the ducted propeller producing slightly higher thrust at lower torque. This advance ratio typically corresponds to the speed of a tilt-duct VTOL aircraft about to exit transition and enter level flight[18]. Higher propulsor performance capacity is important for safer transition. Performance investigations presented in the previous chapter show that this test condition is very close to the critical advance ratio, with the same rotating rate and pitch setting, beyond which the ducted propeller becomes less efficient than its un-ducted counterpart due to the increasing duct drag. Optimisation at this operating point is hence necessary for improved ducted propeller performance capacity. Meanwhile, it is also of interest to investigate how the duct shape changes would affect the overall performance.

In this chapter, a gradient-based optimisation framework is compiled to improve the ducted propeller performance at $\mu = 0.191$ altering the duct and blade shapes. The key results and novelties are a novel parametrisation method for the duct shape allowing leading- and trailing-edge

[1] This chapter has been published in Zhang, T. and Barakos, G.N., "High-fidelity numerical analysis and optimisation of ducted propeller aerodynamics and acoustics," Aerospace Science and Technology, Vol. 113, 2021, p.106708.

offsets, a systematic comparison of optimisation results involving different geometric variables, as well as, a detailed analysis of flow and acoustic changes brought by the shape optimisation. The gradients of the aerodynamic performance were computed through the adjoint approach and passed to the optimisation framework to drive design changes. The acoustics is not involved directly in the optimisation objectives/constraints, as the aerodynamic performance is the primary concern. Nonetheless, the acoustics of the optimised designs was later examined and for this case it was found to be good.

5.1 Parametrisation and Optimisation Formulation

Prior to design optimisation, it is important to represent specific designs with a set of design variables and to define the design space of exploration. It is also important to state clearly the optimisation objectives and constraints to drive the design changes. This section presents the parametrisation methods for the duct and blade shapes. Also presented are the formulation of the optimisation problem to be solved and the test matrix of the optimisation study.

5.1.1 Duct Shape Parametrisation

As presented in the previous chapter, for an axisymmetric ducted propeller, the thrust augmentation mostly comes from the combination of the leading-edge suction and recovered pressures at the diffuser exit. The mid-chord part of the duct usually has a relatively modest thrust contribution and is often composed by straight lines in real-world designs [18] [19]. The mid-chord was hence fixed in the current optimisation work to exclude varying blade tip gaps and duct thickness. This is also due to the consideration that the duct thickness is often constrained by the structure or volume in practice. In this light, the parametrisation and deformation of duct shapes in this work take into account the duct leading-edge and trailing-edge shapes, as presented in Figure 5.1. Nevertheless, the deforming curve region can be extended to include most of the middle chord.

The proposed parametrisation allows a comprehensive set of variations of the duct chord

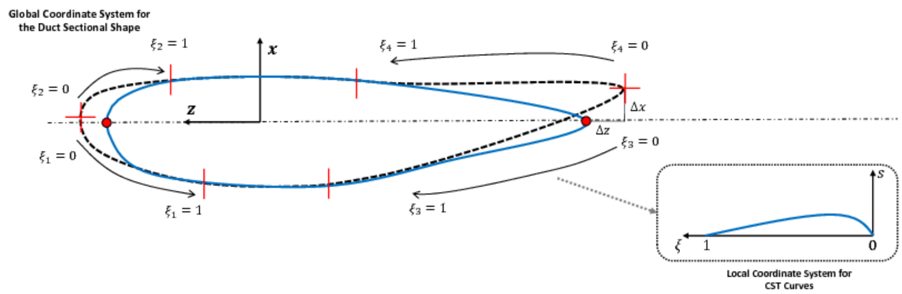

Figure 5.1: Illustration of duct shape parametrisation and deformation.

length, camber, inlet lip radius, and inlet/outlet expansion ratios, i.e. most geometric parameters governing the ducted propeller performance. The design variables are the parameters governing the curve shape, as well as, offsets of the leading/trailing edge points relative to their original positions. Compared to other popular parametrisation methods such as Free-Form Deformation (FFD), the proposed parametrisation approach is strongly physics-based and focuses on a narrower but more relevant design space.

This duct shape parametrisation problem can be simplified using 4 curved segments, i.e. the inner leading edge, the outer leading edge, the inner trailing edge, and the outer trailing edge. The curves are locally represented using the classic CST (Class Shape Transformation) method[141] which is often used in aerofoil parametrisation. The local coordinate system for CST parametrisation is illustrated in Figure 5.1.

This system is used for the CST representation of curve shapes. The horizontal axis ξ denotes the chord-wise direction, with $\xi = 0$ at the starting point(leading edge) and $\xi = 1$ at the ending point(sharp trailing edge). The vertical axis s is norm to chord. s can be written as a function of ξ if using classic CST representations

$$s = CST(\xi, \alpha_{\mathbf{i}}), \tag{5.1}$$

where $CST(\xi, \alpha_{\mathbf{i}})$ is a generalised CST function subject to a set of coefficients $\alpha_{\mathbf{i}}$. This coefficient array is recognised as part of the design variables. Specifically, the Bernstein basis functions were used in the current study. To enforce a rounded shape at the starting point, the $N1$ value is set as

0.5 with $N2 = 1$.

The CST curves are later mapped back to the original global system using coordinates of curve starting and ending points. The mapping is performed linearly using the equations below

$$z = (1-\xi)(z_0 + \Delta z) + \xi z_1, \tag{5.2}$$

$$x = s(\xi, \alpha_{\mathbf{i}}) + (1-\xi)(x_0 + \Delta x) + \xi x_1, \tag{5.3}$$

where (x_0, z_0) and (x_1, z_1) are global coordinates of the starting and ending points, respectively. Δx and Δz are the offset of the starting point, which were taken as design variables. This mapping method is universal for both duct leading edge and trailing edge curve segments.

5.1.2 Blade Twist Parametrisation

For a ducted propeller, typically, the blades face higher inflow velocities due to duct induction. It is therefore of interest to include the blade pitch/twist variations in the optimisation while changing the duct shape. The current parametrisation of the blade twist is based on polynomial approximations of pitch distributions along the radial direction. The twist distribution is represented by

$$\beta(r_0) = \sum_{i=1}^{N} \alpha_i f_i r_0, \tag{5.4}$$

where $r_0 = r/R$ is the non-dimensional radius, f_i is the basis function (in the current case Bernstein polynomials were used), α_i are coefficients recognised as design variables, and N is the number of coefficients. Note that the proposed parametrisation describes the attack angle distribution of local blade elements along the radial direction, and therefore includes variations of the blade pitch. Through this parametrisation, the optimisation framework will deliver the optimal distribution of local pitch angles subject to specific objectives.

5.1.3 Optimisation Problem Formulation and Test Matrix

The objective was set to increase the thrust subject to torque constraints. The overall efficiency of the propulsor was not constrained, since it is more important to expand the performance capacity at this operating condition for the safer transition from hover to forward flight for a typical tilt-duct aircraft[18]. Besides, such objective and constraint settings were expected to deliver larger changes in the geometry and flow-field, which is beneficial for the study of how duct/blade shape changes affect the overall performance. This will provide more guidance on ducted propeller designs and will pave the way for future investigations of variable-geometry ducts for propulsor performance control, which combined with the classic pitch control approach is expected to greatly extend the performance space of ducted propellers. The current optimised designs were also examined at different pitch settings compared with the pitch variation study of the initial ducted/un-ducted propellers. The optimisation problem is formulated as follows

$$
\begin{aligned}
Find:& \\
& max(T(\alpha, \mathbf{W})), \\
\text{by varying:}& \\
& \alpha_{i,min} \leq \alpha_i \leq \alpha_{i,max}, i \in 1, ..., n, \\
\text{subject to:}& \\
& Q(\alpha, \mathbf{W}) \leq Q_{feasible},
\end{aligned}
\tag{5.5}
$$

where T and Q are the total thrust and torque, respectively. $Q_{feasible}$ is a feasible torque constraint that cannot be exceeded, imitating redundant engine power. α is the design variable vector involving both the duct and blade shapes. $\mathbf{W}$ is the conservative flow variable.

The test matrix of the optimisation study is presented in Table 5.1. The optimisation was first performed on the duct inlet/outlet shapes with the blade twist fixed using 16 design variables, and then on the blade twist with the duct shape fixed, using 4 design variables. Optimisation studies were afterwards carried out with the duct outlet shape and the blade twist allowed to change at the same time using 12 design variables. The coupled optimisation is expected to provide a larger performance improvement.

The optimisation calculations were performed on coarse grids of about 4 million cells for lower computational costs. The optimisation results were later verified using finer grids to reduce uncertainties, and minor differences were noted in the aerodynamic loads. Each optimisation case converged after about 10 to 15 iterations. Each optimisation iteration involved a CFD calculation of the flow-field and occasionally the sensitivity calculation, carried out using adjoint methods. The adjoint calculation was of the similar cost to the flow calculation, but whether the calculation was conducted at each iteration was decided by the SLSQP optimiser. The initial baseline flow calculation took about 6 hours using 32 CPUs, while successive CFD calculations in each iteration took only 1 hour restarting from previous solutions. Considering the amount of design variables involved and compared to meta-model-based optimisation, the current adjoint-based optimisation implementation has saved the time and resources for extra hundreds of CFD simulations.

Table 5.1: Test matrix for the adjoint-based ducted propeller optimisation.

Case	Design Variables	Configuration	Objective	Constraints	Advance Ratio	RPM	Blade Pitch ($\beta_{0.75}$)/[deg]
1	Duct Inlet/Outlet	Ducted Propeller		110% torque			29.58
2	Blade Twist(Pitch)	Ducted Propeller	Maximised Thrust	120% torque	0.191	8000	-
3	Duct Outlet & Blade Twist (Pitch)	Ducted Propeller		120% torque			-

5.2 Optimisation Results

Results of the optimisation cases of Table 5.1 are summarised in this section. The duct deformation through the duct shape optimisation and the coupled duct/blade optimisation, i.e. cases 1 and 3 of Table 5.1, are presented in Figure 5.2 along with the original design. The leading-edge and trailing-edge points were allowed to offset within a circle of $0.1C$ radius. The duct shape was allowed to deform except for the region between $x/C = 0.2$ to 0.53. Note the duct inlet shape was not involved in the coupled optimisation case (case 3). The blade pitch distributions of the blade twist optimisation (case 2) and the coupled optimisation (case 3) are shown in Figure 5.3 along with the original distribution. The performance changes relative to the original design are listed in Table 5.2.

The component and total thrust changes of the optimised designs are shown in Table 5.3. The thrust changes are denoted by the relative variations with respect to the original corresponding thrust, i.e. $\delta T = \frac{T_{opt}}{T_0} - 100\%$, where T_{opt} is the new component or total thrust through optimisation,

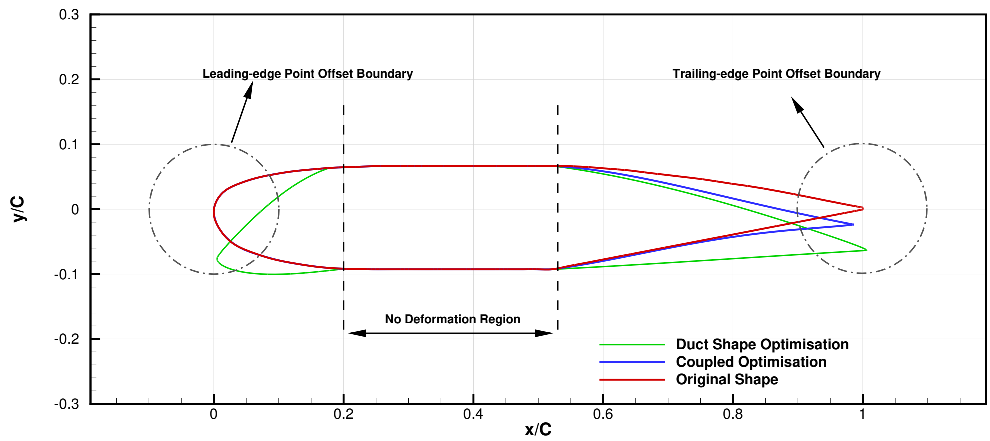

Figure 5.2: Illustration of the duct shape deformation through the duct shape optimisation and coupled duct exit and blade twist optimisation. Note only the duct exit was involved in the coupled optimisation.

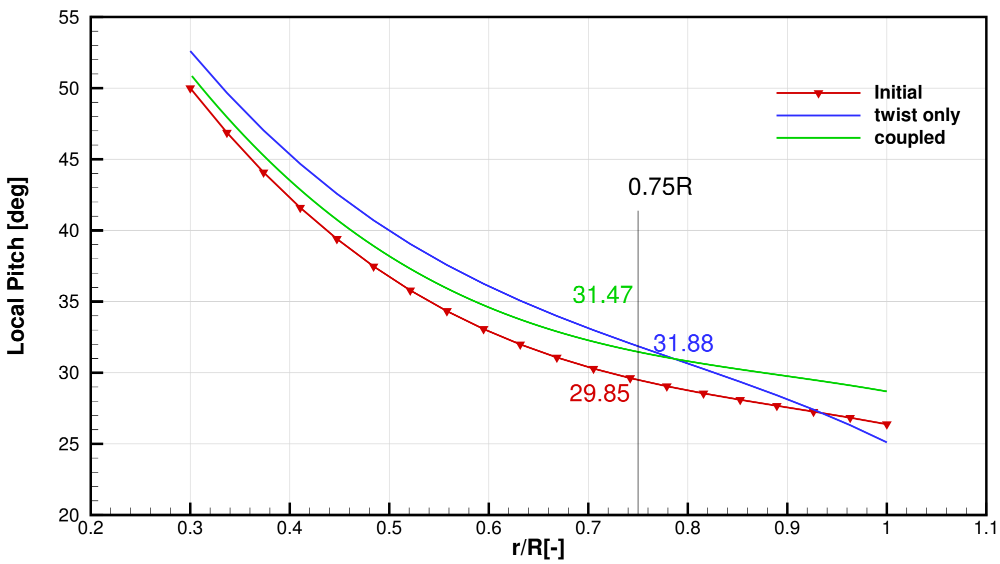

Figure 5.3: Illustration of the blade pitch distribution changes through the blade twist optimisation and coupled duct exit and blade twist optimisation.

and T_0 is the original component or total thrust. The component contributions are represented as the ratio of the component thrust to the total thrust, i.e. $\frac{T_{com}}{T_{total}} \times 100\%$, where T_{com} is the component thrust and T_{total} is the total thrust.

Table 5.2: Performance changes through optimising different components. The changes are denoted by variations with respect to the original corresponding values.

Case	Optimisation Component	Thrust Changes	Torque Changes	Efficiency Changes
1	Duct Shape	8.2%	10.0%	-1.6%
2	Blade Twist	11.6%	20.0%	-7.0%
3	Coupled Duct Shape &Blade Twist	18.3%	20.0%	-1.4%

Table 5.3: Thrust changes of the ducted propeller components through optimisation of the duct shape and blade twist.

Case	Optimisation Component	Propeller Thrust Change/[N]	δT/[%]	Contribution/[%]	Duct&Centre-body Thrust Change/[N]	δT/[%]	Contribution/[%]	Total Thrust Change/[N]	δT/[%]
1	Duct Shape	16.60	27.1%	84.7%	-10.41	-40.7%	15.3%	7.12	8.2%
2	Blade Twist	5.65	9.2%	70.6%	4.56	17.8%	29.4%	10.09	11.6%
3	Duct Shape & Blade Twist	12.62	20.6%	73.5%	3.21	12.5%	26.5%	15.94	18.3%

5.2.1 Duct Shape Optimisation (Case 1)

For the optimisation of the duct inlet and outlet shapes, 16 design variables were used in the current study, 4 for the leading-/trailing-edge point offsets and 12 for the leading-/trailing-edge shapes. The convergence history of the duct inlet/outlet shape optimisation is presented in Figure 5.4. As can be noted, the optimisation converged in about 14 loops subject to the inequality constraint, indicating the efficiency of the adjoint-based CFD optimisation.

As in Table 5.2, by altering the duct shape, the thrust was increased by about 8.2% subject to the constraint of 110% torque. The propulsor efficiency was reduced very slightly by about 1.6% for this thrust increase. As in Table 5.3, the propeller thrust was increased by 27.1% while the duct and centre-body thrust was decreased by about 40.7%, and the total thrust was increased by 8.2% subject to the 110% torque constraint. The propeller disk was hence heavily loaded with 84.7% of the total thrust carried.

The optimisation brought both leading- and trailing-edges inwards, as shown in Figure 5.2, decreasing the expansion ratios of the duct inlet and outlet. The duct camber was hence reversed compared to the original design. Only very small offsets are noticed for the leading-/trailing-edge points, hence the chord length remains the same. The inner surface of the duct is now almost flat and conforming with the mid-chord part, with a slightly expanded diffuser exit. In general, the optimised shape is expected to induce lower flow rates through the propeller disk and improves the inflow conditions for the propeller, increasing the propeller and the total thrust.

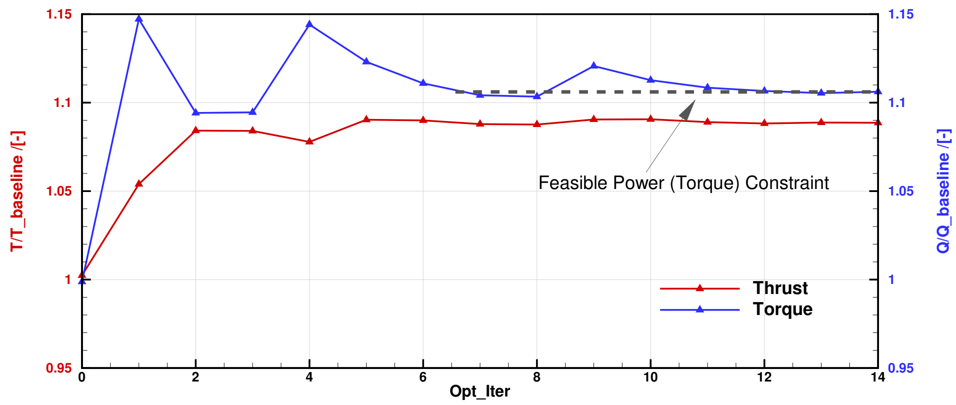

Figure 5.4: Optimisation convergence history of the duct inlet/outlet shapes with torque constraint.

5.2.2 Blade Twist Optimisation (Case 2)

The current optimisation of the blade twist (case 2) involved 4 design variables, i.e. the Bernstein coefficients describing the pitch distribution along the blade span. The convergence history of both optimisation studies is presented in Figure 5.5. The blade twist optimisation converged in 6 loops as fewer design variables were involved.

As in Table 5.2. With the 120% torque constraint, only optimising the blade twist delivered a thrust increase of about 11.6%. For such thrust increase, the efficiency was penalised by 7%. As for the contributions from each components, as in Table 5.3, the propeller thrust was increased by 9.2% while the duct thrust was also increased by 17.8%, and the total thrust was increased by about 11.6% subject to the 120%. The increases in both propeller and duct thrust have also been noticed in a previous pitch variation study [142] due to the increased propeller suction. The thrust ratio between the propeller and the duct was changed only very slightly compared to the original design.

The corresponding optimised pitch distribution is shown in Figure 5.3. Compared to the original design, the optimised blade has constantly increased blade pitch by about 2° throughout the span except for the tip. Beyond the 75% span, the blade is highly twisted resulting in lower pitch at the tip. The global pitch increase is expected in order to accommodate the high axial velocity at this advance ratio. The twist changes are similar to what optimisation results of conventional open rotor twist show, where typically the twist is increased to offload the tip region for higher efficiencies. However, in the current ducted propeller case, only minor changes in the efficiency are observed.

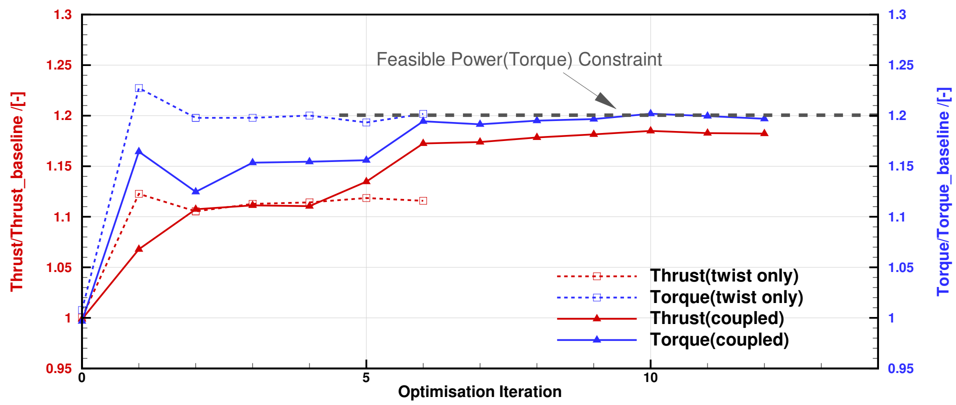

Figure 5.5: Optimisation convergence history of the coupled duct outlet shape and the blade twist with torque constraint.

5.2.3 Coupled Duct Shape & Blade Twist Optimisation (Case 3)

The coupled optimisation (case 3) of the duct exit and blade twist involved 12 design variables, 4 for the twist, 2 for the trailing-edge point offsets, and 6 for the trailing-edge shapes. The leading-edge shape was excluded from this case to reduce the number of design variables. Also, the trailing-edge shape is expected to be more crucial as it determines the expansion ratio of the duct shape. The objective was again set to increase the thrust subject to a 120% torque constraint. As in Figure 5.5, the coupled optimisation took about 10 iterations to converge with 12 design variables.

Subject to the same torque constraints as Case 2, however, the coupled optimisation managed to increase the thrust by about 18.3%. For this large thrust increase, the efficiency was very slightly decreased by about 1.38%. In Table 5.3, the propeller thrust was increased by about 20.6% while the duct thrust was increased by 12.5%, and the total thrust was increased by about 18.3% subject to the 120% torque constraint. The propeller loading was increased slightly carrying about 73.5% of the total thrust.

The duct deformation is presented in Figure 5.2. Note the inlet shape was not included to reduce the amount of design variables and to reduce the computational cost. The duct diffuser is allowed to deform for $x/C > 0.53$ (see Figure 5.2). The trailing-edge point is slightly moved to reduce the expansion ratio, and very slightly the chord length. The lower expansion ratio at this high advance ratio of 0.191 is reasonable as it reduces the duct-induced axial flow rates through the propeller disk and improves the propeller inflow condition. The optimised blade pitch distribution is shown in Figure 5.3. The pitch angles are slightly increased by about 1° from the root to about the 60% span. Larger pitch angle increases by about 2° to 3° are seen towards the tip. Therefore, the blade twist is different from conventional open rotor optimisation. Nevertheless, combined with the duct shape change, such blade changes bring higher performance improvement. It is also noted that the changes in the pitch distribution and the duct shape are generally small, yet the thrust increment is large. It can be hence argued that the coupled deformation of the duct shape and blade twist brings a larger performance capacity for the ducted propeller to accommodate variable operating conditions and requirements.

5.2.4 Flow-field Changes

The instantaneous flow-fields are presented in Figures 5.6(a) to 5.6(h) using contours of pressure coefficients and normalised axial velocities at the $azimuth = 0^\circ$ slice. The pressure coefficients were calculated using the free-stream velocity and the ambient pressure. The axial velocity is normalised by the free-stream axial speed. Note the axial flow travels towards the $-Z$ axis. The flow-field of the original design is presented in Figures 5.6(a) and 5.6(b) for comparisons.

Flow-fields of the duct optimisation are shown in Figures 5.6(c) and 5.6(d). As can be seen in Figure 5.6(c), the propeller disk had a larger high pressure area towards the blade root. The propeller disk hence carried higher loading. Further, as shown in Figure 5.6(d), the axial velocity through the propeller disk was slowed comparing to the original design in Figure 5.6(b). Given the same blade shape and the constant RPM during the duct shape optimisation, it can be concluded that the propeller thrust was increased due to the improved inflow condition because of the duct deformation. The deformed duct shape is expected to induce lower mass and momentum flow rates through the propeller disk, which is necessary at high advance ratios and has been noted in Figure 5.6(b).

Flow-fields of the blade twist optimisation are shown in Figures 5.6(e) and 5.6(f). In Figure 5.6(e), it can be seen that the blade also saw a larger high pressure region towards the root area and the propeller disk loading was hence increased. From Figure 5.6(e), the axial velocity through the propeller disk was slightly increased compared to the original design in Figure 5.6(b), except that faster flow was seen through the mid-span and root regions in the optimised case. In other words, the axial velocity was more evenly distributed along the blade radius compared to the original case. These are consistent with the blade pitch and twist changes from the optimisation as shown in Figure 5.3. Since the global pitch was increased by about 2°, which is reasonable for propellers at high advance ratios and higher thrust was hence expected. Further, with the increased blade twist at the tip, higher loadings were hence expected at mid-span and root regions, and the wake was expected to be more evenly distributed approaching the uniform wake distribution for an ideal rotor. The duct thrust was also increased due to the higher propeller suction.

Flow-fields of the coupled duct exit and blade twist optimisation are presented in Figures 5.6(g) and 5.6(h). It can be noted from Figure 5.6(g) that the blade saw a higher loading through the optimisation. The axial velocity, as in Figure 5.6(h) was slightly increased compared to the original design in Figure 5.6(b). Compared to the original design, the blade pitch was increased along the span, especially at the tip. This is reasonable due to the high advance ratio and the high inflow velocity. Compared to the separate blade twist optimisation, the local pitch angles in the coupled optimisation were lower at the root and mid-span regions, but the angles were higher beyond 0.8 r/R. This is not favourable for the propeller efficiency from simple theoretical analyses. Nevertheless, the coupled optimisation managed to offer about 7% more thrust than the separate blade twist optimisation. This should be due to the slightly reduced duct exit expansion ratio that improves the inflow conditions for the propeller disk. Also, small coupled deformation of the blade and duct leads to large performance changes. This indicates a better performance capacity of the ducted propeller to cover various operating conditions and requirements using the coupled deformation.

Overall, it can be concluded that the duct and blade twist optimisations increased the total propulsor thrust at this high advance ratio of $\mu = 0.191$ in different ways. At this high axial speed, the duct deformation reduces the induced flow rates through the propeller disk, thereby creating a more favourable working condition for the propeller at high speeds, and the propeller disk loading is increased. The duct-propeller thrust sharing is therefore altered. In a different perspective, it is possible to use the duct deformation for the performance control of ducted propellers, by altering the propeller inflow conditions and the thrust sharing between the duct and the propeller. However, issues regarding mechanism complexity, control response, structure etc. must be accounted for, beforehand. The blade twist optimisation adjusts the local pitch angles for the blade elements to accommodate high inflow velocities and improve the efficiency by redistributing the loads among the propeller disk. The duct thrust is also increased since the propeller suction is increased and the duct shape remains the same. The coupled deformation of the duct shape and blade twist combines both means and offers larger and more sensitive overall performance changes.

5.2.5 Performance at Varying Blade Pitch, Advance Ratio, and Crosswind

Since the optimisation in this chapter was performed at a specific operating point, it is of interest to examine whether the performance is improved or penalised in other conditions. This subsection examines the influence of the blade pitch, advance ratio, and non-axial inflow.

In practice, the thrust increase of a propeller is mostly realised by conventional pitch increases. Therefore, the optimisation results are compared with the thrust-torque map of the original design at $\mu = 0.191$ subject to pitch variations as shown in Figure 5.7. Blade pitch variations were also applied to the coupled optimisation case to examine the performance of the new designs

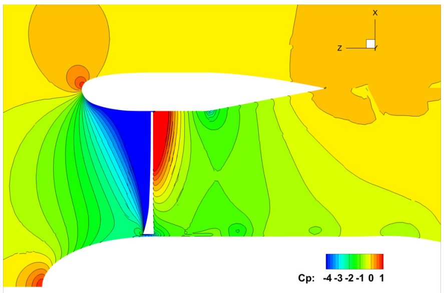

(a) Pressure coefficient contours of the original design.

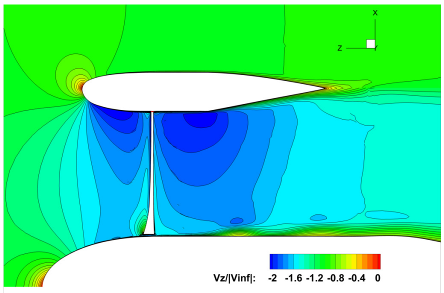

(b) Axial velocity contours of the original design.

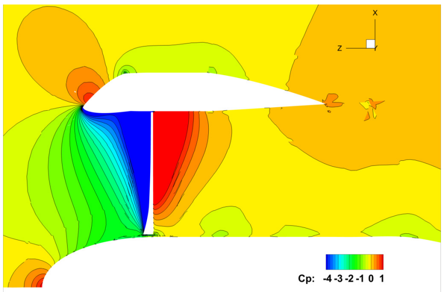

(c) Pressure coefficient contours of the duct shape optimised design (Case1).

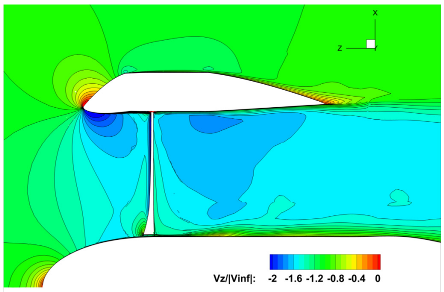

(d) Axial velocity contours of the duct shape optimised design (Case1).

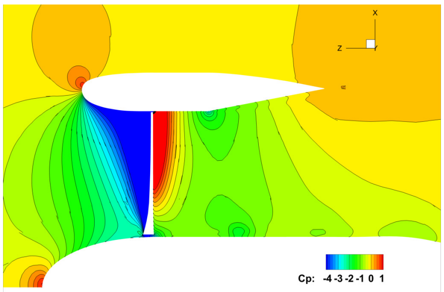

(e) Pressure coefficient contours of the blade twist optimised design (Case2).

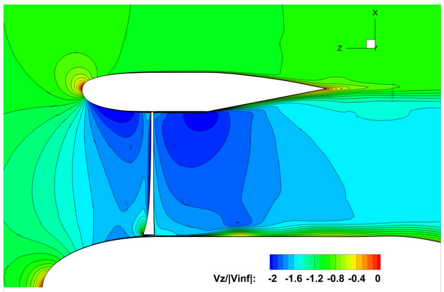

(f) Axial velocity contours of the blade twist optimised design (Case2).

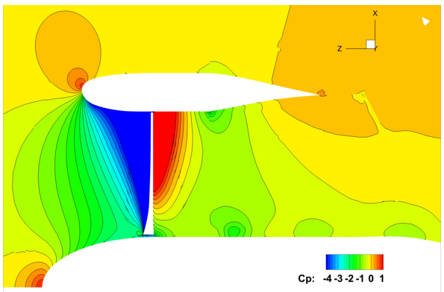

(g) Pressure coefficient contours of the coupled duct shape/blade twist optimised design (Case3).

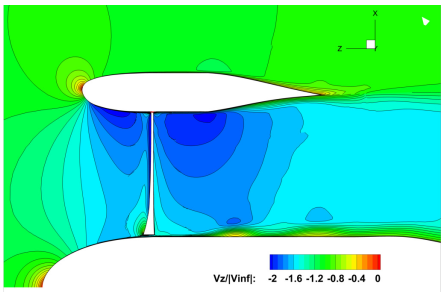

(h) Axial velocity contours of the coupled duct shape/blade twist optimised design (Case3).

Figure 5.6: Instantaneous flow-fields of the original and optimised shapes on $y = 0$ slice. The pressure coefficients are normalised using the free-stream velocity. The axial velocity values are normalised by the free-stream axial velocity.

at different disk loadings. Compared to the original design, for the same thrust required, the duct shape optimisation (Case 1) produces almost the same torque, while the blade twist optimisation (Case 2) generates slightly lower torque. The coupled duct/blade optimisation (Case 3) shows the greatest improvement with a large torque reduction. Performance variations of the coupled case were also examined at different disk loadings by blade pitch variations as shown in Figure 5.7. The coupled optimisation brings much better performance at higher pitch settings/disk loadings with lower torque, while the performance at lower disk loadings is similar to and slightly lower than the original design.

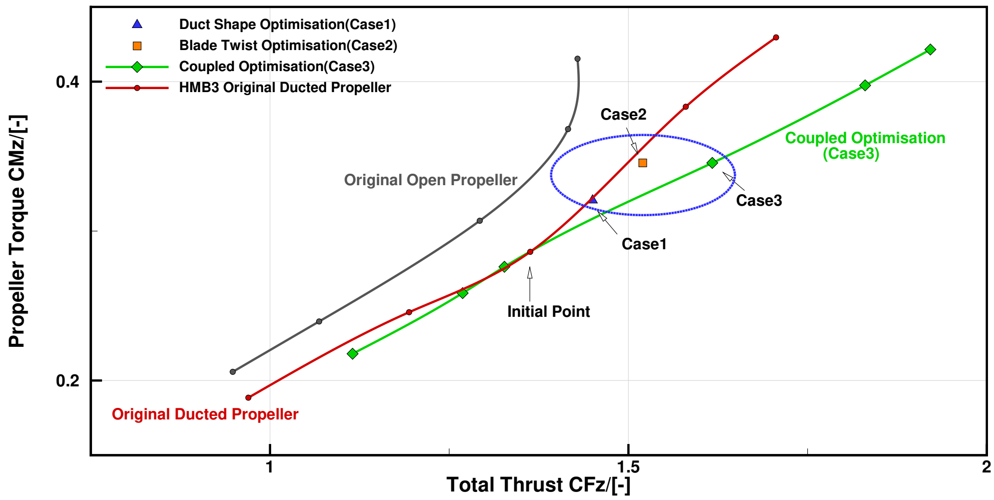

Figure 5.7: Thrust-torque map of the original ducted/un-ducted Grunwald[18] propellers at $\mu = 0.191$ subject to blade pitch variations. Performances of the optimised cases are also plotted using scatters.

Performance of the coupled optimisation (Case 3) was also examined at other advance ratios of $\mu = 0.0955$ and $\mu = 0.382$ and compared with the original open propeller and ducted propeller, as shown in Figure 5.8. The advance ratio was changed by varying the free-stream speed while keeping the rotating rate constant. The initial coupled optimisation (Case 3) managed to produce higher thrust at higher and lower advance ratios than the original ducted propeller, although at higher torque costs. The blade pitch of the coupled optimisation case was later reduced by 2.5° to deliver similar thrust level as the original design at $\mu = 0.191$. This reduced blade pitch required slightly larger power input for a thrust similar to the original design. The optimised design also showed slightly penalised performance than the original at the lower advance ratio of $\mu = 0.0955$. This was expected as the reduced duct expansion ratio is more beneficial at higher advance ratios. Its thrust at the very high advance ratio of $\mu = 0.382$, although still close to zero, was improved than the original design, which is producing negative thrust. At this high advance ratio, the duct causes large drag rather than propulsion due to the fast free-stream and low propeller induction, so increasing the blade pitch at high advance ratios is still necessary[142].

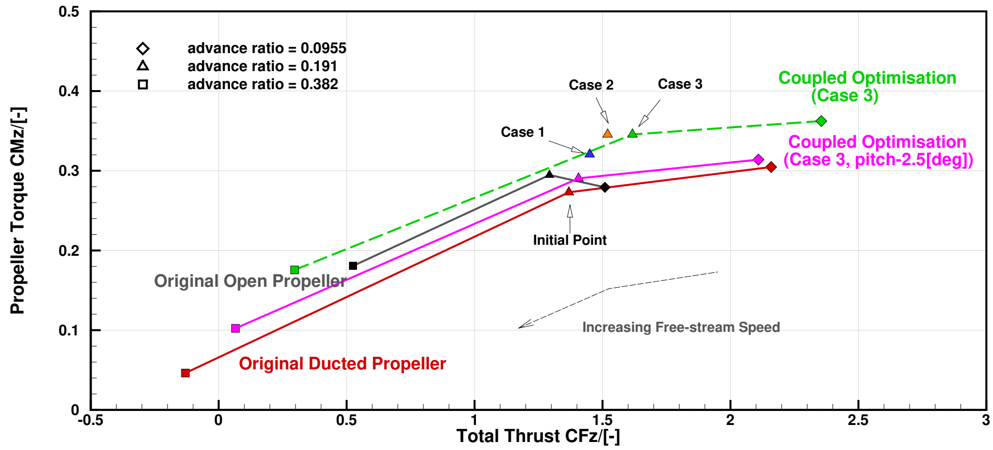

Figure 5.8: Performance comparisons between the optimised designs and the original designs at different advance ratios at initial pitch settings.

To examine the crosswind performance of the optimised designs, initial simulations of the duct optimisation (Case 1), where large duct shape deformation was observed, with non-axial inflows were also performed. Performance comparisons, in terms of lifting forces C_l and propulsion forces C_{F_z}, are presented in Figure 5.9. It can be seen that at $AoA = 20°$, the optimised duct shape produces the similar amount of lift and slightly lower propulsion. This suggests that the crosswind performance of the optimised design is only very slightly penalised, despite the large shape changes which improve its axial performance.

In summary, the optimised design through the coupled optimisation showed improved performance at varying blade pitch angles, especially at higher disk loadings. Its performance was also better than the original at higher advance ratios, although the performance at lower advance ratios was slightly penalised. With the large duct shape deformation, the ducted propeller performance

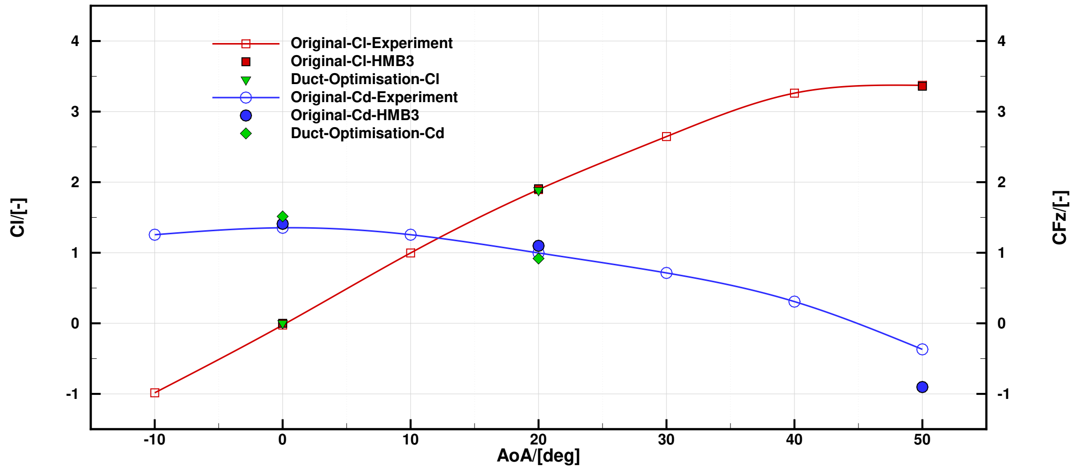

Figure 5.9: Performance comparisons between the optimised duct design (case 1) and the original design at crosswind.

was not much affected at crosswind.

5.3 Far-field Acoustics of Optimised Shapes

As stated earlier, the acoustic performance was not formulated in the optimisation, as the aerodynamic performance is considered as the primary concern. Nonetheless, the far-field acoustic performances of the optimised designs are also examined in this subsection to explore changes brought by the duct shape and blade deformation. The far-field acoustics was calculated at microphone points on a spherical surface of 20-duct-chord radius surrounding the propulsor to investigate the directivity, the same as in Chapter 4.

The SPL values of the total noise signals for the original and optimised designs are presented in Figure 5.10. The acoustic levels vary little along the propeller azimuth, hence comparisons are made at the azimuth station of 0°. Compared to the original open propeller, the optimised designs still show similar acoustic levels in the axial directions and lower levels in a large range between -60° to 60°. Compared to the original ducted propeller, the acoustic levels maintained similar trends.

Still, variations in the directivities due to design changes can be noted. For the blade twist optimisation (Case 2), the acoustic directivity is almost identical to that of the original design. The duct shape optimisation (Case 1) and the coupled optimisation (Case 3) mostly shifted the location of the local acoustic minimum towards the inflow direction while maintaining the minimum values still at around 65 dB. The duct shape optimisation moved the lowest acoustic level to around 0° directivity, while the coupled optimisation moved the lowest to around 15° directivity. It can be seen that the duct shape plays a more significant role, compared to the blade design, in the far-field acoustic pattern of the ducted propeller.

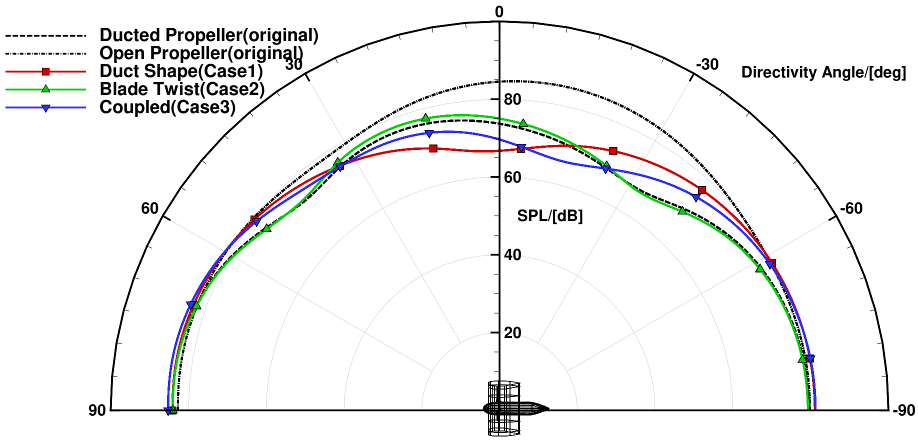

Figure 5.10: Far-field acoustic directivity spheres (20 duct chords away) of the optimised designs.

The perceived noise signals at fixed ground positions were also calculated for the optimised designs and compared with the original ducted/un-ducted designs. The microphone position was placed at 10 duct chords below as illustrated in Figure 4.26. The moving RMS values of the acoustic signals were calculated using signals within a time window of one propeller revolution and are presented in Figure 5.11. Acoustics of all three optimised designs are very similar to that of the original ducted propeller and are only a quarter or half the strength of the un-ducted. The moving RMS of the optimised designs was also mildly smoother than the original design. Two acoustic peaks were still noticed, respectively before and after the propeller passage. The acoustic valley was also noted at the propeller passage. For the duct shape optimisation, the moving RMS of the signal had similar peak values to the original but had a lower minimum. The signal was also slightly phase-shifted with the second peak delayed. The moving RMS of the twist optimisation was almost identical to the original. For the coupled optimisation, the moving RMS peaks were slightly higher than those of the original, and the valley value was also lower regardless.

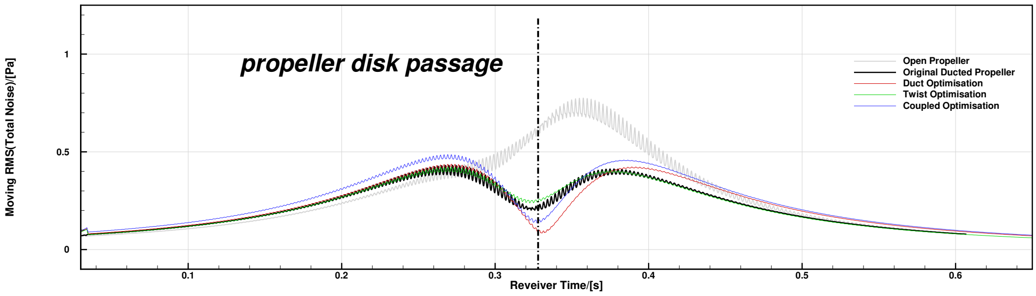

Figure 5.11: Moving root-mean-square (RMS) values (calculated using signals within a time window of one blade rotation, i.e. 0.0075s, at each time point) of the fly-by acoustic signals recorded 10 duct chords below (Figure 4.26)of the optimised designs.

The acoustic results suggest that the acoustic performance was not severely affected by the optimisation but the duct shape played a more significant role in the ducted propeller acoustics. It is hence also possible to alter the acoustic performance by changing the duct shape. In combination with blade twist deformation or pitch regulation, the aerodynamic performance may not be penalised for this purpose. This can be achieved by coupling the aerodynamics and acoustics altogether in the optimisation formulation in future work.

5.4 Chapter Summary

This chapter presented the gradient-based aerodynamic shape optimisation of ducted propellers to improve the performance at high advance ratios. Far-field acoustics of the optimised designs were also examined afterwards. The following conclusions can be drawn from the optimisation study:

1. By altering the duct and blade shapes, the ducted propeller performance was effectively improved at $\mu = 0.191$ by the proposed adjoint-based optimisation framework. Especially, the coupled duct/blade shape optimisation brought the greatest performance improvement compared to the separate cases respectively for the duct and the blade. Subject to the 120% torque constraint, the coupled optimisation managed to increase the total thrust by

18.3%. While for the same power input, the original design could only increase the thrust by about 10% by increasing the blade pitch. Compared to the original design, the coupled optimisation also delivered better performance at higher disk loadings/pitch settings. The performance was also improved at higher advance ratios but slightly penalised at lower advance ratios. The cross-wind performance of the duct shape optimisation, where the largest duct deformation is observed, was shown only slightly penalised.

2. To improve the ducted propeller performance at high axial speeds, the gradient-driven optimisation decreased the duct inlet/outlet expansion ratio and reversed the original section camber. This deformation caused the duct to induce lower inflow velocity and flow rates through the propeller disk, thereby improving the inflow condition for the propeller and improving its thrust. For the blade shape, the global pitch was increased to accommodate the high inflow velocity. The blade twist optimisation increased the blade twist to offload the tip and to improve the efficiency. However, in the coupled optimisation, the blade twist was slightly eased. Regardless, combined with the duct deformation, the coupled optimisation offered the greatest performance improvement.

3. The far-field acoustic performance of the optimised designs was also examined to ensure the acoustic benefits were maintained after the aerodynamic optimisation. The far-field noise levels of the optimised designs remained almost the same as the original design and the acoustics was better than that of the open propeller counterpart. Particularly, the duct shape had a strong impact on the overall far-field acoustics. The duct shape optimisation and the coupled optimisation, where duct deformation was involved, altered both the far-field acoustic directivities and the fly-by noise signal. With the reduced expansion ratios, the low far-field acoustic region was moved closer to the propeller disk. Signals of the blade twist optimisation were almost identical to that of the original without the duct deformation.

The next chapter will study and compare the performance of installed ducted/open propellers under a main rotor as auxiliary sources of propulsion for novel rotorcraft configurations.

Chapter 6

Aerodynamic Interactions between the Main Rotor and Ducted/Open Propellers[1]

For applications as auxiliary sources of lift or propulsion for novel rotorcraft configurations, the ducted/open propellers are typically subject to the main rotor downwash. Results of ducted/open propellers at crosswind conditions presented in previous sections may be indicative for the installation cases, but the aerodynamic interactions are expected to be much more complex due to the unsteady, impulsive, and non-uniform main rotor downwash.

This chapter hence investigates the performance changes of ducted/open propellers installed under a main rotor. A generic rotor/propeller combination was adopted for the investigation. Performance of the open and ducted configurations of the propeller were first studied. The aerodynamic interactions and the performance changes of the rotor/propeller combination were then analysed in detail. The key contributions from this chapter are the evaluation of the actuator disk/line models for the modelling of rotor/propeller interactions, and the detailed comparisons of performance and interactional aerodynamics between the open and ducted propellers.

[1] This chapter has been published in T. Zhang, G. N. Barakos, "High-fidelity Numerical Investigations of Rotor-Propeller Aerodynamic Interactions", Aerospace Science and Technology (accepted), 2022

6.1 Case Descriptions

A generalised rotor/propeller integration [143] has been built for the investigation of the interactional aerodynamics within the GATEUR AG25 project. The test rig used by ONERA is illustrated in Figure 6.1(a) and 6.1(b).

(a) Front view.

(b) Side view.

Figure 6.1: Illustration of the ONERA test rig for the rotor/propeller interaction study. [143]

The test model consists of a 1/7-scaled Dauphin fuselage, a 1.5-m-diameter main rotor, and a 11-inch-diameter commercial propeller (APC 11x9-4). The same fuselage and rotor combination has been used in previous studies of rotor/fuselage interactions[144]. Dimensions and relative positions of the test models are presented in Figure 6.2. In the experiments, the main rotor rotates clockwise viewed from above, and the propeller rotates counter-clockwise viewed from the front. However, as in Figure 6.2, all geometries and motions have been mirrored about the x-z plane comparing to the original in Figures 6.1(a) and 6.1(b). This is for easier implementations of actuator disk models and mesh motions in HMB3. Therefore, the main rotor rotates counter-clockwise viewed from above, and the propeller rotates about the positive x axis in all simulations of the rotor/propeller combination within this thesis. Note the fuselage was excluded in the present study, as done in references [143, 145].

More descriptions of the main rotor geometry and motions are listed in Table 6.1. The rotor was trimmed in isolation to a specific thrust with no lateral flapping and no longitudinal forces. The trimming values were not altered after the installation of the propeller. More information of

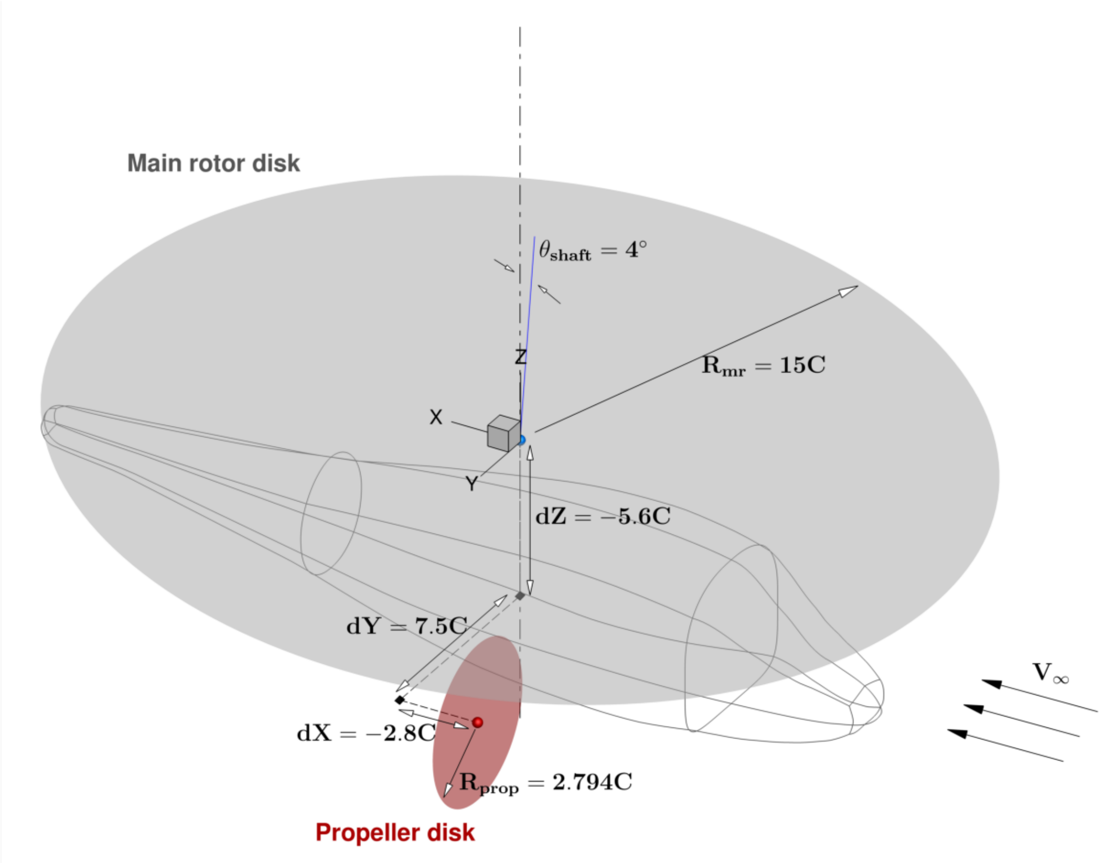

Figure 6.2: Dimensions and relative positions of the rotor/propeller interaction test rig by ONERA. Dimensions are normalised by the main rotor chord $C = 0.05m$. Note the model and all the motions are mirrored about the x-z plane comparing to the actual experimental test.

the APC 11x9-4 propeller is presented in Table 6.2 and Figure 6.3. The propeller RPM and pitch angle were kept constant throughout the test.

High-fidelity simulations are necessary to resolve the complex interactional aerodynamics between the main rotor and the propeller for this case. Nevertheless, the modelling is challenging due to large temporal and spatial differences between the main rotor and propeller. As presented in Tables 6.1 and 6.2, the propeller to rotor rotational speed ratio is 6:1, while the radius ratio is about 0.186:1. The temporal and spatial resolution of the CFD modelling hence must prioritise the propeller that has the higher frequency and smaller spatial size, and the computational cost can be prohibitively large.

Simplified modelling with reduced computational costs is therefore necessary. Previous CFD simulations by Boisard [143] suggest that the main rotor sees minor influence from the pro-

Table 6.1: Geometry and operating conditions of the main rotor.

radius	0.75 m
chord	0.05 m
twist	linear -16°
number of blades	4
shaft angle	4 ° nose down
planform	− rectangular − no swept − no taper
blade section	OA209
rotational speed	RPM 1272 ($V_{tip} = 100m/s, Ma_{tip} = 0.294$)
Free-stream velocity	$V_\infty = 0, 5, 10, 15, 20, 25m/s$
Main rotor advance ratio	$\mu_{mr} = 0, 0.05, 0.1, 0.15, 0.2, 0.25$
Propeller climb ratio	$\mu_{prop} = 0, 0.0448, 0.0896, 0.134, 0.179, 0.224$
trimming target	− Ct = 0.0123 − trimmed in isolation − zero longitudinal force − zero lateral flapping

Table 6.2: Geometry and operating conditions for the APC 11x9-4 propeller.

radius	0.1397 m
twist	non-linear -41 °
number of blades	4
rotational speed	RPM 7632 (V_{tip} = 111.65m/s)
75% span pitch	21 ° (fixed)

peller, whereas the propeller suffers more from the main rotor wake and downwash. This is expected considering that the main rotor is placed upstream the propeller and it has to produce lift to counter the total weight. In view of this, it is reasonable to model the main rotor with simplified and efficient models and to focus on the aerodynamic interactions near the propeller with blade-resolved simulations. Therefore, the actuator disk and actuator line models are adopted to model the main rotor for the rotor/propeller interaction study in this thesis. The actuator disk models have been assessed in Chapter 3 and were shown capable of resolving the interactional aerodynamics at much reduced computational costs. Similar approaches were also used in previous studies of rotor/propeller interaction studies by Stokkersman et.al. [146]

It is also noted that the main rotor advance ratio ($\mu = 0 \sim 0.25$ for the current study) plays a

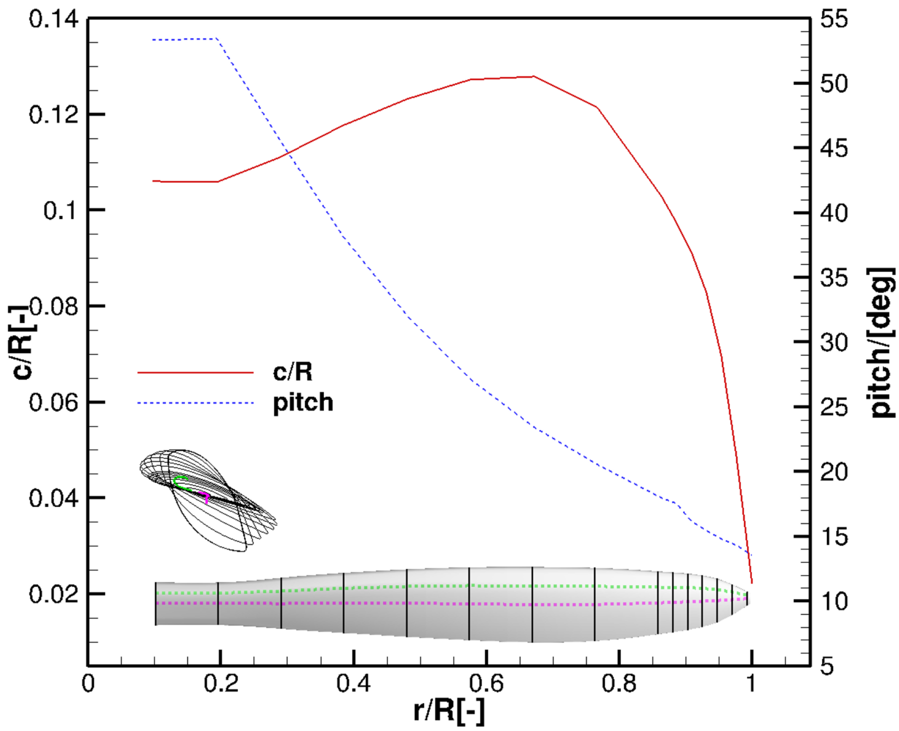

Figure 6.3: Blade shape of the APC 11x9-4 propeller.

significant role in the aerodynamic interactions, as the advance ratio determines the wake boundary. At higher advance ratios beyond $\mu = 0.1$, the main rotor wake passes above the propeller disk, inducing only small fluctuations in the propeller thrust. In the intermediate advance ratio range near $\mu = 0.05$, the main rotor wake partially impinges on the propeller disk. The propeller hence sees large influences from the main rotor within certain azimuth ranges. Otherwise, the influence is rather small. In hover, the propeller is immersed in the main rotor downwash, and significant fluctuations in the propeller thrust can be noted. Unsteady simulations of the hover condition can be very costly due to the lack of free-stream and to the complex flow details often exhibited. The current work has hence chosen the low advance ratio of $\mu = 0.05$ as a typical condition that has significant aerodynamic interactions and requires moderate computational costs for the high-fidelity simulations.

6.2 Validation and Performance of the Isolated Ducted/Open APC Propellers

To validate the geometry and numerical settings, simulations were first performed on the isolated APC 11×9-4 propeller, as shown in Figure 6.4(a). A large test matrix in Table 6.3 was compiled to test the propeller performance in axial flight and to assess the effects of spinner and fairing, turbulence modelling, and steady/unsteady approaches. The spinner and fairing, as shown in Figure 6.4(a), have the exact shapes as the experiments. However, the aft-part of the fairing was extended as a circular cylinder with a smooth sealing to model the effects of the wind tunnel support structures. Moreover, a ducted configuration was also proposed, as shown in Figure 6.4(b) using the same Grunwald duct shape [18] from previous chapters. The duct was scaled to enclose the propeller with the same tip gap to radius ratio of about 0.53%.

(a) Original APC 11×9-4 propeller. (b) APC 11×9-4 propeller fitted with Grunwald duct.

Figure 6.4: Geometries of the original open and ducted APC 11×9 propeller.

Table 6.3: Test matrix for simulations of the APC 11x9 four-bladed propeller.

Case Name	RPM	V_∞/[m/s]	Spinner & Fairing	Duct	Turbulence Modelling	Steady/Unsteady
PC 1	7632	0.00, 5.58, 11.17, 15.00, 16.75, 22.33, 25.00, 27.91	N	N	k-ω SST	steady
PC 2		0.00, 5.58, 16.75	N	N	k-ω SST & SAS	unsteady
PC 3		0.00, 5.00, 10.00, 15.00, 20.00, 25.00	Y	N	k-ω SST	steady
PC4		5.00, 15.00, 20.00	Y	Y	k-ω SST	steady

Simulations of the open/ducted propellers in axial flight were carried out following similar approaches as in previous sections, using the Rotating Reference Frame and periodic boundaries with only 1/4 of the entire computational domain. The unsteady simulations used the same grids and periodic boundaries, but resolved the rotational motions. The grids were again generated with the help of the automation framework presented in Chapter 2. The Reynolds number based on the 75% blade chord and the tip speed is about 1.38×10^5.

Simulation results in terms of the propeller thrust and torque are presented in Figures 6.5(a) and 6.5(b), respectively. Also presented are wind tunnel test data by ONERA at three rotating rates. The differences between numerical results were mostly within $1N$ and $0.05Nm$. Such small differences in the simulations were expected for a small-scale propeller working at this medium to low Reynolds number, due to complex flow features e.g. transition, separation, and interactions. In general, the numerical results are in close agreement with each other and with the test data, especially at higher axial velocities.

For the open propeller with and without the centre-body using steady methods, i.e. cases PC1 and PC3, the thrust and torque results are very close across the axial speed range, but slightly larger thrust differences can be noticed in hover. Without the spinner and fairing, the propeller produced about 1 Newton more thrust in hover, and the torque was also very slightly lower. Otherwise, the absolute differences in thrust and torque were negligible. These suggest that the spinner and fairing had very limited effects in axial flight for this case.

As for the unsteady simulations of the open propeller, i.e. cases PC2-SST and PC2-SAS, the thrust results differ a little more from the steady results at low axial speeds. The SST modelling gave slightly higher thrust predictions by about 1 Newton at the axial speeds between 0 and 5 m/s. At higher speeds, the unsteady SST predictions were almost identical to the steady results. The SAS modelling, however, gave slightly lower thrust predictions throughout the speed range considered. Comparisons of flow-fields resolved by the two modelling approaches at $V_\infty = 16.75m/s$ are presented in Figures 6.6(a) and 6.6(b). The disk loading distributions were also extracted and presented in Figures 6.7(a) and 6.7(b). It can be seen that the differences reside mostly near the blade root, with the SAS simulation resolving more fluctuations. Nonetheless, these were only small absolute differences.

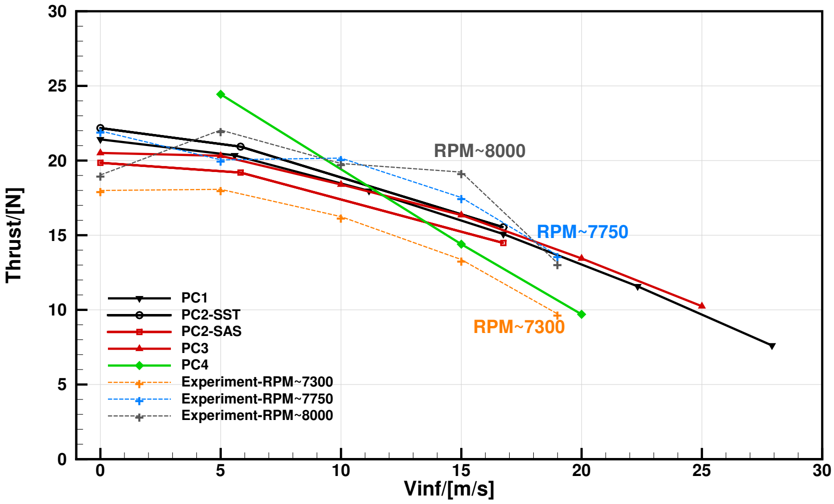

(a) Thrust variations.

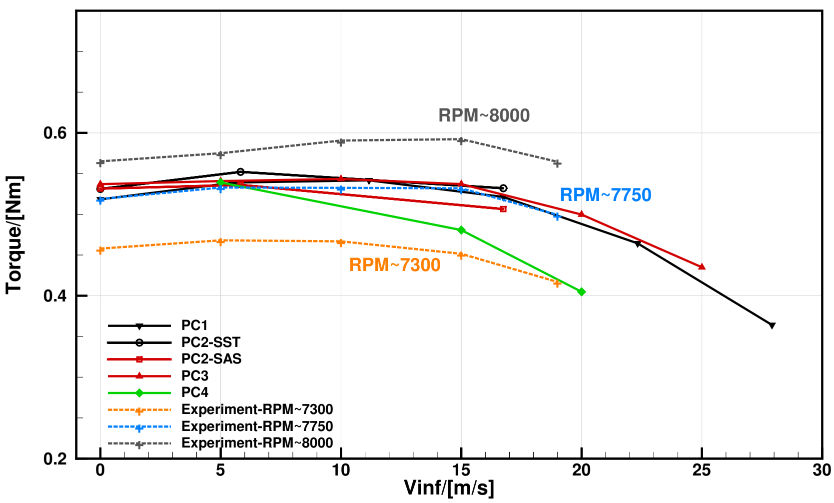

(b) Torque variations.

Figure 6.5: Thrust and torque variations of the APC propeller subject to advance ratio changes in axial flight as in Table 6.3. The propeller *RPM* was kept constant at 7632 while the axial speed was varied.

Table 6.4: Aerodynamic loadings of the ducted propeller at $V_\infty = 5m/s$. Values normalised by the isolated open propeller thrust T_0 and torque Q_0 at $V_\infty = 5m/s$.

Component	T/T_0	Q/Q_0
propeller	79.6%	100.5%
duct	40.9%	-0.6%
total	120.5%	100.0%

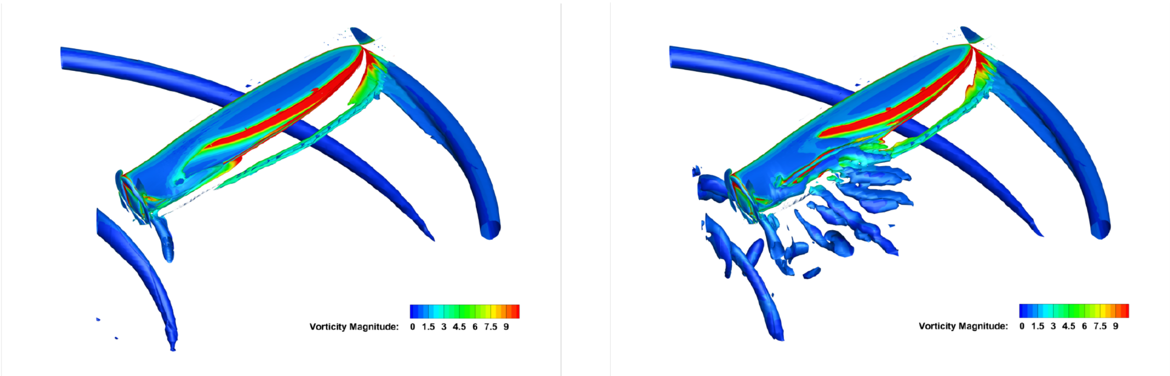

(a) Unsteady SST simulation (PC2-SST). (b) Unsteady SAS simulation (PC2-SAS).

Figure 6.6: Instantaneous flow-field comparisons in terms of dimensionless q criterion iso-surfaces (coloured by vorticity magnitudes) between the unsteady SST and SAS simulations of the APC propeller at $V_\infty = 16.75m/s$.

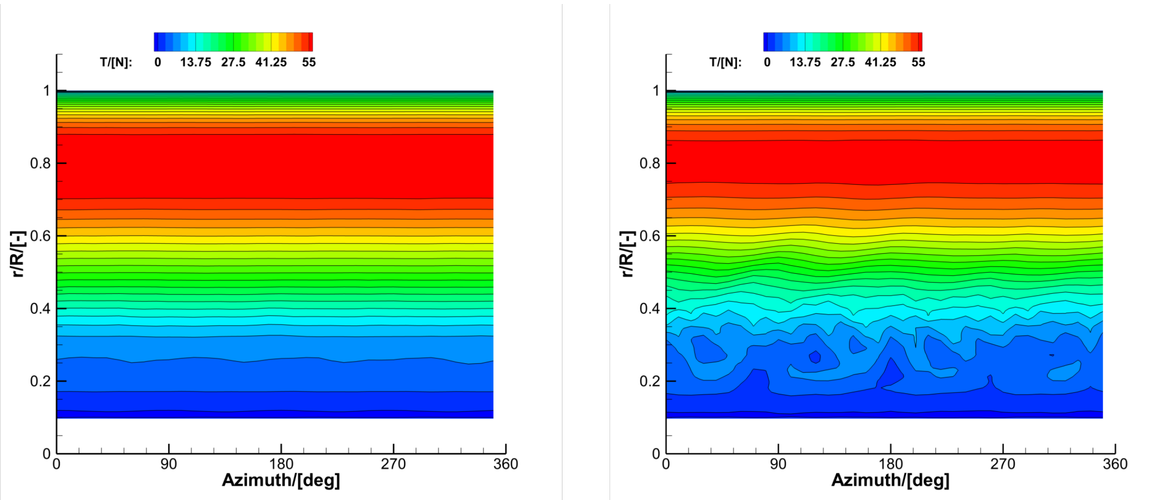

(a) Unsteady SST simulation (PC2-SST). (b) Unsteady SAS simulation (PC2-SAS).

Figure 6.7: Disk loading (thrust per unit span) comparisons between the unsteady SST and SAS simulations of the APC propeller at $V_\infty = 16.75m/s$.

For the ducted APC propeller, i.e. case PC-4, the thrust and torque dropped faster than the open propeller following increasing axial speeds. At low axial speeds, the ducted configuration produced about 5 Newton higher thrust than the open propeller at the same torque. As the axial speed increased, the ducted configuration produced less thrust and torque. Aerodynamic loading comparisons at $V_\infty = 5m/s$ are presented in Table 6.9. All values have been normalised by the isolated open propeller loadings at the same $V_\infty = 5m/s$ to bring out the relative changes. For the current ducted configuration, the propeller blades were also offloaded, although the torque

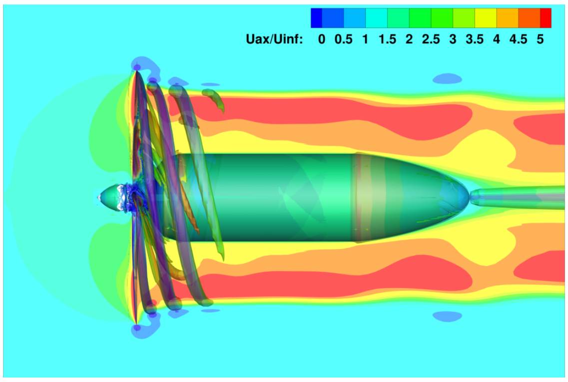

(a) Original APC propeller.

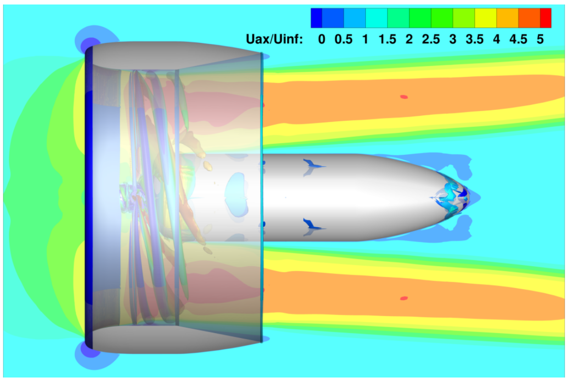

(b) Ducted APC propeller.

Figure 6.8: Instaneous flow-field comparisons between the open and ducted APC propellers at $V_\infty = 5m/s$.

remained almost the same. The duct contributed about one-third of the total thrust. The total ducted thrust was 20.5% higher than the open propeller configuration, while the overall torque was almost the same. Comparisons of flow-fields are presented in Figures 6.8(a) and 6.8(b). As expected, the ducted wake was diffused and slowed down by the duct. These agree well with the previous investigations of open/ducted propellers of Chapter 4.

6.3 Simulation Strategies for the Rotor/Propeller Combinations

For the rotor/propeller integration simulations, the grid topologies used in the current thesis are shown in Figures 6.9 and 6.10. The simulations involved the main rotor, propeller, centre-body, and the duct for the ducted configuration. The fuselage was excluded for simplicity. Grids were generated for each component separately to ensure high quality, and were assembled for computation using Chimera approaches. In the present study, the propeller blades were fully resolved, while the main rotor was represented by actuator disks or lines, as listed in Table 6.7. The off-body grids had uniform cell sizes near the main rotor and the propeller. The simulations were performed using the 3^{rd}-order MUSCL scheme and the $k-\omega$ SST model. Simulations were first performed using the isolated open/ducted propellers without the main rotor.

A first study was performed to evaluate the required spatial and temporal resolutions for

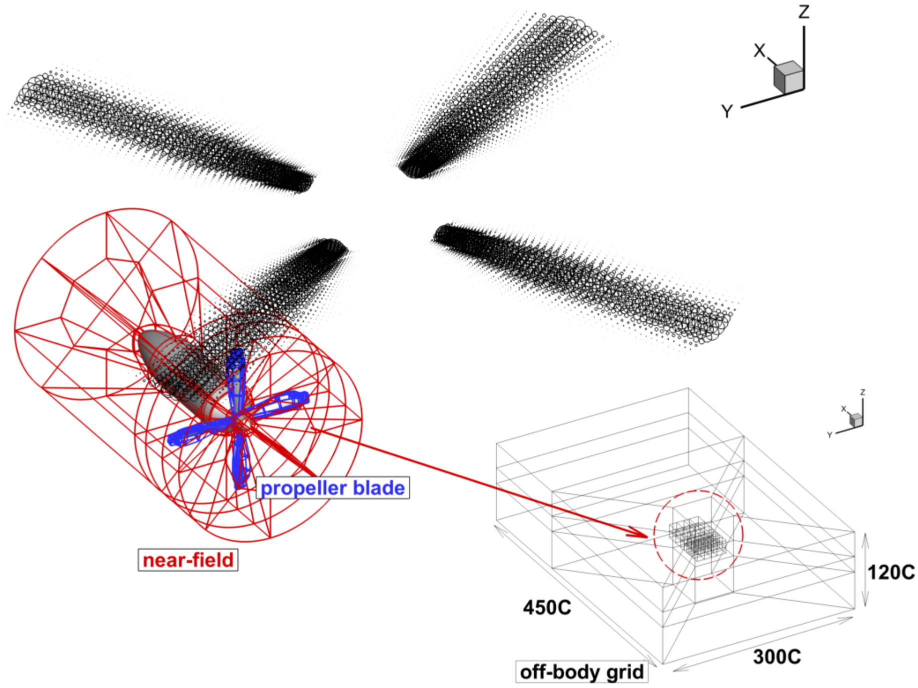

Figure 6.9: Grid topology for HMB3 simulations of the rotor/propeller configuration.

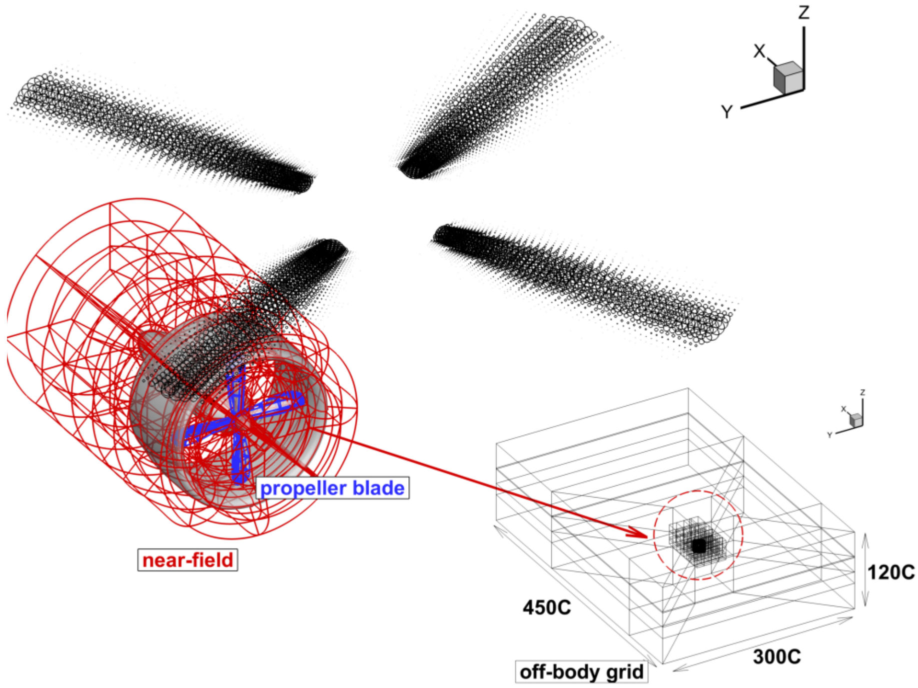

Figure 6.10: Grid topology for HMB3 simulations of the rotor/ducted propeller configuration.

the current simulations of rotor/propeller interactions. This study focused on the open propeller case. Grids of different sizes were used as listed in Table 6.5. Three different time steps were also examined, and the test matrix is shown in Table 6.6. The computations required about 5 to 6 main rotor revolutions, i.e. 30 to 40 propeller revolutions to reach a stable state when the main rotor was modelled with the unsteady actuator line models. With actuator disks, the computations were less expensive but still required about 10 propeller revolutions to settle. The grid dependence study hence used the larger step size with actuator disks due to the computational cost.

Table 6.5: Grid details for the mesh dependence study of the rotor/propeller interaction simulations.

Grids	Coarse	Medium	Fine
Total cell number/[in million cells]	11.9	18.9	34.1
Near field resolution/[in propeller 75% chords]	0.2	0.13	0.08

Table 6.6: Test matrix for the spatial and temporal resolution dependence study.

Grid\Propeller step size	$3^\circ/step$	$1^\circ/step$	$0.5^\circ/step$
Coarse	✓	-	-
Medium	✓	✓	✓
Fine	✓	-	-

The predictions of the phase-averaged total propeller thrust and torque using different grids and propeller steps (Table 6.6) are plotted in Figure 6.11. In general, the absolute differences were small while using different spatial and temporal resolutions, as the thrust varied within $2N$ and the torque differed within $0.05Nm$. The propeller produced a thrust at around $20N$ with a torque output of about $0.55Nm$. Nonetheless, different grids using the same larger time step size of $3^\circ/step$ showed minor differences in the thrust and torque predictions. While using the medium grid at different time step sizes, larger changes can be observed when the time step was reduced to $1^\circ/step$ from $3^\circ/step$. The differences between $1^\circ/step$ and $0.5^\circ/step$ remained small.

After evaluating the required spatial and temporal resolutions, a test matrix for the rotor/propeller interaction study was compiled as presented in Table 6.7. Simulations of the isolated ducted/open propellers were also performed for further reference. The main rotor was then modelled with actuator disks or actuator lines. A further simulation was also performed to verify the minimised interactions at an optimised position, as detailed in the next chapter. For simulations of the open propeller configuration, the medium grid in Table 3.7 was used. For the ducted propeller, a

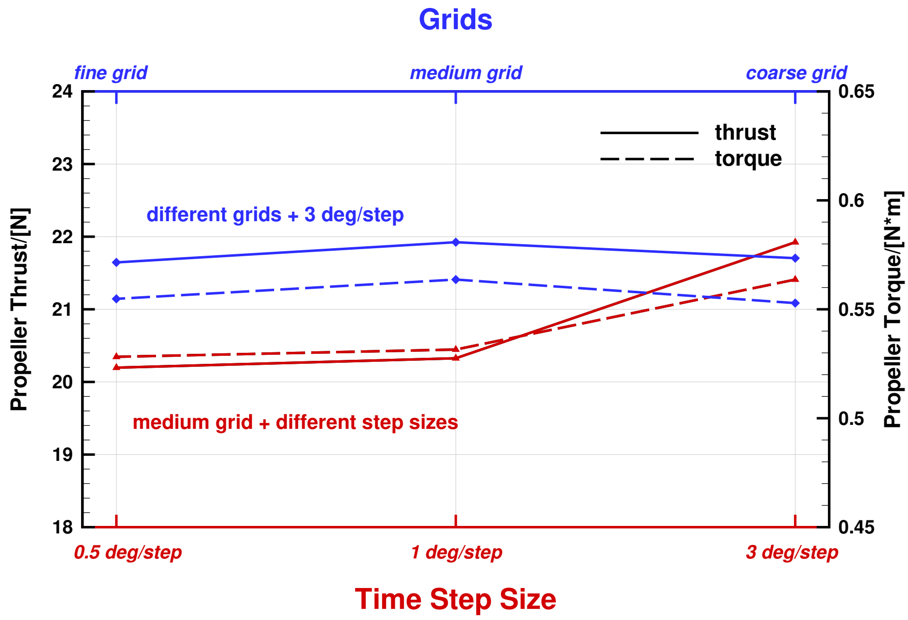

Figure 6.11: Examination of grid sizes and propeller time step sizes for the rotor/propeller interaction study.

fine grid of about 34.1 million cells was used. The increased cell number was mostly to fulfil the chimera interpolation requirement between the blades and duct.

Table 6.7: Test matrix for the propeller blade-resolved simulations.

Case	Main rotor modelling	Propeller modelling	Configuration	Grid size/[million cells]	Time step size/[$^\circ/step$]	Propeller position
1	non-uniform AD	resolved blades	open propeller	18.9	1	initial
2	non-uniform AL	resolved blades	open propeller	18.9	3	initial
3	non-uniform AD	resolved blades	ducted propeller	34.1	1	initial
4	non-uniform AL	resolved blades	open propeller	18.9	3	optimised

Later simulations using actuator disks employed the medium grid with a time resolution of $1^\circ/step$. However, for simulations using actuator lines, the medium grid and the larger time step of $3^\circ/step$ were adopted. This was mainly due to the restriction of computational costs. Because with actuator lines, 5 or 6 main rotor revolutions are necessary for the converged solution, which correspond to 30 and 36 propeller revolutions, respectively. Besides, with the resolved main rotor blade, to include all the frequencies, one must have flow solutions of at least 1 main rotor revolution, i.e. 6 propeller revolutions. These lead to excessively large computational costs when using finer time steps. To minimise the impact of the step size, the actuator line results were compared with the isolated propeller using the same step size.

6.4 Open Propeller Interactions

Simulation results using resolved propeller blades (while the main rotor was modelled by a non-uniform actuator disk) are shown in Figures 6.12(a) and 6.12(b). The actuator disk provided a constant but non-uniform downwash. The propeller blades hence experienced non-uniform and non-axial inflows, and the propeller wake was distorted by the downwash. The propeller wake later joined the main rotor wake downstream, forming a strong and complex super vortex. The cylindrical centre-body also contributed to the wake due to the downwash.

Simulation results using resolved propeller blades while the main rotor was modelled by non-uniform actuator lines are shown in Figures 6.13(a) and 6.13(b). Comparing to the steady actuator disk approach, the dominant flow features are similar, with the main rotor generating a non-uniform downwash for the propeller and the propeller wake joining the super vortex. However, the actuator lines managed to provide more realistic and complex flow details thanks to the time-resolved blade motion. The tip and root vortices by the discrete blades were resolved, providing time-varying downwash as inflow to the propeller. Interactions between the propeller and main rotor wakes were also more complex due to the added flow details.

Phase-averaged integrated aerodynamic loads of the propeller under the main rotor are presented in Table 6.8. All forces and moments were normalised using the isolated propeller thrust T_0 and torque Q_0, respectively, to bring out the relative changes due to the interactions. The subscripts x, y, z denote the Cartesian directions as shown in Figure 6.9. In general, the propeller in-plane forces were almost negligible compared to the thrust, but the vertical forces were relatively larger due to the main rotor downwash. The disk pitching moment due to the unbalanced disk loading was also negligible, but the yawing moment was larger.

Comparing the isolated propeller, the actuator disk model predicted a thrust reduction by about 5.5% and a torque reduction by about 4.3%. It should be noted that these corresponded to very small absolute thrust and torque changes of about $1.1N$ and $0.024Nm$, respectively. The predicted thrust and torque reductions agreed well with free-wake predictions by Boisard[143] and the blade-resolved simulations using the Helios solver [145]. However, blade-resolved simulations

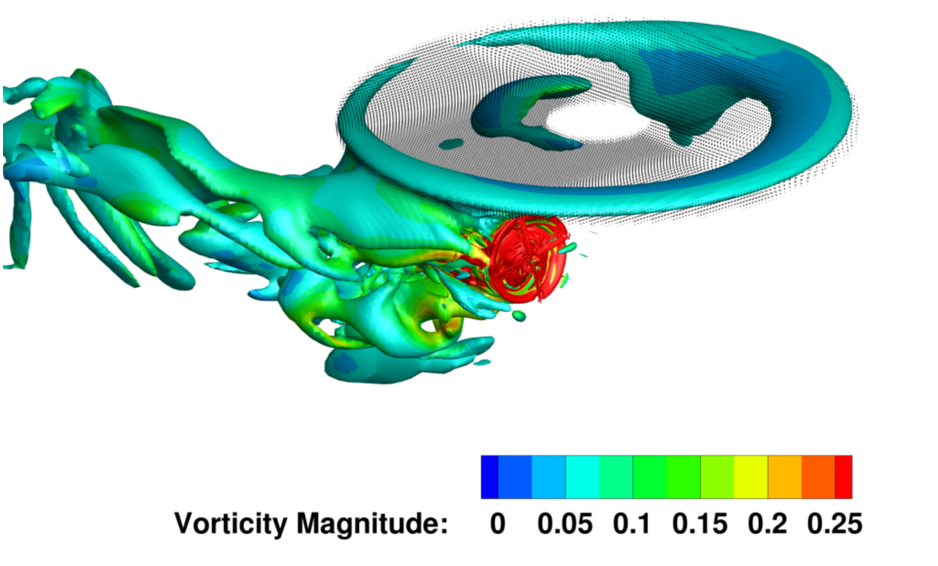

(a) Iso-surface of dimensionless q criteria, coloured by vorticity magnitude.

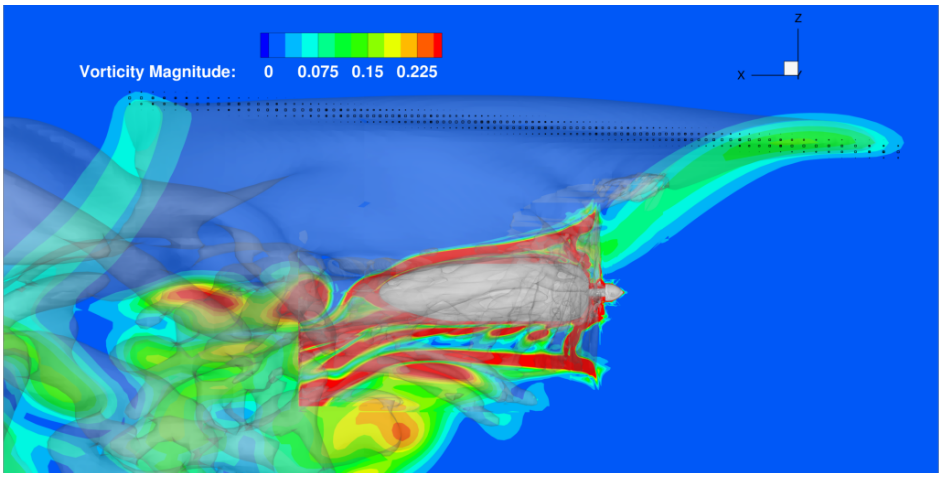

(b) Vorticity contours through the propeller disk.

Figure 6.12: Instantaneous flow details of the rotor/propeller wake interactions using resolved propeller blades and steady, non-uniform actuator disk for the main rotor(k-ω SST).

using the elsA solver [143, 145] predicted a small thrust increase by 1.7%, which differed from the current AD modelling by a small absolute value of about 1.5N. The Helios results reported a thrust reduction similar to the current AD modelling. The yawing moment predicted was about 25% of the propeller torque. The actuator line model suggested almost unchanged overall thrust and torque values. It also predicted a lower disk yawing moment of about 16.3% the disk torque. These were due to the slightly weaker downwash by the actuator line, as the Gaussian tends to smooth out the

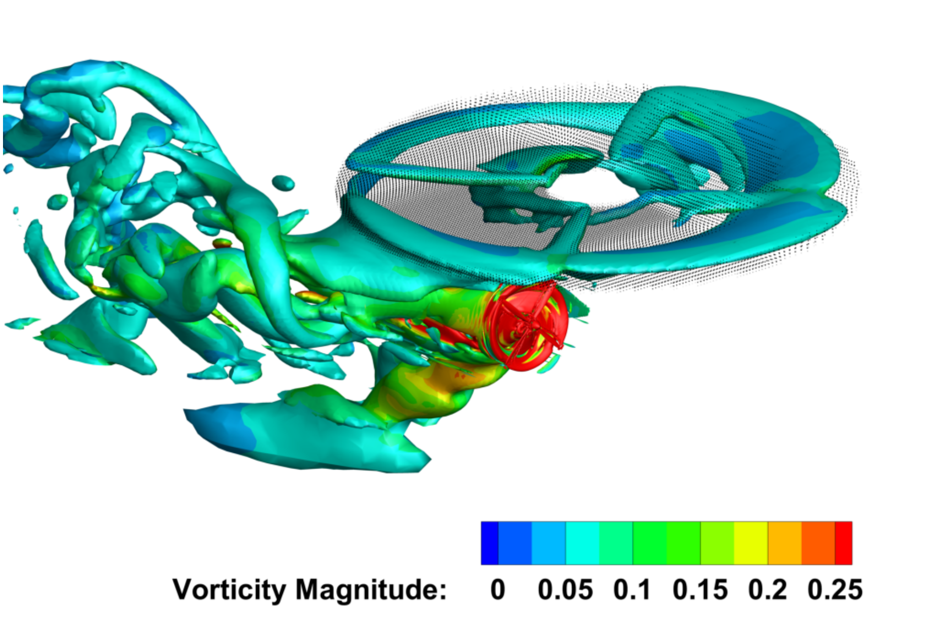

(a) Iso-surface of dimensionless q criteria, coloured by vorticity magnitude.

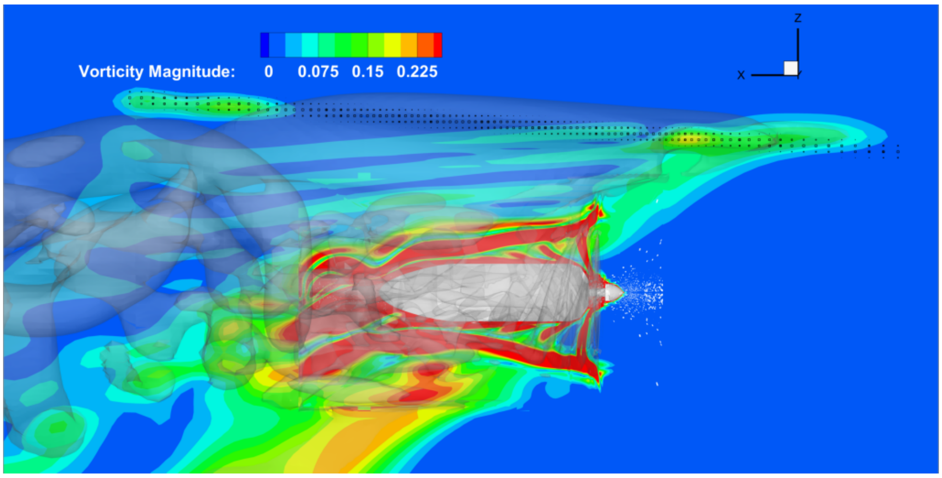

(b) Vorticity contours through the propeller disk.

Figure 6.13: Instantaneous flow details of the rotor/propeller wake interactions using resolved propeller blades and unsteady, non-uniform actuator lines for the main rotor (k-ω SST).

pressure jumps.

More flow details close to the open propeller subject to the main rotor downwash are presented in Figures 6.14(a) to 6.14(d). The flow features are rather complex as the propeller wake was distorted by the downwash, and later hit on the centre-body and broke into more delicate structures. A pair of super vortices were also forming up because of the distorted wake. It is also interesting to notice that the wake was not deflected simply downwards, but also slightly outboards.

This should be attributed to the non-uniform downwash together with the propeller blade rotation.

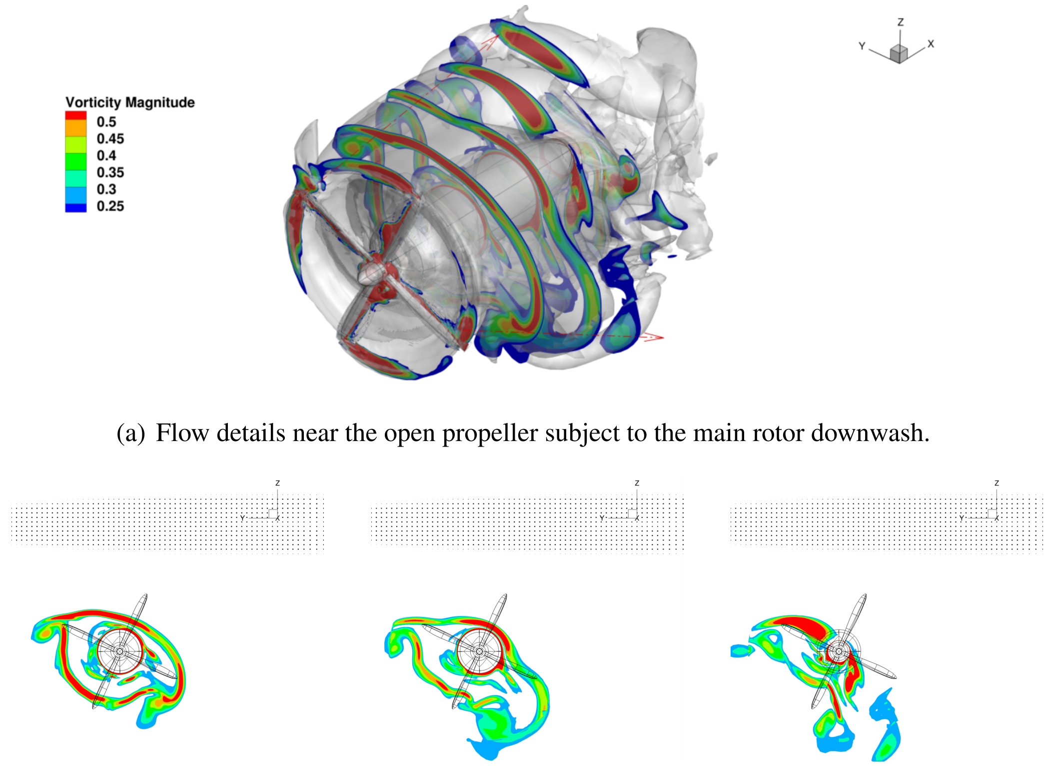

(a) Flow details near the open propeller subject to the main rotor downwash.

(b) Vorticity contours at $x/C = 2$ slice.

(c) Vorticity contours at $x/C = 4$ slice.

(d) Vorticity contours at $x/C = 6$ slice.

Figure 6.14: Instantaneous Flow details close to the open propeller subject to the main rotor downwash. C is the main rotor chord length.

Table 6.8: Propeller forces and moments subject to main rotor downwash using different rotor modelling approaches. T_0 and Q_0 refer to the isolated propeller thrust and torque.

Case	Condition	F_x/T_0 (Thrust)	F_y/T_0	F_z/T_0	M_x/Q_0 (Torque)	M_y/Q_0 (Pitching)	M_z/Q_0 (Yawing)
1	AD+initial position	94.5%	0.4%	2.2%	95.7%	4.5%	24.9%
2	AL+initial position	100.5%	0.8%	2.3%	99.8%	5.8%	16.3%

Thrust and torque variations on a single blade due to the non-axial inflow were also extracted as shown in Figures 6.15. The thrust values were also normalised by T_0. For the isolated propeller, the blade thrust also saw a small variation because of flows at the blade root and interactions with the centre-body. When the main rotor was modelled either through the steady AD or the unsteady AL, the blade experienced large temporal variations in the axial force due to the non-axial inflow.

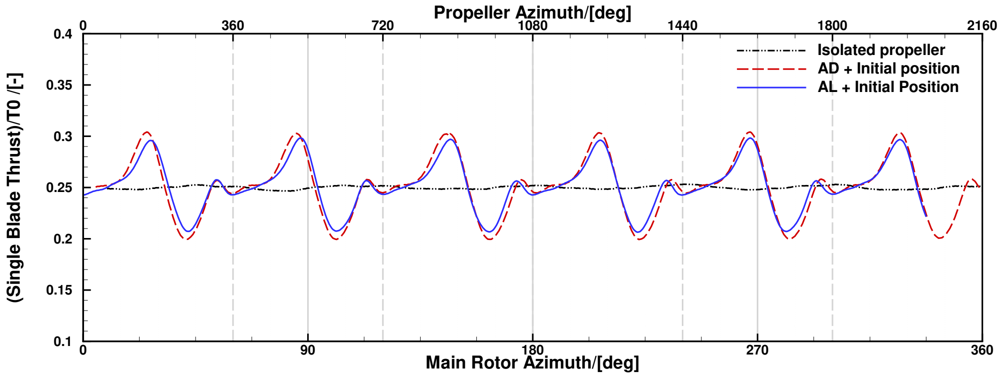

Figure 6.15: Single blade thrust variations of the open propeller subject to main rotor downwash.

Disk loading distributions of the propeller in axial flight, under the main rotor, and their relative changes are plotted in Figures 6.16(a) to 6.16(c). Due to the main rotor downwash, the disk thrust loading became asymmetric. In Figure 6.16(c), the loading distribution was obtained by subtracting the isolated propeller loading distributions from the non-uniform actuator disk results. It can be seen that the blade experienced a thrust increase as it is encountering the main rotor downwash between 90° and 180° azimuth angles. The thrust was decreased as the blade leaves the downwash between $\psi = 180°$ and 270°. These also agree well with the single blade thrust variations in Figure 6.15. The imbalanced disk loading also caused the larger disk yawing moment in Table 6.8. The pitching moment was not significantly affected as the pitching moment contributions from the thrust changes cancelled out each other. Overall, the interactions affected mostly the upper half of the propeller disk, which is consistent with Figure 6.12(b) where the main rotor wake mostly penetrated the disk upper half.

Relative Standard Deviation (RSD) values of the total thrust and the single blade thrust are analysed in Figure 7.12 to quantify the level of fluctuations. It can be seen in Figure 6.17 that the total thrust only has small variations of less than 1% at the initial position under the main rotor, as suggested by both steady AD and unsteady AL results. However, the single blade thrust experienced large levels of fluctuation around 10%, due to the main rotor interactions. The steady AD brought slightly larger fluctuations, which should be due to the stronger time-averaged downwash.

Fast Fourier Transformations (FFT) of the overall thrust signals are shown in Figure 6.18.

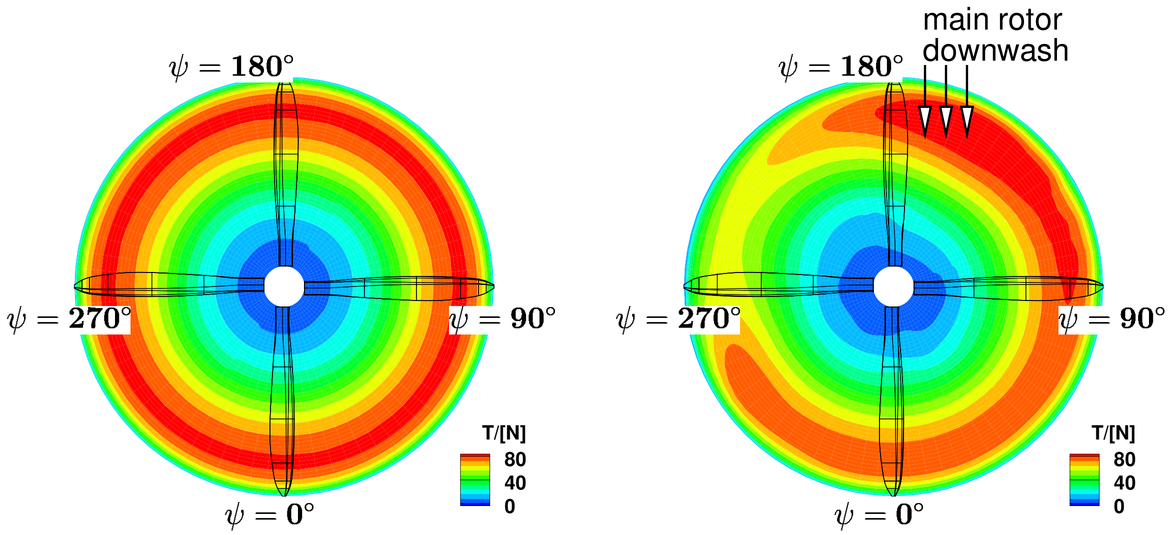

(a) Open propeller in axial flight.

(b) Open propeller under main rotor downwash.

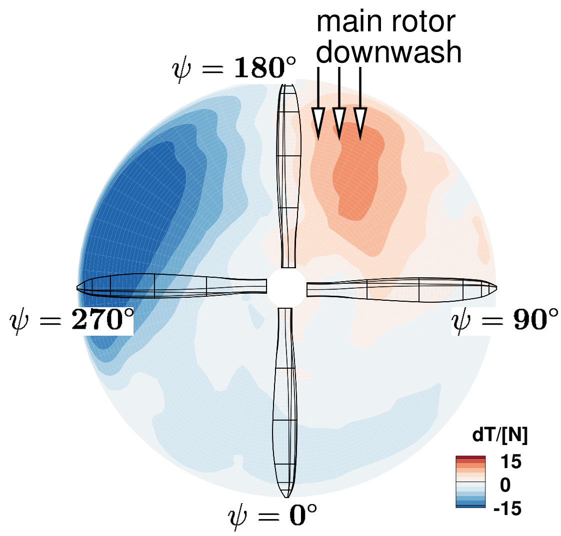

(c) Loading variations due to downwash.

Figure 6.16: Open propeller disk loading distributions in axial flight and under downwash (viewed from behind).

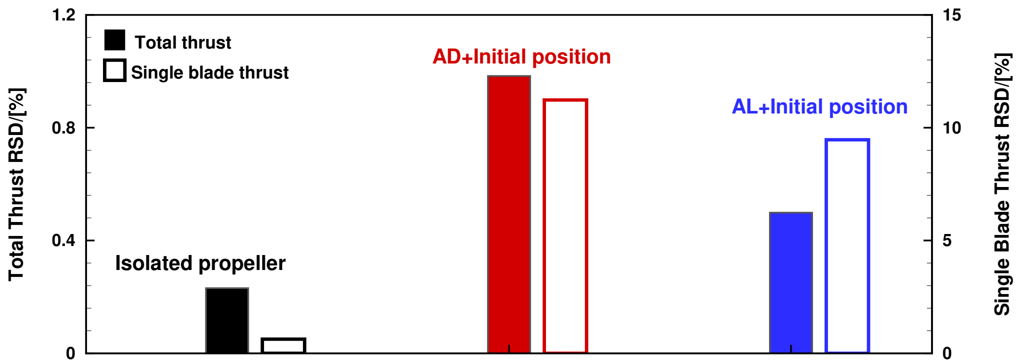

Figure 6.17: Relative Standard Deviation (RSD) levels of the total blade thrust and single blade thrust in comparison with the isolated propeller, with different main rotor representations.

For the clean propeller, the magnitude of the harmonic components is minor due to the modest temporal variations. Nonetheless, a small peak is noticed at the first propeller BPF (Blade Passing Frequency). Another small peak at the lower frequency should be due to the wake and interactions with the centre-body. For steady AD, the signal shows a strong peak at the first propeller BPF, and a rather weak peak at the second propeller BPF. As for the unsteady AL, several peaks with different magnitudes across the spectrum can be observed. The strongest peak is also at the propeller BPF, but its magnitude is lower than the steady AD results. The second strongest, which is of about half the magnitude of the first, is at the first main rotor BPF. Other peaks can be observed at the harmonics of either the propeller BPF or the main rotor BPF. These complex frequency compositions along with the temporal variations in the blade loading may lead to significant vibration and structural problems that need further investigations.

Overall, for the current rotor/propeller combination at the low advance ratio of $\mu = 0.05$, the aerodynamic interactions between the propeller and rotor mainly affect the propeller performance, especially the upper half of the propeller disk. The propeller blade experienced a thrust increase when encountering the downwash near $\psi = 150°$ and soon saw a thrust decrease as it is leaving the downwash near $\psi = 210°$. Frequency analyses show that the loading variation consists of strong high-frequency components corresponding to the propeller rotation, and relatively weak low-frequency components corresponding to the main rotor blade passage. The time-averaged total propeller thrust and torque varied little in terms of absolute values because of the interactions,

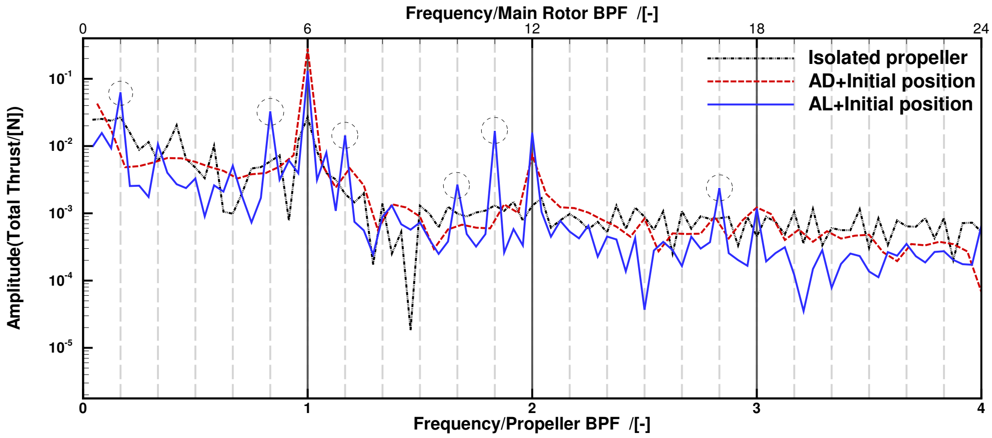

Figure 6.18: Frequency component of the overall blade thrust of the propeller in isolation and under the main rotor, with different main rotor modelling strategies.

and generally, reductions are seen within $1N$ and $0.05Nm$, respectively. The relative changes, however, were larger because of the small baseline values. The AD model predicted a thrust decrease by about 5.5%, as well as, a torque decrease by about 4.3%. The AL model predicted almost unchanged time-averaged thrust and torque values, which should be due to the weaker downwash induced. Both models predicted negligible disk in-plane forces and a slightly larger disk yawing moment because of the imbalanced disk loading. Nonetheless, larger temporal variations in the total and single blade loading signals were increased due to the downwash, which was consistent between the AD and AL modellings. Fluctuation levels of total thrust were generally within 1%, while the single blade thrust varied by 10% about the mean values.

6.5 Ducted Propeller Interactions

Simulations of the ducted propeller under the main rotor were also performed using non-uniform actuator disks to reduce the computational cost. The resolved flow details are shown in Figures 6.19(a) and 6.19(b). Similar to the open propeller case in Figures 6.12(a) and 6.12(b), the main rotor wake hit mostly the upper half of the propeller disk, but the wake was moderately accelerated by the duct curvature. The propeller wake was very mildly affected by the downwash near the propeller disk due to the duct shielding. The propeller wake was distorted by the downwash later further downstream as it exited the duct.

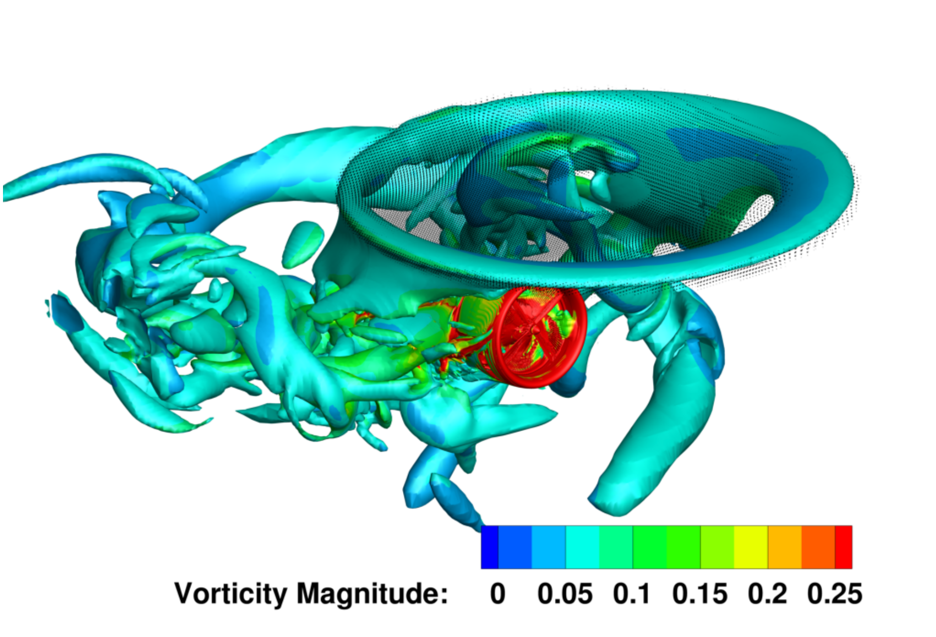

(a) Iso-surface of dimensionless q criteria, coloured by vorticity magenitude.

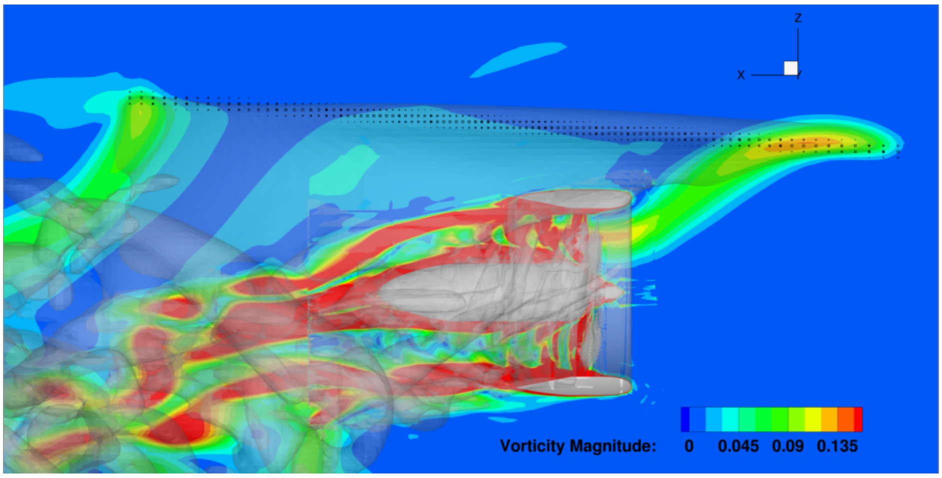

(b) Vorticity contours through the propeller disk.

Figure 6.19: Instantaneous flow details of the rotor/ducted propeller wake interactions using resolved propeller blades and non-uniform actuator disks for the main rotor (k-ω SST).

More flow details close to the ducted propeller are presented in Figures 6.20(a) to 6.14(d). Compared to the open propeller in Figure 6.14(a), the ducted wake was distorted only mildly, and the distortion happened only after the duct exit. It is also noted the ducted wake were of lower magnitudes. Despite of these, the wake was also deflected by the downwash, and a pair of super vortices were also forming up. The wake deflection, however, was mostly towards the downwards direction, as effects of the blade rotation were largely blocked by the duct.

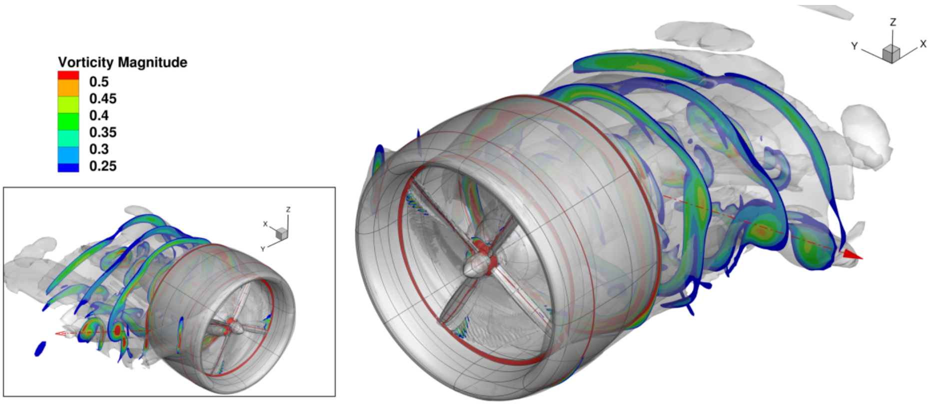

(a) Flow details near the ducted propeller subject to the main rotor downwash.

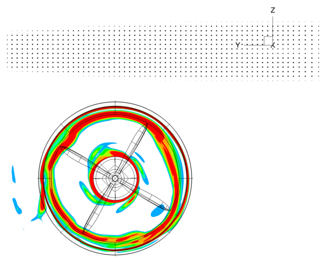

(b) Vorticity contours at $x/C = 2$ slice.

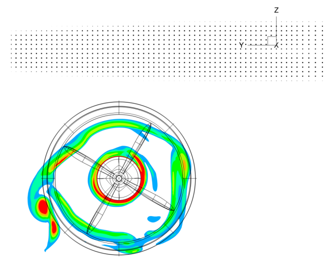

(c) Vorticity contours at $x/C = 4$ slice.

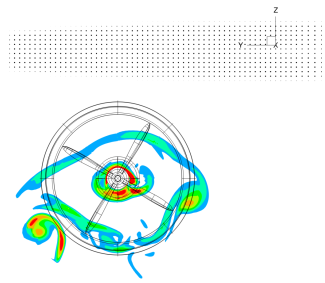

(d) Vorticity contours at $x/C = 6$ slice.

Figure 6.20: Instantaneous flow details close to the ducted propeller subject to the main rotor downwash. C is the main rotor chord length.

The component and total phase-averaged aerodynamic loadings are shown in Table 6.9. The loading data is also normalised by the isolated open propeller values T_0 and Q_0. Comparing to the open propeller under the main rotor downwash in Table 6.8, the duct and propeller combination generated more thrust by $17.5\%T_0$, of which 38% was contributed from the duct. The sideways force in the y direction was still small, but a considerable amount of downwards force was observed, corresponding to about $25\%T_0$. This mostly came from the duct due to its blockage of the main rotor downwash.

As for the moments about the propeller centre of rotation, the total torque was $90.9\%Q_0$. However, it should be noted that the duct contributed $2.5\%Q_0$ to the anti-torque due to the non-uniform downwash. The propeller torque was about $93.4\%Q_0$, which was slightly lower than the open propeller under downwash. The combination also showed a significant nose-down pitching moment of $54.7\%Q_0$, which is considerably higher than the open propeller configuration. Note that contributions from the propeller and duct were of opposite directions. The propeller produced a large nose-up pitching moment of $10.6\%Q_0$, while the duct generated a larger nose-down moment of $65.3\%Q_0$. The propeller also had a yawing moment of $17.2\%Q_0$ towards the port side (positive z axis), but it was balanced by the duct contribution of $-19.6\%Q_0$ towards the opposite direction. The overall yawing moment was $2.3\%Q_0$, which is lower than the open propeller case.

Table 6.9: Propeller forces and moments subject to main rotor downwash using different rotor modelling approaches. T_0 and Q_0 refer to the isolated open propeller thrust and torque.

Component	F_x/T_0 (Thrust)	F_y/T_0	F_z/T_0	M_x/Q_0 (Torque)	M_y/Q_0 (Pitching)	M_z/Q_0 (Yawing)
ducted blades	68.7%	0.1%	-1.4%	93.4%	10.6%	17.2%
duct	42.2%	3.3%	-23.5%	-2.5%	-65.3%	-19.6%
total	111.0%	3.4%	-24.9%	90.9%	-54.7%	-2.3%

Thrust and torque changes compared to the isolated ducted propeller at $V_\infty = 5m/s$ are presented in Table 6.10. Due to the downwash, the propeller thrust was decreased, and so was its torque. The duct thrust was very slightly increased, and a small anti-torque moment was also produced due to the non-uniform downwash. Comparing to the isolated case, the overall thrust and torque were both reduced. Nonetheless, it should be pointed out that the duct torque reduction corresponds to reductions of moments in the axial direction, and does not correspond to overall power reductions. The power input should be computed by the product of the propeller torque and its rotational speed.

Table 6.10: Loading changes of the ducted propeller under downwash compared to the isolated case. Values normalised by the isolated open propeller thrust T_0 and torque Q_0.

Component	dT/T_0	dQ/Q_0
propeller	-10.9%	-4.8%
duct	1.3%	-1.9%
total	-9.5%	-9.1%

The phase-averaged duct surface pressure distributions were extracted and presented in Figures 6.21(a) to 6.21(e). In Figure 6.21(a), a low-pressure region is noted at the inner side of the inlet between $\psi = 135°$ and $270°$, while a high-pressure region is noted at the duct outer surface due to the downwash.

Figure 6.21(b) compares the duct sections at $\psi = 0°$ and $180°$. It is noted that at $\psi = 180°$ the pressure at the duct inlet was much lower, while the pressure at the outer surface was stronger. This agrees with the previous investigations of ducted propellers at crosswind and explains the strong nose-down pitching moment of the duct. At the symmetric sections of $\psi = 45°$ and $315°$ at the duct lower half (Figure 6.21(c)), the pressure distributions were almost identical. At $\psi = 90°$ and $270°$ (Figure 6.21(d)), only small differences can be noted. However, at $\psi = 135°$ and $225°$ at the upper half, larger differences can be noted as the $\psi = 225°$ section had lower pressure at the leading edge. The pressure differences at these symmetric sections resulted in the duct torque along the x axis. This is also a difference from the ducted propeller at uniform crosswind as presented in Chapter 4. Overall, the duct was affected by the main rotor downwash mostly between $\psi = 135°$ to $270°$.

Loading distributions of the ducted propeller disk in axial flight and under downwash are shown in Figures 6.22(a) and 6.22(b). Note that the ducted blades were offloaded, hence the disk loadings were lower than the open propeller case in Figures 6.16(a) and 6.16(b). The loading variations due to the downwash were subtracted and presented in Figure 6.22(c). For the ducted propeller under downwash, the thrust decreased between $\psi = 150°$ to $300°$ and increased elsewhere. The maximum blade thrust was near $\psi = 120°$. The integrated single blade thrust variation is shown in Figure 6.23, and it agrees well with the disk loading distribution. The disk loading distribution also explains the disk out-of-plane moments results of Table 6.9.

In terms of thrust variation level, the Relative Standard Deviation values are presented in Table 6.11. The total blade thrust RSD level is still small, while the single blade thrust variation level is slightly lower than the open propeller blades. As shown in Figure 6.23, the ducted blades had lower absolute thrust values, as well as, lower absolute variations. The duct thrust was higher than the single blade thrust, but its variation was negligible.

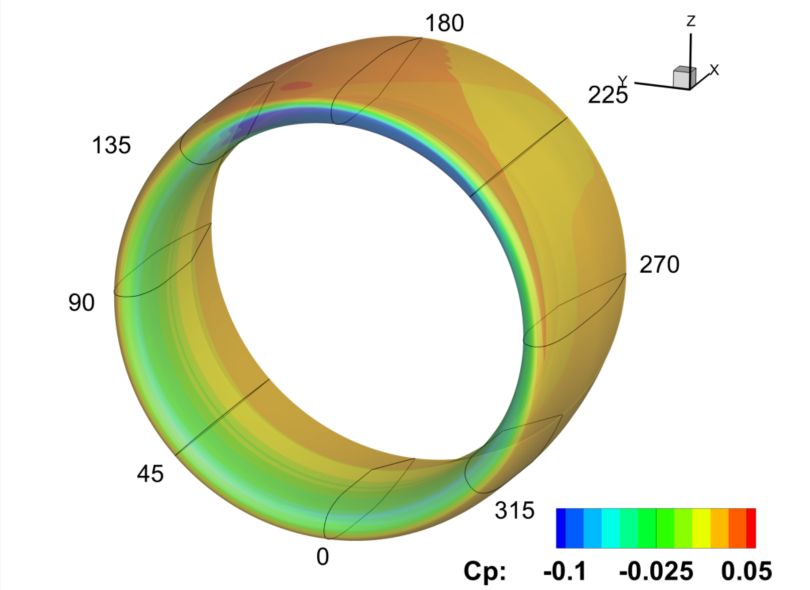

(a) Duct surface pressure coefficient distributions.

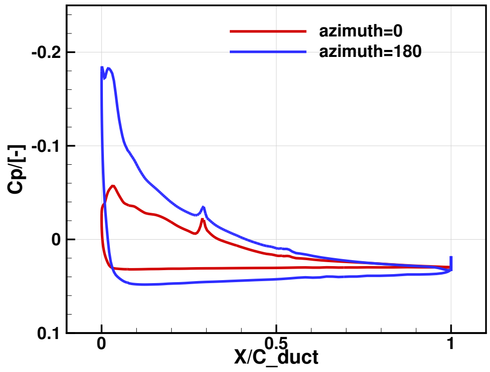

(b) Cp distributions at propeller $\psi = 0^\circ$ and 180°.

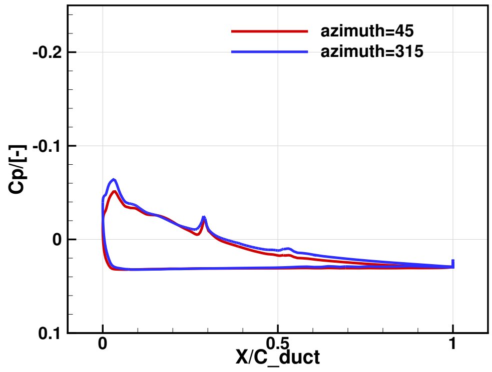

(c) Cp distributions at propeller $\psi = 45^\circ$ and 315°.

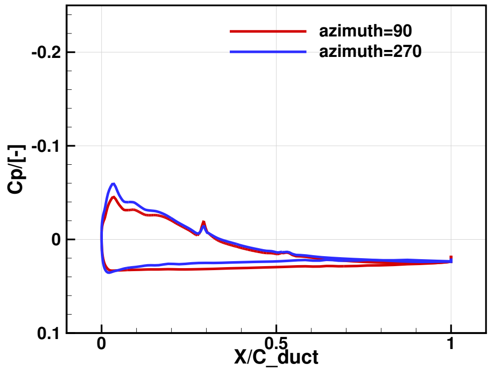

(d) Cp distributions at propeller $\psi = 90^\circ$ and 270°.

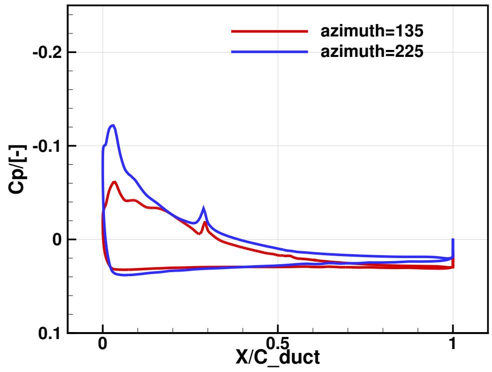

(e) Cp distributions at propeller $\psi = 135^\circ$ and 225°.

Figure 6.21: Phase-averaged duct surface pressure distributions. The pressure coefficients were computed using the main rotor tip speed.

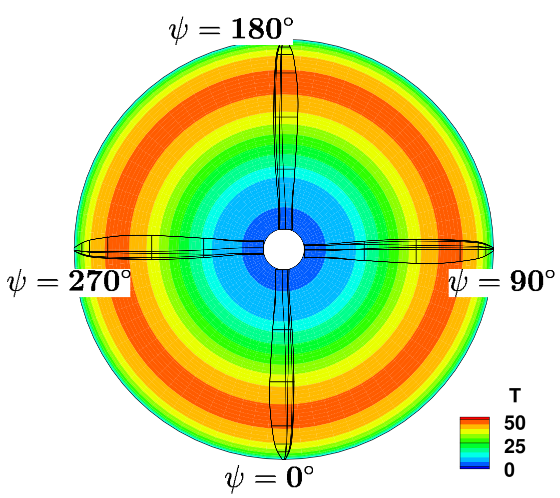

(a) Ducted propeller in axial flight.

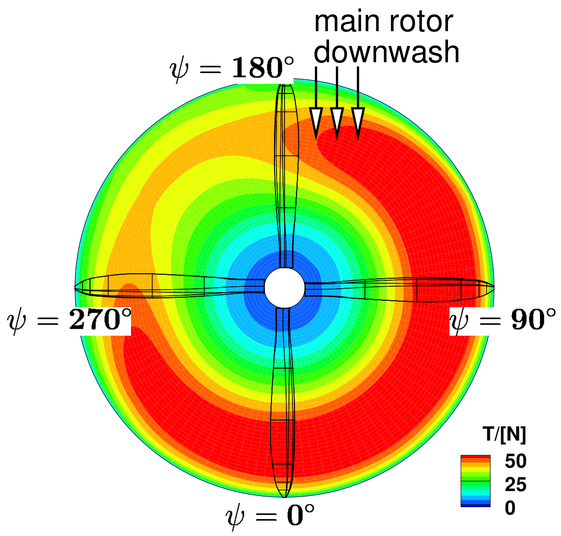

(b) Ducted propeller under main rotor downwash.

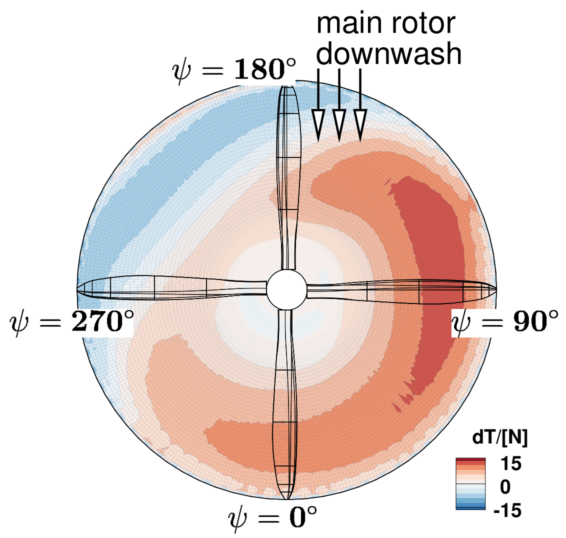

(c) Loading variations due to downwash.

Figure 6.22: Ducted propeller disk loading distributions in axial flight and under downwash (viewed from behind).

Table 6.11: Thrust variation level of the ducted propeller under downwash.

Component	Total thrust RSD	Single blade thrust RSD
ducted blades	1.2%	10.6%
duct	0.6%	-

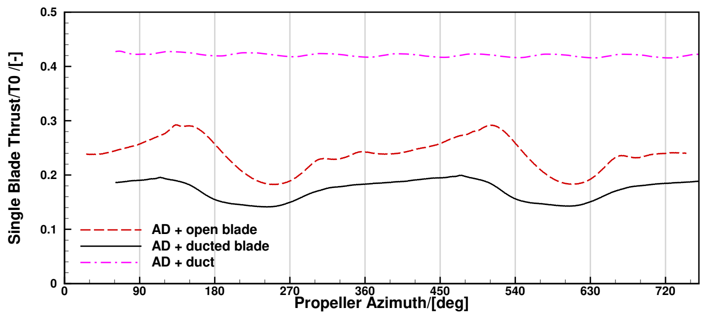

Figure 6.23: Component thrust variations due to the downwash and comparisons with the open propeller thrust.

6.6 Chapter Summary

This chapter investigated the aerodynamic interactions between the main rotor and the ducted and open propellers. The following conclusions can be derived from the study:

1. For the current rotor/propeller combination at the low advance ratio of $\mu = 0.05$, the aerodynamic interactions between the propeller and rotor mainly affect the propeller performance, especially the upper half of the propeller disk. The propeller blade experienced a thrust increase when encountering the downwash near $\psi = 150°$, and a thrust decrease near $\psi = 210°$. Frequency analyses show that the loading variation consists of strong high-frequency components corresponding to the propeller rotation, and relatively weak low-frequency components corresponding to the main rotor blade passage. The time-averaged total propeller thrust and torque varied little in terms of absolute values because of the interactions. The relative changes, however, were larger because of the small baseline values. The AD model predicted a thrust decrease by about $5.5\%T_0$, as well as, a torque decrease by about $4.3\%Q_0$. The AL model predicted almost unchanged overall thrust and torque values, which should be due to the weaker downwash induced. Both models predicted negligible disk in-plane forces and a slightly larger disk yawing moment of about $25\%Q_0$ because of the imbalanced disk loading. Nonetheless, larger temporal variations in the total and single blade loading signals were seen due to the downwash, which was consistent between the AD and AL modellings. Fluctuation levels of total thrust were generally within 1%, while

the single blade thrust varied about 10% about the mean values.

2. A rotor/ducted propeller combination was also examined and compared with the open propeller case at the same operating condition. Compared to the open propeller case, the ducted blades were offloaded but the overall thrust was higher due to contributions from the duct. The overall torque and yawing moments were also reduced. The ducted blades experienced lower levels of loading variations thanks to the duct shielding. However, a considerable downwards force ($24.9\%T_0$) and a nose-down pitching moment ($54.7\%Q_0$) were observed. These mostly came from the duct surface due to its blockage of the downwash. The duct also produced a considerable anti-toque moment ($12.9\%Q_0$) in the axial direct because of the non-uniform downwash. Under the main rotor downwash, the ducted blades produced lower thrust and torque by about $9.5\%T_0$ and $9.1\%Q_0$, respectively, compared to the isolated ducted propeller case, which is consistent with the open propeller case.

The next chapter will focus on the configuration optimisation for minimised aerodynamic interactions between the main rotor and the auxiliary propulsors by adjusting their relative positions.

Chapter 7

Configuration Optimisation for Minimised Rotor/Propeller Interactions[1]

By representing the main rotor with actuator disks/lines, the previous chapter shows that the interactional aerodynamics can be resolved at reasonable accuracy while the computational cost has been greatly reduced compared to fully blade-resolved simulations. However, this approach can still be excessively costly for parametric investigations or optimisation studies.

This chapter presents novel methods for the modelling and optimisation of interactional aerodynamics between rotors. A further simplified modelling approach for the rotor/propeller interactions was proposed by representing the main rotor and the propeller as actuator disks. A novel inflow distortion metric was proposed to quantify the aerodynamic interference. Combined with Kriging surrogate models, parametric investigations of the interactional aerodynamics between rotors were enabled. The novel inflow distortion metric was also differentiated following the adjoint formulation to provide gradient information. Novel gradient-free and gradient-based optimisation frameworks were also compiled to minimise the interference between the main rotor and the propeller by varying the propeller position, i.e. the configuration optimisation. The optimisation results were later verified with blade-resolved simulations.

[1] This chapter has been published in T. Zhang, G. N. Barakos, " Towards Vehicle-level Optimisation of Compound Rotorcraft Aerodynamics", AIAA Journal, Vol. 60, No.3, pp. 19371957, 2021.

7.1 Simplified Modelling and the Inflow Distortion Metric

The implementation and flow details of the actuator disk models are shown in Figures 7.1(a) and 7.1(b). The propeller actuator disk injects momentum and energy into the flow passing through it, thereby accelerating the flow and inducing a pressure jump corresponding to the rotor thrust. The main rotor was modelled by a non-uniform disk, while the propeller was represented by a uniform disk. Although the strength of the injected momentum and energy have been prescribed, the induced flow features are still subject to the non-uniform rotor downwash. As can be seen from the figures, the main rotor wake is ingested by the propeller disk, and the propeller wake is distorted due to the main rotor downwash. Comparing to the blade-resolved simulations, although many complex flow details have been missed, the dominant flow features in the velocity and pressure fields have been resolved by the simple momentum-based model. On a coarse grid of about 1.5 million cells, with uniform cell size distributions near the disk region, the computational cost using both steady actuator disks is about 5 CPU hours, a significant reduction compared to the blade-resolved simulations. Such simplifications of rotor modelling enabled quick and systematic investigations of the interactional aerodynamics with different combinations of rotor position, thrust, advance ratio etc.

To quantify the aerodynamic interference while using actuator disk models, an inflow distortion factor metric for a rotor disk is defined as follows

$$I_i = \left(1 - \frac{\int \frac{u_i^2}{V^2} dS}{\int dS}\right) \times 100\%, \tag{7.1}$$

where the subscript i denotes the Cartesian direction of interest, usually the disk axial direction. The integration is carried out over the entire rotor disk plane with dS denoting an infinitesimal disk area element. u_i is the local velocity in the i direction at a disk plane element, and V is the local velocity magnitude. The definition of this metric is rather simple and is linked with the momentum theory analysis of rotor performance. Essentially, it reflects the proportion of axial speed components in the total velocity passing through the rotor disk plane. A 0% inflow distortion represents an ideal rotor disk that induces velocities only in the axial direction, while 100% inflow

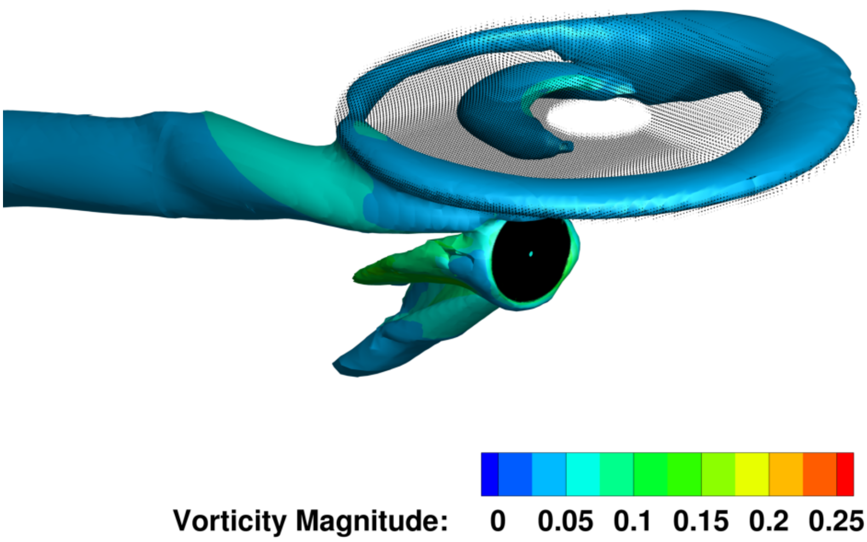

(a) Iso-surface of dimensionless q criteria, coloured by vorticity magnitude.

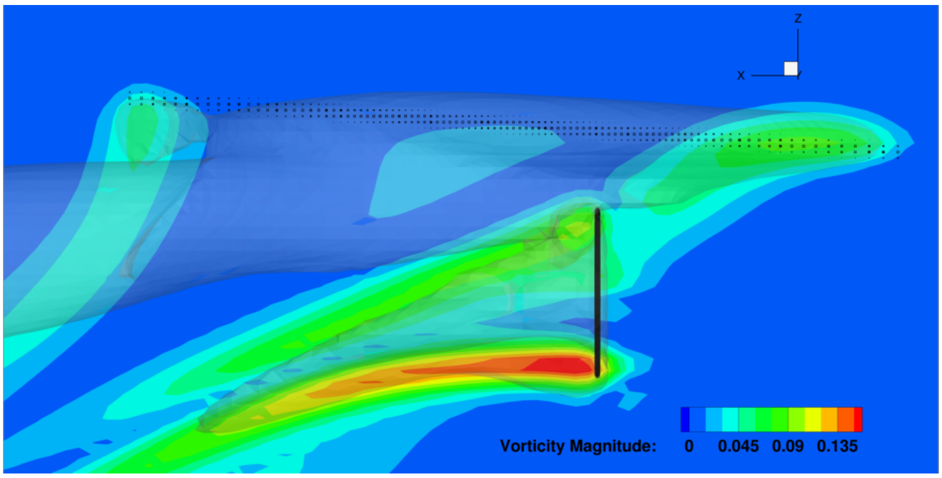

(b) Vorticity contours through the propeller disk.

Figure 7.1: Instantaneous flow details of the rotor/propeller wake interactions using steady, uniform actuator disk for the propeller and steady, non-uniform actuator disk for the main rotor. A nacelle was not included for simplicity.

distortion suggests that the rotor disk is completely distorted and is incapable of produce any axial propulsion. Note that an isolated rotor would still have a small inflow distortion due to radial/tangential velocities and effects of wake systems, especially when the rotor axial velocity is low. In practical use, the inflow distortion factor can be normalised by the isolated rotor value to reflect changes relative to the isolated case. It should be pointed out that this definition has

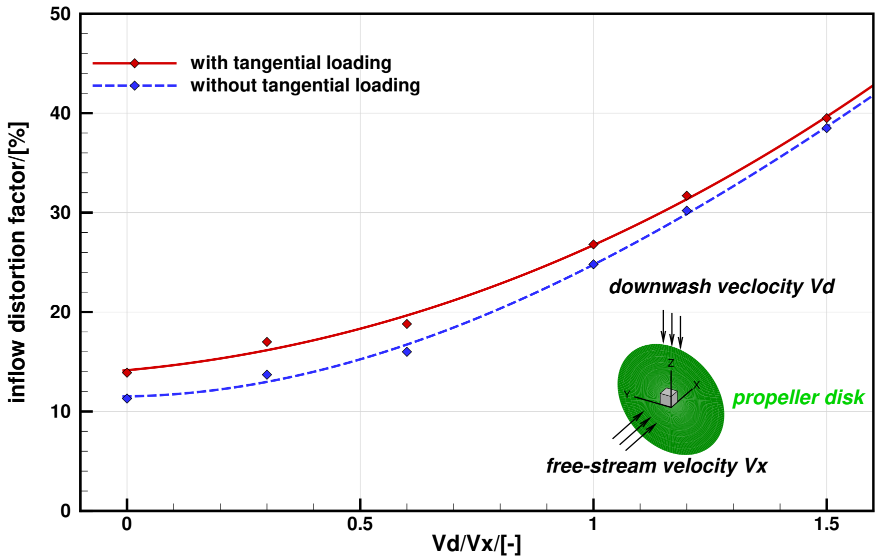

Figure 7.2: Inflow distortion factors for a propeller disk at increasing downwash velocities. The propeller was modelled with a uniform actuator disk with and without the tangential loading.

ignored axial velocity variations and tangential/radial velocities. Nonetheless, this metric was used because of its effectiveness for the current problem and its simple form, which makes the computer implementation and gradient computation especially simple.

The effectiveness of the proposed inflow distortion metric for propellers suffering from downwash flows is illustrated in Figure 7.2. The test was performed by introducing an increasing uniform sideways flow velocity for the APC propeller in axial flight at $5m/s$, imitating rotor downwash for propellers. The propeller was modelled using uniform actuator disks with and without tangential loadings. The inflow distortion variations with the increasing downwash velocity are plotted in Figure 7.2. As can be noted, the distortion factors were low at about 12% for the isolated propeller with only the free-stream velocity, mainly due to the low axial velocity, the in-plane disk radial velocities and pressure-induced flows at the disk edge. With the growing downwash velocity, the inflow distortion increased. When tangential loadings were also included, the inflow distortion factors were about 2% higher because of the tangential velocity component. This difference was small and diminished as the sideways velocity grew, suggesting that the tangential velocity only has a secondary effect on the inflow distortion metric.

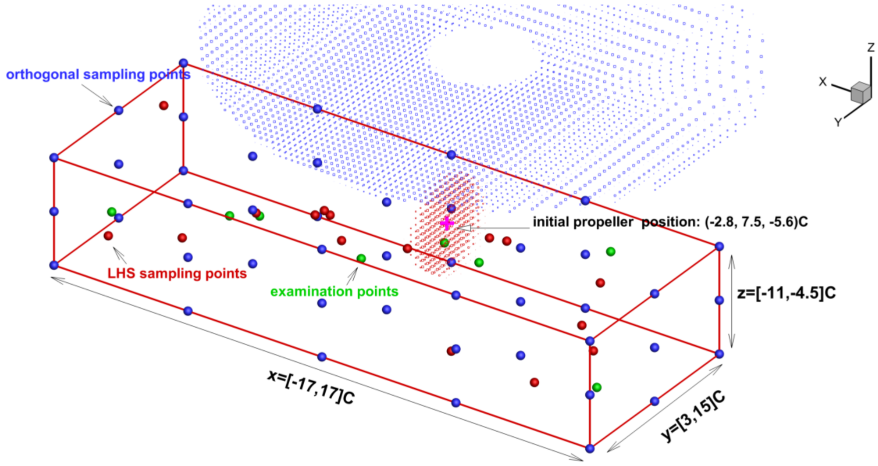

Figure 7.3: Boundary of the allowed propeller centre positions under the main rotor. All units are normalised by the main rotor chord.

7.2 Surrogate Approximations and Parametric Study of Rotor/Propeller Interactions

Using the simplified model and the quantification metric for interactions, the aerodynamics of the propeller was investigated while placed at different positions under the main rotor. The propeller disk was allowed to move within a cuboid region under the main rotor, as shown in Figure 7.3. For this parametric study, a fully-structured, Cartesian grid of about 1.3 million cells was used. The Chimera overset method was used to allow for local mesh refinement near the propeller. Within the large region in Figure 7.3, a uniform cell distribution of $0.4C$ was ensured in all directions, where C is the main rotor blade chord length. This is fine enough to resolve the dominant flow features since both rotors have been modelled by actuator disks and no wall boundaries are present. The use of this relatively coarse grid for the problem is needed to strike a balance between simulation accuracy and computational cost. The initial HMB3 flow computation using this grid took about 25 CPU hours for very fine convergence, while each successive computation restarting from previous solutions took only about 5 CPU hours.

Several positions were studied, featuring a mixture of orthogonal sampling and Latin hypercube sampling (LHS). 45 orthogonal points ($3 \times 3 \times 5$) and 16 LHS points were initially used. The inflow distortion factors were then computed from the flow solutions. The distortion distribution

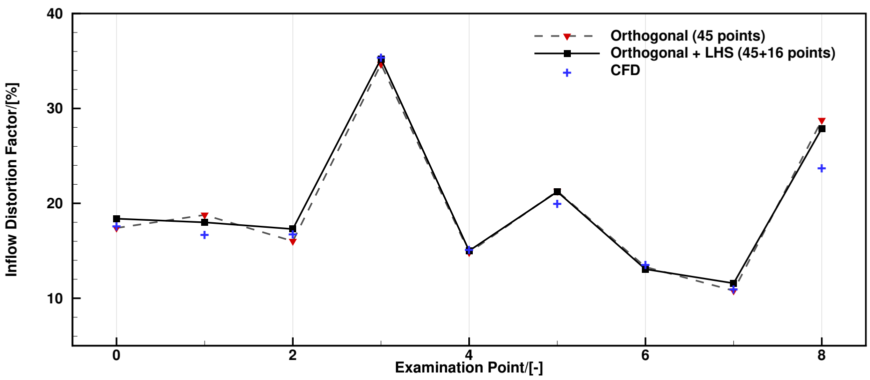

Figure 7.4: Validation of the meta-model at an extra 8 Latin hypercube points and the initial point.

was considered as a function depending on the propeller position and was then approximated using a Kriging model. The accuracy of the Kriging approximation was examined at 8 extra LHS points plus the initial position, as shown in Figure 7.4. The Kriging predictions based on 45 orthogonal sampling points are very close to the CFD results. Adding 16 more LHS sampling points improved the accuracy only slightly. These extra points were also added to the Kriging model to further improve the accuracy, amounting to a total sampling of 70 points as also shown in Figure 7.3.

The final inflow distortion factor distributions for the propeller and the main rotor disks are shown in Figures 7.5(a) and 7.5(b). It can be seen that the maximum distortion for the propeller happened when the propeller was placed downstream and inboard, aft the main rotor, around the region where the main rotor wake was passing through. As the propeller was moved further upstream and downwards, the propeller distortion was effectively reduced. As for the main rotor inflow distortion in Figure 7.5(b), changes in the inflow distortion were very minor responding to propeller offsets. The large inflow distortion was mostly due to the edge-wise flight. Nonetheless, slightly larger distortion was observed when the propeller was placed ahead of and close to the main rotor in the vertical direction. This is due to the influence of the propeller wake.

With the simplified rotor disk representations and the inflow distortion metric, it was straightforward to quickly quantify the aerodynamic interactions at different combinations of operating conditions. This paragraph presents parametric investigations and demonstrations of effects by the

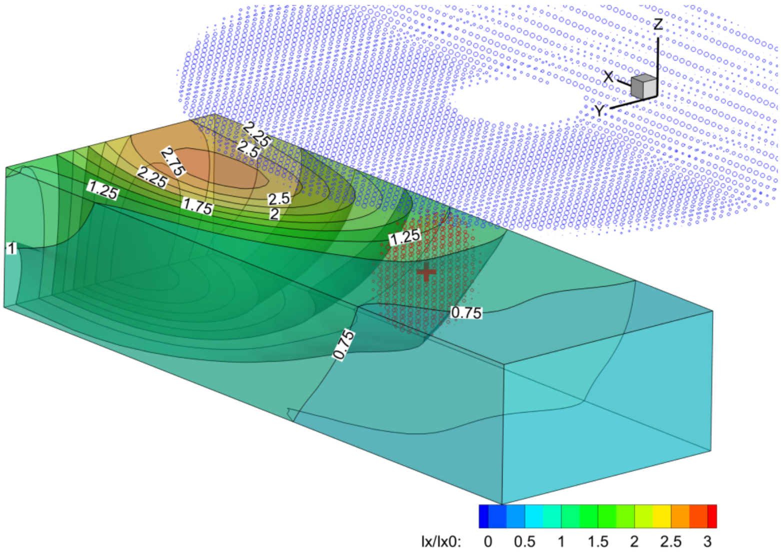

(a) Propeller disk inflow distortion distributions.

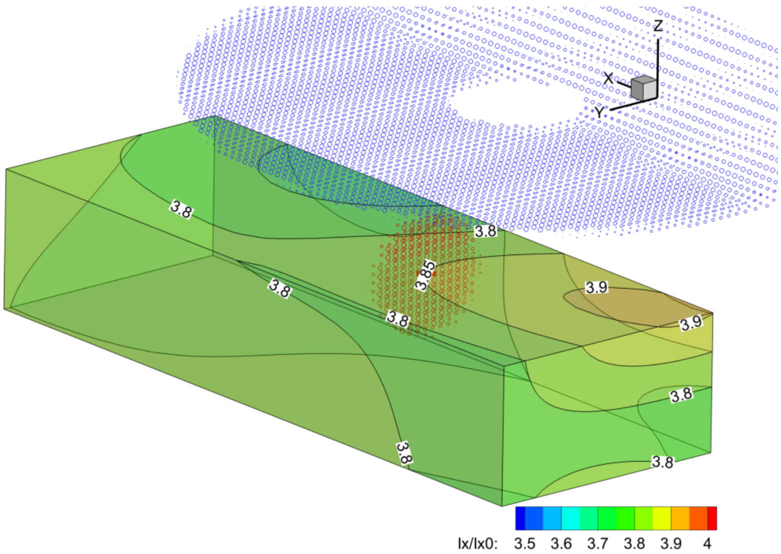

(b) Main rotor disk inflow distortion distributions.

Figure 7.5: Kriging models of disk inflow distortion distributions for the main rotor and the propeller while the main rotor is placed at different positions under the main rotor. Values are all normalised by the initial propeller inflow distortion of 17.8%.

main rotor advance ratio and the propeller thrust. A further test matrix was compiled, as shown in Table 7.1. The main rotor advance ratio varied by changing the free-stream velocity. The propeller thrust was increased or decreased by 50% comparing to the initial case. The same 45 orthogonal sampling set as described earlier was used for each series to investigate the effects of the propeller position. Kriging models were constructed to approximate the distortion distributions under the main rotor.

Table 7.1: Test matrix of investigations of the advance ratio and propeller thrust variations.

Case Series	Main rotor advance ratio	Propeller thrust/original propeller thrust
1	0.025, 0.15	1
2	0.05	0.5, 1.5

Inflow distortion distributions for the propeller at different positions under the main rotor at advance ratios $\mu = 0.025$ and 0.15 are shown in Figures 7.6(a) and 7.6(b), respectively. The inflow distortion values were normalised by the initial distortion factor of $I_{x0} = 17.8\%$ while the propeller is placed at the original position with the original advance ratio and thrust.

Comparing to the original advance ratio in Figure 7.5(a), when the advance ratio was reduced as in Figure 7.6(a), the maximum distortion region was moved upstream and inboard towards the main rotor root. The maximum distortion value was also increased from about $2.7I_{x0}$ to about $3.0I_{x0}$. Along the longitudinal and lateral directions, the distortion distribution followed a concentric pattern. As the propeller was placed away from the maximum distortion region, either upstream or downstream or outboard, the distortion was reduced. The minimal distortion value was about $0.9I_{x0}$, which is higher than the value at the original position. At the higher advance ratio of $\mu = 0.15$ as in Figure 7.6(b), the propeller distortion values were overall reduced comparing to the original case. The maximum value was around $0.5I_{x0}$ while the minimal value was about $0.15I_{x0}$. The maximum distortion region was established further downstream and upwards in the vertical direction. The distortion reduced as the propeller was moved upstream and further away from the main rotor vertically. The distortion varied little along the lateral direction.

The propeller disk suffered a severe inflow distortion when it was immersed in or was very near the main rotor wake. At low advance ratios, the main rotor wake skew angle was reduced, hence the downwash flow was stronger and covered a larger area under the main rotor. The propeller hence suffered stronger inflow distortion at most sampling positions under the main rotor. As the main rotor advance ratio was increased, the wake skew angle was increased, and the wake travelled above the propeller disk. Therefore, the overall propeller distortion was reduced, and the maximum distortion was noted only when the propeller was placed downstream and close to the main rotor disk. These also agree well with computations by Boisard[143].

The effect of the propeller thrust is shown in Figures 7.7(a) and 7.7(b). It is noted that the propeller thrust changes altered the values but varied little the shape of the distortion distribution comparing to the original case. At the lower propeller thrust (7.7(a)), the distortion was increased downstream and slightly decreased upstream. At the higher propeller thrust (7.7(b)), however, the distortion was decreased downstream and slightly increased upstream. These should be due to changes in the relative strength of the propeller suction and the surrounding flow field. The weaker propeller suction made the propeller inflow more dominated by the surrounding flow field. The stronger propeller suction tended to affect the inflow more along the axial direction but also induced some distortion especially in uniform flow fields.

7.3 Minimal Distortion and Propeller Position Optimisation at $\mu = 0.05$

As demonstrated in the previous section, the combination of the simplified rotor modelling and the inflow distortion metric enables quick quantifications of aerodynamic interactions for the propeller under the main rotor. Although at reduced accuracy, the results can be used to guide and improve the configuration design of novel rotorcraft. It is hence of interest to build an extra framework to help locate lower distortion regions and find optimal propeller positions subject to constraints.

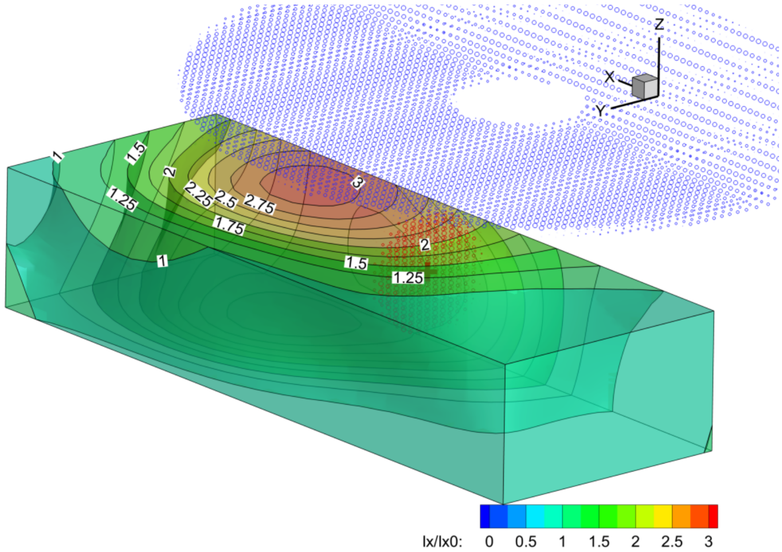

(a) $\mu = 0.025$.

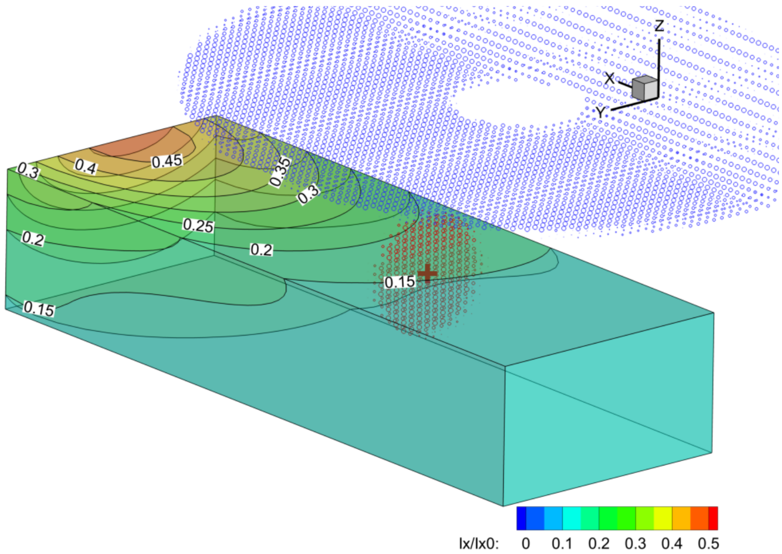

(b) $\mu = 0.15$

Figure 7.6: Propeller inflow distortion variations due to advance ratio changes.

7.3.1 Evaluation of Optimisation Methods

The first attempt was to simply locate the minimal propeller distortion and the corresponding propeller position at the advance ratio of $\mu = 0.05$. To find the minimal distortion, both gradient-based and gradient-free methods were evaluated. A hybrid approach was also examined using the approx-

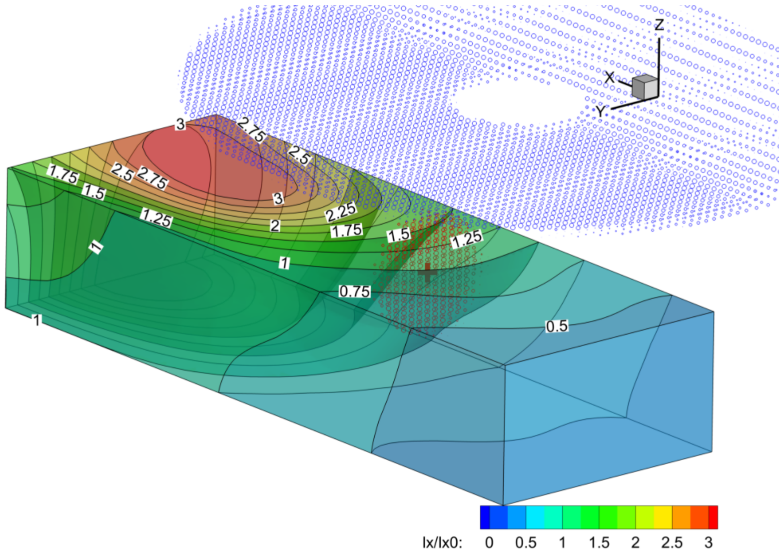

(a) 0.5 original propeller thrust.

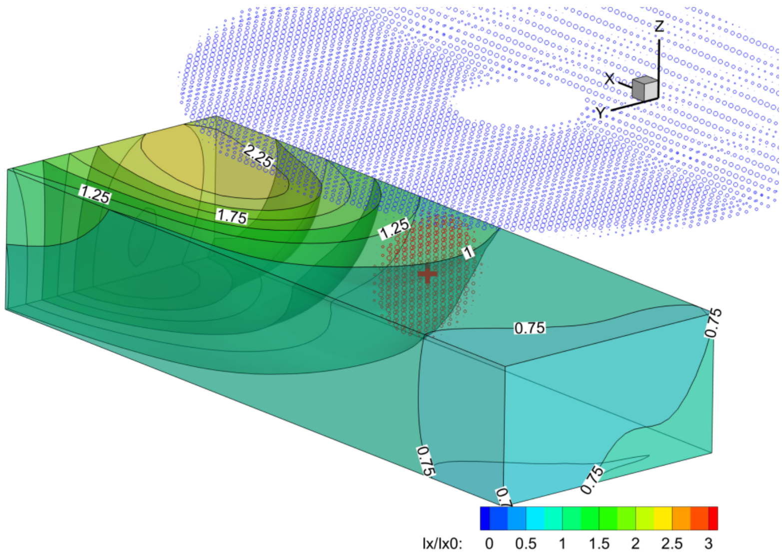

(b) 1.5 original propeller thrust

Figure 7.7: Propeller inflow distortion due to propeller thrust changes.

imated minimum obtained by the meta model as the initial point for the gradient-based approach. This is a non-linear optimisation problem, with the cost function being the propeller distortion factor and the design variables being the propeller position, and with only design variable boundary constraints.

The gradient-based method drives the propeller position changes based on the gradient information of the distortion factor w.r.t the propeller position. The gradient-free method uses the constructed surrogate model approximation and finds the minimal using the EGO algorithm [124]. The gradient-based approach is often more efficient, especially handling large amounts of design variables, but the final solution may be a local optimum rather than the global one due to the gradient-driven nature of the method. The meta-model-based approach offers the global optimum, but it requires a large number of cost function evaluations. When dealing with large numbers of design variables and combining with CFD methods, the computational cost can be excessively large. To combine the advantages of both methods and avoid their respective drawbacks, the proposed hybrid approach launches the gradient-based optimisation from an initial guess of the global optimum provided by the meta model. This section presents the evaluation of all approaches by setting them to find the minimal distortion.

As described in previous sections, the gradients of the cost functions w.r.t the design variables were computed using the adjoint approach. The gradient computation was validated against finite difference results as shown in Table 7.2. The agreement between the adjoint computation and the finite differences was very good despite the small absolute values. The gradients were then fed into a Sequential Least-square Quadratic Programming (SLSQP) [120] optimiser, which was used to govern the optimisation process.

Table 7.2: Validation of the adjoint-based computation of raw gradients using finite differences at the initial propeller position.

Variable	Finite differences	Adjoint gradients
x	-2.38×10^{-3}	-2.65×10^{-3}
y	-1.99×10^{-1}	-1.99×10^{-1}
z	-1.14×10^{-2}	-1.01×10^{-2}

The convergence history of the cost function values and gradients are shown in Figures 7.8(a) and 7.8(b), respectively. The cost function values varied little since the 29th iteration, while all gradients approached zero after about the 35th iteration. Note that the SLSQP optimiser only occasionally requires the gradient information to construct its own quadratic approximation.

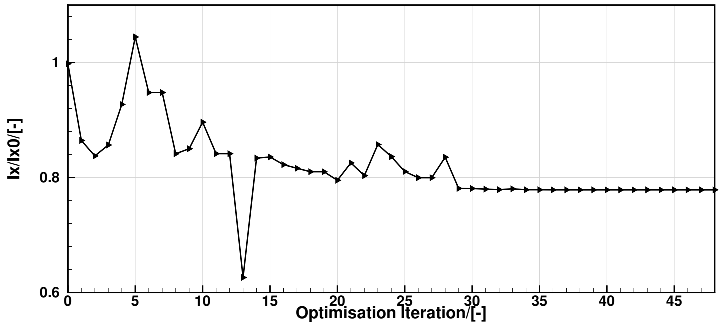

(a) Convergence history of the distortion factor.

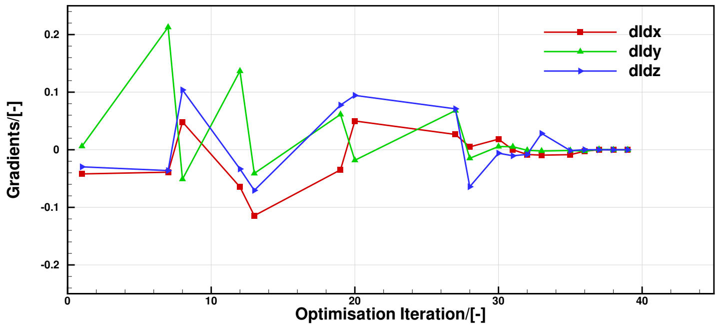

(b) Convergence history of the gradients.

Figure 7.8: Convergence history of the gradient-based propeller disk position optimisation.

For the gradient-free approach, the already constructed Kriging model was used, using a total of 70 sampling points as described earlier, as the initial surrogate model. The EGO algorithm, described in the previous sections, was used here to govern the minimisation process. The convergence history of the EI criterion is presented in Figure 7.9. The EI criterion varied little after the 10th iteration.

The hybrid approach started from the initial guess provided by the Kriging model, using 70 sampling points. Its convergence was very similar to that of the gradient-based approach, but with fewer amounts of iterations. It converged within 25 iterations with all gradients approaching 0.

Detailed comparisons of the three approaches to find the minimal propeller distortion position are presented in Table 7.3. In terms of the computational cost, the gradient-based method required 50 flow evaluations and 20 gradient evaluations. Note that each adjoint computation is of the similar cost to the flow computation, requiring about 5 CPU hours. The total computational

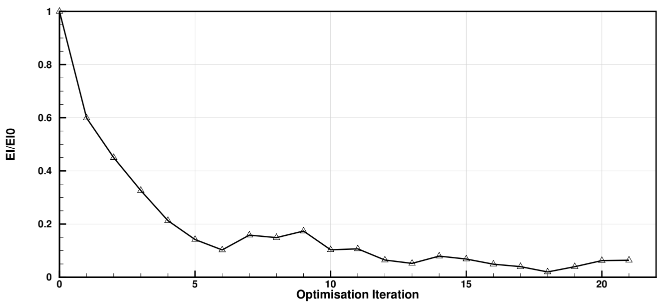

Figure 7.9: Convergence of the EI (Expected Improvement) criterion for the gradient-free minimisation, values normalised by the EI value of iteration 0.

cost is hence about 373 CPU hours. For the gradient-free approach, 92 flow evaluations were invoked taking into account the initial CFD database. The computational cost was about 491 CPU hours. The hybrid approach based on the initial 70 flow computations, invoked a further 25 flow evaluations, and 13 adjoint computations, the computational cost was about 572 CPU hours.

In terms of minimising the interference, the gradient-based approach very slightly moved the propeller disk upstream and downwards in the vertical direction to $(-4.30, 7.43, -6.02)C$. The reduction in inflow distortion relative to the initial position was only about 22%. However, it should be noted that in the cost function history of Figure 7.8(a), the distortion factor at optimisation iteration 13 was much lower than the final solution. Yet the gradient history in Figure 7.8(b) suggests that the final solution was indeed an extremum of the objective function, as the gradients were all approaching zero, suggesting that the final converged solution was a local minimum. As for the gradient-free approach, the propeller disk was moved to $(-17.00, 14.35, -5.03)C$, reaching the design variable boundary in the lateral and longitudinal directions and placed further upstream and outboards. This agrees well with the Kriging approximation in Figure 7.5(a) and the distortion factor varied little in the vertical direction near the minimal position. The relative reduction was about 38% relative to the original. Using the hybrid approach, the propeller disk was moved to $(-13.09, 8.10, -11.00)C$, and the disk inflow distortion was reduced by about 34%. Comparing to the gradient-free approach, the hybrid approach was again trapped in a local minimum in the present application. This also suggests that the current unknown objective function is hilly, and gradient-free approaches are hence more suitable for the optimisation study. However, comparing to the initial gradient-based method, the hybrid approach brought much improved results. The larger computational cost was mostly due to the initial database for the Kriging model.

Table 7.3: Comparisons of the gradient-based and gradient-free approaches to find the minimal propeller distortion position.

Approach	Computational cost			Minimal distortion solution	
	Flow evaluations	Gradient evaluations	Total CPU hours	Propeller position	Normalised inflow distortion I_x/I_{x0}
Gradient-based	50	20	~373	$(-4.30, 7.43, -6.02)C$	78.1%
Gradient-free	70+22	0	~491	$(-17.00, 14.35, -5.03)C$	61.7%
Hybrid	70+25	13	~572	$(-13.09, 8.10, -11.00)C$	66.5%

Overall, it is shown that at the advance ratio of $\mu = 0.05$, to minimise the interaction with the main rotor, the propeller should be placed upstream and outboards, to avoid the main rotor downwash and wake. The vertical direction showed minor influence near the minimal distortion position in the current study. In fact, it should also be noted that the absolute inflow distortion value varied little, generally between 11% and 13%, for the region with $X < -12C$. In other words, the aerodynamic interaction would be a relatively small concern in that region, and more design freedom is allowed if the propeller is placed within this region. The gradient-based approach clearly showed an advantage in saving the computational cost, but the solution was trapped in a local minimum because of the hilly objective function space. The gradient-free approach is hence more suitable for the optimisation study for the current problem.

7.3.2 Propeller Position Optimisation

Optimisation of the propeller position to minimise inflow distortion was later attempted with constraints imposed at the advance ratio of $\mu = 0.05$. The gradient-free, EGO approach was chosen for optimisation after the above evaluations. The optimisation involved only the main rotor and the propeller, both were represented by actuator disk models as described in previous sections. Throughout the optimisation process, the main rotor thrust was kept constant to balance the total weight. The propeller thrust was also kept the same, assuming only minor changes in the total drag while the propeller was placed at different positions. The configuration optimisation is illustrated in Figure 7.10.

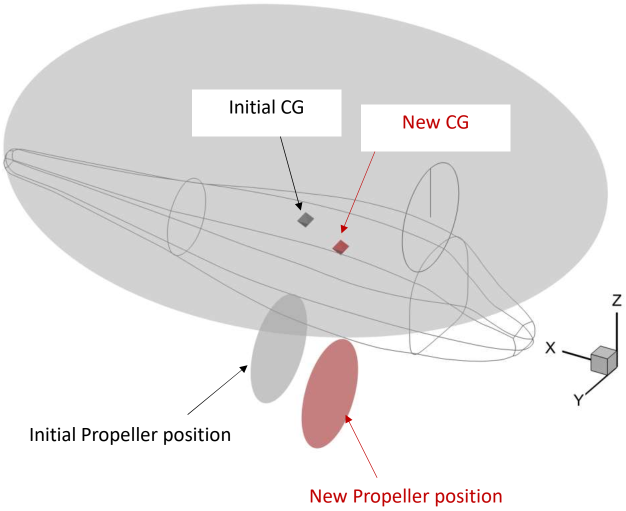

Figure 7.10: Illustration of the configuration optimisation by varying the propeller position.

Constraints for the current optimisation were set to restrict changes in the overall moment. This is because changes in the propeller position alter the centre of gravity of the overall configuration, depending on the ratio of the propulsor unit weight to the total weight. With the centre of gravity moved, the moment arms of other aerodynamic components are also changed. With the current constraints, while optimising the propeller position for reduced aerodynamic interference, trimming changes brought to the original configuration were also constrained.

The optimisation problem was formulated as follows

$$
\begin{aligned}
\text{minimise: } & I(x,y,z,W), \\
\text{subject to: } & dMx_{total} = 0, \\
& dMy_{total} = 0, \\
& x_{il} \leq x_i \leq x_{iu}
\end{aligned}
$$

where $I(x,y,z,W)$ is the inflow distortion factor for the propeller disk subject to its centre position (x,y,z) and the flow solution W. dMx_{total} and dMy_{total} are the changes in the overall rolling and pitching moments due to the propeller position change, respectively. These two are imposed as equality constraints for the current optimisation problem. Overall, the optimisation is set to minimise the propeller distortion by altering its position while introducing only minor changes in the overall rolling and pitching moments. In the current work, the initial CG position was assumed at $(0,0,-3.842)C$ relative to the main rotor centre of rotation, thereby generating zero initial rolling and pitching moments. Throughout the optimisation, the propulsor unit to total weight ratio was assumed to be 5%.

Comparisons between the initial and the optimisation results are shown in Table 7.4. The optimisation converged after just 3 extra flow evaluations with the EI reaching zero, since the search direction has been largely restricted by the moment constraints. With the constraints imposed, the optimisation also moved the propeller propeller upstream and downwards, but the offsets were restricted comparing to the unconstrained case in Table 7.3. At the optimised position, the inflow distortion is about 71.3% of the original, a reduction by about 29%. The rolling and pitching moments were maintained near zero by the constraints at the optimised positions.

Table 7.4: Optimisation results using gradient-free EGO with overall moment constraints. Moments are normalised by the initial overall torque (Z moment) M_{z0}, and distortion factors are normalised by the initial distortion factor I_{x0}.

Case	dMx/M_{z0}	dMy/M_{z0}	Propeller position	I_x/I_{x0}
Initial	0.00E+00	0.00E+00	(-2.80, 7.50, -5.60)C	100%
Optimised	1.07E-04	-3.29E-05	(-10.39, 7.50, -8.28)C	71.3%

Optimisation results using the simplified modelling were later verified through blade-resolved simulations. As shown in Figures 7.11(a) and 7.11(b), the propeller disk is now free from the main rotor wake at the optimised position. The interactions mostly happen in the propeller wake far downstream. The time-averaged propeller loadings normalised by the isolated values are shown in Table 7.5. Comparing to the isolated propeller, the overall thrust and torque were restored to the initial levels. The single blade thrust is presented in Figure 7.13 and the thrust fluctuation levels are shown in Figure 7.12. Compared to the isolated propeller, the total thrust variation levels were similar and small around 0.3% at the optimised position, but the single blade thrust fluctuations were still larger due to the interaction at about 2%. However, compared to the original position, the fluctuation levels were greatly reduced.

Frequency analyses of the total thrust were also conducted and are shown in Figure 6.18. At the optimised position, the propeller thrust had mostly the propeller BPF and its harmonics, sug-

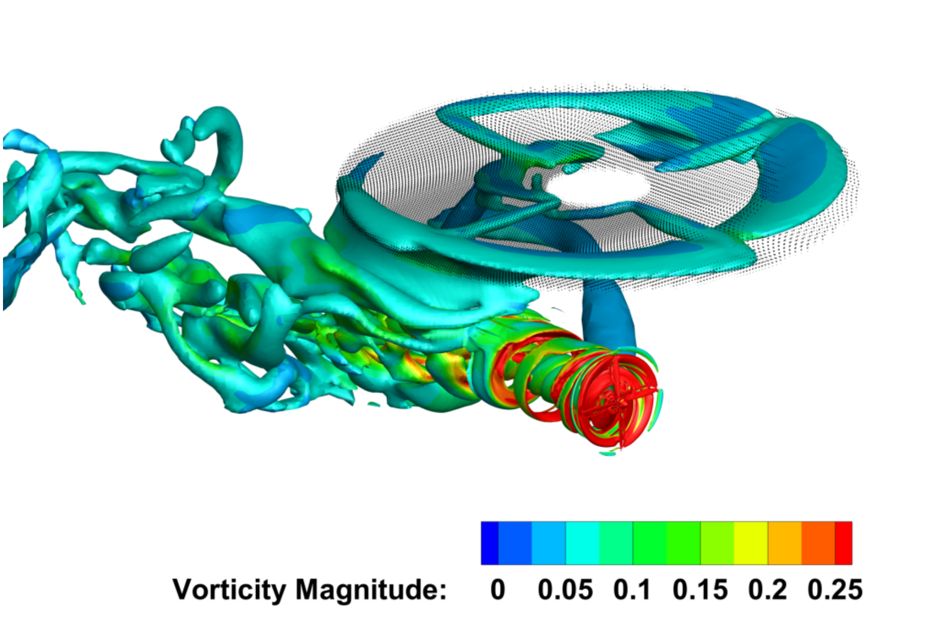

(a) Iso-surface of dimensionless q criteria, coloured by vorticity magnitude.

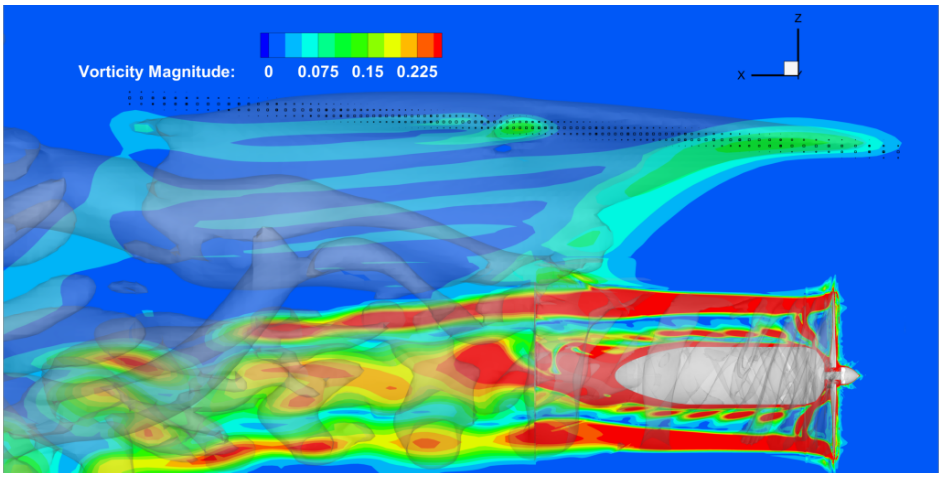

(b) Vorticity contours through the propeller disk.

Figure 7.11: Instantaneous flow details of the rotor/propeller wake interactions using resolved propeller blades and unsteady, non-uniform actuator lines for the main rotor, with the propeller at the optimised position for minimal inflow distortion (k-ω SST).

Table 7.5: Propeller forces and moments subject to main rotor downwash after optimisation. T_0 and Q_0 refer to the isolated propeller thrust and torque.

Case	Condition	F_x/T_0 (Thrust)	F_y/T_0	F_z/T_0	M_x/Q_0 (Torque)	M_y/Q_0 (Pitching)	M_z/Q_0 (Yawing)
4	AL+optimised position	101.2%	0.3%	0.2%	100.6%	0.4%	1.1%

gesting only minor influence from the main rotor. Overall, the optimisation through the simplified

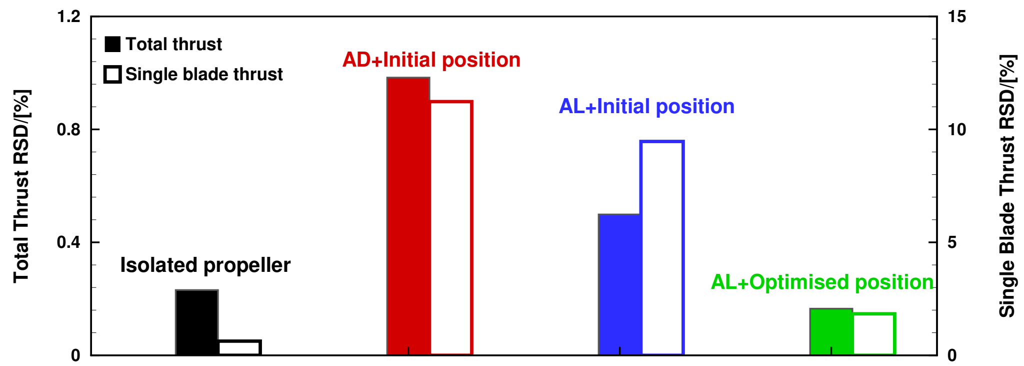

Figure 7.12: Relative Standard Deviation (RSD) levels of the total blade thrust and single blade thrust including comparisons with open and ducted propellers at the initial position.

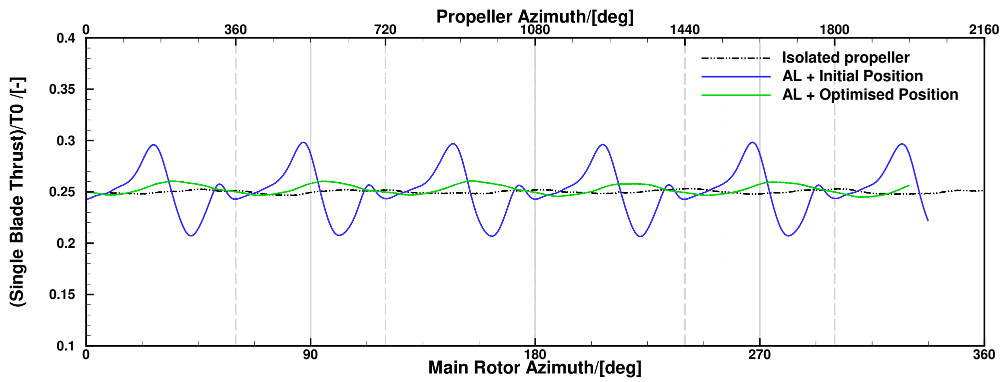

Figure 7.13: Single blade thrust variations after optimisation.

models using actuator disks effectively reduced the interference to the propeller disk.

7.4 Chapter Summary

This chapter proposed and examined a simplified approach for the modelling of aerodynamic interactions between rotors. An inflow distortion metric was also put forward to quantify the aerodynamic interference for rotor disks. Parametric and optimisation studies of rotorcraft configurations were hence enabled. The investigations can be summarised as follows:

1. The simplified modelling of rotor/propeller aerodynamic interactions using actuator disks can effectively model the interactional aerodynamics with reasonable accuracy and at much reduced computational costs. The proposed inflow distortion metric was able to quantify

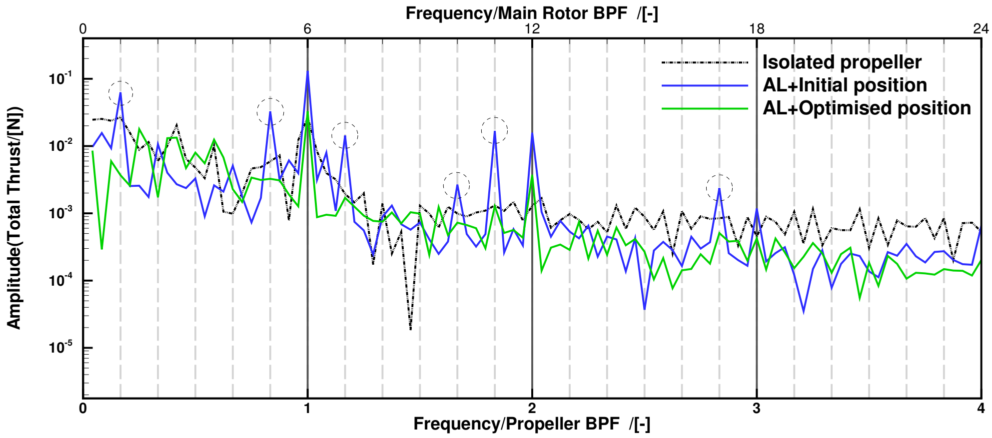

Figure 7.14: Frequency component of the overall blade thrust of the propeller after optimisation.

the aerodynamic interference for rotor disks at edgewise flight, such as propellers under main rotors. With the help of the Kriging surrogate method, the strength of the interaction at different propeller positions under the main rotor was visualised, with variations in advance ratios and propeller thrust. The propeller experienced larger interference when immersed in the main rotor wake. The shape of the high-interference region is cylindrical with a skew angle, reflecting the shape the main rotor super vortex through the region. The propeller inflow condition is effectively improved when moved away from the main rotor wake, either upstream/downstream or inboard/outboard. The simplified modelling effectively reflected changes of the main rotor wake due to the advance ratio, and the corresponding changes in the interference. Stronger propeller thrust or suction leads to reduced interference from the main rotor and vice versa, but the shape of the interference region is mostly determined by the main rotor advance ratio.

2. Optimisation studies based on the simplified modelling are performed at $\mu = 0.05$ to minimise the interference for the propeller by changing its position under the main rotor, with constraints on changes in the overall rolling/pitching moments. Gradient-based optimisation, gradient-free optimisation, and a hybrid approach were evaluated. The employed objective function was found to be hilly with many local optima, hence the gradient-free approach was chosen for the optimisation. The optimisation moved the propeller upstream

in the longitudinal direction and downwards in the vertical direction to escape the main rotor wake, with minimal changes in the overall rolling and pitching moments. The optimisation result was later verified using blade-resolved simulations. Fluctuations in the blade thrust were effectively eased at the optimised position, with the single blade thrust fluctuating around 2%, and the disk out-of-plane moments were also eliminated, suggesting a much reduced aerodynamic interference.

Chapter 8

Conclusions and Future Work

This thesis investigated the aerodynamic and acoustic performance of ducted and open propellers at various operating conditions, as well as, their applications on novel rotorcraft configurations using high-fidelity CFD methods. A parametric study of the equivalent ducted/open propellers was also conducted and shown in Appendix A. Gradient-based shape optimisation of the ducted propeller was performed to improve its performance at high advance ratios. Simulations were also performed for the ducted/open propellers installed under a main rotor to identify performance changes and the aerodynamic interactions. A simplified modelling approach for the rotor/propeller interactions based on actuator disk models was put forward and examined. An inflow distortion metric was proposed to quantify the aerodynamic interference. Parametric investigations of the rotor/propeller interference and optimisation studies of rotorcraft configurations were enabled using the proposed simplified modelling, and inflow distortion metrics.

8.1 Conclusions

HMB3 validation was carried out on empty ducts and ducted propeller configurations at various operating conditions, as well as, evaluations of the actuator disk/line models. The results have shown very good agreement with test data, lower-order predictive methods, and commercial CFD solvers.

The ducted propeller has shown strong aerodynamic benefits over the open propeller configuration at low flight speeds (up to advance ratio 0.2 for the case studied). At crosswind, the duct regulated the inflow to the propeller and the propeller experienced lower levels of unsteady loading. Acoustic reduction in both near- and far-fields compared to the open propeller while producing the similar amount of aerodynamic loadings was observed thanks to the duct shielding. The reduction was up to 10 dB for the case studied. However, the duct contributed to drag at low propeller suction and high axial speed. In addition, it produced considerable amounts of side forces and out-of-plane moments at crosswind.

To improve the performance at high advance ratios, gradient-based aerodynamic shape optimisation was used for the ducted propellers. At high speeds, to improve the performance, the duct expansion ratio was reduced by the optimisation, to decrease the induced inflow for the propeller enclosed. The local propeller blade pitch also needed to be increased to accommodate the higher inflow velocity at high advance ratios. The coupled duct and propeller optimisation delivered the best performance improvement. Far-field acoustics of the optimised designs were also examined afterwards. The far-field acoustic performance was not included in the optimisation, but the overall noise levels remained similar after the optimisation. Nonetheless, the duct shape was found to have significant impacts on the acoustic directivities.

The aerodynamic performance and interactions of ducted/open propellers installed under a main rotor in edgewise flight were also studied. Small variations were observed in the overall propeller thrust due to the downwash, while the propeller blades experienced large loading variations. The aerodynamic interactions for the propeller focused mostly on the upper half of the propeller disk. Ducting the propeller offloaded the propeller blades and reduced the variation level of the aerodynamic loads. However, the duct produced large sideways forces and out-of-plane moments due to the downwash.

A simplified modelling approach for aerodynamic interactions between rotors based on actuator disk modelling was also put forward. An inflow distortion metric was used to quantify interference between rotors. Parametric and optimisation studies of rotorcraft configurations were hence enabled. Surrogate models were built to approximate the aerodynamic interference while the propeller was placed at different positions under the main rotor. Gradient-based and gradient-free optimisation frameworks were explored to locate the minimal interference position for the propeller. The optimisation results were verified using blade-resolved simulations.

Overall, the ducted propeller concept was shown to be a promising choice of propulsion or lift for aeronautical applications at low forward speed. The aerodynamic benefits mostly come from the extra duct thrust at no torque cost. The duct shape has a strong impact on the overall performance by altering the propeller inflow condition and redistributing the duct/propeller loading sharing. At low propeller suction and high forward speeds, the duct may contribute to drag forces, but this may be alleviated by changing the duct shape and the propeller pitch. Another important advantage of the ducted propeller investigated is the reduced acoustic emission due to the duct shielding. This is important for novel rotorcraft designs due to stringent noise regulations. The duct restricts the noise radiations mostly to the duct inlet and outlet. The duct shape was also found to have a strong influence on the acoustic directivities.

At non-axial inflow conditions, the duct also provides aerodynamic shielding for the propeller enclosed and tends to regulate the inflow for the propeller blades. The propeller blades enclosed are offloaded and suffer less from the unsteady loads due to the non-axial inflows. These are beneficial for applications on novel multi-rotor or compound rotorcraft. However, the duct produces considerable amounts of sideways forces and out-of-plane moments at non-axial inflows. These sideways loads of course could be used as added lift or for control if ducts were properly designed. They may also result in aerodynamic blockages if the duct is placed under the main rotor downwash. Asymmetric duct designs or exit guide vanes may be considered to alleviate these sideways loads.

In terms of methodologies, an automated mesh generation framework was first proposed and used throughout this work for most of the grids. It was further exploited in Appendix A for the parametric study of equivalent duct/open rotors. High-fidelity CFD simulation strategies of the ducted propellers at various conditions were also examined and validated through experimental data and simpler numerical methods. Parametrisation methods and gradient-based optimisation frameworks were also put forward and constructed with the help of automatic differentiation for the ducted propeller shapes. Moreover, an acoustic solver based on the FW-H equation was built to compute the far-field acoustic features of the ducted/open propellers.

To study the aerodynamic interference of the ducted/open propeller installed under main rotors for novel rotorcraft configurations, this work explored the actuator disk/line modelling of rotors. A simplified modelling approach for rotor/rotor interactions and an inflow distortion metric to quantify the aerodynamic interactions were also proposed. They were demonstrated to be capable of modelling and quantifying the rotor/propeller aerodynamic interactions at modest computational costs. Surrogate models were built to visualise and approximate the interference effects, as well as, to support gradient-free optimisation of the configuration. The inflow distortion metric was also fully differentiated to support gradient-based optimisation of the configuration. Both gradient-based and gradient-free optimisation frameworks were constructed to optimise the vehicle configuration for minimised aerodynamic interference. The optimisation results were later verified by blade-resolved simulations.

8.2 Future Work

To guide future research work on the ducted propeller concept, the following could be explored:

1. Investigations of thrust vectorising devices. To exploit or alleviate these non-axial aerodynamic loads, a possible solution is adding thrust vectorising devices, e.g. exit guide vanes or active flow control approaches. For the rotor/ducted propeller combination studied, exit guide vanes could effectively deflect the propeller wake downwards to counter the blockage and the pitching moments. The effectiveness of the thrust vectorising at various operating conditions, as well as, its influence on the overall performance requires further careful evaluations.

2. Investigations of asymmetric or morphing duct shapes. Actively morphing the duct geometry and using asymmetric shapes may be an effective approach for both aerodynamic and acoustic controls. Asymmetric duct shapes may also be exploited to alleviate non-axial

loads. However, the complexity, mechanism, and potential control laws need extensive investigations.

3. Investigations of coaxial systems and swirl recovery devices. Adding a second row of blades to the ducted propeller configuration can be an effective way of further enhancing the aerodynamic performance and neutralising the overall torque. Even locked in stationary states or used as the structural support, the second row can still work as swirl recovery devices to exploit the swirl velocity from the previous blade row.

4. High-fidelity methods for the far-field acoustic computation of ducted configurations. Phenomena such as duct scattering, structural vibration, and impedance have been neglected in this work but should be studied and quantified.

5. Future UAMs will likely adopt multi-rotor configurations with distributed propulsion/lift for reduced noise emission and electric propulsion. Nonetheless, as studied in Chapter 4, at high crosswind angles, flow separation may dominate the duct surface causing severe performance losses and lead to non-axial loads that can be used for lift or control.

Bibliography

[1] Filippone, A. and Barakos, G., "Rotorcraft systems for urban air mobility: A reality check," *The Aeronautical Journal*, 2020, pp. 1–19.

[2] Stipa, L., "Experiments with intubed propellers," Tech. rep., NACA-TM-655, 1932.

[3] Carlton, J., *Marine propellers and propulsion*, Butterworth-Heinemann, 2018.

[4] Gilbert, B., Oman, R., and Foreman, K., "Fluid dynamics of diffuser-augmented wind turbines," *Journal of Energy*, Vol. 2, No. 6, 1978, pp. 368–374.

[5] Ohya, Y., Karasudani, T., Sakurai, A., Abe, K.-i., and Inoue, M., "Development of a shrouded wind turbine with a flanged diffuser," *Journal of wind engineering and industrial aerodynamics*, Vol. 96, No. 5, 2008, pp. 524–539.

[6] Johnson, W., Elmore, J., Keen, E., Gallaher, A., and Nunez, G., "Coaxial compound helicopter for confined urban operations," 2016, pp. 210–239.

[7] Gaffey, T. M., Zhang, C., Quackenbush, T. R., Sheng, C., and Hasbun, M., "Aeromechanics of the Coaxial Compound Helicopter," *56th AIAA/ASCE/AHS/ASC Structures, Structural Dynamics, and Materials Conference*, 2015.

[8] Sacks, A. and Burnell, J., "Ducted propellers: A critical review of the state of the art," *Progress in Aeronautical sciences*, Vol. 3, 1962, pp. 85–135.

[9] Pereira, J. L., *Hover and wind-tunnel testing of shrouded rotors for improved micro air vehicle design*, Ph.D. thesis, 2008.

[10] Akturk, A. and Camci, C., "Double Ducted Fan (DDF) as a Novel Ducted Fan Inlet Lip Separation Control Device," *the International Powered Lift Conference*, 10 2010.

[11] Goodson, K. W. and Grunwald, K. J., "Aerodynamic Characteristics of a Powered Semispan Tilting-Shrouded-Propeller VTOL Model in Hovering and Transition Flight," Tech. rep., NASA TN D-981, 1962.

[12] Kruger, W., "On wind tunnel tests and computations concerning the problem of shrouded propellers," Tech. rep., NACA-TM-1202, 1949.

[13] Platt Jr, R. J., "Static tests of a shrouded and an unshrouded propeller," Tech. rep., NACA-RM-L7H25, 1948.

[14] Hubbard, H. H., "Sound measurements for five shrouded propellers at static conditions," Tech. rep., NACA-TN-2024, 1950.

[15] Parlett, L. P., "Aerodynamic characteristics of a small-scale shrouded propeller at angles of attack from 0 to 90 degrees," Tech. rep., NACA-TN-3547, 1955.

[16] Taylor, R. T., "Experimental investigation of the effects of some shroud design variables on the static thrust characteristics of a small-scale shrouded propeller submerged in a wing," Tech. rep., National Advisory Committee for Aeronautics, 1958.

[17] Yaggy, P. F. and Mort, K. W., "A Wind-Tunnel Investigation of a 4-foot-diameter Ducted Fan Mounted on the Tip of a Semispan Wing," Tech. rep., NASA-TN-D-776, 1961.

[18] Grunwald, K. J. and Goodson, K. W., "Aerodynamic loads on an isolated shrouded-propeller configuration for angles of attack from -10 degrees to 110 degrees," Tech. rep., NASA-TN-D-995, 1962.

[19] Mort, K. W. and Gamse, B., "A wind-tunnel investigation of a 7-foot-diameter ducted propeller," Tech. rep., NASA-TN-D-4142, 1967.

[20] Black, D. and Rohrbach, C., "Shrouded propellers-a comprehensive performance study," *5th Annual Meeting and Technical Display*, 1968, p. 994.

[21] Abrego, A. I., Bulaga, R. W., and Rutkowski, M., "Performance study of a ducted fan system," *the American Helicopter Society Aerodynamics, Acoustics, and Test and Evaluation Technical Specialists Meeting, San Francisco, CA*, 2002.

[22] Fleming, J., Jones, T., Ng, W., Gelhausen, P., and Enns, D., "Improving control system effectiveness for ducted fan VTOL UAVs operating in crosswinds," *2nd AIAA" Unmanned Unlimited" Conf. and Workshop & Exhibit*, 2003, p. 6514.

[23] Martin, P. and Tung, C., "Performance and flowfield measurements on a 10-inch ducted rotor vtol uav," Tech. rep., Army Research Development and Engineering Command, Moffett Field CA, Aviation Aeroflight Dynamics Directorate, 2004.

[24] Graf, W., Fleming, J., and Ng, W., "Improving ducted fan uav aerodynamics in forward flight," *46th AIAA Aerospace Sciences Meeting and Exhibit*, 2008, p. 430.

[25] Akturk, A., Shavalikul, A., and Camci, C., "PIV measurements and computational study of a 5-inch ducted fan for V/STOL UAV applications," *47th AIAA Aerospace Sciences Meeting including The New Horizons Forum and Aerospace Exposition*, 2008, p. 332.

[26] Ohanian, O. J., Karni, E. D., Londenberg, W. K., Gelhausen, P. A., and Inman, D. J., "Ducted-fan force and moment control via steady and synthetic jets," *Journal of Aircraft*, Vol. 48, No. 2, 2011, pp. 514–526.

[27] Akturk, A. and Camci, C., "Tip Clearance Investigation of a Ducted Fan Used in VTOL UAVS: Part 1Baseline Experiments and Computational Validation," *ASME 2011 Turbo Expo: Turbine Technical Conference and Exposition*, American Society of Mechanical Engineers, 2011, pp. 331–344.

[28] Rhee, W., Myers, L., and McLaughlin, D., "Aeroacoustics of Vertical Lift Ducted Rotors," *15th AIAA/CEAS Aeroacoustics Conference (30th AIAA Aeroacoustics Conference)*, 2013, p. 3333.

[29] Yilmaz, S., Erdem, D., and Kavsaoglu, M., "Effects of duct shape on a ducted propeller performance," *51st AIAA Aerospace Sciences Meeting including the New Horizons Forum and Aerospace Exposition*, 2013, p. 803.

[30] Raeisi, B., *Aerodynamic study of tilting asymmetrical ducted fans mounted at the wing tips of a VTOL UAV*, Ph.D. thesis, 2016.

[31] Grunwald, K. J. and Goodson, K. W., "Division of aerodynamic loads on a semispan tilting-ducted-propeller model in hovering and transition flight," Tech. rep., NASA TN D-1257, 1962.

[32] Mort, K. W. and Yaggy, P. F., "Aerodynamic Characteristics of a 4-foot-diameter Ducted Fan mounted on the Tip of a Semispan Wing," Tech. rep., NASA-TN-D-1301, 1962.

[33] Mort, K. W., "Performance Characteristics of a 4-foot-diameter Ducted Fan at Zero Angle of Attack for Several Fan Blade Angles," Tech. rep., NASA-TN-D-3122, 1966.

[34] Yaggy, P. F. and Goodson, K. W., "Aerodynamics of Tilting Ducted-Fan Configurations," Tech. rep., NASA Langley Research Center, 1961.

[35] Kriebel, A. R. and Mendenhall, M. R., "Predicted and measured performance of two full-scale ducted propellers," Tech. rep., NASA-CR-578, 1966.

[36] Xu, H.-Y., Xing, S.-L., and Ye, Z.-Y., "Numerical study of ducted-fan lip stall suppression based on inflatable leading lip cell," *Procedia Engineering*, Vol. 126, 2015, pp. 158–162.

[37] Ohanian, O., Gelhausen, P., and Inman, D., "A compact method for modeling the aerodynamics of ducted fan vehicles," *48th AIAA Aerospace Sciences Meeting Including the New Horizons Forum and Aerospace Exposition*, 2010, p. 1052.

[38] Chang, I.-C. and Rajagopalan, R., "CFD analysis for ducted fans with validation," *21st AIAA Applied Aerodynamics Conference*, 2003, p. 4079.

[39] Lind, R., Nathman, J., and Gilchrist, I., "Ducted Rotor Performance Calculations and Comparison with Experimental Data," *44th AIAA Aerospace Sciences Meeting and Exhibit*, 2006, p. 1069.

[40] Camci, C. and Akturk, A., "Double-ducted fan," 2014, US Patent 8,821,123.

[41] Akturk, A. and Camci, C., "Experimental and computational assessment of a ducted-fan rotor flow model," *Journal of Aircraft*, Vol. 49, No. 3, 2012, pp. 885–897.

[42] Akturk, A. and Camci, C., "Tip Clearance Investigation of a Ducted Fan Used in VTOL UAVS: Part 2Novel Treatments via Computational Design and Their Experimental Verification," *ASME 2011 Turbo Expo: Turbine Technical Conference and Exposition*, American Society of Mechanical Engineers, 2011, pp. 345–357.

[43] Thwaites, B., "A Note on the Design of Ducted Fans," *The Aeronautical Quarterly*, Vol. 3, 1951.

[44] Thwaites, B., "A Note on the Performance of Ducted Fans," *The Aeronautical Quarterly*, Vol. 4, 1953.

[45] Bontempo, R. and Manna, M., "Solution of the flow over a non-uniform heavily loaded ducted actuator disk," *Journal of Fluid Mechanics*, Vol. 728, 2013, pp. 163–195.

[46] Bontempo, R. and Manna, M., "Effects of duct cross section camber and thickness on the performance of ducted propulsion systems for aeronautical applications," *International Journal of Aerospace Engineering*, Vol. 2016, 2016.

[47] Youngren, H., Drela, M., and Sanders, S., "Ducted Fan Design Code," http://web.mit.edu/drela/Public/web/dfdc/, December 2005, Ducted Fan Design Code homepage, available on-line.

[48] Bi, N., Kimmel, K., and Haas, D. J., "Performance Investigation of Ducted Aerodynamic Propulsors," *First International Symposium on Marine Propulsors, Smp*, Vol. 9, 2009.

[49] Ko, A., Ohanian, O., and Gelhausen, P., "Ducted fan UAV modeling and simulation in preliminary design," *AIAA modeling and simulation technologies conference and exhibit*, 2007, p. 6375.

[50] Ahn, J. and Lee, K., "Performance prediction and design of a ducted fan system," *40th AIAA/ASME/SAE/ASEE Joint Propulsion Conference and Exhibit*, p. 4196.

[51] Ahn, J. and Drela, M., "Newton method on axisymmetric transonic flow and linearized 3D flow prediction," *36th AIAA Aerospace Sciences Meeting and Exhibit*, 1998, p. 928.

[52] Drela, M. and Youngre, H., "Axisymmetric Analysis and Design of Ducted Rotors," http://web.mit.edu/drela/Public/web/dfdc/DFDCtheory12-31.pdf, December 2005, Ducted Fan Design Code theory, available on-line.

[53] Guerrero, I., Londenberg, W. K., Gelhausen, P., and Myklebust, A., "A powered lift aerodynamic analysis for the design of ducted fan uavs," *2nd AIAA" Unmanned Unlimited" Conf. and Workshop & Exhibit*, 2003, p. 6567.

[54] Rajagopalan, R. and Zhang, Z., "Performance and flow field of a ducted propeller," *25th Joint Propulsion Conference*, 1989, p. 2673.

[55] Ye, K., Ye, Z.-Y., and Qu, Z., "Aerodynamic optimization method for duct design," *Journal of Aerospace Power*, Vol. 28, 08 2013, pp. 1828–1835.

[56] Sheng, C., Zhao, Q., and Bi, N. P., "Numerical Investigations of Ducted Fan Hover Performance for FIW Applications," *53rd AIAA Aerospace Sciences Meeting*, 2015, p. 1935.

[57] Jimenez, B. G. and Singh, R., "Effect of duct-rotor aerodynamic interactions on blade design for hover and axial flight," *53rd AIAA Aerospace Sciences Meeting*, 2015, p. 1030.

[58] Biava, M. and Barakos, G. N., "Optimisation of ducted propellers for hybrid air vehicles using high-fidelity CFD," *The Aeronautical Journal*, Vol. 120, No. 1232, 2016, pp. 1632–1657.

[59] Chen, J., Li, L., Huang, G., and Xiang, X., "Numerical investigations of ducted fan aerodynamic performance with tip-jet," *Aerospace Science and Technology*, Vol. 78, 2018, pp. 510–521.

[60] Rubio, R. C., Diaz, P. V., and Yoon, S., "High-Fidelity Computational Analysis of Ducted and Coaxial Rotors for Urban Air Mobility," *Proceedings of the 75th Annual Forum*, Philadelphia, May 2019.

[61] Qing, J., Hu, Y., Wang, Y., Liu, Z., Fu, X., and Liu, W., "Kriging Assisted Integrated Rotor-Duct Optimization for Ducted Fan in Hover," *AIAA Scitech 2019 Forum*, 2019, p. 0007.

[62] Singh, R., Jimenez, B., and Avera, M., "Investigation of Aerodynamic Interactions in Ducted Rotor Systems," *the AHS 70th Annual Forum*, 2014.

[63] Li, L., Huang, G., Chen, J., and Yuan, J., "Numerical experiment of tip-jet ducted fans with various nozzles," *53rd AIAA/SAE/ASEE Joint Propulsion Conference*, 2017, p. 5093.

[64] Schaller, D. F., *A technique for shape optimization of ducted fans*, Master's thesis, Iowa State University, 2007.

[65] Rajagopalan, R. G. and Mathur, S. R., "Three dimensional analysis of a rotor in forward flight," *Journal of the American Helicopter Society*, Vol. 38, No. 3, 1993, pp. 14–25.

[66] Myers, L. M., *Aerodynamic Experiments on a Ducted Fan in Hover and Edgewise Flight*, Master's thesis, 2009.

[67] Kondor, S. A. and Moore, M., "Experimental Investigation of a Morphing Nacelle Ducted Fan (NASA/CP-2005-213509)," *2004 NASA/ONR Circulation Control Workshop, March 16-17, 2004*, 2004, pp. 435–468.

[68] Colman, M., Suzuki, S., and Kubo, D., "Wind Tunnel Test Results and Performance Prediction for a Ducted Fan with Collective and Cyclic Pitch Actuation for VTOL with Efficient Cruise," *AIAA Atmospheric Flight Mechanics Conference*, 2011, p. 6379.

[69] Gilmore, A. and Grahame, W., "Research studies on a ducted fan equipped with turning vanes," *Journal of the American Helicopter Society*, Vol. 4, No. 4, 1959, pp. 11–21.

[70] Oweis, G. F., Fry, D., Chesnakas, C. J., Jessup, S. D., and Ceccio, S. L., "Development of a tip-leakage flow - Part 1: The flow over a range of Reynolds numbers," *Journal of Fluids Engineering*, Vol. 128, No. 4, 2006, pp. 751–764.

[71] Oweis, G. F., Fry, D., Chesnakas, C. J., Jessup, S. D., and Ceccio, S. L., "Development of a tip-leakage flow - Part 2: comparison between the ducted and un-ducted rotor," *Journal of Fluids Engineering*, Vol. 128, No. 4, 2006, pp. 765–773.

[72] Martin, P. and Boxwell, D., "Design, analysis and experiments on a 10-inch ducted rotor vtol uav," *American Helicopter Society (AHS) International Specialists Meeting on Unmanned Rotorcraft: Design, Control and Testing, Chandler, AZ, January*, 2005, pp. 18–20.

[73] Ryu, M., Cho, L., and Cho, J., "The Effect of Tip Clearance on Performance of a Counter-Rotating Ducted Fan in a VTOL UAV," *TRANSACTIONS OF THE JAPAN SOCIETY FOR AERONAUTICAL AND SPACE SCIENCES*, Vol. 60, No. 1, 2017, pp. 1–9.

[74] Rumsey, C. L., Biedron, R., Farassat, F., and Spence, P., "Ducted-fan engine acoustic predictions using a Navier–Stokes code," *Journal of Sound and Vibration*, Vol. 213, No. 4, 1998, pp. 643–664.

[75] Nark, D., Farassat, F., Pope, D. S., and Vatsa, V., "The development of the ducted fan noise propagation and radiation code CDUCT-LARC," *9th AIAA/CEAS Aeroacoustics Conference and Exhibit*, 2003, p. 3242.

[76] Reboul, G., Polacsek, C., Lewy, S., and Heib, S., "Aeroacoustic computation of ducted-fan broadband noise using LES data," *Journal of the Acoustical Society of America*, Vol. 123, No. 5, 2008, pp. 3539–3539.

[77] Shur, M., Strelets, M., Travin, A., Christophe, J., Kucukcoskun, K., Schram, C. F., Sack, S., and Åbom, M., "Effect of inlet distortions on ducted fan noise," *22nd AIAA/CEAS Aeroacoustics Conference*, 2016, p. 2819.

[78] Eversman, W., "Theoretical models for duct acoustic propagation and radiation," 1991.

[79] Groeneweg, J. F., Sofrin, T., Rice, E., and P.R., G., *Aeroacoustics of Flight Vehicles: Theory and Practice, Vol 1: Turbomachinery noise*, chap. 3, NASA Rep 1258, 1991, pp. 151–210.

[80] Motsinger, R. and Kraft, R., *Aeroacoustics of Flight Vehicles: Theory and Practice, Vol 2: Design and performance of duct acoustic treatment*, chap. 14, NASA Rep 1258, 1991, pp. 165–206.

[81] Astley, R., Sugimoto, R., Achunche, I., Kewin, M., Mustafi, P., and Deane, E., "A review of CAA for fan duct propagation and radiation, with application to liner optimisation," *Procedia IUTAM*, Vol. 1, 2010, pp. 143–152.

[82] Tyler, J. M. and Sofrin, T. G., "Axial flow compressor noise studies," Tech. rep., SAE Technical Paper, 1962.

[83] Dunn, M., Tweed, J., and Farassat, F., "The application of a boundary integral equation method to the prediction of ducted fan engine noise," *Journal of sound and vibration*, Vol. 227, No. 5, 1999, pp. 1019–1048.

[84] Dunn, M. H., "TBIEM3D: A Computer Program for Predicting Ducted Fan Engine Noise. Version 1.1," Tech. rep., NASA/CR-97-206232, 1997.

[85] Wang, T., Yang, B., and Guan, Y., "A study on the prediction of the ducted fan noise," *11th AIAA/CEAS Aeroacoustics Conference*, 2005, p. 3069.

[86] Choi, H. L., Jeon, W., and Lee, D.-J., "Duct effects on aeroacoustic noise of an axial fan," *ICA 2004*, Acoustical society of Japan, 2004, pp. 3261–3264.

[87] Bulaga, R., "Ducted Fan Efficiency and Noise," *Aerospace Technology Conference and Exposition*, 2005.

[88] Malgoezar, A. M., Vieira, A., Snellen, M., Simons, D. G., and Veldhuis, L. L., "Experimental characterization of noise radiation from a ducted propeller of an unmanned aerial vehicle," *International Journal of Aeroacoustics*, 2019.

[89] Zhao, J., Hou, Q., Jin, H., Zhu, Y., and Li, G., "CFD analysis of ducted-fan uav based on magnus effect," *2012 IEEE International Conference on Mechatronics and Automation*, IEEE, 2012, pp. 1722–1726.

[90] Hou, Q.-M., Zhu, Y.-H., Zhao, J., Li, G., and Jin, H.-Z., "A Novel Ducted-Fan UAV Model Using Magnus Effect Steering Engine," *Journal of Aeronautics, Astronautics and Aviation*, Vol. 46, No. 3, 2014, pp. 209–217.

[91] Lee, T. E., *Design and Performance of a Ducted Coaxial Rotor in Hover and Forward Flight*, Master's thesis, University of Maryland.

[92] Geldenhuys, H. J., *Aerodynamic Development of a Contra-Rotating Shrouded Rotor System for a UAV*, Master's thesis, Stellenbosch University.

[93] Jiang, Y., Li, H., and Jia, H., "Aerodynamics Optimization of a Ducted Coaxial Rotor in Forward Flight Using Orthogonal Test Design," *Shock and Vibration*, Vol. 2018, 2018.

[94] Nemnem, A. F., Zakaria, M. Y., and Elzahaby, A. M., "Contra-rotating Ducted Fan Aerothermodynamic Design Procedure for Unmanned Applications," *2018 AIAA Information Systems-AIAA Infotech@ Aerospace*, 2018, p. 0745.

[95] Steijl, R., Barakos, G. N., and Badcock, K., "A framework for CFD analysis of helicopter rotors in hover and forward flight," *International Journal for Numerical Methods in Fluids*, Vol. 51, No. 8, 2006, pp. 819–847.

[96] Biava, M., Woodgate, M., and Barakos, G. N., "Fully implicit discrete-adjoint methods for rotorcraft applications," *AIAA Journal*, Vol. 54, No. 2, 2015, pp. 735–749.

[97] Garcia, A. J. and Barakos, G. N., "Numerical simulations on the ERICA tiltrotor," *Aerospace Science and Technology*, Vol. 64, 2017, pp. 171–191.

[98] Higgins, R., Barakos, G., Shahpar, S., and Tristanto, I., "A computational fluid dynamic acoustic investigation of a tiltwing eVTOL concept aircraft," *Aerospace Science and Technology*, Vol. 111, 02 2021, pp. 106571.

[99] Higgins, R., *Investigation of Propeller Stall Flutter*, Ph.D. thesis, 04 2021.

[100] Fitzgibbon, T., *Advanced Rotor Blade Design based on High-Fidelity Computational Fluid Dynamics*, Ph.D. thesis, 01 2021.

[101] Leble, V. and Barakos, G., "A Coupled Floating Offshore Wind Turbine Analysis with High-fidelity Methods," *Energy Procedia*, Vol. 94, 2016, pp. 523–530.

[102] Osher, S. and Chakravarthy, S., "Upwind schemes and boundary conditions with applications to Euler equations in general geometries," *Journal of Computational Physics*, Vol. 50, No. 3, 1983, pp. 447–481.

[103] Van Leer, B., "Towards the ultimate conservative difference scheme. V. A second-order sequel to Godunov's method," *Journal of computational Physics*, Vol. 32, No. 1, 1979, pp. 101–136.

[104] van Albada, G., van Leer, B., and Roberts, "A Comparative Study of Computational Methods in Cosmic Gas Dynamics," *Astronomy and Astrophysics*, Vol. 108, 04 1982, pp. 76–84.

[105] Axelsson, O., *Iterative solution methods*, Cambridge university press, 1996.

[106] Cantariti, F., Dubuc, L., Gribben, B., Woodgate, M., Badcock, K., and Richards, B., "Approximate Jacobians for the solution of the Euler and Navier-Stokes equations," *Aerospace Engineering Report*, Vol. 5, 1997.

[107] Jameson, A., "Time dependent calculations using multigrid, with applications to unsteady flows past airfoils and wings," *10th Computational Fluid Dynamics Conference*, 1991, p. 1596.

[108] Hideaki Sugawara, Y. T., "A Study of Rotor/Wing Aerodynamic Interaction at High Speed Flight on a Compound Helicopter," *The 6th Asian/Austrailian Rotorcraft Forum/Heli Japan 2017,Kanazawa, Japan*, 2017.

[109] Menter, F., "Two-Equation Eddy-Viscosity Turbulence Models for Engineering Applications," *AIAA Journal*, Vol. 32, No. 8, 1993, pp. 1598–1605.

[110] Wilcox, D. C., "Reassessment of the scale-determining equation for advanced turbulence models," *AIAA journal*, Vol. 26, No. 11, 1988, pp. 1299–1310.

[111] Menter, F. and Egorov, Y., "A scale adaptive simulation model using two-equation models," *43rd AIAA aerospace sciences meeting and exhibit*, 2005, p. 1095.

[112] Menter, F. and Egorov, Y., "The scale-adaptive simulation method for unsteady turbulent flow predictions. Part 1: theory and model description," *Flow, Turbulence and Combustion*, Vol. 85, No. 1, 2010, pp. 113–138.

[113] Rotta, J., "über eine methode zur berechnung turbulenter scherströmungsfelder," *Zeitschrift Angewandte Mathematik und Mechanik*, Vol. 50, No. 1-4, 1970, pp. 204–205.

[114] Menter, F. R., Egorov, Y., and Rusch, D., "Steady and unsteady flow modelling using the k-kL model," *Turbulence Heat and Mass Transfer 5. Proceedings of the International Symposium on Turbulence Heat and Mass Transfer*, Begel House Inc., 2006.

[115] O'Brien Jr, D. M., *Analysis of computational modeling techniques for complete rotorcraft configurations*, Ph.D. thesis, Georgia Institute of Technology, 2006.

[116] Stokkermans, T., van Arnhem, N., Sinnige, T., and Veldhuis, L., “Validation and Comparison of RANS Propeller Modeling Methods for Tip-Mounted Applications,” *AIAA Journal*, Vol. 57, 12 2018, pp. 1–15.

[117] Barakos, G., Fitzgibbon, T., Kusyumov, A., Kusyumov, S., and Mikhailov, S., “CFD simulation of helicopter rotor flow based on unsteady actuator disk model,” *Chinese Journal of Aeronautics*, Vol. 33, No. 9, 2020, pp. 2313–2328.

[118] Martins, J. and Ning, A., *Engineering Design Optimization*, 10 2021.

[119] Anon, “The TAPENADE Homepage,” https://team.inria.fr/ecuador/en/tapenade/, 2020, retrieved 3 Sep 2020.

[120] Kraft, D., “Algorithm 733: TOMP-Fortran Modules for Optimal Control Calculations,” *ACM Transactions on Mathematical Software*, Vol. 20, No. 3, 1994, pp. 262–281.

[121] Johnson, S., “The NLopt Nonlinear-Optimization Package,” https://nlopt.readthedocs.io/en/latest/, retrieved 3 Sep 2020.

[122] Sacks, J., Schiller, S. B., and Welch, W. J., “Designs for Computer Experiments,” *Technometrics*, Vol. 31, No. 1, 1989, pp. 41–47.

[123] Bouhlel, M. A., Hwang, J. T., Bartoli, N., Lafage, R., Morlier, J., and Martins, J. R. R. A., “A Python surrogate modeling framework with derivatives,” *Advances in Engineering Software*, 2019, pp. 102662.

[124] Jones, D. R., Schonlau, M., and Welch, W. J., “Efficient global optimization of expensive black-box functions,” *Journal of Global optimization*, Vol. 13, No. 4, 1998, pp. 455–492.

[125] Blank, J. and Deb, K., “Pymoo: Multi-Objective Optimization in Python,” *IEEE Access*, Vol. 8, 2020, pp. 89497–89509.

[126] Chirico, G., Barakos, G. N., and Bown, N., “Propeller installation effects on turboprop aircraft acoustics,” *Journal of Sound and Vibration*, Vol. 424, 2018, pp. 238 – 262.

[127] Ffowcs Williams, J. E. and Hawkings, D. L., “Sound generation by turbulence and surfaces in arbitrary motion,” *Philosophical Transactions of the Royal Society of London. Series A, Mathematical and Physical Sciences*, Vol. 264, No. 1151, 1969, pp. 321–342.

[128] Farassat, F., “Derivation of Formulations 1 and 1A of Farassat,” Tech. rep., NASA / TM-2007-214853, 2007.

[129] Dighe, V. V., Avallone, F., and van Bussel, G., “Effects of yawed inflow on the aerodynamic and aeroacoustic performance of ducted wind turbines,” *Journal of Wind Engineering and Industrial Aerodynamics*, Vol. 201, 2020, pp. 104174.

[130] Smith, D. A., Filippone, A., and Barakos, G. N., “Acoustic Analysis of Counter-Rotating Open Rotors with a Locked Blade Row,” *AIAA Journal*, 2020(avialable online).

[131] Luo, B., Chu, W., and Zhang, H., “Tip leakage flow and aeroacoustics analysis of a low-speed axial fan,” *Aerospace Science and Technology*, 2020, pp. 105700.

[132] Drela, M. and Youngren, H., “XROTOR user guide,” http://web.mit.edu/drela/Public/web/xrotor/, 2003, available on-line.

[133] Leishman, J. G. and Bi, N.-p., “Experimental investigation of rotor/lifting surface interactions,” *Journal of aircraft*, Vol. 31, No. 4, 1994, pp. 846–854.

[134] Roache, P. J., “Perspective: A Method for Uniform Reporting of Grid Refinement Studies,” *Journal of Fluids Engineering*, Vol. 116, No. 3, 09 1994, pp. 405–413.

[135] Roache, P. J., “Verification of Codes and Calculations,” *AIAA Journal*, Vol. 36, No. 5, 1998, pp. 696–702.

[136] Sugawara, H. and Tanabe, Y., “Numerical Investigation of Rotor/Wing Aerodynamic Interactions at High Advance Ratios,” *Journal of Aircraft*, Vol. 56, No. 6, 2019, pp. 2285–2298.

[137] Chaffin, M. S. and Berry, J. D., “Helicopter Fuselage Aerodynamics Under a Rotor by Navier-Stokes Simulation,” *Journal of the American Helicopter Society*, Vol. 42, No. 3, 1997, pp. 235–243.

[138] Fletcher, H. S., “Experimental investigation of lift, drag, and pitching moment of five annular airfoils,” Tech. rep., NACA-TN-4117, 1957.

[139] Higgins, R. J., Zarev, A., Barakos, G. N., and Green, R. B., “Numerical investigation of a two-bladed propeller inflow at yaw,” *Journal of Aircraft*, Vol. 57, No. 2, 2020, pp. 292–304.

[140] Öhrle, C., Schaferlein, U., Keßler, M., and Krämer, E., “Higher-order Simulations of a Compound Helicopter using Adaptive Mesh Refinement,” *the AHS International 74th Annual Forum & Technology Display, Phoenix, Arizona, USA*, 2018.

[141] Kulfan, B. M., “Universal parametric geometry representation method,” *Journal of aircraft*, Vol. 45, No. 1, 2008, pp. 142–158.

[142] Zhang, T. and Barakos, G. N., “High-Fidelity CFD Validation and Assessment of Ducted Propellers for Aircraft Propulsion,” *Journal of the American Helicopter Society*, Vol. 66, No. 1, 2021, pp. 1–28.

[143] Boisard, R., “Aerodynamic investigation of rotor/propeller interactions on a fast rotorcraft,” *44th European Rotorcraft Forum, Delft, The Netherland*, 2018.

[144] Potsdam, M., Smith, M., and Renaud, T., “Unsteady computations of rotor-fuselage interaction,” *35th European Rotrocraft Forum*, 2009.

[145] Boisard, R. and Lim, J. W., “Aerodynamic Analysis of Rotor/Propeller Wakes Interactions on High Speed Compound Helicopter,” *47th European Rotorcraft Forum(vitual).*, 2021.

[146] Stokkermans, T., Veldhuis, L., Soemarwoto, B., Fukari, R., and Eglin, P., “Breakdown of aerodynamic interactions for the lateral rotors on a compound helicopter,” *Aerospace Science and Technology*, Vol. 101, 2020, pp. 105845.

[147] Zhang, T. and Barakos, G. N., “High-fidelity numerical analysis and optimisation of ducted propeller aerodynamics and acoustics,” *Aerospace Science and Technology*, Vol. 113, 2021, pp. 106708.

Appendix A

Parametric Study of the Equivalent Open/Ducted Propellers[1]

This chapter presents the performance analysis and parametric study of the equivalent ducted and open propellers. The ducted propeller model tested by Grunwald and Goodson [18] was adopted as the baseline design and was scaled to real size to support a four-rotor vehicle of 6,000 kg. Comparing to the equivalent open rotor, the ducted propeller had a significantly reduced frontal area and was also able to deliver the desired thrust at lower torque and reduced noise, but the power was higher due to the higher RPM. A parametric study was then performed in hover and in forward flight to study the performance trends subject to variations of tip speed, blade pitch, blade radius, chord, twist, and duct thickness. Kriging surrogate models were constructed to provide an impression of the performance response to the particular design change. Both configurations showed similar responses to most design variables, but the sensitivity was different between configurations and between flight conditions. Detailed analyses of the parametric results are presented to guide ducted propeller designs.

A.1 The 'Equivalent' Propellers and Scaling

To compare the relative performance between open and ducted configurations, the concept of the '*equivalent*' propeller is introduced. The momentum theory was used to derive the equivalent propellers between open and ducted configurations. The equivalent propeller is derived under hover conditions.

Firstly, considering the open propeller, from the momentum theory the thrust of an open propeller in hover is:

$$T_{op} = \dot{m}V_3 \tag{A.1}$$

where V_3 is the velocity far downstream equal to twice the induced velocity at the disk. The mass flow is $\dot{m} = \rho A_{op} v_i$, with v_i being the induced velocity at the propeller disk and A_{op} being the propeller disk area. Therefore:

$$T_{op} = 2\rho A_{op} {v_i}^2 \tag{A.2}$$

[1] This chapter has been published in Zhang, T., Qiao, G., Smith, D.A., Barakos, G.N. and Kusyumov, A., "Parametric study of aerodynamic performance of equivalent ducted/un-ducted rotors," Aerospace Science and Technology, Vol. 117, 2021, pp. 106984.

as from the conservation of energy, the propeller power is:

$$P_{op} = \frac{1}{2}\dot{m}{V_3}^2 = 2\rho A_{op}{v_i}^3 \tag{A.3}$$

Rearranging Equation (A.2) in terms of induced velocity, the open propeller power can be related to its thrust using:

$$P_{op} = \frac{{T_{op}}^{3/2}}{\sqrt{2\rho A_{op}}} \tag{A.4}$$

As for the ducted configuration in hover, the total thrust (i.e. duct plus propeller contributions) is given by:

$$T_{dp} = \dot{m}V_3 \tag{A.5}$$

where V_3 in this case is the flow velocity at the duct diffuser exit. The mass flow at the propeller disk is $\dot{m} = \rho A_{dp} v_i$, with A_{dp} being the propeller disk area. From continuity, the velocity at the duct exit V_3 is related to the induced velocity v_i:

$$v_i A_{dp} = V_3 A_3 \implies V_3 = \frac{v_i}{\Lambda} \tag{A.6}$$

Here, A_3 is the area of the duct diffuser exit and Λ is the duct exit area ratio (A_3/A_{dp}) and is assumed constant. The thrust of the ducted propeller is then:

$$T_{dp} = \rho A_{dp}\Lambda {v_i}^2 \tag{A.7}$$

From the conservation of energy, the power of the ducted propeller is:

$$P_{dp} = \frac{1}{2}\dot{m}{V_3}^2 = \frac{1}{2}\Lambda^2\rho A_{dp}{v_i}^3 \tag{A.8}$$

and rearranging Equation (A.7) in terms of induced velocity, the ducted propeller power can be related to its thrust using:

$$P_{dp} = \frac{{T_{dp}}^{3/2}}{\sqrt{4\Lambda\rho A_{dp}}} \tag{A.9}$$

The equivalent propeller is found when the power and thrust of both systems are equal, i.e. the same propulsive efficiency. Equating Equations (A.4) and (A.9), the blade radius correlation between the equivalent open and ducted propellers is found:

$$R_{dp} = \frac{R_{op}}{\sqrt{2\Lambda}} \tag{A.10}$$

To ensure the results of the parametric study are relevant to modern multi-rotor concepts, the baseline design was scaled to provide a realistic propeller loading. For the scaling, a four-rotor vehicle of 6,000 kg mass was used to be representative of modern concepts. This weight is representative of a current medium to large utility helicopter. This realistic size is also a good challenge for the current scaling and simulation methods due to the compressibility effects and high Reynolds number. Hover conditions were used for scaling as these represent the most demanding conditions for the vehicle. In hover, the proposed vehicle would require a total thrust of 58,860N.

Using a load factor of 1.2, this requires each propeller to deliver a total thrust of 17,658 N. This allows for good manoeuvrability for a multi-rotor aircraft.

The rotor scaling was carried using the simple blade element momentum theory and was later verified using CFD calculations. The scaling was carried out at the constant tip speed, as used in the baseline design $Ma_{tip} = 0.468$. The scaling analysis was constrained to a range of 1 to 4m for the tip radius. A preliminary analysis showed that an open propeller radius of $R = 3.75m$ and an equivalent ducted propeller of $R = 2.5m$ radius met the required performance. However, the blade number had to be increased to 4 (from the baseline of 3) to meet the loading constraints. The increase in blade number resulted in an increased solidity for the scaled propellers. However, the solidity remained equal for both configurations at $\sigma = 0.1834$.

Figure A.1 compares the geometry of the equivalent open and ducted propellers. The equivalent ducted propeller configuration, including the duct surface, offers a significant reduction in frontal area for delivering the same thrust in comparison to the open propeller configuration. The analysis in the present work sets to quantify the benefits of the equivalent ducted propeller configuration of Figure A.1.

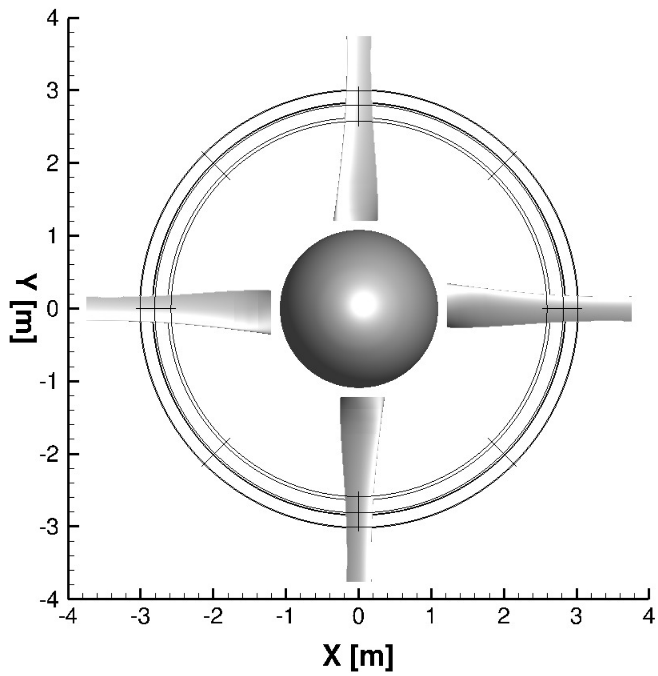

Figure A.1: Comparison of equivalent open and ducted propellers. The ducted propeller is shown using black outlines.

A.1.1 Parametric Study

In addition to comparing the baseline equivalent open and ducted propeller configurations, a parametric study was carried out to allow further evaluations of the relative benefits of each configuration and their sensitivity to design changes. The chosen parameters and their variation are shown in Table A.1. The parameters involve geometric variables of blade radius, blade chord, blade twist, and duct thickness, and operating variables of tip Mach number and blade pitch.

Table A.1: Design variables for parametric study.

Design Variable	Value 1	Value 2	Value 3
Tip Mach No. [-]	0.3	0.468	0.7
Pitch [$\Delta\%$]	-5	$+5$	$+10$
Blade Radius [m]	1.5	2.5	3.75
Blade Chord [$\Delta\%$]	-5	$+5$	$+10$
Blade Twist [$\Delta\%$]	-5	$+5$	$+10$
Duct Thickness [$\Delta\%$]	-5	$+5$	$+10$

Each design variable was varied independently and considered at hover and forward flight at ISA sea-level conditions. For hover conditions, the baseline configurations were trimmed to deliver the required thrust, about $T = 17,658$ N. For forward flight conditions, both configurations were considered in axial flight with a freestream Mach number of $Ma_\infty = 0.2$. Both initial configurations were trimmed to deliver 50% of the specified take-off thrust. Note that for all other cases, the propellers were not trimmed, having the pitch angle of the baseline cases.

A.2 Aerodynamic Performance of Equivalent Propellers

Steady CFD computations were used to investigate these equivalent propellers at hover and axial forward flight conditions, whilst unsteady simulations were required for the yawed flight conditions. For the hover conditions, the propellers were trimmed to approximately the required thrust specified by the propeller scaling. The forward flight case was trimmed to approximately half of the value required under hover conditions. The pitch angle found for the forward flight case was also used for the yawed flight conditions. The required pitch angles and corresponding thrust and torque for the equivalent propellers are presented in Table A.2.

The hover case shows that both open and ducted propellers have been trimmed to similar values, closely matching the required thrust loading. However, the ducted propeller configuration required a notably higher blade pitch angle, resulting from the higher propeller inflow induced by the duct. Additionally, this resulted in a reduced torque output compared to the open propeller configuration.

For the forward flight case, the results are similar to that of the hover case, both configurations were trimmed to a similar value, approximately half the value at hover conditions. Again, whilst the ducted propeller required a higher pitch angle, the thrust was delivered with a reduced torque output. Note, however, that the power will be higher for the ducted configuration due to the higher rotational speed required to have the same tip Mach number.

Overall, the equivalent propeller concept has successfully demonstrated that ducting the propeller allows for the same thrust to be delivered with a significantly reduced tip radius (here, -40%) and frontal area (here, -75%). The ability to provide the same thrust for the reduced area results in part from the additional contribution to the thrust from the duct. For the hover case, the duct is found contributing to almost 50% of the thrust generation. On the other hand, for the

Table A.2: Computed loads for equivalent open and ducted propeller configurations.

Configuration		Pitch Angle [°]	Thrust [kN]	Torque [kNm]
Hover	Open Propeller	5.25	18.3	6.76
	Ducted Propeller	13.0	18.9	5.41
Forward Flight	Open Propeller	27.3	8.73	18.2
	Ducted Propeller	37.3	9.05	14.7

forward flight case, the duct actually subtracts from the total thrust contribution, with the propeller providing almost all of the thrust. This is expected as the duct may contribute to drag at high advance ratios and low disk suction [18, 142]. For the forward flight case, the centre-body provides a small contribution to the thrust, whereas for the hover case, it has a negligible effect on the total thrust.

The inflow and wake profiles of the two configurations in hover, are also extracted and presented in Figures A.2(a) and A.2(b). For both configurations, the inflow profiles were extracted $0.25m$ upstream the propeller disk, while the wake profiles were extracted $2.5m$ downstream the propeller disk. As shown in Figure A.2(a), the ducted propeller experienced higher inflow velocity, which is expected as the duct induces large inflow through the propeller disk. The wake profiles of the open propeller in Figure A.2(b) show a typical wake contraction with the wake concentrating at about $r/R \leq 0.75$, or $R \leq 2.8m$. The wake of the ducted propeller is close to, but slightly stronger than that of the open propeller, resulting from the fact that the ducted configuration has a -40% reduced blade radius while producing the same thrust. No obvious wake contraction is noticed for the ducted propeller, which should be due to the duct diffuser effect. The ducted wake is quite evenly distributed within the blade radius, i.e. $R \leq 2.5m$, and gradually reduces to zero outwards. Overall, although at reduced blade radius and with higher inflow, the ducted configuration showed quite similar wake strength to the open propeller in hover.

Performance of the baseline equivalent designs was also examined at 20° yawed inflow at $Ma = 0.2$. The resolved flow-fields are shown in Figure A.3(a) and A.3(b). The open propeller wakes consists mostly of the tip vortices, while the duct circulation contributes the most to the ducted propeller wake at this yawed condition.

The unsteady loads at the non-axial inflow condition are shown in Figure A.4. The aerodynamic forces are decomposed into propulsion components in the wind axis, while the torque is calculated in the axial direction. Both configurations delivered more lift than thrust. The open propeller experienced more variations in loads due to the axisymmetric inflow. On the other hand, the blades of the ducted propeller were offloaded and saw smaller variations in loads. The ducted propeller blades were producing thrust in the yawed condition, but the total thrust was negative due to the large negative contribution from the duct. Nonetheless, the ducted propeller produced large lifting forces with the major contribution from the duct. As for the torque, the propellers contributed the most in both configurations. The ducted propeller produced lower torque than the open propeller, with minor contributions from the duct.

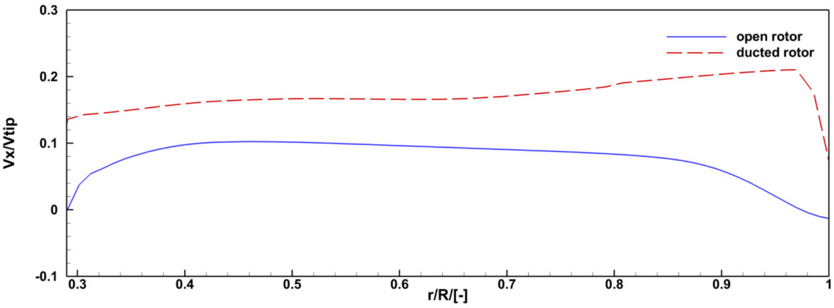

(a) Inflow profiles extracted 0.25m upstream the propeller disks.

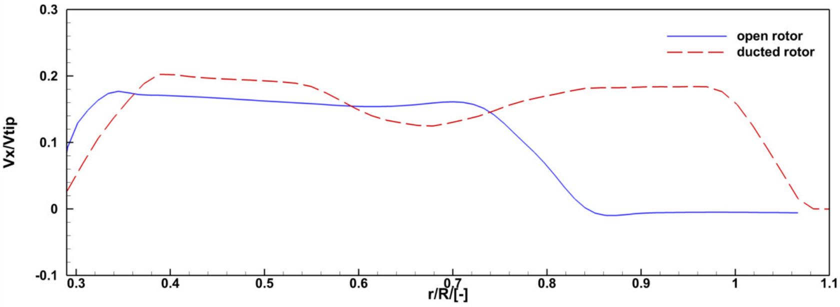

(b) Wake profiles extracted 2.5m downstream the propeller disks, near the duct exit.

Figure A.2: Inflow and wake profiles of the ducted and open configurations in hover.

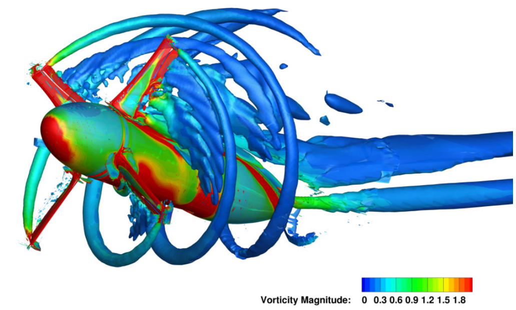

(a) Wake of the equivalent open propeller.

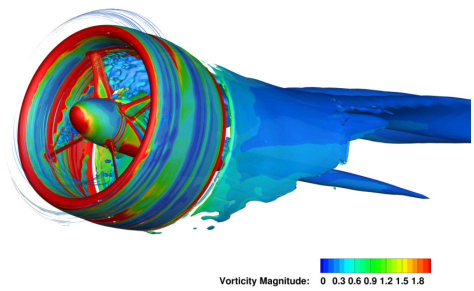

(b) Wake of the ducted propeller.

Figure A.3: Iso-surface of dimensionless Q-criterion=0.005 of the equivalent ducted/un-ducted propellers with 20° yawed inflow.

A.3 Fly-by Noise of the 'Equivalent' Propulsors

The fly-by noise in the current work refers to the acoustic signals received at fixed ground microphones while the propulsors were flying overhead, in level flight. This scenario is often seen in aircraft noise certification. In the present work, the CFD solution was used as the input to the FW-H acoustic code. The calculations were performed assuming the two propulsor configurations are at the forward flight conditions of Table A.2 at $Ma = 0.2$. The propulsors are assumed to be

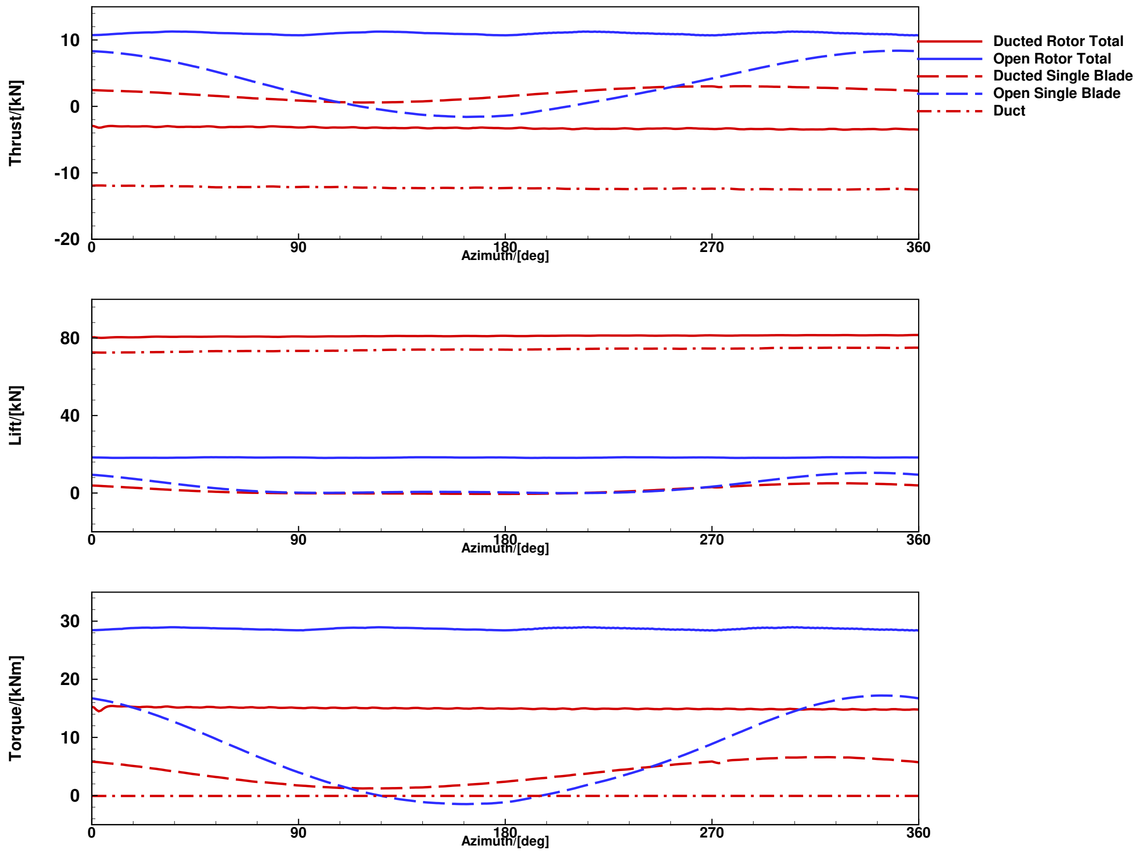

Figure A.4: Unsteady aerodynamic loads of ducted/un-ducted propellers with 20° yawed inflow. The forces are project in the wind direction.

in level flight, 50*m* above ground. Three microphones were placed on the ground: one 50*m* to the port-side, one directly below the flight path, and the final one 50*m* to the starboard side.

The computed acoustic signals of the two equivalent configurations are shown in Figure A.5. Note that the ducted propeller was operating at a higher RPM to achieve the same tip speed as the larger-diameter open propeller, hence the frequency components are largely different. SPL values calculated using sound pressure signals within a propeller revolution are presented in Figure A.6. For the open propeller, the acoustics is around 80 dB, with a slight increase near the propeller disk passage. For the ducted propeller, there is a low noise window slightly after the propeller disk passage for the ducted propeller, which is due to the duct shielding and the altered acoustic directivity. The duct tends to redirect the acoustic waves towards the axial direction [147]. This feature agrees well with our previous near-field acoustic study based on high-fidelity CFD solutions [147]. As both propellers are moving further away, the acoustics becomes similar and reduces to around 75 dB. At the distance studied, the ducted configuration produces noise levels consistently lower and with a maximum reduction of about 15 dB comparing to the open propeller.

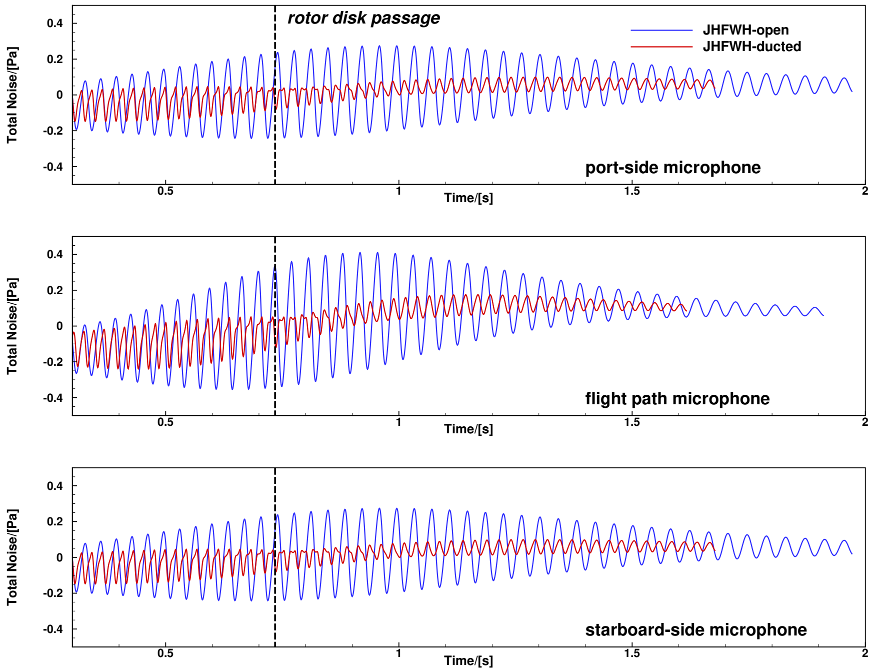

Figure A.5: Computed acoustic signals on the 3 ground microphones while the equivalent open and ducted configurations are flying by.

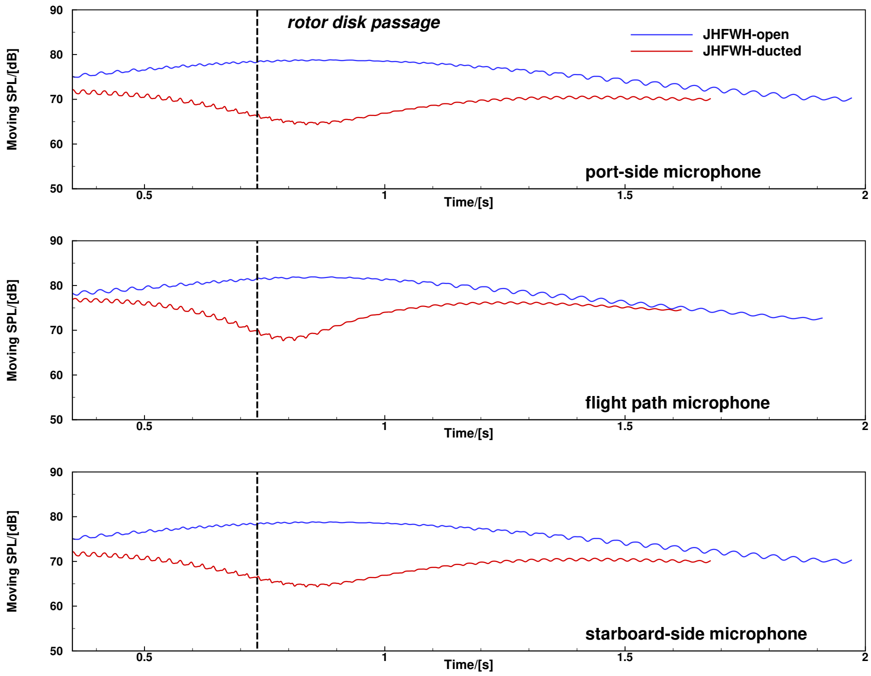

Figure A.6: Computed SPL values from the 3 ground microphones using signals within a propeller revolution while the equivalent open and ducted configurations are flying by.

A.4 Parametric Study Results

First, a summary of the parametric study results, in terms of total thrust/power loadings in hover and forward flight, is shown in FigureA.7. In general, the ducted propeller required slightly higher power than the equivalent open propeller for the same thrust, both in hover and in forward flight. This is because the ducted propeller has a higher RPM to have the same tip Mach number as the open propeller. The total thrust and power loadings of the ducted configuration are higher than the open propeller, due to the much reduced frontal area. For the current parametric study, the ducted/un-ducted configurations mostly showed consistent trends responding to the parametric variables. Variations in the tip Mach number caused significant changes in the thrust/power and the thrust/power loadings in both hover and forward conditions. Variations in the blade radius led to large thrust/power variations but had only a minor effect on the thrust/power loadings. Influences of the blade pitch are shown larger in forward flight than in hover for both thrust/power and their loadings. Responses to other parametric variables are relatively small around the initial point. Detailed discussion of the effect of each parameter follows.

Kriging curves have been fitted to the thrust, torque, and efficiency data to provide an impression of the response of the configuration to the particular design change. For hover cases, the Figure of Merit (*FoM*) is used to measure the efficiency, while for forward flight cases, the Froude efficiency is used. For most cases in the present work, there are three design points in addition to the baseline. Also presented are the uncertainty quantification of the Kriging predictions. In general, it is noticed that the Kriging model gives more confident prediction for data interpolations rather than extrapolations.

A.4.1 Tip Mach Number

The effect of tip Mach number was first studied. Figure A.8 compares the computed loads for open and ducted propellers for the three tip Mach numbers studied at hover conditions. The dots denote the respective data sampling points evaluated by CFD computations, the lines denote the Kriging prediction, and the shaded area represent the 99% confidence interval. This notation applies to all following figures.

The open propeller configuration showed a significant variation on both thrust and torque with Tip Mach number. The change in tip Mach number resulted in significant changes in the local angle of attack, thereby resulting in this significant variation. The Kriging curve shows a peak *FoM* around $Ma_{tip} = 0.6$. A similarly large variation in thrust and torque was also observed for the ducted propeller configuration in Figure A.8(b). The Kriging curve shows the peak *FoM* lies at a tip Mach number a little higher than the baseline value. The ducted propeller configuration also showed a higher *FoM* than the open configuration, and at times higher than 1. This is because the total thrust is supported by the contribution from the duct at no cost of torque. The breakdown of loads found that at lower tip speeds the total thrust was provided by the propeller. However, as the tip speed increased, the duct made an increasing contribution to the total thrust. This should be due to the larger propeller suction and hence the flow acceleration at the duct surface.

The effect of tip speed was next evaluated at forward-flight conditions. Figure A.9 presents the computed loading of both configurations with Kriging at forward flight conditions. Again, the tip Mach number was seen to have a significant effect on both open and ducted propeller configurations. For both configurations, without changing the blade pitch angle, reducing the tip

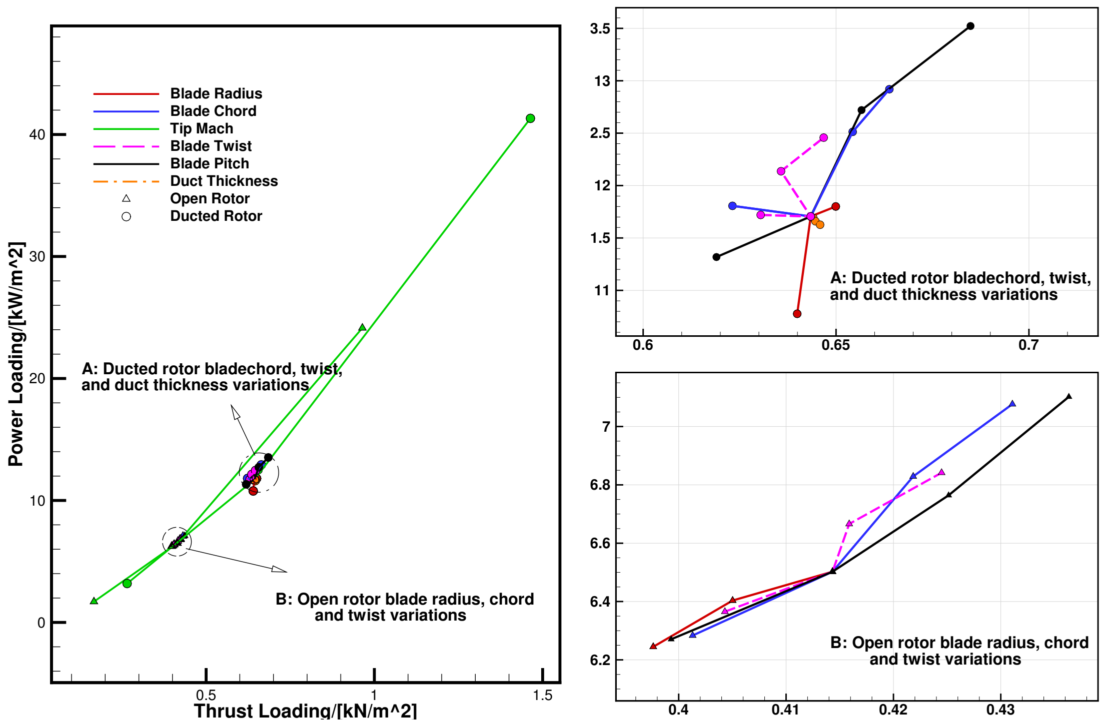

(a) Thrust loading-power loading map of the ducted/un-ducted propellers in hover.

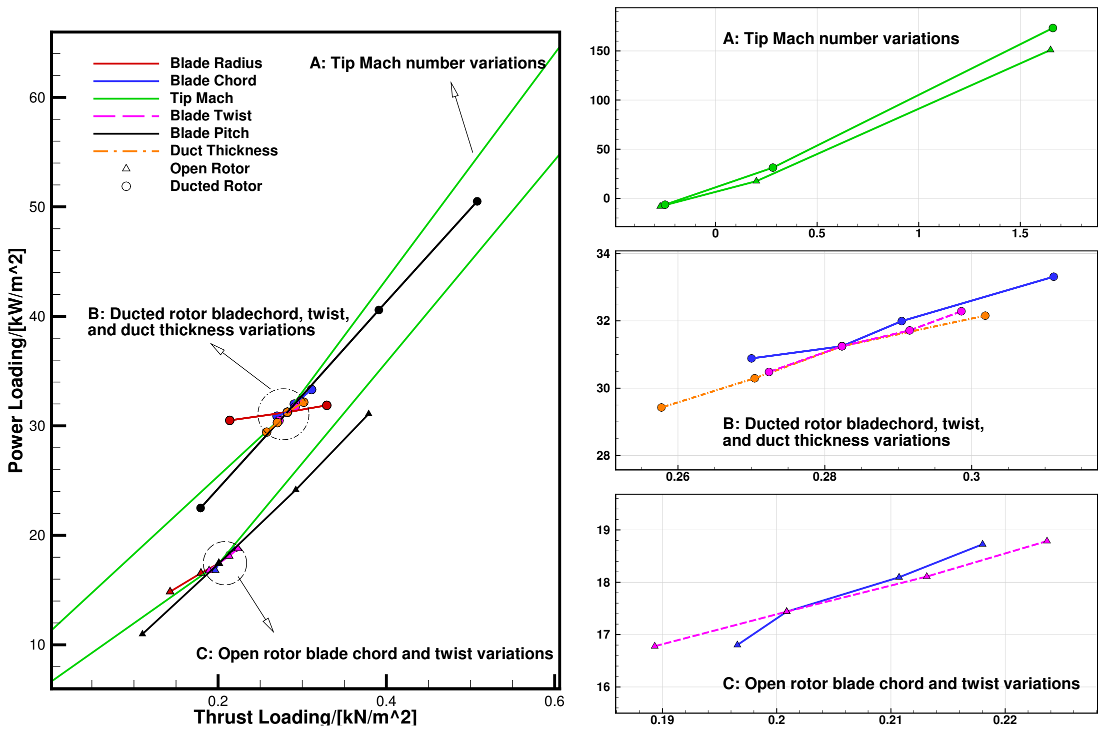

(b) Thrust loading-power loading map of the ducted/un-ducted propellers in forward flight.

Figure A.7: Thrust loading-power loading map of the equivalent ducted/un-ducted propellers in hover and forward flight.

speed below $Ma_{tip} = 0.3$ resulted in negative thrust values. This is typical as the local blade

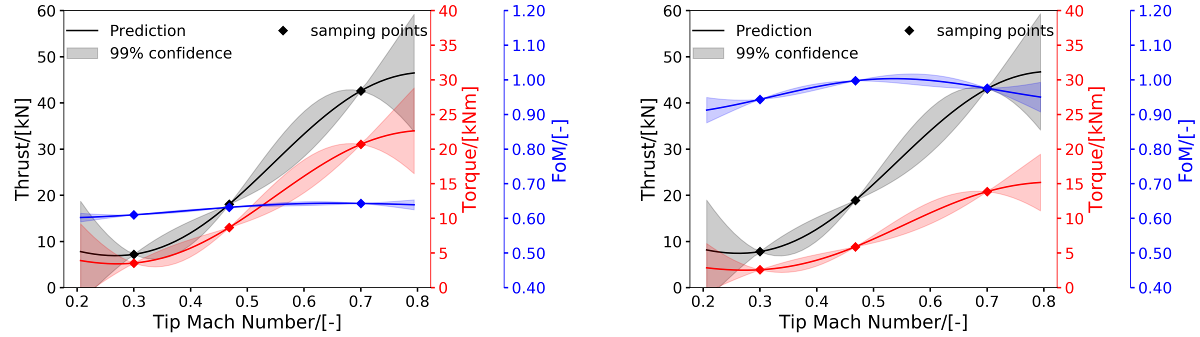

(a) Open propeller

(b) Ducted propeller

Figure A.8: Effect of tip Mach number on computed loading for open and ducted propellers with Kriging fitted for hover case.

element may be facing negative effective angles of attack, due to the low rotational speed and the fast axial forward speed. On the other hand, as the tip speed increased, similarly to the hover case, there was a significant increase in the blade loads. The peak efficiency was predicted to occur near $Ma_{tip} = 0.6$ for both configurations. The ducted configuration shows generally lower efficiency than the equivalent open propeller in forward flight, due to the duct drag in forward flight. The efficiency of both configurations was set to zero below $Ma_{tip} = 0.3$ due to the negative thrust calculated at and below this point. The loads breakdown found that the open blades were more sensitive to tip Mach number changes. For the ducted configuration, the blade thrust changed significantly with tip speed variations, while the duct showed relatively small increases responding to the tip speed changes.

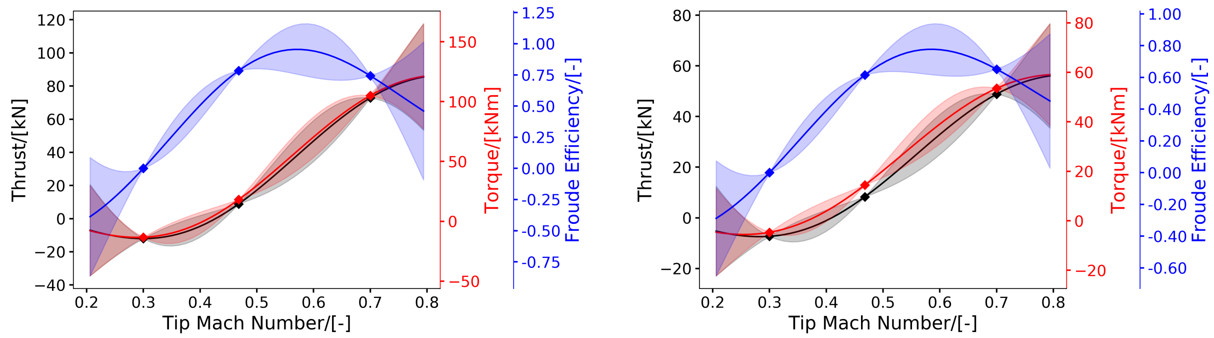

(a) Open propeller

(b) Ducted propeller

Figure A.9: Effect of tip Mach number on computed loading for open and ducted propellers with Kriging fitted for forward flight case.

Overall, the tip Mach number had a significant effect on the resulting loads. Peak efficiency was observed for both configurations at both hover and forward flight conditions above the baseline value. However, the tip Mach number will also have a significant impact on the acoustic emissions of both configurations and must therefore be considered in the design choice.

A.4.2 Propeller Pitch

The blade pitch angle is typically used to trim the propellers to deliver the required thrust. As part of the parametric study, the propeller pitch angle for both open and ducted configurations was investigated. Figure A.10 presents the computed performance of both configurations over a range of pitch angles at hover conditions.

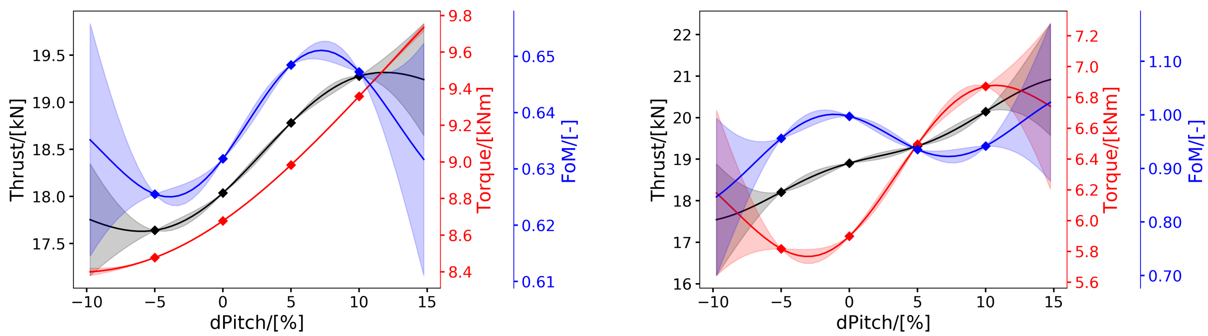

(a) Open propeller (b) Ducted propeller

Figure A.10: Effect of blade pitch on computed loading for open and ducted propellers with Kriging fitted for hover case.

Both configurations showed the expected increase in both thrust and torque with increasing pitch angles. It should also be noted that the ducted configuration required a higher pitch angle to trim to the required thrust. Whilst the open propeller showed the greatest *FoM* near +5% pitch angles, but the absolute efficiency changes are generally minor. The ducted configuration had the peak *FoM* near the initial pitch angle. The Kriging curve has a sinusoidal shape and suggests that the efficiency may be further increased at higher pitch settings, yet this needs to be verified with more data points. Nonetheless, the *FoM* of the ducted configuration was greater than that of the open configuration over the range of pitch angles studied. The thrust breakdown found that open blade thrust was more sensitive to the pitch changes than the ducted blades. The duct thrust was also slightly increasing as the pitch angle was increased, which is due to the increased propeller suction.

Figure A.11 evaluates the effect of pitch angle on both configurations at forward flight conditions. The forward flight conditions showed similar trends as those at hover conditions. For both configurations, the thrust and torque were increasing almost linearly with the increasing pitch angle, which led to very small uncertainties in the Kriging approximation. For the open propeller configuration, there was a peak efficiency located near and beyond +5% pitch. Whilst for the ducted propeller, the peak efficiency was located beyond the positive range of pitch values. It is also worth noticing that as the pitch angle is increased, the ducted propeller efficiency becomes comparable to the open propeller in this forward flight condition. The thrust breakdown also found that the open blades are more sensitivities to pitch changes. The duct thrust was also increasing as the pitch angle was increased.

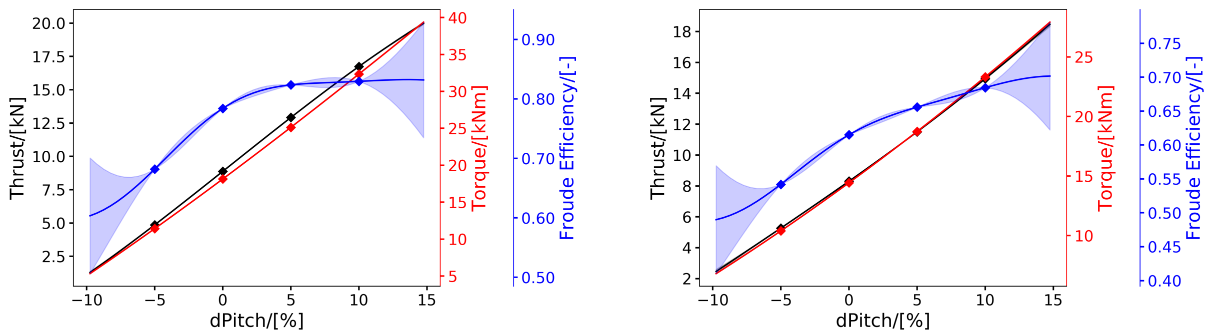

(a) Open propeller

(b) Ducted propeller

Figure A.11: Effect of blade pitch on computed loading for open and ducted propellers with Kriging fitted at forward flight conditions.

A.4.3 Blade Radius

The sensitivity of both configurations to the tip radius was next evaluated. In the present case, the tip speed was held constant (i.e. resulting in a change in rotational speed for each case), and the solidity was also held constant (i.e. resulting in scaling of the blade chord) for changes in the tip radius. In addition, the tip gap ratio between duct and propeller was also maintained, resulting in an increased duct radius for increasing propeller radius.

The open propeller configuration showed an increase in both thrust and torque for increasing radii in Figure A.12(a). The ducted configuration in Figure A.12(b) also showed an increase in loading for increasing radii. The increase in both thrust and torque was much more significant than that of the open propeller. Both configurations showed increased efficiency with increased radii. However, the efficiency of the ducted configurations varied very little and maintained near 1.0, while the open propeller efficiency varied between 0.5 to 0.65. The thrust breakdown of the ducted configuration found that the significantly higher thrust came from the additional contribution of thrust from the duct. In fact, the duct was found to produce an almost equal thrust to the open propeller configuration over the range of tip radii. At hover conditions, the ducted propeller was shown to be a much more effective propulsive device for increasing tip radii. The propeller of the ducted configuration produced higher thrust at increased radii compared to the open propeller when fixing the pitch and tip Mach number.

The effect of blade radius was evaluated at forward flight conditions in Figure A.13. The two configurations again showed very similar positive responses to the radius variations, with the ducted propeller having larger variations in the thrust and torque values. The efficiency of the two configurations are also similar in this forward flight condition. The thrust breakdown of the ducted configuration found that the ducted blades produced the majority of the thrust at this forward flight condition, while the duct contributed to an increasing amount of drag as the blade radius was increased. This is because the duct radius had to be increased to accommodate the increasing blade radius. Nonetheless, the propeller of the ducted configuration produced greater thrust for a given blade radius, than the equivalent open propeller.

Overall, the two configurations showed similar and positive responses to blade radius variations, but the ducted propeller configuration was shown to be more sensitive. Further, in hover

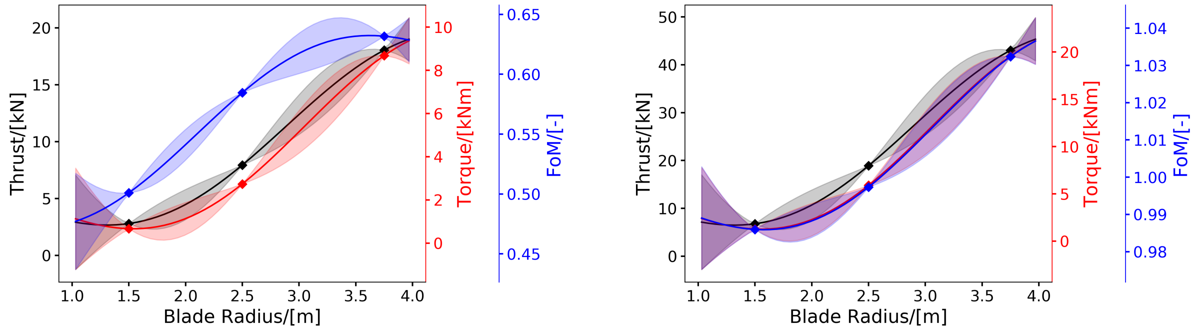

(a) Open propeller (b) Ducted propeller

Figure A.12: Effect of tip radius on computed loading for open and ducted propellers with Kriging fitted for hover case.

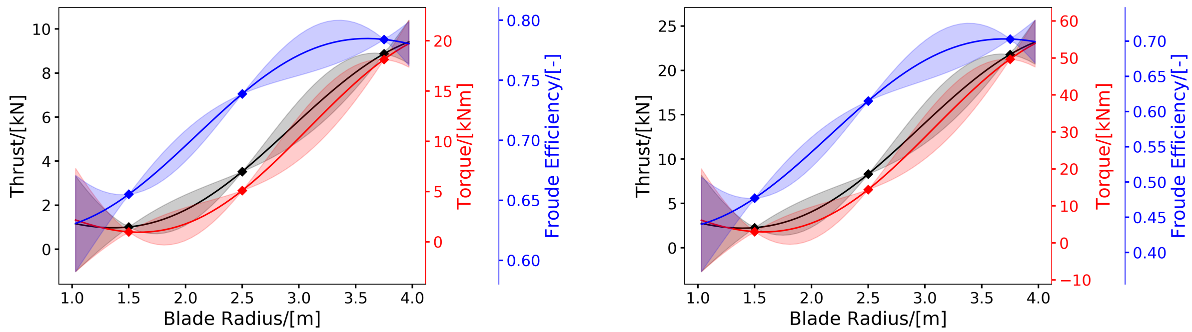

(a) Open propeller (b) Ducted propeller

Figure A.13: Effect of blade radius on computed loading for open and ducted propellers with Kriging fitted for forward flight case.

conditions, the duct could produce as much thrust as the open propeller configuration. However, in forward flight this translated to an increase in drag. Therefore, the duct or propeller blade radius must be finely tuned for high performance across hover and forward flight operations.

A.4.4 Blade Chord

The propeller chord was investigated as a design choice on both configurations. The propeller chord was scaled over a range of values from the baseline. This affected the solidity of the propeller, which may also be indicative of changes in blade count and tip radius.

Figure A.14 presents the effect of chord variation on both open and ducted propeller configuration performance in hover. For both configurations, changes in the blade chord brought relatively small changes in the thrust and torque, but the performance variations tend to be wavy as suggested by the Kriging fitting. For the open propeller, the *FoM* was higher at reduced blade chords. For the ducted propeller, a peak *FoM* is observed near the baseline chord, but higher efficiency may be possible at larger chords as suggested by the Kriging fitting. Thrust breakdown of the ducted

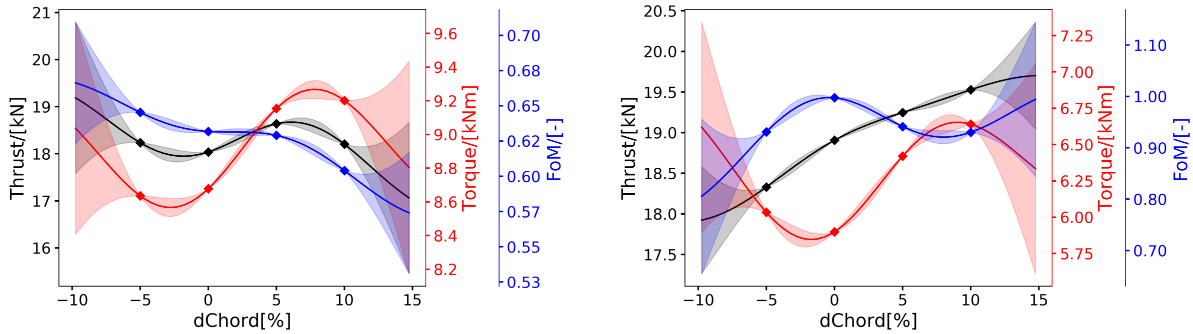

(a) Open propeller

(b) Ducted propeller

Figure A.14: Effect of blade chord on computed loading for open and ducted propellers with Kriging fitted for hover case.

configuration found that the blade thrust was increasing with increasing chords, while the duct was found to deliver the peak thrust around the location of peak efficiency.

Figure A.15 evaluates the effect of chord on both configurations at forward flight conditions. Both configurations showed consistently increasing loading with increased chord. However, in terms of efficiency, whilst the ducted configuration showed an increased propulsive efficiency with increased chord, the open configuration showed the opposite trend, although the absolute efficiency values varied little. Furthermore, the efficiency of the open configuration was greater than that of the ducted configuration across the range of blade chord values. No peak value was observed for either configuration, suggesting the optimal efficiency lies outwith the considered range. The thrust breakdown of the ducted configuration found that the change in chord had only a small effect on the duct. On the other hand, the change in chord shows the expected increase for the blade contribution.

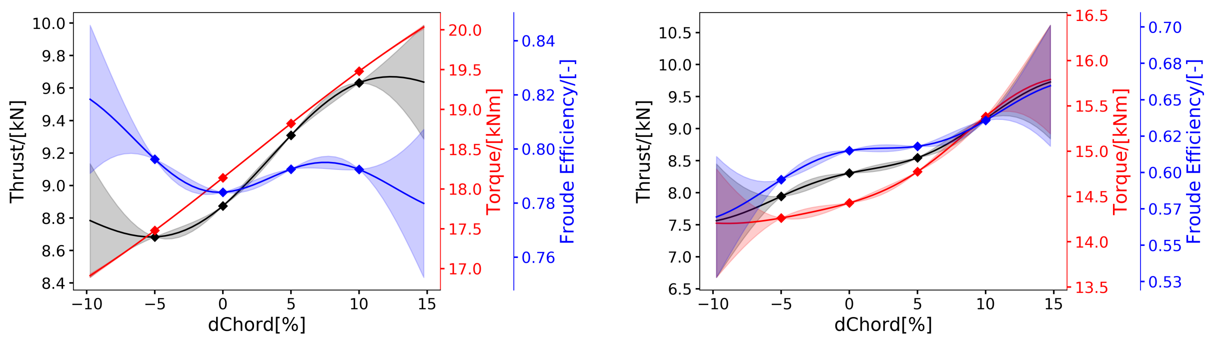

(a) Open propeller

(b) Ducted propeller

Figure A.15: Effect of blade chord on computed loading for open and ducted propellers with Kriging fitted for forward flight conditions.

Overall, the effect of chord was not consistent between hover and forward flight conditions, requiring a compromise in the design between the two conditions. However, at forward flight conditions, the effect of chord was found having a minimal effect on the duct performance, allowing for greater freedom in the design of the propeller.

A.4.5 Blade Twist

The propeller blade twist was next evaluated. The baseline case had a twist of about $-23°$. The twist was varied from the baseline for the current study.

The resulting loading for both open and ducted configurations was evaluated for hover conditions in Figure A.16. For the open propeller, changes in the twist brought very little change in the thrust and torque values. Both thrust, torque, and efficiency were all found to increase with increasing twists. The open propeller efficiency also varied little around 0.64. For the ducted propeller, the variations in thrust and torque are also relatively small, and the trends are wavy. The ducted propeller efficiency experienced a slight variation near 0.95, with a peak *FoM* near the baseline twist.

The thrust breakdown of the ducted propeller found that the increased *FoM* can again be attributed to the contribution of the duct at hover conditions. Both the duct and blade were shown to have small but opposite responses to changes in twist around the baseline value. An overall small effect on the total ducted propeller thrust was resulted. Compared to the open configuration, the overall ducted propeller configuration hence had a reduced sensitivity to changes in blade twist.

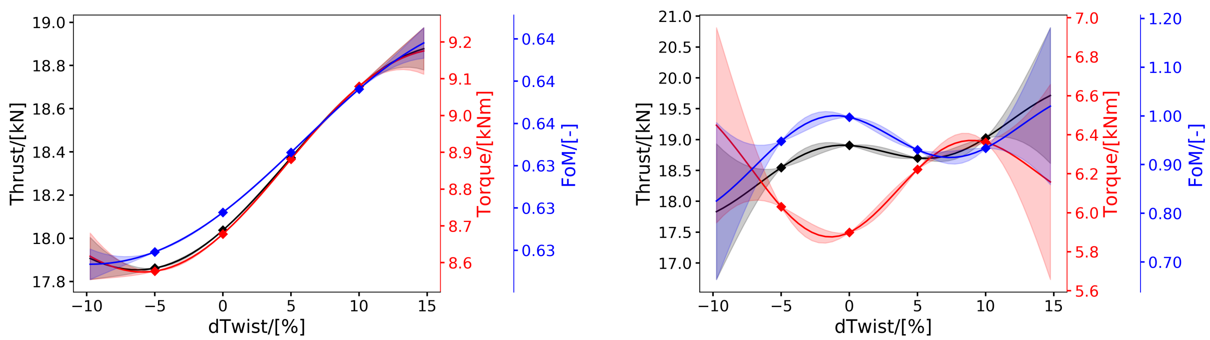

(a) Open propeller (b) Ducted propeller

Figure A.16: Effect of blade twist on computed loading for open and ducted propellers with Kriging fitted for hover case.

Figure A.17 evaluates the effect of blade twist now at forward flight conditions. Both open and ducted configurations showed increased loading with the increasing twist, with little uncertainties in the Kriging fitting. For the open propeller, the propulsive efficiency was shown to increase with increasing twist, with a possible peak value near $+10\%$ of the baseline design. For the ducted propeller configuration, the optimal value was also shown to be around $+10\%$ of the baseline design. The thrust breakdown of the ducted propeller found that the duct thrust was almost unchanged by the twist variations. The blade thrust variations were also small. Comparing the open configurations, the ducted configuration showed reduced sensitivity to the twist angle.

Overall, both open and ducted configurations showed the expected increasing loading for increasing twist. Under both hover and forward flight conditions, the ducted configuration appeared less sensitive to changes in twist comparing to other design variables. This reduced sensitivity of

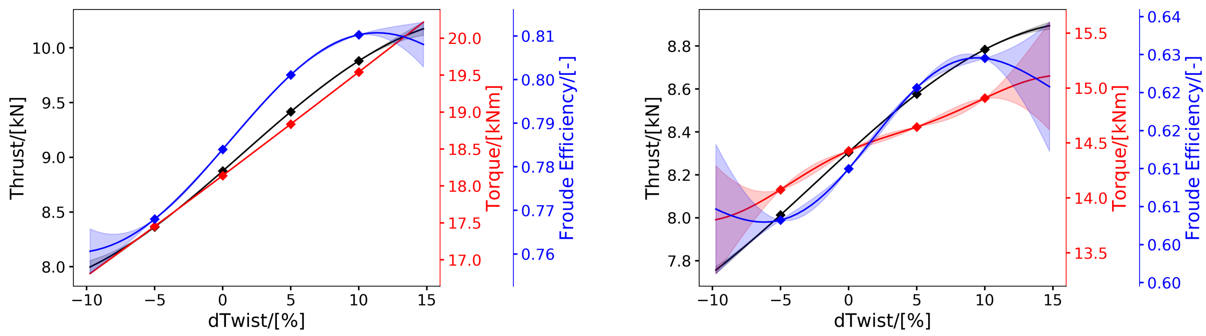

(a) Open propeller

(b) Ducted propeller

Figure A.17: Effect of blade twist on computed loading for open and ducted propellers with Kriging fitted for forward flight conditions.

the ducted configuration to the twist is beneficial, as more freedom can be allowed in the blade twist.

A.4.6 Duct Thickness

The previous analysis has shown that the duct can have a significant affect on the ducted propeller performance at both hover and forward flight conditions. The duct thickness was included in the parametric study to evaluate further its impact on the ducted propeller configuration.

Figure A.18(a) presents the effect on the ducted propeller performance over a range of duct thickness-chord ratios in hover. The performance of the ducted propeller was shown to be relatively unaffected by the duct thickness under hover conditions. The thrust breakdown found that both the propeller and duct thrust was relatively unaffected by changes in duct thickness. This is expected as the interior surface of the duct and the leading-edge region, which are responsible for the contribution to the total thrust in hover conditions, remained mostly unchanged by the thickness variation. Therefore, the duct thickness changes, which mostly alter the outer shapes, had little effect on the hover performance of the ducted propeller.

The duct thickness was also examined at forward flight conditions as shown in Figure A.18(b). The thrust, torque and resulting propulsive efficiency were all shown to degrade for increasing duct thickness. This is due to the increase in duct drag (negative thrust) with increasing thickness. However, a reduction in the propeller thrust was also observed, which should be due to induction changes brought by the duct shape variations.

The analysis shows that a duct with a much lower thickness would be optimal for the forward flight conditions. The hover analysis shows that this can be achieved with minimal impact on the hover performance.

A.5 Chapter Summary

This chapter investigated the size correlation between the ducted rotor and the equivalent open rotor. A ducted rotor design and the equivalent open rotor were proposed to support a four-rotor

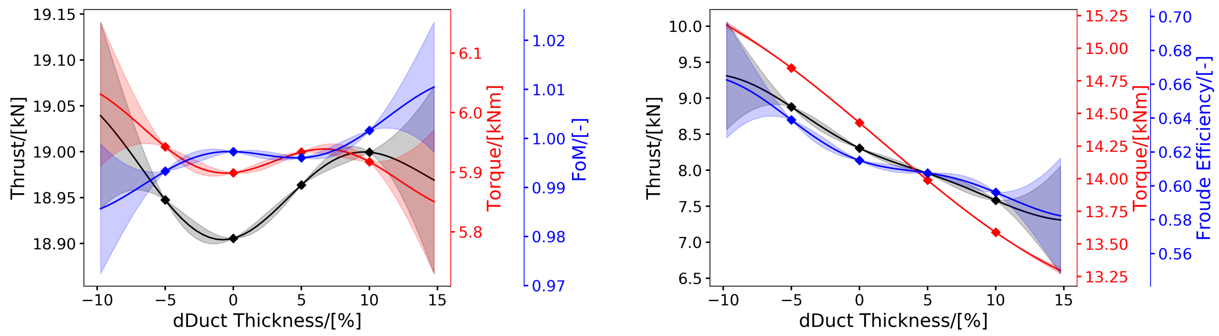

(a) Ducted propeller hover

(b) Ducted propeller forward

Figure A.18: Effect of duct thickness on computed loading for ducted propeller with Kriging fitted at hover and forward flight conditions.

vehicle of 6,000 kg, based on a model-size NASA ducted rotor test case. The aerodynamic and far-field acoustic performance of the baseline designs was examined and compared using modern CFD methods. A parametric study was performed to investigate performance variations with respect to changes in geometric and operating parameters of the equivalent rotors. Kriging-based surrogate models were built to further inspect the performance variations to particular design changes. From the current investigation, the following conclusions can be derived:

1. A pair of equivalent ducted/un-ducted rotor designs were proposed using the momentum theory and BEMT methods. The ducted rotor was able to deliver the desired thrust in hover and in forward flight at the cost of much lower torque, but the power requirement was slightly higher due to the higher RPM. In hover, the ducted rotor showed a higher *FoM* due to the duct thrust. The wake profiles of the two configurations in hover were also found similar, although the ducted rotor has a much reduced radius while producing the same thrust. In the forward flight case tested, however, the ducted rotor showed lower efficiency than the equivalent open rotor due to the duct drag. Compared to the equivalent open rotor, the ducted rotor has a 40% reduced radius and a 70% reduced frontal area, which is very favourable for confined space. Far-field acoustic calculations of the two configurations using the FW-H equations also showed great acoustic benefits by ducting, despite the higher RPM of the ducted rotor.

2. For the non-axial flight condition examined, the equivalent rotors contributed more to the lift than to the thrust. The ducted blades were offloaded and experienced lower variations in loads caused by the asymmetric inflow, thanks to the duct shielding. The duct surface produced large forces due to the non-axial free-stream. The ducted rotor configuration produced negative thrust at the condition examined, due to the large negative contributions from the duct. However, the ducted lifting force was about 3 times higher than that of the open rotor, with the major contribution from the duct.

3. A parametric study of the equivalent ducted/un-ducted rotors was performed in hover and in forward flight, and Kriging-based surrogate models were built to inspect the performance trends subject to the design changes. The ducted rotor showed higher thrust and power

loadings due to the smaller size. The tip Mach number shows significant effects on the aerodynamic loads. Peak efficiencies were observed for both configurations at both hover and forward flight conditions above the baseline tip Mach number. Increasing the blade pitch leads to increased loadings for both configurations, but optimal efficiencies were noted at specific pitch setting. For the ducted rotor in forward flight, its efficiency can be higher than the open rotor when the pitch angles are large. The ducted rotor configuration is shown to be more sensitive to changes in tip radius. For hover conditions, the enlarged duct alone could produce as much thrust as the open rotor configuration. However, in forward flight, the enlarged duct contributed largely to drag. Effects of chord are not consistent between hover and forward flight conditions for both configurations, hence requiring a compromise in the design between the two conditions. However, at forward flight conditions, the effect of chord is shown to have a minimal effect on the duct performance. Both open and ducted configurations showed the expected increasing loading for increasing twist. Under both hover and forward flight conditions, the ducted configuration appears less sensitive to changes in twist. The duct thickness shows minor effects on hover performance, but lower thickness would be beneficial for the forward flight.

Appendix B

Scripts for Far-field Acoustic Computations

This appendix presents the far-field acoustic code based on the Farassat 1A formulation. The scripts are written in the programming language Julia. Julia is a high-level programming language designed specifically for high-performance computing. It combines the easy implementation of high-level languages such as Python and the high efficiency of low-level languages such as C or FORTRAN. It also features easy implementations of parallel computing across plantforms. These are the reasons why the current implementation of the Farassat 1A formulation used Julia. However, Julia is still a fast-evolving and not-yet-stable language with many experimental features that are often modified in new releases. It must be highlighted that the current codes were based on Julia V1.4.2.

The current program consists of a main file and several supporting scripts. The input files are:

- blade and duct panels with pressure data;
- operating conditions;
- coordinates of observation points.

Note that the program assumes the blades have a constant rotation about the positive z axis. The input panels can either contain only a fraction of the blades (or duct), or the entire geometry.

The output files are:

- visualisation files of the input panels;
- acoustic signals at each observation point.

The program supports parallel computing among processors. It is executed through the following command:

```
julia -p <nprocessors> main_2panels_pmap_full.jl
```

where $< nprocessors >$ is the number of processors the program to be run on, which should be at least 1 and no larger than the number of observer points. The command *julia* is default launcher of Julia scripts that should be configured in advance (or use full path to the binary).

The main scripts for the program is written in List B.1. This script governs the entire program structure and data flow.

Listing B.1: main_2panels_pmap_full.jl

```
using Distributed
@everywhere using Interpolations
@everywhere using Plots
@everywhere using Printf
@everywhere using SharedArrays

@everywhere include("PANEL_GEN_new_array_test.jl")
@everywhere include("para_pmap_full . jl")#parameters
@everywhere include("ROTATION_pmap.jl")
@everywhere include("fara1a . jl")
@everywhere include("post−acoustics . jl")
@everywhere include(" obs_acoustics_func_full . jl")
@everywhere include("copy2full . jl")
time1=time()

include ("obs_def . jl")

for i = 1:Nobs
    println ("MIC$i $(xobs[i ,1]) $(xobs[i ,2]) $(xobs[i ,3])")
end
xyz1, P1 = read_LT2(panel1)

xyzc1, nxyzc1, Pc1, Area1 = panel_gen2(xyz1, P1)



check_panel2(panel1,xyzc1, nxyzc1, Pc1, Area1)

#panel Imx and Jmx
II = size(xyzc1,1)
JJ = size(xyzc1,2)

xyzc1_temp = zeros( II∗JJ, 3)
nxyzc1_temp = zeros( II∗JJ, 3)
Pc1_temp = zeros( II∗JJ)
Area1_temp = zeros( II∗JJ)
for i = 1: II
    for j = 1:JJ
        #don't make mistakes here
        i1d = (i−1)∗JJ+j
        # println (i , j )
        #display (i1d)
        xyzc1_temp[i1d ,:] = xyzc1[i,j ,:]
        nxyzc1_temp[i1d ,:] = nxyzc1[i,j ,:]
        Pc1_temp[i1d] = Pc1[i,j]
        Area1_temp[i1d] = Area1[i,j]
    end
end

if is_2Panels == 1
    xyz2, P2 = read_LT2(panel2)
    xyzc2, nxyzc2, Pc2, Area2 = panel_gen2(xyz2, P2)
    #panel Imx and Jmx
    check_panel2(panel2, xyzc2, nxyzc2, Pc2, Area2)
    II = size(xyzc2, 1)
    JJ = size(xyzc2, 2)
    xyzc2_temp = zeros( II ∗ JJ, 3)
    nxyzc2_temp = zeros( II ∗ JJ, 3)
    Pc2_temp = zeros( II ∗ JJ)
    Area2_temp = zeros( II ∗ JJ)
    for i = 1: II
        for j = 1:JJ
            i1d = (i − 1) ∗ JJ + j
            xyzc2_temp[i1d, :] = xyzc2[i, j, :]
            nxyzc2_temp[i1d, :] = nxyzc2[i, j, :]
            Pc2_temp[i1d] = Pc2[i, j]
            Area2_temp[i1d] = Area2[i, j]
        end
    end

    xyzccat = vcat(xyzc1_temp, xyzc2_temp)
    nxyzccat = vcat(nxyzc1_temp, nxyzc2_temp)
    Pccat = vcat(Pc1_temp, Pc2_temp)
    Areacat = vcat(Area1_temp, Area2_temp)
    # println ("$(Areacat[1])")
    # println ("$(Areacat[end])")
    @everywhere xyzct1 = $xyzccat
    @everywhere nxyzct1 = $nxyzccat
    @everywhere Pct1 = $Pccat
    @everywhere Areat1 = $Areacat
    # println ("$(Area[1])")
    # println ("$(Area[end])")
else
    @everywhere xyzct1 = $xyzc1_temp
    @everywhere nxyzct1 = $nxyzc1_temp
    #if is_Pabs == 0
    @everywhere Pct1 = $Pc1_temp
    #else
    @everywhere Areat1 = $Area1_temp
end

```

```
@everywhere global II = size(xyzct1,1)*Nb
@everywhere global xyzc = zeros(II,3)
@everywhere global nxyzc = zeros(II,3)
@everywhere global Pc = zeros(II)
@everywhere global Area = zeros(II)

@everywhere xyzc, nxyzc, Pc, Area = copy2full(Nb, xyzct1, nxyzct1, Pct1, Areat1, size(xyzct1,1) )

println("Panels concatenated. Total number: $II.")


if is_Pabs == 1
    @everywhere for i = 1:II
        Pc[i] = Pc[i]-P0
    end
end

################Farassat 1A

iobs = 1:Nobs
@time pmap(obs_acoustics, xobs[:,1], xobs[:,2], xobs[:,3], iobs; batch_size=1)

etime = time()-time1

println("elapsed time:")
display(etime)
```

The input operating conditions are configured in the parameter script below:

Listing B.2: para_pmap_full.jl

```
#parameters
global 0 = 1.225 #kg/m^3
#P0 = 101325.0 #Pa
global c = 340.3 #m/s, speed of sound
global RPM = 405.6 #
global Nb = 4 #number of blades(or periodicity )

global Ndt_per = 90 #number of time sample points for each periodicity , to be multiplied by blade number Nb


global Nrot = 2 #number of blade rotations
global Vtrans = [0.0, 0.0 , 68.06] #panel surface translation velocity


global is_Pabs = 1 #is it P rather than dP?
global P0 = 101325.0 #the reference pressure to be subtracted if not yet done[Pa]
global is_2Panels = 0 #2 panel inputs?

global panel1 = "../input_panels/Dale_input_new/LT_hfwh_open_blade-inverse"
global panel2 = "../input_panels/Dale_input_new/LT_hfwh_duct"
global outdir = "../output/Dale_output_new/new-inverse-op-"


#######################################
#######################################
global T = Nrot*60.0/RPM #s, period of rotation , may be different from the TimeInformation
global OMEGA = RPM*2*pi/60.0 # rad/s, angular velocity
global Ndt = Ndt_per*Nb*Nrot

global dazi = Nrot*2.0*pi/(Ndt)
global dtau = T/ (Ndt)

println("Number of rotations : $Nrot")
println("OMEGA: $OMEGA")
println("dazi: $dazi")
println("dtau: $dtau")
```

The observation points are defined in *obs_def.jl*:

Listing B.3: obs_def.jl

```
"""
    define your observation points here
    and store in the 1d array xobs[Nobs,3]
    Nobs: number of observation points in total
"""
#loop over observation potins
th1 = 0.5*pi
th2 = -0.5*pi
Nobs = 1
#theta = LinRange(th1,th2,Nobs)
theta = zeros(1)
dist = 20
xobs= zeros(Nobs,3)

xobs[:,1] = dist*cos.(theta)
xobs[:,2] = zeros(Nobs).+0.0
##xobs[:,3] = dist*sin.(theta)
```

```
xobs [:,3]  =  dist ∗sin .( theta ) #.−3.03∗0.0254
display (xobs)
```

The *ROTATION_pmap.jl* file contains miscellaneous functions for rotations, dot product, etc.

Listing B.4: ROTATION_pmap.jl

```

using LinearAlgebra
#    in rad
function RotateX(X::Vector,      :: Float64)
    cs= cos(   )
    sn= sin(   )
    X1 = zeros(3)
    X1[1] = X[1]
    X1[2] = cs∗X[2]−sn∗X[3]
    X1[3] = sn∗X[2]+cs∗X[3]
    return X1
end

#    in rad
function RotateY(X::Vector,      :: Float64)
    cs= cos(   )
    sn= sin(   )
    X1 = zeros(3)
    X1[1] = cs∗X[1]+sn∗X[3]
    X1[2] = X[2]
    X1[3] = −sn∗X[1]+cs∗X[3]
    return X1
end

#    in rad
function RotateZ(X::Vector,      :: Float64)
    cs= cos(   )
    sn= sin(   )
    X1 = zeros(3)
    X1[1] = cs∗X[1]−sn∗X[2]
    X1[2] = sn∗X[1]+cs∗X[2]
    X1[3] = X[3]
    return X1
end
#    in rad
@inline function RotateZ2(X::Array{Float64,1}, cs :: Float64, sn :: Float64)
    #cs= cos(   )
    #sn= sin(   )
    X1 = zeros(Float64 ,3)
    X1[1] = cs∗X[1]−sn∗X[2]
    X1[2] = sn∗X[1]+cs∗X[2]
    X1[3] = X[3]
    return X1
end
#    in rad
@inline function dRotateZ(X::Array{Float64,1},      :: Float64, Omega::Float64)
    cs= cos(   )
    sn= sin(   )
    X1 = zeros(3)
    X1[1] = (−sn∗X[1]−cs∗X[2])∗Omega
    X1[2] = (cs∗X[1]−sn∗X[2])∗Omega
    X1[3] = 0.0
    return X1
end

@inline function dRotateZ2(X::Array{Float64,1}, cs :: Float64, sn :: Float64, Omega::Float64)
    #cs= cos(   )
    #sn= sin(   )
    X1 = zeros(Float64 ,3)
    X1[1] = (−sn∗X[1]−cs∗X[2])∗Omega
    X1[2] = (cs∗X[1]−sn∗X[2])∗Omega
    X1[3] = 0.0
    return X1
end

@inline function ddRotateZ2(X::Array{Float64,1}, cs :: Float64, sn :: Float64, Omega::Float64)
    #cs= cos(   )
    #sn= sin(   )
    X1 = zeros(3)
    # ddt =0
    X1[1] = (−cs∗X[1]+sn∗X[2])∗Omega∗Omega
    X1[2] = (−sn∗X[1]−cs∗X[2])∗Omega∗Omega
    X1[3] = 0.0
    return X1
end
##forward difference
fdiff (x0:: Any, x1 :: Any, dt :: Float64) = (x1−x0)./dt;



@inline function Interp2Obs(Ain::Array{Float64,1}, Ax::Array{Float64,1}, SamplePnts::Array{Float64,1})
    #Ain = pt_tau_IJ [:, i , j ]
    #Ax = t_re_IJ [:, i , j ]
    p = zeros( Int , size (Ax))
    sortperm !( p, Ax)
```

```
    #display(p)
    nodes = (Ax[p],)
    intp = interpolate(nodes, Ain[p], Gridded(Linear()))
    extp = extrapolate(intp, Periodic())
    #extp = extrapolate(intp, Line())
    return extp(SamplePnts)
end

function BladeImpose2(Pin, N_per::Int64, Nbld, Nt)
    P = zeros( Float64,Nt)
    p_ibld = zeros(Float64,Nt)
    for ibld = 1:Nbld
        ioffset = (ibld-1)*N_per
        for iNt = 1:Nt
            ntid = iNt+ ioffset
            if ntid > Nt
                ntid -=Nt
            end
            p_ibld[iNt] = Pin[ntid]
        end
        display(plot(p_ibld))
        #hold(true)

        P += p_ibld
    end
    display(plot(P))
    return P
end


function BladeImpose(pin, Ndt_per, Nb, Ndt)
    p_bld = zeros(Float64,Ndt_per)
    P = zeros( Float64,Ndt)
    for ibld = 1:Nb
        it_begin = (ibld-1)*Ndt_per+1
        it_end = (ibld)*Ndt_per
        p_bld[:] += pin[it_begin:it_end]
    end

    for ibld = 1:Nb
        it_begin = (ibld-1)*Ndt_per+1
        it_end = (ibld)*Ndt_per
        #for jbld = 1:Nb
        P[it_begin:it_end] = copy(p_bld[:])
        #end
    end
    return P
end

@inline mydot(x::Array{Float64,1}, y::Array{Float64,1}) = x[1]*y[1]+x[2]*y[2]+x[3]*y[3]
```

Key functions regarding the Farassat 1A formulation is written in file *fara1a.jl*:

Listing B.5: fara1a.jl

```

@inline function Cal_Pt_tau(rho0::Float64, vn::Float64, dvn::Float64,c::Float64, Mr::Float64, Mi::Vector{Float64},dMi::Vector{Float64}, rRi::Vector{Float64}, R::Float64,
    Area::Float64)

    Mr1 = (1-Mr)
    Mr12 = Mr1*Mr1
    Mr13 = Mr1*Mr1*Mr1
    ## nearfield
    ptn1 = rho0*vn*c*(Mr-mydot(Mi,Mi))/((R^2)*(Mr13))
    ## farfield
    ptf1 = rho0 * dvn /(R*(Mr12))# equation checked
    ptf2 = rho0 * vn *mydot(rRi, dMi)/(R*(Mr13))#equation checked
    #record thickness pressure at each emmision time
    pt_tau = (ptn1+ ptf1 + ptf2)*Area
    #pt_tau = ( ptf1 + ptf2)*Area

    return pt_tau
end

@inline function Cal_Pl_tau(li::Vector{Float64}, dli::Vector{Float64}, c::Float64, Mr::Float64, Mi::Vector{Float64},dMi::Vector{Float64}, rRi::Vector{Float64}, R::Float64
    , Area::Float64)

    Mr1 = (1-Mr)
    lr = mydot(li,rRi)
    Mr12 = Mr1*Mr1
    Mr13 = Mr1*Mr1*Mr1
    # nearfield
    pln1 = (lr-mydot(Mi, li))/(R^2*Mr12)#checked
    pln2 = lr*(Mr-mydot(Mi, Mi))/(R^2*Mr13)#checked
    ## farfield
    plf1 = mydot(dli,rRi)/(c*R*Mr12)#checked
    plf2 = lr*mydot(dMi, rRi)/(c*R*Mr13)#checked
    #record loading pressure at each emission time
    pl_tau = (pln1+pln2+plf1+plf2)*Area
    #pl_tau = (plf1+plf2)*Area
    return pl_tau
end
```

```
## calculate  li

# Cal_li (P::Float64, P0::Float64, ni :: Vector) = (P-P0)*ni;
@inline Cal_li (P::Float64, ni :: Vector{Float64}) = (P)*ni;

## calculate panel surface normal velocity time derivative  vn
@inline Cal_dvn(dvi :: Vector{Float64}, ni :: Vector{Float64}, vi :: Vector{Float64},dni :: Vector{Float64}) = mydot(dvi,ni)+mydot(vi,dni);

## calculate panel velocity vi, assuming rotation about z axis with arbitrary  translation  velocity
@inline Cal_vi(Vtrans :: Vector{Float64}, Xc::Vector{Float64},   :: Float64) = Vtrans + cross ([0.0,0.0,    ], Xc);
```

A few functions for signal post-processing are available in *post-acoustic.jl*:

Listing B.6: post-acoustic.jl

```
using  Statistics

function Prms(P::Array{Float64,1})
    #prms =  (P .^2.0) ^0.5
    prms = sqrt(mean(P.^2))
    return prms
end

function Calc_OSPL(P::Vector{Float64})
    pref = 2e-5
    prms = Prms(P)
    if prms < pref
        prms = pref
    end
    OSPL = 20.0 * log10(prms/pref)

    return OSPL
end
```

The acousitcs signals are assembled in *obs_acoustics_func_full.jl*:

Listing B.7: obs_acoustics_func_full.jl

```
function  obs_acoustics (obsx, obsy, obsz, iobs)
    # println ("$(Area[1])")
    # println ("$(Area[end])")
    #display (Area[end]
    #display (xyzc[end ,:])
    #time points
    xobs = zeros (3)
    xobs[1]=obsx
    xobs[2]=obsy
    xobs[3]=obsz

    ####these need to be SharedArrays
     pt_tau_IJ  = zeros(Ndt, II) #thickness noise of each panel at each emission time (area included)
    # pt_tau_IJ  = SharedArray{Float64,2}(Ndt, II) #thickness noise of each panel at each emission time (area included)
    # pt_tau_IJ  .= 0.0
     pl_tau_IJ  = zeros(Ndt, II) #loading noise of each panel at each emission time (area included)
    # pl_tau_IJ  = SharedArray{Float64,2}(Ndt, II) #loading noise of each panel at each emission time (area included)
    # pl_tau_IJ  .= 0.0
     t_re_IJ  = zeros(Ndt,II) # receiver time for each panel at each emission time
    # t_re_IJ  = SharedArray{Float64,2}(Ndt,II) # receiver time for each panel at each emission time
    # t_re_IJ  .= 0.0
    R_IJ = zeros(Ndt, II) #distance of panel to receiver point at each emission time
    #R_IJ = SharedArray{Float64,2}(Ndt, II) #distance of panel to receiver point at each emission time
    #R_IJ .= 0.0
    #loop over emission time point
     pt_re_IJ  = zeros(Ndt, II) #thickness noise at sample receiver time
     pl_re_IJ  = zeros(Ndt, II) #loading noise at sample receiver time
    pt = zeros(Ndt)#thickness noise array at receiver time
    pl = zeros(Ndt)#loading noise array at receiver time


     println ("iobs: $iobs")
    #ftime1 = time()
    for  ite = 1:Ndt
        #display (Threads. threadid ())
        azinow = dazi * (ite -1)##cautions!!!
        # println (" ite : $ite azi now: $azinow")
        tau_now = azinow / OMEGA
        # azidiff  = azinow + OMEGA * ddtau
        cs = cos(azinow)
        sn = sin(azinow)
        #cs1 = cos( azidiff )
        #sn1 = sin( azidiff )
        ##loop over panels
        for i = 1:II
            #for i = 1:II
                #panel coordinates
                xyzci = RotateZ2(xyzc[i ,:],  cs, sn)
                #xyzci1 = RotateZ2(xyzc [:, i , j ], cs1, sn1)
                #dxyzci = fdiff (xyzci, xyzci1, ddtau) #this is actually vi

```

```
                #panel norm vectors
                nci = RotateZ2(nxyzc[i ,:],  cs, sn)
                #nci1 = RotateZ2(nxyzc[:, i , j ],  cs1, sn1)
                ##fd
                #dncidff = fdiff (nci, nci1, ddtau)
                dnci = dRotateZ2(nxyzc[i ,:],  cs, sn, OMEGA)
                #display (dnci)
                #display ( dncidff )
                #display (norm(dnci−dncidff))
                #== velocities ==#
                ##panel velocity
                #vi=Cal_vi(Vtrans, xyzci, OMEGA) #linear velocity
                vi = dRotateZ2(xyzc[i ,:],  cs, sn, OMEGA)+Vtrans

                #vi1 = Cal_vi(Vtrans, xyzci1, OMEGA)
                #dvi = fdiff (vi, vi1, ddtau) #linear velocity derivative wrt tau
                dvi = ddRotateZ2(xyzc[i ,:],  cs, sn, OMEGA)
                # println ("dvi−dff")
                #display (dvi)
                # println ("dvi")
                #display (dvi2)
                Mi = vi/c #Mach number vector
                dMi = dvi/c # Mach number derivative

                ##panel normal velocity
                vn = mydot(vi,nci)
                dvn = mydot(dvi,nci)+ mydot(vi, dnci)
                # radiation vectors
                ri= xobs − xyzci
                R= norm(ri) #distance
                R_IJ[ ite , i ] = copy(R)
                ##normalised radiation vector
                rRi = ri / R
                ##Mach in radiation direction
                Mr = mydot(Mi, rRi)
                # lighthill tensor without viscosity
                li = Cal_li (Pc[i ], nci)
                #li1 = Cal_li (Pc[i , j ], nci1)
                #dli = fdiff ( li , li1 , ddtau)
                dli = Pc[i ] ∗ dnci #  lighthill tensor derivative

                #thickness noise
                pt_tau_IJ [ ite , i ] = Cal_Pt_tau ( 0 , vn, dvn, c, Mr, Mi, dMi, rRi, R, Area[i ])
                #loading noise
                pl_tau_IJ [ ite , i ] = Cal_Pl_tau ( li , dli , c, Mr, Mi, dMi, rRi, R, Area[i ] )
                #record the according receiver time at each emission time
                t_re_IJ [ ite , i ] = tau_now + R/c
        end
    end
    #ftime2 = time()
    # println ("ftime:")
    #display (ftime2 − ftime1)

    #find the minimum and maximum receiver time
    #tobs_min = minimum(t_re_IJ)
    #tobs_max = maximum(t_re_IJ)
    Rmin = minimum(R_IJ)
    Rmax = maximum(R_IJ)
    #tobs1 = 0.5∗(tobs_min+tobs_max)
    tobs1 = (Rmax)/c
    #tobs1 = 0.5∗(Rmin+Rmax)/c
    #tobs1 = 0.0
    tobs2 = tobs1 + T/Nrot
    #tobs2 = tobs_max

    # println (" start tobs: $tobs1")
    # println ("end tobs: $tobs2")
    # println (" difference : $T , $(tobs2−tobs1)")

    #construct sample receiver time for interpolation
    t_re_sample = convert(Array{Float64,1}, LinRange(tobs1, tobs2, Ndt))

    # interpolate pt and pl values of each panel to the sample receiver time point


    for i = 1:II
            Ax = copy( t_re_IJ [:, i ])
            Ain = copy( pt_tau_IJ [:, i ])
            pt_re_IJ [:, i ] = Interp2Obs(Ain, Ax, t_re_sample )
            Ain = copy( pl_tau_IJ [:, i ])
            pl_re_IJ [:, i ] = Interp2Obs(Ain, Ax, t_re_sample )
    end

    for ite = 1:Ndt
        #display ( ite )
        pt[ ite ] = sum( pt_re_IJ [ ite ,:]) ∗0.25/pi
        pl[ ite ] = sum( pl_re_IJ [ ite ,:]) ∗0.25/pi
    end


    #superimpose for Nblades
    #PT = BladeImpose(pt, Ndt_per, Nb, Ndt)
    #PL = BladeImpose(pl, Ndt_per, Nb, Ndt)
    PT = pt
```

```
    PL = pl

    #display ( plot ( t_re_sample ,PT))
    #display ( plot !( t_re_sample ,PL))

    #output
    fname = outdir *(@sprintf("PMicLT−pmap−%d",iobs))
    fout = open(fname,"w")
    for ite = 1:Ndt
        line = @sprintf("%20.12e %20.12e %20.12e %20.12e\n", t_re_sample[ite ], PT[ite ]+PL[ite ], PT[ite ], PL[ite ])
        write ( fout , line )
    end
    close ( fout )

#OSPL[iobs] = Calc_OSPL(PT+PL)
#line = @sprintf("%d %20.16e\n", iobs, OSPL[iobs])
#write ( fosplout , line )
end
```

Last but not least, the *copy2full.jl* constructs the singal of a full propeller if the input panel is only a fraction:

Listing B.8: copy2full.jl

```
@inline function localRotateZ2 (X::Array{Float64,1}, cs :: Float64, sn :: Float64 )
    #cs= cos(   )
    #sn= sin (   )
    X1 = zeros (Float64 ,3)
    X1[1] = cs*X[1]−sn*X[2]
    X1[2] = sn*X[1]+cs*X[2]
    X1[3] = X[3]
    return X1
end

function copy2full (Nblade, xyzc1, nxyzc1, Pc1, Area1, Npanel::Int64 )
    newNp = Nblade * Npanel
    dazi = 2*pi/Nblade
    println ("copying $Npanel panels to $Nblade blades: $newNp panels\n")
    cxyzc = zeros (newNp, 3)
    cnxyzc = zeros (newNp, 3)
    cPc1 = zeros (newNp)
    cArea = zeros (newNp)
    for ibld = 1:Nblade
        dazi_now = ( ibld −1)*dazi
        cs = cos(dazi_now)
        sn = sin (dazi_now)
        for jp = 1:Npanel
            jpn = ( ibld −1)*Npanel + jp
            #ipn_end = ( ibld )*Npanel
            cxyzc[jpn ,:] = localRotateZ2 (xyzc1[jp ,:], cs ,sn)
            cnxyzc[jpn ,:] = localRotateZ2 (nxyzc1[jp ,:], cs ,sn)
            cPc1[jpn] = Pc1[jp ];
            cArea[jpn] = Area1[jp]
            #cArea[jpn] = Area1[jp]
        end
    end
    return cxyzc, cnxyzc, cPc1, cArea
end
```